

## EFFECT OF GeO<sub>2</sub> DOPANTS IN FBG SENSOR PERFORMANCE FOR TEMPERATURE AND STRAIN<sup>†</sup>

Wasmaa A. Jabbar<sup>a†</sup>, Ayser Hemed<sup>a\*</sup>, Mayyadah Fadhala<sup>b‡</sup>, Ismaeel Al-Baidhany<sup>a§</sup>

<sup>a</sup>Department of Physics, College of Education, Mustansiriyah University, Baghdad, Iraq

<sup>b</sup>Alsalam Distinguished Students Secondary School, 2<sup>nd</sup> Karkh directorate of education, Baghdad, Iraq

\*Corresponding author e-mail: [ayser.hemed@uomustansiriyah.edu.iq](mailto:ayser.hemed@uomustansiriyah.edu.iq), <sup>†</sup>E-mail: [wasmaajabbar@uomustansiriyah.edu.iq](mailto:wasmaajabbar@uomustansiriyah.edu.iq)

<sup>‡</sup>E-mail: [mayads539@gmail.com](mailto:mayads539@gmail.com); <sup>§</sup>E-mail: [ismaeel\\_2000@uomustansiriyah.edu](mailto:ismaeel_2000@uomustansiriyah.edu)

Received May 7, 2023; revised June 19, 2023; accepted June 19, 2023

In this simulation study, the response of fiber Bragg grating (FBG) sensors is investigated and optimized. Uniform and nonuniform FBG spectra with new component are suggested by fine selection with (COMSUL program) and compared theoretically under the effect of several external strain values (0.005, 0.006, 0.007, 0.008, 0.009 and 0.01). These two types operation have been examined by the Optisystem programmer. The measured sensitivity was based on VCSEL laser source with operation wavelengths of 1650, 1600, and 1550 nm via non-uniform and uniform configuration. The achieved sensitivity was found to have different values; 5.7, 2.6, and 1.77, while the highest observed sensitivity value is recorded at a wavelength of 1550 nm. Accordingly, this wavelength was chosen to advance the study. Temperatures of 20, 30, 40, 50, and 60 degrees Celsius were applied. Measured sensitivity between them varied, and satisfied the following functions: sine, Gauss, and Boltzmann indicating altering in sensor responses.

**Key words:** FBG sensor; Bragg wavelength; Elastic-optical coefficient; Thermo-optic effect; Strain-optic effect; Sellmeier formula

**PACS:** 42.81.-i; 42.81. Pa

### INTRODUCTION

Due to their sensitivity, dependability, low intrusiveness, galvanic insulation, and potential for quasi-distributed remote measurements, optical fiber sensors based on fiber Bragg grating (FBG) technology are used in a variety of fields, including civil engineering and aviation [1]. In addition, monitoring strain [2], vibration [3] and temperature [4].

Furthermore, the FBG sensor itself has recently been continuously enriched by research due to its applications in optical communications [5], such as smart frequency filtering [5], [6], [7], dynamical encrypting with chaotic communications [8], [9], [10], [11].

FBGs are extensively utilized in optical sensing and can compete with traditional electrical strain gauges to determine various parameters, such as temperatures, strain, refractive index, pressure, gas, etc. Furthermore, FBG sensors have been widely recognized for their features such as erosion resistance, resistance to electro-magnetic (EMI) and radio frequency interference, and ability to operate in harsh environments where traditional sensors cannot [12].

Since more than few decades, FBG sensors have meets a lot of attention in the field of structural health monitoring [13] [14]. Earlier application of these types of sensors is load screening and characterizing absolute strain and temperature variations, either individually [15] or at the same time [16]. Changes in average strain and temperature would primarily cause a change in the location of the resonance wavelength of the FBG output due to their linear wavelength shift response [17]. The whole reflection spectra of the sensor output signal are, however, affected by the strain (or even temperature) field.

The shape and wavelength shift of the reflection spectra were measured and studied by simulation in this study to investigate the impacts of strain and temperature changes dispersed along the length of FBG sensors. Under these two circumstances, shifts were examined using various FBG architectures.

More benefits than that mentioned above are recorded to FBG based sensors, such as small size, light weight, high resolution, multiplexing capability, and immunity to electromagnetic fields. They have been used in biological diagnosing and structural health monitoring [18]. Due to its uniquely intelligent physical properties, such as its innately huge multiplexing capacities, remote sensing, resistance to electromagnetic fields, and safety, the uniform FBG sensor has been extensively used in sensing applications [12]. The UFBG sensor are also used in dynamical spectral filters invented inside fibers [19].

### THEORETICAL CONCEPTS

The FBG transmits all wavelengths of light while reflecting some due to the periodic (or aperiodic) disruption in the refractive index of its core, known as gratings. The Bragg wavelength, at which there is the most reflection, can be determined by applying the following equation [15]:

$$\lambda_{Br.} = 2n_{eff} \Lambda \quad (1)$$

<sup>†</sup> Cite as: W.A. Jabbar, A. Hemed, M. Fadhala, I. Al-Baidhany, East Eur. J. Phys. 3, 501 (2023), <https://doi.org/10.26565/2312-4334-2023-3-57>

© W.A. Jabbar, A. Hemed, M. Fadhala, I. Al-Baidhany, 2023

where  $n_{eff}$  is the effective refractive index of the grating and  $\Lambda$  is the grating period.

Strain has two distinct impacts on a Bragg grating. First, the grating's Bragg wavelength will shift as a result of the alteration in the physical distance between succeeding index modulations. Second, a change in refractive index brought on by the strain-optic effect will result in a shift in the Bragg wavelength. For a specific change in strain, the change in a Bragg grating's center wavelength is given by [20]:

$$\Delta\lambda_{Br.} = 2 \left[ \Lambda \frac{\partial n_{eff}}{\partial l} + n_{eff} \frac{\partial \Lambda}{\partial l} \right] \Delta l \tag{2}$$

where  $l$  is the effective length.

An optical fiber's strain effect is depicted in equation (2). This is consistent with a shift in grating spacing and the strain-optic-induced shift in refractive index. [20]. Under the condition of a uniform strain along the optical fiber axis and no temperature changes, the wavelength shift is related to the strain via the elastic-optical coefficient  $\mathcal{P}e$  [20]:

$$\Delta\lambda_{Br.} = \lambda_{Br.} (1 - \mathcal{P}e) \varepsilon \tag{3}$$

Equation (3) points out that the resulted shift in Bragg peak wavelength is linearly proportional to the applied strain. In the sensing theory of FBG, the strain value should be expressed as;

$$\varepsilon = \frac{\Delta\lambda_{Br.}}{\lambda_B(1-\mathcal{P}e)} \tag{4}$$

where  $\varepsilon$  is the strain along the lengthwise direction of the fiber and  $\mathcal{P}e$  is an effective strain optic constant, which is defined as [1]:

$$\mathcal{P}e = \frac{n_{eff}^2}{2[\mathcal{P}_{12} - \nu(\mathcal{P}_{11} + \mathcal{P}_{12})]} \tag{5}$$

Such that  $\mathcal{P}_{11}$  and  $\mathcal{P}_{12}$  are strain-optic tensor two components, and  $\nu$  is the ratio of Poisson. For a typical Germano-Silicate optical fiber,  $p_{11} = 0:113$ ,  $p_{12} = 0:252$ ,  $\nu = 0:16$ , and  $n_{eff} = 1.45$ , giving [21]  $\mathcal{P}_{12} = 0:213$ .

### SIMULATION PART

#### Selection for refractive index concentration by COMSOL Software

By applying the last values in eq. (5), we got the value of  $\mathcal{P}e$  (effective strain optic constant). The calculated value of  $\mathcal{P}e$  was then used in eq. (3) for the specific wavelengths 1550, 1600, and 1650 nm for each strain value (0.005, 0.006, 0.007, 0.008, 0.009). Finally, we got the values of shift in wavelength for each value of strain, and for each wavelength, as shown in tables 1, 2, and 3.

Via COMSOL simulation, numerical Finite Element Method (FEM) has been used for the modal analysis of an optical fiber. This fiber is designed to investigate the effect of doping concentration of both core and clad silica glass to the application as a sensor. The variation of the effective refractive index has a significant impact on the sensitivity of such fiber sensors. The influence of doping silica optical fiber with Ge in a different concentration. Also doping concentration effect on effective refractive index and optical intensity has been. The refractive index has been calculated for the doped silica fiber with Ge samples by Sellmeier formula:

$$n(\lambda) = \left[ 1 + \sum_{i=1}^M \frac{A_i \lambda^2}{\lambda^2 - \lambda_i^2} \right]^{1/2} \tag{6}$$

For dopants  $GeO_2$ ,  $n$  is the optical index at light wavelength  $\lambda$  and  $\lambda_i$  is a constant such that  $\lambda_1, \lambda_2, \lambda_3$  and  $A_1, A_2, A_3$  are called Sellmeier coefficients to be determined by the fitting process. This means measuring the refractive index of the medium at least for six different wavelengths. In this study, identical last coefficients are calculated, to approximate the dispersion curve.

#### Measurement of temperature by FBGs

Measurement of temperature, a crucial parameter in various sectors of industry, can be done with the help of FBGs. As reported by Ref. [22], both low and high temperatures can be measured using FBGs with equal accuracy. However, practically measurement of high temperature with FBGs poses some additional challenges compared to others. In this section, we shall discuss the FBG-based temperature sensors subjected to no variation in other physical parameters of the FBG.

#### Analytical formulation for temperature measurement

The Bragg wavelength ( $\lambda_B$ ) of an FBG can be expressed as [23] [17]:

$$\lambda_{Br.}(T) = 2n_{eff}(T)\Lambda(T) \tag{7}$$

Hence, a small change in operating temperature  $T$  will result a change in the peak wavelength which can be represented as [17]:

$$\delta\lambda_{Br.} = \frac{d\lambda_{Br.}}{dT} \delta T = 2 \left( \Lambda \frac{dn_{eff}}{dT} + n_{eff} \frac{d\Lambda}{dT} \right) \delta T = \lambda_{Br.} \left( \frac{1}{n_{eff}} \frac{dn_{eff}}{dT} + \frac{1}{\Lambda} \frac{d\Lambda}{dT} \right) \delta T \quad (8)$$

So, the change in the temperature can be retrieved directly from  $\Delta\lambda$  [24]:

$$\lambda_{Br.} = \lambda_{Br.} (\alpha_{n,T} + \alpha_{\Lambda,T}) \delta T = \lambda_{Br.} (\xi + \beta_T) \delta T \approx \lambda_{Br.} \xi \delta T \quad (9)$$

Therefore, it is possible to control the mechanical and thermal expansion coefficients by changing the cross-section characteristics. It is important that the packaging allows for a limited range of temperature variation. At high temperatures approaching the melting point of the packaging material, the packaging starts to distort whereby the Young's modulus begins to change and thus the thermal expansion coefficient will no longer exist. The work has been done on achieving the highest sensor sensitivity [25].

### Simulation set-up design for FBG operation by Optisystem software

As given in Figure (1), a VCSEL laser source with 1550 nm operation wavelength is selected to submit the optical signal. This source is followed with a directional coupler with equivalent splitting ratio. One of these two new paths is considered as a reference path, while the remaining path represents the tested path. Both reference and tested paths include a distinct FBG, i.e., the refence one contains a standard Uniform FBG sensor, the remaining path contains a laboratory Nonuniform FBG sensor. Two types of observation tools are connected, which are, Optical spectrum analyzers (OSA) and optical time domain, virtual oscilloscopes (OTV) both for track the development for passed signals during the experiment conditions variations.

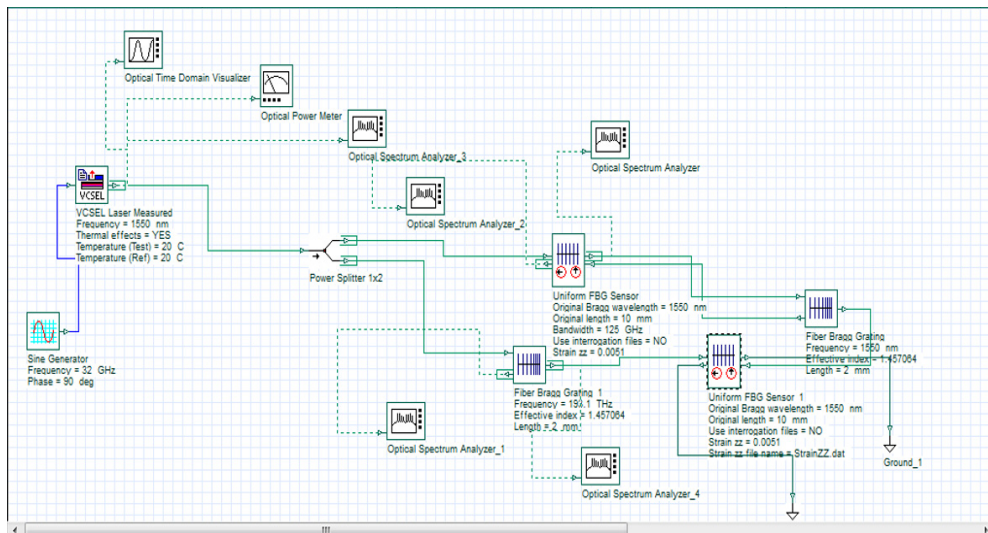


Figure 1. Simulation set-up for the investigated design.

## RESULTS AND DISCUSSION

The two types of suggested FBGs have identical constant Bragg wavelengths before the application of the external environmental effect. Original effective length in the software is changed by values 10, 20, 30 all in mm units. The selected effective refractive index for both FBGs is  $n_{eff}=1.45$ , with length of 2mm.

### Measurements for UFBG

#### Effect of strain on sensing wavelength shift

Three Bragg wavelengths ( $\lambda_{Br.}$ ) for investigated FBG sensors were tested, these wavelengths are: 1550, 1600 and 1650 nm. Calculations for the deflected wavelength shift is carried out manually and individually for each wavelength by using of eq. (5). Where the measured shifts are resulted from the virtually applied strain. The latter effect selected values are: (0.005, 0.006, 0.007, 0.008, 0.009, 0.01)  $\mu\text{m}$ , as shown in tables 1.

Table 1. Theoretical computed wavelengths shift for tested UFBGs sensors  $\lambda_{Br.}$

| Initial wavelength $\lambda_{Br.}$ (nm) | Strain Experienced by FBG | Wavelength shift (nm) |
|---|---------------------------|-----------------------|
| 1550                                    | 0.005                     | 6.1987755             |
|   | 0.006                     | 7.4385306             |
|   | 0.007                     | 8.6782857             |
|   | 0.008                     | 9.9180408             |
|   | 0.009                     | 11.1577959            |
|   | 0.01                      | 12.397551             |

| Initial wavelength $\lambda_{Br}$ (nm) | Strain Experienced by FBG | Wavelength shift (nm) |
|--|---------------------------|-----------------------|
| 1600                                   | 0.005                     | 6.398736              |
|  | 0.006                     | 7.6784832             |
|  | 0.007                     | 8.9582304             |
|  | 0.008                     | 10.2379776            |
|  | 0.009                     | 11.5177248            |
| 1650                                   | 0.005                     | 6.5986965             |
|  | 0.006                     | 7.9184358             |
|  | 0.007                     | 9.2381751             |
|  | 0.008                     | 10.5579144            |
|  | 0.009                     | 11.8776537            |
|  | 0.01                      | 13.197393             |

Results for the first run measurements are given in the following table (2) and resulted relations are shown in the next Figure (2).

**Table 2.** Calculated sensitivity for indicated UFBGs sensors  $\lambda_{Br}$ .

| Bragg wavelength value $\lambda_{Br}$ (nm) | Sensitivity ( $\text{pm}/^\circ\text{C}$ ) |
|--|--|
| 1550                                       | 5.7  |
| 1600                                       | 2.6  |
| 1650                                       | 1.77                                       |

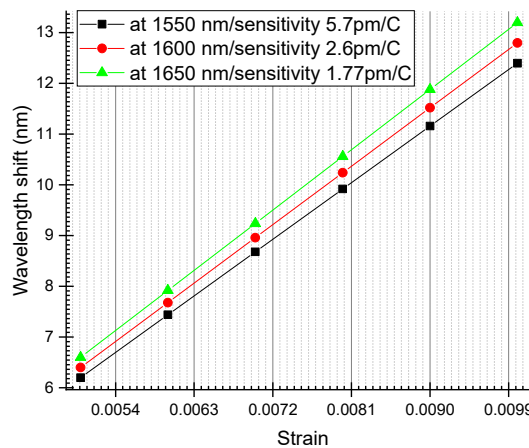


**Figure 2.** Resulted for strain – wavelength relations to the tested UFBGs sensor.

According to calculated results for sensitivity given in table (4), the selection is located at the maximum value, which is  $5.7 \text{ pm}/^\circ\text{C}$  which corresponds to 1550 nm. A strain–wavelength relation, with an effective wavelength of 1.45, is plotted in Figure (2), and the resultant shape is followed by a linear fitting. Accordingly, from Figure (2), part A, 1550 nm, the maximum measured sensitivity value is (5.7) corresponding to wavelength (1550) with a sensitivity of  $5.7 \text{ pm}/^\circ\text{C}$ , while in the same figure, part B, 1600nm, the maximum measured sensitivity value is (2.6) corresponding to wavelength (1600) with a sensitivity of  $2.6 \text{ pm}/^\circ\text{C}$ , finally in part C, 1650nm, the maximum measured sensitivity value is (1.77) corresponding to wavelength (1650) with a sensitivity of  $1.77 \text{ pm}/^\circ\text{C}$ .

### Effect of temperature on sensing wavelength shift

In current study, the stabilization of type I gratings complies with telecommunication requirements, thus the selected temperature range is 20-60 °C, this is based on range given in Ref. [26]. In the following Figure (2), deflected measured Bragg wavelength shift is plotted against sensitivity for seven temperature values, all ranging from 20 to 60 °C. The FBGs parameters are as follows: effective refractive index of 1.45, length 2mm, wavelength of 1550nm. The temperature and wavelength are changing as given in Figure 3(A), for an original length of 10 mm.

Temp. values range from 20.3331 to 60.067°C, while wavelengths range from 1.549976 nm to 1.54995272 nm. While in the same figure, part (B), for the original length of 20mm, T values range from 20.0353 to 60.0672135°C, but wavelength range from 1.54997726 to 1.54997686 nm. In part (C) from the same figure, for an original length of 30mm, the temperature ranges from 19.9327865, to 59.9646844 °C, but the wavelength is now ranging from 1.54991417 to 1.54995338 nm. In part (D), after doping, T values range from 20.0353156 to 59.8735475 °C, but wavelengths range from 1.54984538 to 1.54984468 nm.

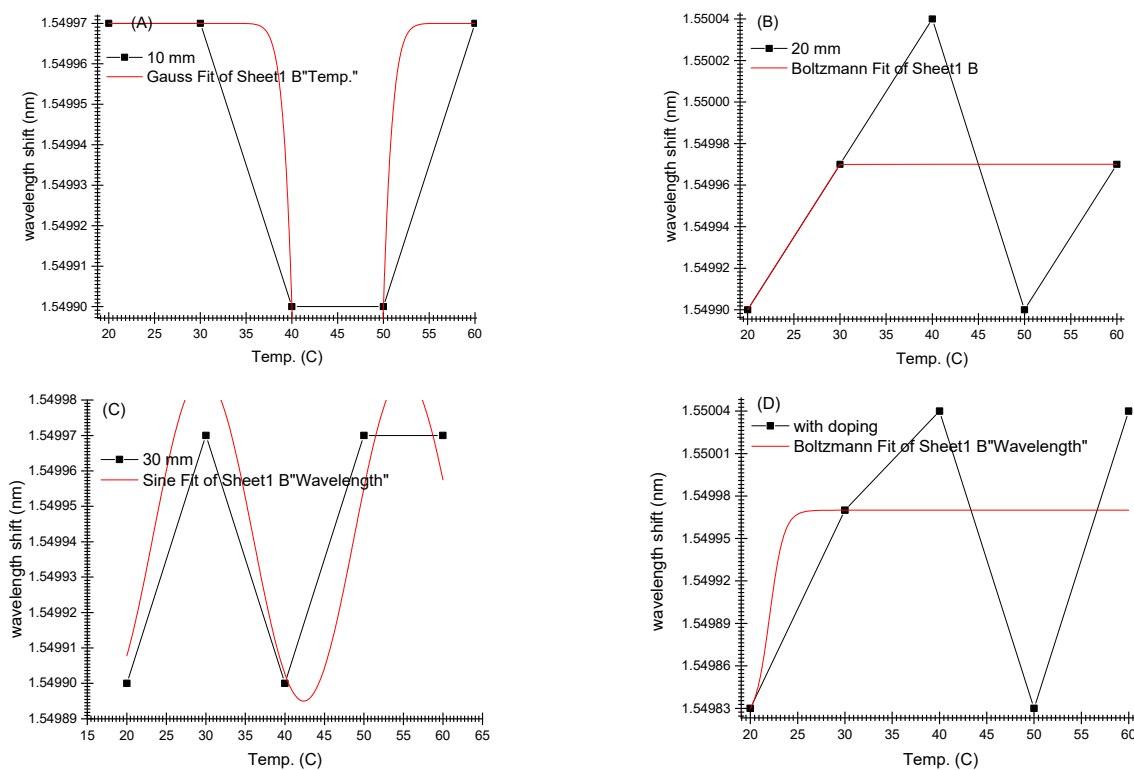


**Figure 3.** Results for temperature – shifted wavelengths with changed sensor temp. (A) L=10mm, (B) L=20mm, (C) L=30mm (D) after doping

For the same previous set-up, the transmitted power spectrum is observed separately for each FBG applied temperature. Results are given in the following Figure (4), with which transmitted power behavior fluctuates from sine function to Gauss. The temperature and wavelength are changed as the following form: in part (A) for the original length 10mm from 20.0353156 to 60.1583504 °C, but the transmitted power (TR) was changed from TR=8.96362864 to 9.02625248 °C. In part (B), for the original length of 20mm, T is changed from 20.0353156 to T=60.0672135 °C, but the transmitted power is changed from TR=8.49448061 to 8.5161336 °C. Finally, in part (C), T is changed from 20.4226475 to 60.0672135 °C, while the transmitted power is changed from TR = 7.4483448 to 7.45740164 °C.

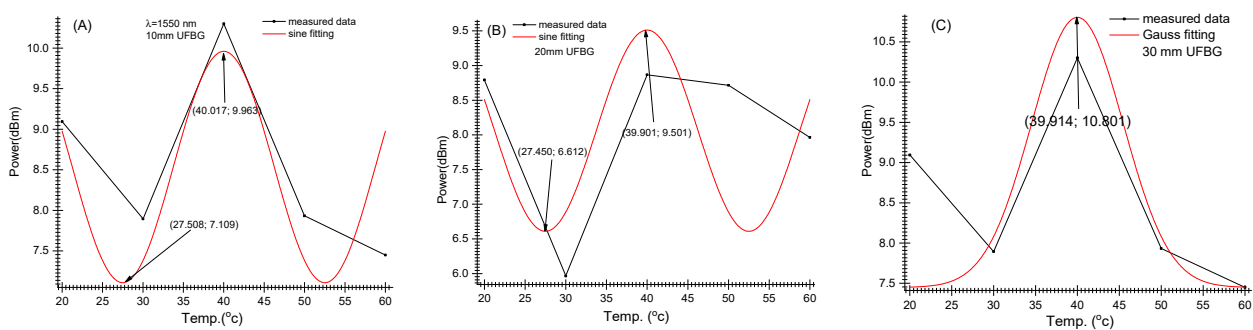


**Figure 4.** Results for power- temperature variation in UFBG with lengths; 10 mm (B) 20 mm and, (C) 30 mm

**Measurements of NUFBG**

**Effect of temperature on sensing wavelength shift**

In this section, insertion of a signal of 1550 nm wavelength into the input of NUFBG has been carried out where the FBG has specific active lengths; 10, 20, and 30mm and a constant effective refractive index of 1.45 with variable applied temperature. Results observed from the deflection side give different responses, as shown in Figure (5) and its entire subfigures A, B, C and D based on equation (6). As shown in part (A), the FBG active length was 10mm from T=20.1264 °C to T=59.9646844°C, but the wavelength ranged from 1.54989965 nm to 1.54996984 nm, as shown in part (A). The FBG active length was 20 mm from T = 20.1264525°C to T = 59.9646844°C in part (B), but the wavelength ranged from 1.54992244 nm to 1.54984271 nm in part C. Finally, in part D, after doping, the effective refractive index is constant at 1.46 with variable applied temperature gives different responses as deflected wavelengths from T=19.8416496 °C to T=5 8735°C. The wavelengths are 1.54996967 nm to 1.54984357 nm.

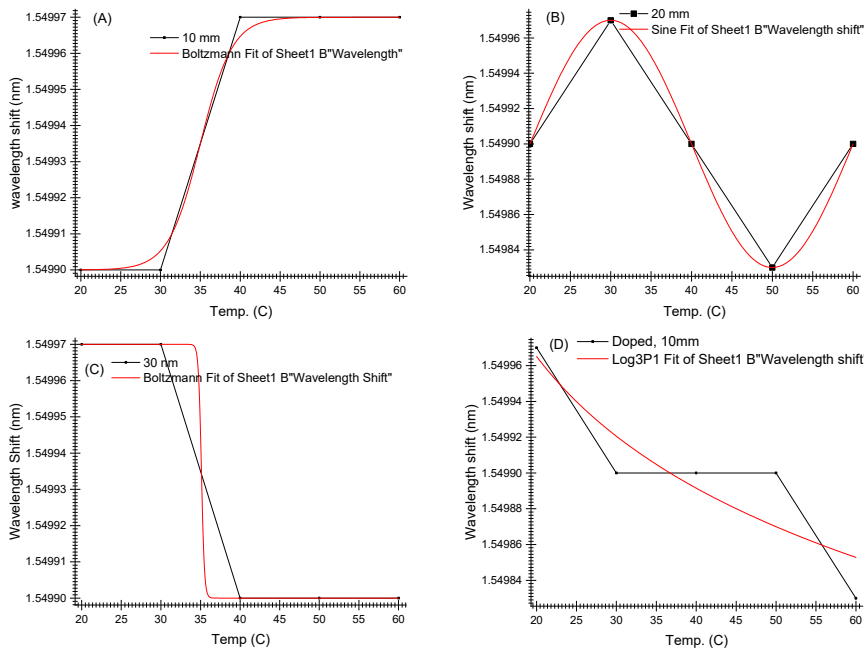


**Figure 5.** Results for shifted wavelength – applied temperature for a NUFBG with lengths (L) in mm. (A)10, (B) 20, (C) 30 and (D) 10, after doping

These results indicate the existence of three types of behavior functions followed by the NUFBG under the influence of applied temperature. In the dopant case, these two functions are Boltzmann and sine in additional logarithm. Under the influence of variable applied temperature, we expect to meet a different response than that measured by UFBG. Previous results shown in Figure (3), indicates the response with only a sine function.

**Effect of temperature on sensing power**

In the case of measuring power instead of wavelength, the results for NUFBG response indicate variant Gauss functions depending on active sensor wavelength, shown in Figure (6). In comparison to last section results, in which the response obeys varied functions. For the same previous setup, transmitted spectrum power is measured for each applied temperature. Observed values for temperature and wavelength is shown inside part (A) from that figure, for the original length of 10 mm. While in part (B) and (C), another observed value is diagnosed. With comparisons by Ref. [27], the current combination is 1.5 times larger sensitivity than it.

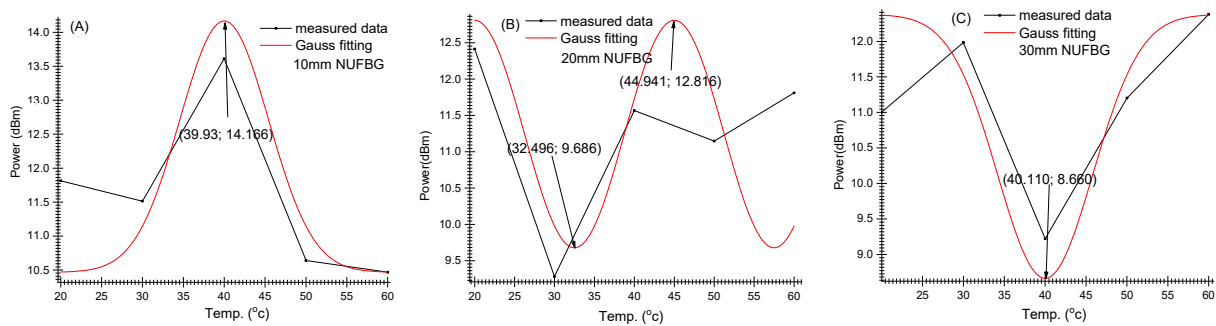


**Figure 6.** Results for power-temperature relations for different NUFBGs lengths (L) in mm. (A) 10, (B) 20 and (C) 30.

Uniform and nonuniform FBG Sensor design of (L=10mm) active length with Bragg wave length 1550 nm tested under temperatures (20- 60 °C) with step 10 degree.

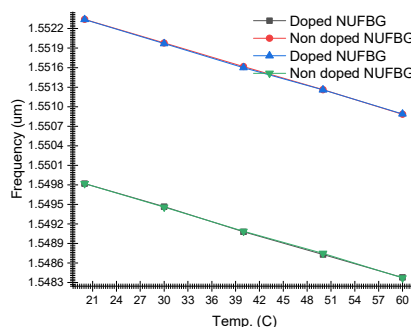


**Figure 7.** Measured values of wavelengths and intensity for uniform FBG before and after doping

Where the values plotted in figure (7) are drawn from radio frequency spectra for all tested values which is given in figure (8). In which the frequency shift is easy to observe versus the changed parameter in comparisons with multi regions FBG that experimentally investigated by Ref. [6].

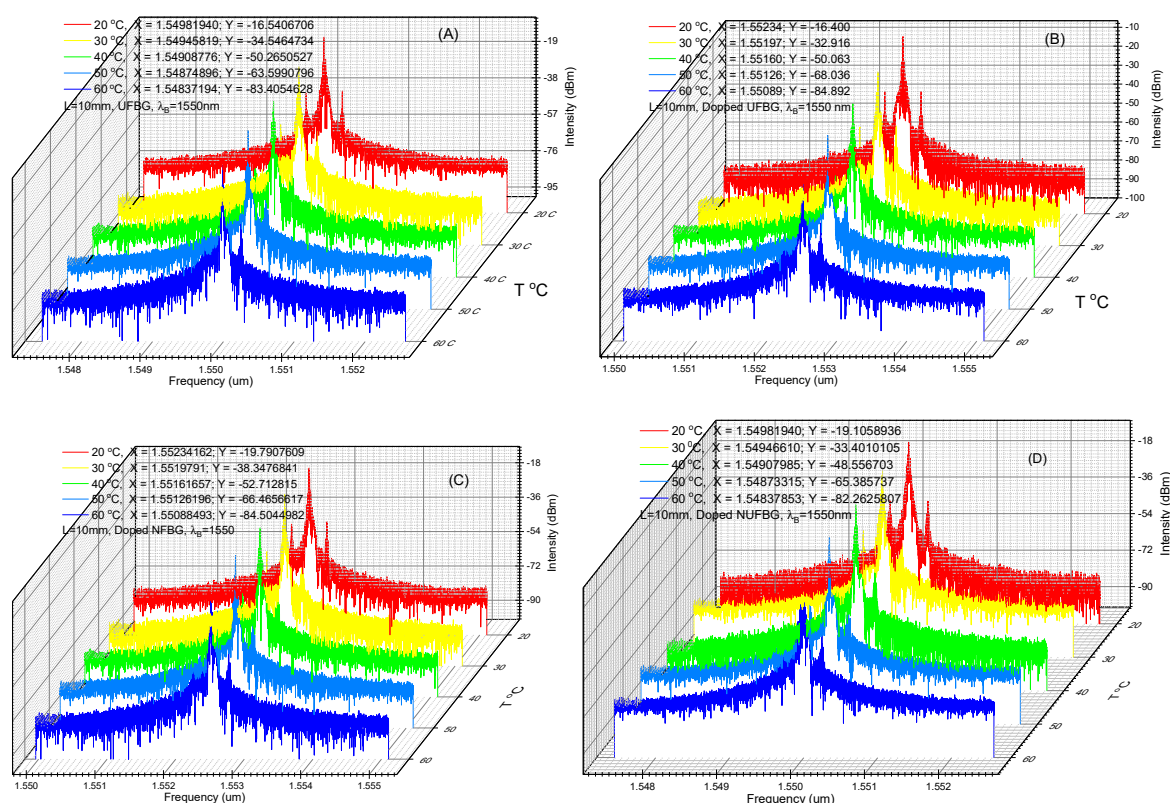


**Figure 8.** Results for reflected spectra shift for: (A) Non-doped UFBG, (B) Doped UFBG, (C) Non-doped NUFBG, and (D) Doped NUFBG.

## CONCLUSIONS

Constructing FBG combination improves the sensing properties for the FBG sensor. Uniform and non-uniform FBGs plays the role of precise filter to the temperature and strain fluctuations. The sensitivity becomes high with introducing impurities of GeO<sub>2</sub> dopants. Results for shifted wavelength – applied temperature for a NUFBG shows variations from Poltzman to Log. Functions, while the same measurements for power-temperature relations for lengths shows behaviors fluctuated within one function which is a Gauss function.

**Acknowledgement:** Authors for the study would like to thank Mustansiriyah University ([www.uomustansiriyah.edu.iq](http://www.uomustansiriyah.edu.iq)) Baghdad, Iraq for support in the present work.

## ORCID

© Ayser Hemed, <https://orcid.org/0000-0003-0319-1650>; © Wasmaa A. Jabbar, <https://orcid.org/0000-0003-3966-9468>  
© Ismaeel Al-Baidhany, <https://orcid.org/0000-0001-5273-9921>

## REFERENCES

- [1] B.A. Tahir, M.A. Saeed, A. Ahmed, S.M.Z. Iqbal, R. Ahmed, M.G.B. Ashiq, H.Y. Abdullah, and R.A. Rahman, "Effect of Sensor Gauge Length on Strain Sensitivity of a Fiber Bragg Grating System," *Chinese Journal of Physics*, **49**(5), 1035-1045 (2011).
- [2] J. Zhou, Z. C. Orcid, P. Zhao, and A. Tang, "Efficient Sensor Placement Optimization for Shape Deformation Sensing of Antenna Structures with Fiber Bragg Grating Strain Sensors," *Sensors*, **18**(8), 2481 (2018). <https://doi.org/10.3390/s18082481>
- [3] F. Xiao, G.S. Chen, and J.L. Hulsey, "Monitoring Bridge Dynamic Responses Using Fiber Bragg Grating Tiltmeters," *Sensors (Basel)*, **17**(10), 2390 (2017). <https://doi.org/10.3390/s17102390>
- [4] Y. Liu, and J. Zhang, "Model Study of the Influence of Ambient Temperature and Installation Types on Surface Temperature Measurement by Using a Fiber Bragg Grating Sensor," *Sensors*, **16**(7), 975 (2016). <https://doi.org/10.3390/s16070975>
- [5] M. Fdhala, and S.M. Khorsheed, "Characterization of Uniform FBG sensor Operation for Signal Filtering Application," *European Journal of Advances in Engineering and Technology*, **7**(2), 1-6 (2020).
- [6] A.A. Hemed, M.M. Fdhala, and S.M. Khorsheed, "Modified superstructure fiber Bragg grating for a filter application," *Kuwait J. Sci.* **49**(1), 1-18 (2022). <https://doi.org/10.48129/kjs.v49i1.12487>
- [7] S.M. Khorsheed, A.A. Hemed, and M.M. Fdhala, "Investigation of Performance for a Two Regions Superstructure Fiber Bragg Grating," *World Scientific News*, **137**, 42-57 (2019). <http://www.worldscientificnews.com/wp-content/uploads/2019/09/WSN-137-2019-42-57.pdf>

- [8] Z.R. Ghayib, and A.A. Hemed, "Simulating chaotic dynamics with variable polarisation of VCSEL twin lasers using FBG as a dynamic sensor," *Pramana – J. Phys.* **96**, 86 (2022). <https://doi.org/10.1007/s12043-022-02305-2>
- [9] Z.R. Ghayib, and A.A. Hemed, "Smart control for the chaotic dynamics using two regions uniform fiber Bragg grating," *Optoelectronics and advanced materials-Rapid communications*, **16**(7-8), 307-318 (2022).
- [10] A.A. Hemed and Z.R. Gaiab, "Chaotic Dynamics for VCSEL Subjected to Time Delayed and Filtered Injection Using FBG Array Sensor," in: *2022 International Conference on Computer Science and Software Engineering (CSASE)*, Duhok, Iraq, 2022. pp. 194-200, <https://doi.org/10.1109/CSASE51777.2022.9759612>
- [11] A.A. Hemed, Z.R. Ghayib and H.G. Rashid, "Controlling a chaotic anti-synchronized oscillator by a phase interplayed optical injected seed with an FBG sensor," in: *2nd International Conference on Physics and Applied Sciences (ICPAS 2021) 2nd International Conference on Physics and Applied Sciences (ICPAS 2021)*, College of Education, Mustansiriyah University, Baghdad, Iraq, (2021). <https://doi.org/10.1088/1742-6596/1963/1/012063>
- [12] Q.-b. Wang, H.-t.Z.Y. Qiu, J.-a. Chen, Y.-y. Wang, and Z.-m. Fan, "Analysis of strain transfer of six-layer surface-bonded fiber Bragg gratings," *Applied Optics*, **51**(8), 4129-4138 (2012). <http://dx.doi.org/10.3390/app8071171>
- [13] I.A. Naseef, A.I. Mahmood, A.A. Jabor, M.M. Azzawi, S.A. Kadhim, N.F. Muhammed, and W.A. Jabbar, "Characterization study of modified cladding optical fibre sensor for low radiation dosimeters," *AIP Conference Proceedings*, **2290**, (2020). <https://doi.org/10.1063/5.0027535>
- [14] W.A. Jabbar, N.F. Muhammad, S.A. Kadhim, A.H. Dagher, A.I. Mahmood, and I.A. Naseef, "Investigation the doping influence on the characteristics of optical fiber for radiation dosimeter applications," *Materials Today: Proceedings*, **20**, 524-530 (2020). <https://doi.org/10.1016/j.matpr.2019.09.181>
- [15] Y.-J. Rao, "In-fibre Bragg grating sensors," *Measurement Science and Technology*, **8**(4), 355 (1997). <https://doi.org/10.1088/0957-0233/8/4/002>
- [16] Y. Mizutani, and R.M. Groves, "Multi-Functional Measurement Using a Single FBG Sensor," *Experimental Mechanics*, **51**(9), 1489-1498 (2011). <https://doi.org/10.1007/s11340-011-9467-2>
- [17] R. Kashyap, *Fiber Bragg Gratings 2nd Edition*, (Academic Press, Montréal, 2009).
- [18] K. Grattan, and T. Sun, "Fiber optic sensor technology: an overview," *Sensors and Actuators A: Physical*, **82**(1-3), 40-61 (2000). [https://doi.org/10.1016/S0924-4247\(99\)00368-4](https://doi.org/10.1016/S0924-4247(99)00368-4)
- [19] A.S Mansour, and F.M. Abdulhussein, "Dual Measurements of Pressure and Temperature With Fiber Bragg Grating Sensor," *Al-Khwarizmi Engineering Journal*, **11**(2), 86-91 (2015). <https://www.iasj.net/iasj/pdf/eef5012601618008>
- [20] J. Frieden, J. Cugnoni, J. Botsis, and T. Gmür, "Low energy impact damage monitoring of composites using dynamic strain signals from FBG sensors – Part II: Damage identification," *Composite Structures*, **94**(2), 593-600 (2012). <https://doi.org/10.1016/j.compstruct.2011.08.025>
- [21] A. Onoufriou, K. Kalli and G. E. Kohnke, "Fiber Bragg Gratings: Fundamentals and Applications in Telecommunications and Sensing," *Physics Today*, **53**(5), 61-62 (2000). <https://doi.org/10.1063/1.883086>
- [22] C.V.N. Bhaskar, S. Pal, and P.K. Pattnaik, "Recent advancements in fiber Bragg gratings based temperature and strain measurement," *Results in Optics*, **5**, 100130 (2021). <https://doi.org/10.1016/j.rio.2021.100130>
- [23] K.O. Hill, and G. Meltz, "Fiber Bragg grating technology fundamentals and overview," *Journal of Lightwave Technology*, **15**(8), 1263-1276 (1997). <https://doi.org/10.1109/50.618320>
- [24] E.S.D.L. Filho, M.D. Baiad, M. Gagné, and R. Kashyap, "Fiber Bragg gratings for low-temperature measurement," *Optics Express*, **22**(22), 27681-27694 (2014). <https://doi.org/10.1364/OE.22.027681>
- [25] M.R. Mokhtar, T. Sun, and K.T.V. Grattan, "Bragg Grating Packages With Nonuniform Dimensions for Strain and Temperature Sensing," *IEEE Sensors Journal*, **12**(1), 139-144 (2012). <https://doi.org/10.1109/JSEN.2011.2134845>
- [26] M. Cavillon, M. Lancry, B. Poumellec, Y. Wang, J. Canning, K. Cook, T. Hawkins, P. Dragic, and J. Ballato, "Overview of high temperature fibre Bragg gratings and potential improvement using highly doped aluminosilicate glass optical fibres," *Journal of Physics: Photonics*, **1**(4), 042001 (2019). <https://doi.org/10.1088/2515-7647/ab382f>
- [27] J. Lai, J. Qiu, H. Fan, Q. Zhang, Z. Hu, J. Wang, and J. Chen, "Fiber Bragg Grating Sensors-Based In Situ Monitoring and Safety Assessment of Loess Tunnel," *Journal of Sensors*, **2016**, 8658290 (2016). <https://doi.org/10.1155/2016/8658290>

### ВПЛИВ ДОПАНТІВ GeO<sub>2</sub> НА ХАРАКТЕРИСТИКИ ДАТЧИКА FBG ДЛЯ ТЕМПЕРАТУРИ І ДЕФОРМАЦІЇ

Васма А. Джаббар<sup>а</sup>, Айсер Хемед<sup>а</sup>, Майяда Фадхала<sup>б</sup>, Ісмаїл Аль-Байдхані<sup>а</sup>

<sup>а</sup>Кафедра фізики, педагогічний коледж, університет Мустансірія, Багдад, Ірак

<sup>б</sup>Середня школа видатних учнів Алсалам, 2-й Карх директорат освіти, Багдад, Ірак

У цьому моделювальному дослідженні досліджується та оптимізується відгук датчиків волоконної брегівської решітки (FBG). Рівномірні та неоднорідні спектри FBG з новим компонентом пропонуються шляхом тонкого відбору за допомогою (програма COMSUL) і теоретично порівнюються під впливом кількох значень зовнішньої деформації (0,005, 0,006, 0,007, 0,008, 0,009 і 0,01). Ці два типи роботи були перевірені програмістом Optisystem. Вимірною чутливістю була заснована на лазерному джерелі VCSEL з робочими довжинами хвиль 1650, 1600 і 1550 нм через нерівномірну та однорідну конфігурацію. Виявлено, що досягнута чутливість має різні значення; 5,7, 2,6 та 1,77, а найбільше значення чутливості спостерігалось на довжині хвилі 1550 нм. Відповідно, ця довжина хвилі була обрана для просування дослідження. Застосовувалися температури 20, 30, 40, 50 і 60 градусів Цельсія. Вимірною чутливістю між ними змінювалася та задовольняла такі функції: синус, Гаусс і Больцман, що вказує на зміну відповідей датчика.

**Ключові слова:** датчик FBG; довжина хвилі Бреґґа; пружно-оптичний коефіцієнт; термооптичний ефект; тензооптичний ефект, формула Зелмайєра

## CHARACTERIZATION STUDY OF DOUBLE FILTERED SENSOR LENGTH EFFECT ON STRAIN SENSITIVITY<sup>†</sup>

Wasmaa A. Jabbar<sup>a\*</sup>, Ayser Hemed<sup>a†</sup>, Mayyadah Fadhala<sup>b‡</sup>, Ismaeel Al-Baidhany<sup>a§</sup>

<sup>a</sup>Department of Physics, College of Education, Mustansiriyah University, Baghdad, Iraq

<sup>b</sup>Alsalam Distinguished Students Secondary School, 2<sup>nd</sup> Karkh directorate of education, Baghdad, Iraq

<sup>†</sup>Corresponding author e-mail: [ayser.hemed@uomustansiriya.edu.iq](mailto:ayser.hemed@uomustansiriya.edu.iq),

\*E-mail: [wasmaajabbar@uomustansiriya.edu.iq](mailto:wasmaajabbar@uomustansiriya.edu.iq), ‡E-mail: [mayads539@gmail.com](mailto:mayads539@gmail.com); §E-mail: [ismaeel\\_2000@uomustansiriya.edu.iq](mailto:ismaeel_2000@uomustansiriya.edu.iq)

Received April 15, 2023; revised June 7, 2023; accepted June 8, 2023

In this simulation study, Optisystem 18 software is used to monitor and study the effectiveness of side strain on selected lengths of two virtual uniform fiber Bragg grating (FBG) sensors. The operational FBG sensor Bragg wavelength was 1550 nm, which is used to find the measured shift in deflected light source optical spectrum. This value is also supplied by the light source to offer the minimum absorption and attenuation during transmission inside the optical fiber. Reliability of the sensor and technique of transferring the signal under such effect are screened. The investigation is also used to observe the shift in wavelength with altered applied side strain. The influence of sensor active length on side strain sensitivity is studied where according to theory, the length of the FBG influences the sensitivity via reflectivity  $R$ . The constructed sensor sensitivity is observed against length before and during the experiment. The sensing principle, in essence, depends on tracking the wavelength shift due to the variation of such strain. Results achieved in this study show an inverse relationship between sensor effective length and shift in the observed wavelength. The measured strain sensitivity is carried out for the active sensor length, which ranges from 0.05 to 15 cm, with corresponding sensitivity values of 1.19 pm/°C to 0.9 pm/°C, respectively, under the same strain conditions. The empirical results also show the success of the suggested sensing system in measuring strain. The strain measurement,  $\epsilon$ , is linearly increasing, identical to the increasing values of the wavelength shift of Bragg. It's also been observed that the wavelength of Bragg is shifting during small ratios in the length protraction of the FBGs.

**Keywords:** Bragg-Grating; Elasto-Optic Effect; Optisystem; Strain-Sensor; Strain-Optic Tensor

**PACS:** 42.81.-i; 42.81. Pa

### INTRODUCTION

Due to its properties such as; high sensitivity, small size, light weight, low price, material qualities, and sensing capabilities, optical fiber has emerged as a possible candidate for sensing applications. Other primary advantages of fiber optic sensors are chemical passivity, high temperature tolerance, immunity to electromagnetic interference, and long life with the possibility of usage in a hazardous environment [1]. Optical fiber sensors based on FBG technology, from the other hand, included additional advantages such as sensitivity, reliability, low intrusiveness, galvanic insulation, and the possibility to provide quasi-distributed remote measurements. FBGs are extensively utilized in optical sensing and can compete with traditional electrical strain gauges. To determine many parameters such as temperature, strain, refractive index, pressure, etc. FBGs also have many applications in civil engineering and aeronautics [2]. Furthermore, FBG sensors have received widespread recognition for features such as erosion resistance, immunity to electromagnetic and radio frequency interference, and the ability to operate in harsh environments where traditional sensors cannot [3]. For the time being, many interferometry techniques, including Mach-Zehnder and Fabry-Perot, have been suggested for heat sensing implementation [4]. From the other hand, applications with FBGs includes in additional to sensing, laser experiments for chaotic generation in parallel to sensing such as studies listed in Refs. [5] [6] [7].

### THEORETICAL APPROACH

Despite the rotating cross-section of an optical fiber, examine only an average stack, in that the doubled layers are distinct with indices of interleaved of refraction  $n_1$  and  $n_2$ , for core and cladding, respectively, where  $n_1$  differs from  $n_2$  in magnitude to ensure the light guiding [8]. A light beam possessing monochromatic wavelength perpendicularly launches into the stack. Suppose the thickness of all medium layer is controllable, one may discover once the thickness of each layer reaches  $\lambda_B/4$ , in where  $\lambda_B$  is the relative wavelength in the medium, or  $\lambda_B = \lambda_o/n_{avr}$ . where  $n_{avr}$ . is the average index of refractive of the intermediate stack, such that all the reflected waves of light from the stack interfere constructively at the interface where light is injected and give rise to a substantial reflection at wavelength  $\lambda_B$ . If the number of layers is sufficient, and/or the medium stacks refractive index modulation becomes deeper, eventual reflection will approach unity at  $\lambda_B$ . Subsequently, if the above depicted refractive index grating is constructed in the center of the optical fiber, a fiber Bragg grating is produced.

For a single mode fiber, the only mode propagating is  $LP_{01}$ , if the fiber grating pitch is known as the thickness of double layers of neighboring, the FBG condition (first order condition [1]) can then be expressed as [9]:

$$\lambda_B = 2n_{eff}\Lambda \quad (1)$$

where  $n_{eff}$  is the effective core index of refraction for fundamental mode.

<sup>†</sup> Cite as: W.A. Jabbar, A. Hemed, M. Fadhala, I. Al-Baidhany, East Eur. J. Phys. 3, 509 (2023), <https://doi.org/10.26565/2312-4334-2023-3-58>

© W.A. Jabbar, A. Hemed, M. Fadhala, I. Al-Baidhany, 2023

A portion of the propagating light scatters at each grating plane, which causes the scattered light to either transmit or reflect at the grating planes. Destructive interference causes the reflected beams to cancel each other out if they are out of phase. The reflected wave constructively interferes and back-reflects, satisfying the Bragg condition, when the light rays reflected from each grating plane are in phase [1].

The influences of strain on a fiber grating have two-fold; firstly, the alteration in physical spacing between sequential index amendments (fiber grating pitch) will cause a shift of  $\lambda_B$  and, secondly, the strain-optic influence will induce an alteration in the index of the refraction causing additional shift of  $\lambda_B$ . Because of this, a technique to gauge temperature and strain fluctuations has been made possible by changes in these two physical characteristics [1]. Periodic difference in  $\Lambda$  inside the FBG, and the index of refractive affected the deflected wavelength [11]. Altering in last grating parameter due to strain is calculated by the following Equation [10]:

$$\Delta\lambda_B = 2 \left[ \Lambda \frac{\partial n_{eff}}{\partial l} + n_{eff} \frac{\partial \Lambda}{\partial l} \right] \Delta l \quad (2)$$

where  $\Delta\lambda_B$  is the change in Bragg's wavelength and  $l$  is the effective length.

Last equation measures the strain influence on the FBG. This matches the influence of the grating spacing and the strain-optic induced influence in index of refraction [8]. Under the case of a uniform strain along the axis of the optical fiber and no temperature alteration, the shift of wavelength is linked to the strain ( $\epsilon_z$ ) by the coefficient of elastic-optical ( $\rho_e$ ) [8] [10]:

$$\Delta\lambda_B = \lambda_B(1 - \rho_e)\epsilon_z \quad (3)$$

Equation (3) indicates that in the Bragg peak shift of wavelength is proportional to applied strain. In the sensing theory of FBG, the strain value  $\epsilon_z$  should be expressed as

$$\epsilon_z = \frac{\Delta\lambda_B}{\Delta\lambda_B(1-\rho_e)} \quad (4)$$

where  $\epsilon$  is the strain direction along the lengthwise of the fiber,  $\rho_e$  is calculated as the following [11]:

$$\rho_e = \frac{n_{eff}^2}{2[\rho_{12} - \nu(\rho_{11} + \rho_{12})]} \quad (5)$$

here  $\rho_{11}$  and  $\rho_{12}$  are components of the strain-optic tensor, and  $\nu$  is the ratio of Poisson. For a model Germanium-Silicate optical fiber, parameters for last equation are reported in Ref. [11] as the following:  $\rho_{11} = 0.113$ ,  $\rho_{12} = 0.252$ ,  $\nu = 0.16$  and  $n_{eff} = 1.482$ .

A Bragg grating region is a result of a permanent periodic refraction index modulation in the core area of an optical fiber when exposure to UV. The phenomenon of a permanent refractive index change is called photosensitivity, to enhance this effect Germanium is doped into fiber core [1]. The magnitude of the change is also affected by the intensity and duration of the exposure. The operations principle of an FBG sensor are observed by observing the shift in wavelength of the output signal with the variations in the measurement as strain or the light reflected heat using an FBG [12].

There are various kinds of sensors obtainable using optical fiber. It is classified into three kinds: extrinsic, intrinsic, and hybrid [13]. The optical characteristics of intrinsic type are sensitive to strain and temperature [14]. For the information transition to a long-range site, extrinsic is the better option [15] [1]. Here, the length of the FBG influences the sensitivity via reflectivity  $R$ , which is itself function to length of FBG and light wavelength according to the following Equation [1]:

$$R(l, \lambda) = \frac{\Omega^2 \sinh^2(sl)}{\Delta k^2 \sinh^2(sl) + s^2 \cosh^2(sl)} \quad (6)$$

where  $\Delta k$  is detuning of wave vector and  $\Omega$  is a coupling coefficient.

Thus, length term ( $l$ ) in last equation indicate an important factor of the grating when determining its sensitivity. Different groups studied the relationship between the grating length and the sensitivity. When the direction of the highest strain is parallel to the fiber axis, the sensitivity of FBGs to strain in the static is greatest, and it is least sensitive when it is orthogonal to the axis [16]. According to Liang Ren et al., the lateral strain can be neglected in comparison with the longitudinal strain of the fiber [17]. Frieden *et al.* reported that the longitudinal strain predominates on the optical fiber, and the transverse strain sensed by the optical fiber is six times smaller than the surrounding transverse strain, also known as a transverse or traction transverse bending [16].

Ref. [1] has developed FBG sensors which may be applied to scale the kinematics of body, by using optisystem program software. This mode, huge long sensors, is wearable system that may watch most knee flexibility, motion, and all the alterations during the full period of human motion [18].

Based on that, it is very desirable to discuss the variation of the strain sensitivity of FBG sensor systems with a selected sensor length. This work represents an attempt to fulfill such a demand and also to develop a systematic approach for deciding the sensor length corresponding to an application. The focus of this study is to analyze the execution of the sensor while it is being used with a certain strain. Hence, the values of strain that can be applied to analyze the most useful values of strain that can be used on the FBG. The paper calculations were all completed by applying simulation with the software "Optisystem version 18" with the consideration for specific light source wavelength.

**SIMULATION SET-UP**

As shown in Fig. (1), the set-up includes one source of white light, its light is launched into a single mode fiber with 60 Km length. Two uniform FBG sensors, with  $\lambda_B = 1550 \text{ nm}$  receives the light. These two sensors subject to selected values of longitudinal strain, named "zz". Two optical nulls are used to close the effect of back-reflected portion or transmitted light. Observations were recorded by using two optical spectrum analyses and three FBG sensors investigator. FBG 1 can respond to both heat and strain whilst FBG 2 sensors is for only for scaling temperature. The FBG investigator is for display the shift of wavelength from the reflecting spectra of both two FBG sensors, separately. Strain is selected to vary from the value 0.005 to 0.01. All remaining parameters in the Optisystem software follow their default setting.

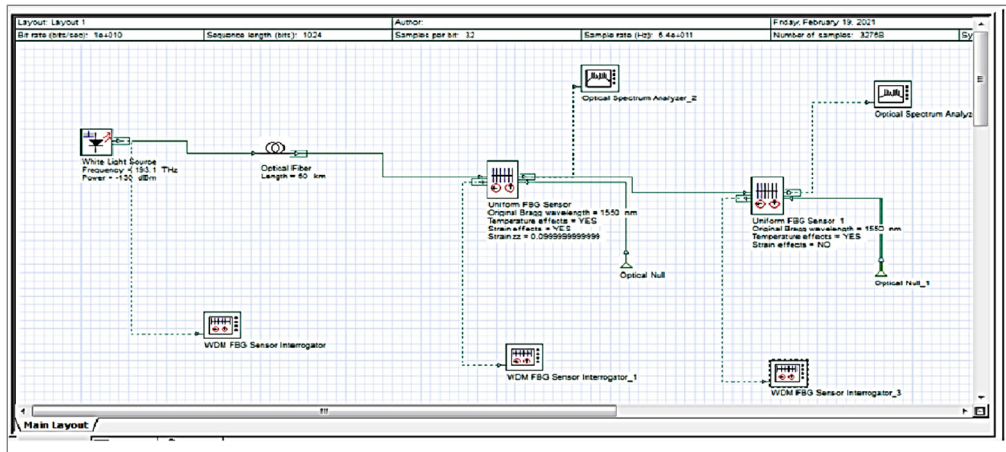


**Figure 1.** Simulation set-up for double-filtered FBG sensor design

**RESULTS AND DISCUSSIONS**

The results are obtained by applying six various values of strain to analyze the effectiveness of axial strain on FBG. The resulted shift in peak wavelength decreased with an increase in axial strain value. For comparisons, the theoretical computation of sensitivity was first performed by applying Equation (3) for the value of temperature (3°C) and strain. Results for the theoretical computation of peak shift by wavelength are shown in Tables (1, 2, and 3) for wavelengths of 1550, 1310, and 980 nm, respectively.

From Figure (2), we found that the sensitivity for each wavelength was different from the other, but the largest sensitivity was found with  $\lambda=1550 \text{ nm}$  which equals 53 pm/pe, so the sensor of wavelength, 1550 nm, was chosen to make a simulation in this work.

**Table 1.** Computation for peak wavelength shift with 1.550 um.

| Initial wavelength $\lambda_B$ (um) | Temperature (°C) | Strain experienced by FBG | Peak wavelength shift (nm) |
|-------------------------------------|------------------|---------------------------|----------------------------|
| 1550                                | 3                | 0.0051                    | 6.63820                    |
|                                     |                  | 0.0061                    | 7.96584                    |
|                                     |                  | 0.0071                    | 9.29348                    |
|                                     |                  | 0.0081                    | 10.6211                    |
|                                     |                  | 0.0091                    | 11.9487                    |
|                                     |                  | 0.01                      | 13.2764                    |

**Table 2.** Calculation of peak wavelength shift with 1310 nm.

| Initial wavelength $\lambda_B$ (nm) | Temperature (°C) | Strain experienced by FBG | Peak wavelength shift (nm) |
|-------------------------------------|------------------|---------------------------|----------------------------|
| 1310                                | 3                | 0.005                     | 5.61035                    |
|                                     |                  | 0.006                     | 6.73242                    |
|                                     |                  | 0.007                     | 7.85449                    |
|                                     |                  | 0.008                     | 8.97656                    |
|                                     |                  | 0.009                     | 10.0986                    |
|                                     |                  | 0.01                      | 11.2207                    |

**Table 3.** Calculation of peak wavelength shift with 980 nm.

| Initial wavelength $\lambda_B$ (nm) | Temperature (°C) | Strain Experienced by FBG | Peak wavelength shifted (nm) |
|-------------------------------------|------------------|---------------------------|------------------------------|
| 980                                 | 3                | 0.005                     | 4.1970                       |
|                                     |                  | 0.006                     | 5.036                        |
|                                     |                  | 0.007                     | 5.875                        |
|                                     |                  | 0.008                     | 6.715                        |
|                                     |                  | 0.009                     | 7.554                        |
|                                     |                  | 0.01                      | 8.394                        |

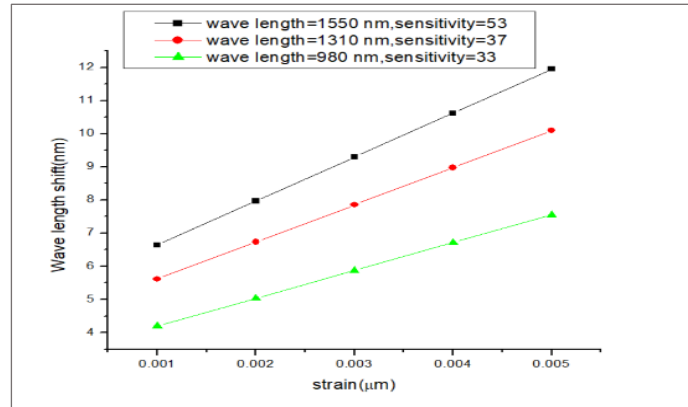


Figure 2. Results for peak wavelength shift experienced by FBG versus strain.

Measured results for wavelength peak shifting according to simulations are given in Table 4. Fig. 3 displays shifting of wavelength against strain experienced by FBG, theoretically. Sensor sensitivity shows directly proportional with increasing of FBG active length within the range (0.05-15 cm). Also increasing the FBG active length shows linear relation between wavelength shift as with applied strain variation showed in the same figure. Fig. 4 displays wavelength peak shift against strain experienced by FBG via simulation. Figure 5 displays comparison between the theoretical calculations and simulation results of the peck shifted of wavelength. The FBG sensor in Optisystem also has strain value limitation that cause the wavelength were shifting when the value of strain changed.

Table 4. Results for peak wavelength shift calculations by simulation

| Initial wavelength $\lambda_B$ (nm) | Temperature change (°C) | Strain experienced by FBG | Peak wavelength shifted (nm) |
|-------------------------------------|-------------------------|---------------------------|------------------------------|
| 1550                                | 3                       | 0.0051                    | 3.370                        |
|                                     |                         | 0.0061                    | 4.054                        |
|                                     |                         | 0.0071                    | 4.718                        |
|                                     |                         | 0.0081                    | 5.392                        |
|                                     |                         | 0.0091                    | 6.000                        |
|                                     |                         | 0.01                      | 6.740                        |

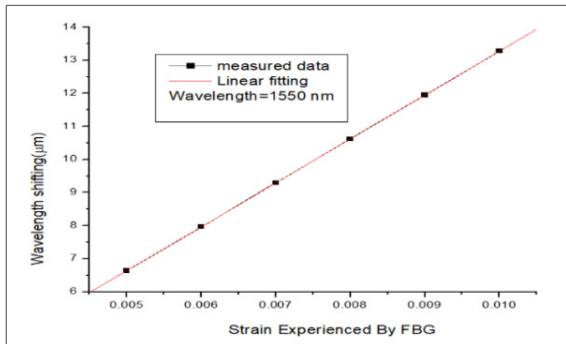


Figure 3. Results for theoretical calculations of shifted-wavelength against strain experienced by FBG

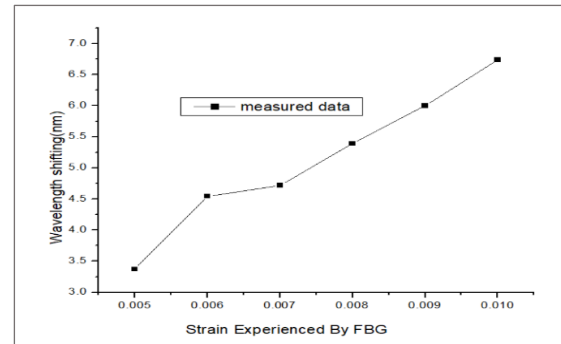


Figure 4. Wavelength peak-shift against the strain experienced by FBG (simulations)

From the Figure (5), the values of simulation and theory weren't the same due to the design of the parameter groups in the simulation software. In addition, there was a special optical fiber composition used in the simulation that could influence the wavelength values via dispersion, as mentioned in theory as material dispersion relations, such as Ref. [19]. Furthermore, the effects of the shift in wavelength in a Bragg grating engraved in fiber with a diameter of 125  $\mu\text{m}$  and the index of effective index  $n_{eff} = 1.4473$ . This result agrees will with experimental work reported by Ref. [20], while simulation results present better behaviors than theoretical calculations in comparison with Ref. [21].

Figure 5 shows the relationship between wavelength shift of three different values of wave lengths and strain of six different values. This work searches for the influence of the length of the sensor on the strain sensitivity of the FBG. Sensitivity for grating region protection, pre-tensioning, the adhesive of the sensor, and the choice of length of the sensor are based on experimental work presented by Ref. [22]. Concerns examined before and during the experimentation structure of an FBG sensor.

In general, an FBG sensor can be made in any length, where for every measurement, the system resolution defines the potential accuracy and precision of its performance. For an FBG sensor system, the strain-to-length relationship is shown in Figure 6. This is an inverse relationship between sensor length and strain. It is concluded that an integer multiplied by the FBG effective length of a longer sensor has a better strain resolution. If the monitoring requirements have a resolution of 1  $\mu\text{m}/\mu\text{e}$  suggested sensor active length will

be (0.05 to 0.15) cm. If the size of the structure is relatively small, then a compromise has to be made between the sensor resolution and gauge length.

According to the operating principle, the grating reflects the various wavelength components of the signal at various points along the grating. Also, it's clear from the transportation that the Bragg wavelength results and the shift of Bragg wavelengths are progressively increased with increased loading. If the used loading is uniform, then the shifting of wavelengths by Bragg happens without amendment to the initial form of the spectrum. The strain of the 0.05 cm sensor was studied versus all results of shifted Bragg wavelengths applied in simulation, as shown in Figure 7. When it is regular, shifts take place without adjustment of the initial spectrum form. The strain is determined from the shift in wavelengths acquired under the used loading. The strain measurement  $\epsilon$ , obtained after computation, is linearly increasing, identical to the increasing shifted Bragg wavelength value. So, a plot between the Bragg wavelength shift and the strain for a 0.05 cm sensor is drawn as a straight line.

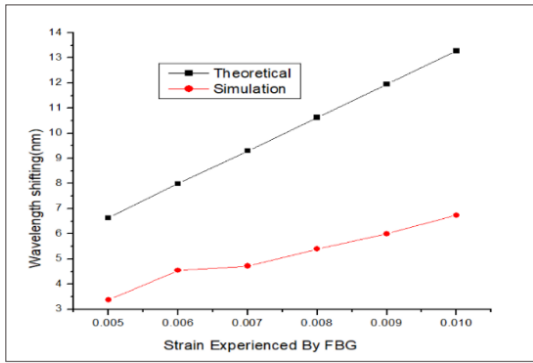


Figure 5. Comparisons between and the simulation and theoretical shifted of wavelength

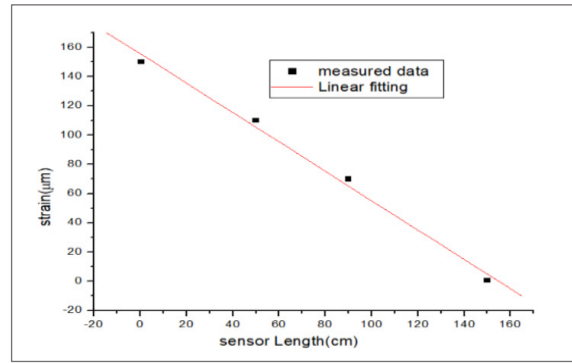


Figure 6. Strain resolution of the FBG sensor (sensor accuracy)

After application of longitudinal tense to FBG, during the test, the first and last identical transmission spectra observed by the optical spectrum analyzer are displayed to proceed the shift of the Bragg wavelength. An alteration in load with sensor length equal to 15 cm is observed in this experiment, as displayed in Fig. 8.

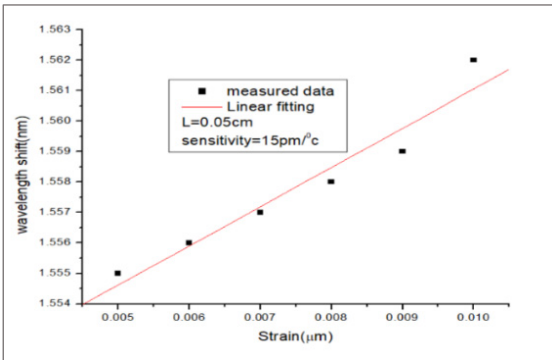


Figure 7. Shift of Wavelength against used strain for the 0.05 cm sensor (simulation)

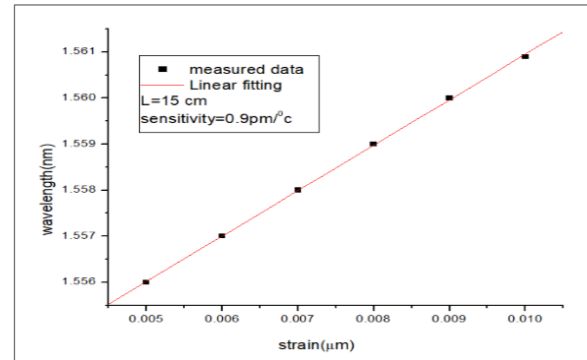


Figure 8. Shift of wavelength against applied strain for the 15 cm sensors length

During the simulation run, the strain measurement for the 15 cm long sensor was studied versus each value of wavelength shift. The strain measurement,  $\epsilon$ , is linearly increasing, identical to the increasing values of the wavelength shift of Bragg. It's also been observed that the wavelength of Bragg is shifting during small ratios in the length protraction of the fiber gratings.

This test is carried out for two different lengths of grating, which are 0.05 and 15 cm. Analysis of the optical spectra was done for the detected signal of Bragg wavelength. Figure 9 shows the relation between wavelength shift and intensity for the wavelengths of 1550 nm, 1310 nm, and 980 nm on strain sensitivity.

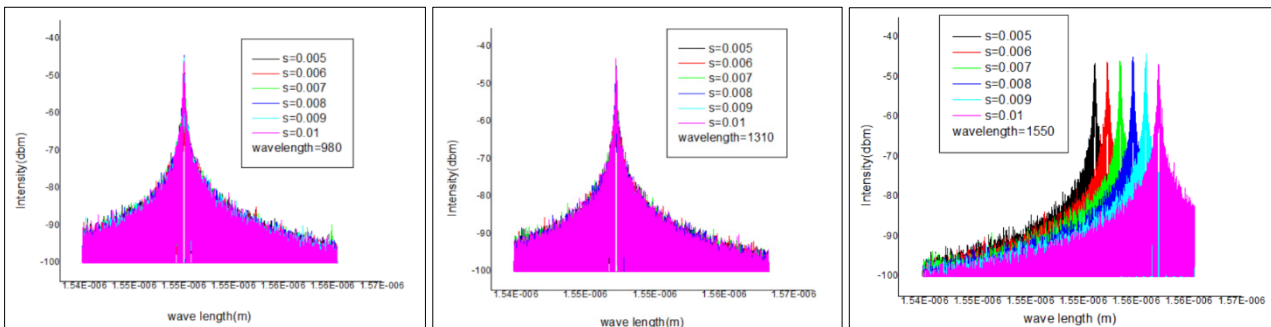


Figure 9. Relation between intensity and wavelength shift for; 1550, 1310 and 980 nm for mentioned strains

## CONCLUSIONS

According to the consequence of simulations, shifted wavelengths have been observed with several active lengths for virtual FBGs. Comparisons for observations based on theoretical calculations are carried out indicates that there is only a little variation between simulation and theoretical results. Based on the FBG sensors suggested in the experiment, the consequences show that efficient length is inversely related with shift in Bragg wavelength when axial strain increased. This means FBG sensor is most sensitive to the shortest FBG sensor length and less sensitive to the largest length of sensor due to the complicated math effect of reflectivity R parameter. It's also concluded from the relationship of the theoretical computation against empirical values and then the linearity of the strain against the shifted wavelength of Bragg that it may be applied in implementations in optical sensing as a sensor of high heat, a sensor of fire alarm, a sensor of vibration, or a sensor of pressure.

## Acknowledgments

The authors would like to thank Mustansiriyah University ([www.uomustansiriyah.edu.iq](http://www.uomustansiriyah.edu.iq)) and Ministry of Science and Technology, Baghdad, Iraq for their support in the present work.

## ORCID

© Wasmaa A. Jabbar, <https://orcid.org/0000-0003-3966-9468>; © Ayser Hemed, <https://orcid.org/0000-0003-0319-1650>  
© Ismaeel Al-Baidhany, <https://orcid.org/0000-0001-5273-9921>

## REFERENCES

- [1] N. Dedyagala, PhD. Dissertation, Optical Fiber Bragg Grating Analysis Through FEA and its Application to Pressure Sensing, College of Engineering and Science, Victoria University, 2019.
- [2] B.A. Tahir, M.A. Saeed, A. Ahmed, S.M.Z. Iqbal, R. Ahmed, M.G.B. Ashiq, H.Y. Abdullah, and R.A. Rahman, *Chinese Journal of Physics*, **49**(5), 1035-1045 (2011).
- [3] G. Zhou, L.M. Sim, and J. Loughlan, *Smart Materials and Structures IOP Publishing Ltd*, vol. 13, no. 6, p. 1291, (2004), <https://doi.org/10.1088/0964-1726/13/6/003>
- [4] N. S. Sahidan, M. A. M. Salim, S. S. Osman, H. Bakhtiar, N. Bidin, G. Krishnan, M. H. D. Othman, M. A. Rahman, A. F. Ismail and N. Yahya, in *International Laser Technology and Optics Symposium 2019 (iLATOS2019)*, (2019, Senai, Malaysia), <https://doi.org/10.1088/1742-6596/1484/1/012015>
- [5] Z.R. Ghayib, and A.A. Hemed, Springer Link, *Pramana - J Phys*, **96**(86), (2022), <https://doi.org/10.1007/s12043-022-02305-2>
- [6] Z.R. Ghayib, PhD. Dissertation, Controlling a chaotic synchronization by modified FBG sensor, College of Education, Mustansiriyah University, 2022.
- [7] Z.R. Ghayib, and A.A. Hemed, "Smart Control For The Chaotic Dynamics Using Two Regions Uniform Fiber Bragg Grating," *Optoelectronics and Advanced Materials-Rapid Communications*, **16**, 307-318, (2022), <https://oam-rc.inoe.ro/articles/smart-control-for-the-chaotic-dynamics-using-two-regions-uniform-fiber-bragg-grating>
- [8] S. Cheng, W. Hu, H. Ye, L. Wu, Q. Li, A. Zhou, M. Yang, Q. Zhao, and D. Guo, *Optics Express*, **29**(22), 35765-35775 (2021). <https://doi.org/10.1364/OE.441896>
- [9] M.I.M. Razi, M.R.C. Beson, S.N. Azem, and S.A. Aljuni, *Indonesian Journal of Electrical Engineering and Computer Science*, **14**(2), 564-572 (2019). doi: <http://doi.org/10.11591/ijeecs.v14.i2.pp564-572>
- [10] M.M. Werneck, R.C.S.B. Allil, B.A. Ribeiro, and F.V.B.D. Nazaré, "A Guide to Fiber Bragg Grating Sensors," in *Current Trends in Short- and Long-period Fiber Gratings*, London, UK, Edited by Christian Cuadrado-Laborde (IntechOpen 2013), pp. 7-8.
- [11] Othonos, and K. Kalli, *Fiber Bragg Gratings: Fundamentals and Applications in Telecommunications and Sensing* (Artech House Optoelectronics Library) Illustrated Edition, vol. 53, (Artech House Print on Demand, 1999).
- [12] E. Al-Fakih, N.A.A. Osman, and F.R.M. Adikan, *Sensors (Basel)*, **12**(10), 12890-12926 (2012), <https://doi.org/10.3390/s121012890>
- [13] Razzaq, H. Zainuddin, F. Hanaffi, and R.M. Chyad, *IET Science, Measurement & Technology*, **13**(5), 615-621 (2019). <https://doi.org/10.1049/iet-smt.2018.5076>
- [14] M. Boerkamp, D.W. Lamb, and P.G. Lye, in *Journal of Physics: Conference Series, Volume 76, Sensors and their applications XIV 11–13 September 2007, Liverpool John Moores University*, Liverpool, UK, 2007.
- [15] P.C. Beard, and T.N. Mills, *Applied Optics*, **35**(4), 663-675 (1996). <https://doi.org/10.1364/AO.35.000663>
- [16] Z. Fang, K. Chin, R. Qu, H. Cai, and K. Chang, *Fundamentals of Optical Fiber Sensors*, (Wiley Series in Microwave and Optical Engineering 2012).
- [17] L. Huo, H. Cheng, Q. Kong, and X. Chen, *Sensors*, **19**, 1231 (2019), <https://doi.org/10.3390/s19051231>
- [18] R.P. Rocha, A.F. Silva, J.P. Carmo, and J.H. Correia, "FBG in PVC foils for monitoring the knee joint movement during the rehabilitation process," in *33rd Annual International Conference of the IEEE EMBS*, <https://doi.org/10.1109/IEMBS.2011.6090064> (Boston, Massachusetts USA, 2011) pp. 458-461
- [19] Hemed, MSc. Thesis, Studying the Effective Factors on Producing Modal Birefringence (High and Low) in the Single Mode Optical Fiber, College of Education, Mustansiriyah University, 2005.
- [20] S.M. Khorsheed, A.A. Hemed, and M.M. Fdhala, *World Scientific News*, **137**, 42-57 (2019), <http://www.worldscientificnews.com/wp-content/uploads/2019/09/WSN-137-2019-42-57.pdf>
- [21] M.M. Fdhala, and S.M. Khorsheed, *European Journal of Advances in Engineering and Technology*, **7**(2), 1-6 (2020). <https://ejaet.com/archive/volume-7-issue-2-2020>
- [22] A.A. Hemed, M.M. Fdhala, and S.M. Khorsheed, *Kuwait J. Sci.* **49**(1), 1-18 (2022). <https://doi.org/10.48129/kjs.v49i1.12487>

**ХАРАКТЕРИСТИЧНЕ ДОСЛІДЖЕННЯ ВПЛИВУ ДОВЖИНИ ДАТЧИКА З ПОДВІЙНИМ ФІЛЬТРОМ  
НА ЧУТЛИВІСТЬ ДО ДЕФОРМАЦІЙ****Васма А. Джаббар<sup>а</sup>, Айсер Хемед<sup>а</sup>, Майяда Фадхала<sup>б</sup>, Ісмаїл Аль-Байдхані<sup>а</sup>**<sup>а</sup>*Департамент фізики, педагогічний коледж, університет Мустансірія, Багдад, Ірак*<sup>б</sup>*Середня школа Алсаламу, управління освіти Карха, Багдад, Ірак*

У цьому моделювальному дослідженні програмне забезпечення Optisystem 18 використовується для моніторингу та вивчення ефективності бокової деформації на вибраних відрізках двох віртуальних однорідних волоконних датчиків Брегга (FBG). Довжина хвилі робочого датчика FBG Брегга становила 1550 нм, що використовується для визначення вимірюваного зсуву в оптичному спектрі відхиленого джерела світла. Це значення також забезпечується джерелом світла, щоб забезпечити мінімальне поглинання та ослаблення під час передачі всередині оптичного волокна. Перевірено надійність датчика та техніку передачі сигналу при такому впливі. Досліджування також використовується для спостереження за зсувом довжини хвилі зі змінним прикладеним боковим натягом. Досліджується вплив активної довжини датчика на чутливість до бокової деформації, де, згідно з теорією, довжина FBG впливає на чутливість через відбивну здатність R. Побудовану чутливість датчика спостерігалась відносно довжини до та під час експерименту. Принцип чутливості, по суті, залежить від відстеження зсуву довжини хвилі через зміну такої деформації. Результати, отримані в цьому дослідженні, демонструють обернену залежність між ефективною довжиною датчика та зміщенням спостережуваної довжини хвилі. Вимірювана чутливість до деформації проводиться для довжини активного датчика, яка коливається від 0,05 до 15 см, з відповідними значеннями чутливості від 1,19 пм/°C до 0,9 пм/°C, відповідно, за однакових умов деформації. Емпіричні результати також показують успішність запропонованої системи вимірювання деформації. Вимірювана деформація,  $\epsilon$ , лінійно зростає, ідентично зростаючим значенням зсуву довжини хвилі Брегга. Було також помічено, що довжина хвилі Брегга зміщується під час малих коефіцієнтів подовження довжини FBG.

**Ключові слова:** *решистка Брегга; еластооптичний ефект; Optisystem; сенсор напруги; деформаційно-оптичний тензор*

## INVESTIGATING THE IMPACT OF VARYING QUANTITIES OF TiO<sub>2</sub> NANOPARTICLES ON THE ANTI-CORROSIVE CHARACTERISTICS OF TiO<sub>2</sub>-EPOXY NANOCOMPOSITE COATINGS<sup>†</sup>

 **Ahmed Ibrahim Dawood\***,  **Ahmed Qasim Abdullah**

*Department of Physics, College of Science, University of Baghdad, Baghdad, Iraq*

*\*Corresponding author's e-mail: [ai766142@gmail.com](mailto:ai766142@gmail.com)*

Received May 17, 2023; revised June 4, 2023; accepted June 5, 2023

Prepared were pills coated with TiO<sub>2</sub>-epoxy nanocomposites, and their anti-corrosive properties were studied by examining the impact of varying amounts of TiO<sub>2</sub> nanoparticles in the epoxy resin. The anti-corrosive characteristics of pills were investigated employing electrochemical impedance spectroscopy (EIS). Based on the EIS results, the sample containing 0.01 mg of TiO<sub>2</sub> demonstrated the highest impedance value, indicating superior corrosion resistance and better anti-corrosion properties than the other samples. Also, this sample has the lowest corrosion current density among the all samples, with a value of 1.329E-07 mA/cm<sup>2</sup>, which shows that this sample has the best corrosion resistance and a slower rate of corrosion compared to the other samples.

**Keywords:** Epoxy; TiO<sub>2</sub> nanoparticles; Nanocomposite; Electrochemical Impedance Spectroscopy (EIS); Coatings; Sol-gel synthesis

**PACS:** 81.05.Lg, 81.15.-z, 81.20.Fw, 81.65.Kn

### 1. INTRODUCTION

Corrosion is a natural process that can occur when metallic materials are exposed to the environment. It is the gradual degradation or deterioration of the material and its properties, typically a metal, due to electrochemical reactions occurring at the surface. Corrosion can induce material damage and eventual destruction, leading to economic burden and endangering human well-being and safety [1]. To prevent corrosion of metal materials, it is essential to apply a protective coating. This practice is commonly employed globally to address a wide range of corrosion issues and mitigate their associated consequences. Despite efforts to combat it, corrosion remains a major challenge for Steel-framed structures, as it can lead to material property degradation, reduced Support capacity, compromised safety, and shortened Performance life of structures [2]. Corrosion has attracted much research interest, and various methods have been developed to provide proper protection. However, the cost of corrosion and its consequences can be substantial. Hence, it is imperative to persist in the exploration and advancement of fresh approaches to combat corrosion and minimize its societal consequences. Accordingly, discovering a corrosion prevention technique that is highly effective, sustainable, durable, environmentally friendly, and economical is of utmost importance. The polymeric coating is a popular option for corrosion prevention because of its ease of production and ability to create a barrier on the material surface. Epoxy resin is commonly used as an anticorrosion coating due to its excellent adhesion, chemical resistance, and mechanical properties. Epoxy coatings are particularly effective in protecting metal surfaces from corrosion caused by exposure to harsh environments, such as saltwater, acidic solutions, and extreme temperatures. When applied as a coating, epoxy resin forms a hard, durable film that separates the metal surface from its surrounding conditions. This protective coating impedes moisture, oxygen, and other corrosive agents from reaching the metal surface, which helps to prevent corrosion [3,4].

In recent decades, researchers have conducted numerous studies to enhance the barrier properties of polymeric coatings [5-10]. One approach is to incorporate nanoscale particles into the polymer coatings, aiming to improve the coatings' anticorrosion and protective characteristics through various pathways. Pore filling, matrix defect reduction, and crack bowing, deflection and bridging are some of the methods identified [11]. Additionally, nano-additives can serve as connecting bridges between matrix molecules, decreasing the total unoccupied volume and promoting bonding [12-14]. These mechanisms delay the infiltration activity, slowing the spread of corrosive substances within the coating and reducing the corrosion rate on the material surface. To significantly improve the properties of epoxy, a larger interfacial area within the epoxy and fillers is required, which is influenced by factors such as particle size, the uniformity of nanoparticle distribution, and the volume proportion of nanoparticles in the epoxy matrix. TiO<sub>2</sub> nanoparticles are widely used as useful nano-sized filler due to their photocatalytic effect [15].

This phenomenon causes the TiO<sub>2</sub> nanoparticles to emit a large quantity of electrons when exposed to UV radiation. The electrons that are emitted trigger a photochemical reaction that acts on the Corrosive substances present on the surface of the coating, leading to additional corrosion inhibition. Although ultraviolet light can release radicals that may break down the polymer coating layer's molecular structure, this mechanism also provides the nanoparticles with an antimicrobial property that can eliminate bacteria found on the surface, potentially causing corrosion [16,17]. Because of their photocatalytic effect, Titanium dioxide nanoparticles are widely used for their ability to inhibit odors, self-clean, and resist fouling.

<sup>†</sup> *Cite as:* A.I. Dawood, A.Q. Abdullah, East Eur. J. Phys. 3, 516 (2023), <https://doi.org/10.26565/2312-4334-2023-3-59>

© A.I. Dawood, A.Q. Abdullah, 2023

The objective of this research was to examine how the anti-corrosion properties of pills coated with a TiO<sub>2</sub>-epoxy nanocomposite were impacted by different quantities of TiO<sub>2</sub> nanoparticles. The anti-corrosion properties of the samples were assessed by performing EIS after exposing the coated pills to a 1 M HCL solution. In addition, TiO<sub>2</sub> nanoparticles were examined utilizing XRD, AFM, SEM, UV-Vis spectrophotometry, and FTIR to gain insight into their properties. By investigating the relationship between the amount of TiO<sub>2</sub> and the Corrosion resistance of coatings, this study contributes to the development of more effective coatings for various applications. The findings may also have implications for the design of more efficient corrosion-resistant materials.

## 2. EXPERIMENTAL PROCEDURE

### 2.1. Synthesis of Titanium dioxide nanoparticles

TiO<sub>2</sub> nanoparticles were prepared via the sol-gel technique using Titanium tetra iso propoxide, ethanol (C<sub>2</sub>H<sub>6</sub>O), nitric acid (HNO<sub>3</sub>), and distilled water. First, the initial solution was prepared by dissolving a certain amount (2.5 ml) of TTIP in 45 ml of solvent, including distilled water (37.5 ml) and ethanol (7.5 ml). This solution was stirred for 1h. Then, drops of 1 ml of HNO<sub>3</sub> were added to the solution until it became transparent and clear. The obtained solution was refluxed at 70°C for 2h. After forming the gel, it was further slowly dried at 60°C for 3h. Finally, the prepared nano-powders were annealed at 400°C for 3h in the furnace in an air atmosphere.

### 2.2. Preparation of TiO<sub>2</sub>-epoxy nanocomposites

To prepare TiO<sub>2</sub>-epoxy nanocomposites, the specified amount of TiO<sub>2</sub> nanoparticles (0.002, 0.004, 0.006 and 0.01 mg) was transferred into separate clean and dry beakers. An equal amount of epoxy (obtained from Ahlia Chemicals Company) was added to each beaker, ensuring that the ratios were consistent across all mixtures. The contents of each beaker were mixed thoroughly using a clean stirrer until a homogeneous mixture was obtained. Once the mixtures were ready, they were sonicated using an ultrasonic bath for 2h to improve their dispersion. After that, the hardener was added to the beaker and mixed for one minute.

### 2.3. Coating pills with TiO<sub>2</sub>-epoxy nanocomposites

Four iron pills measuring 1.5 cm in diameter and 3 mm in thickness were used as the substrate for coating. Prior to coating, the iron pills were cleansed and degreased with acetone and subsequently dried completely. Using the spin coating method, each iron pill was coated with the different TiO<sub>2</sub>-epoxy mixtures one at a time, starting with the mixture containing 0.002 mg of TiO<sub>2</sub>, followed by 0.004 mg, and so on. After each coating, the pill was spun at a constant speed of 2000 rpm for a set time to ensure uniform coverage of the TiO<sub>2</sub>-epoxy nanocomposite. After all plates were coated and rotated, they were left at room temperature for at least 5 days to cure.

### 2.4. Characterization

The XRD spectra of titanium dioxide nanoparticles were recorded utilizing a D8 Advance Bruker system with Ni filtering and Copper K-alpha radiation with a wavelength of 0.15406 nm, covering a 2θ range of 20°-80°. A Nanosurf AG Naio AFM was utilized to capture the AFM image of the TiO<sub>2</sub> nanoparticles. The SEM Vega 3LM was used to analyze the morphology of both the nanoparticles and nanocomposites. The FTIR spectrums were recorded with Shimadzu 8300 over a range of wave numbers from 400 to 4000 cm<sup>-1</sup>. Optical analysis was conducted using the Unico 4802 dual beam spectrophotometer. To assess the anti-corrosion characteristics of the coated pills, the samples were submerged in a 1 M HCL solution, which served as an electrolyte and provided a conductive medium for the electrochemical reactions that occurred during corrosion. Then, The EIS analysis was performed using Ivium Technology to investigate the anti-corrosion properties of pills coated by TiO<sub>2</sub>-epoxy nanocomposites containing different amounts of TiO<sub>2</sub> nanoparticles.

## 3. RESULTS AND DISCUSSION

### 3.1. XRD Analysis

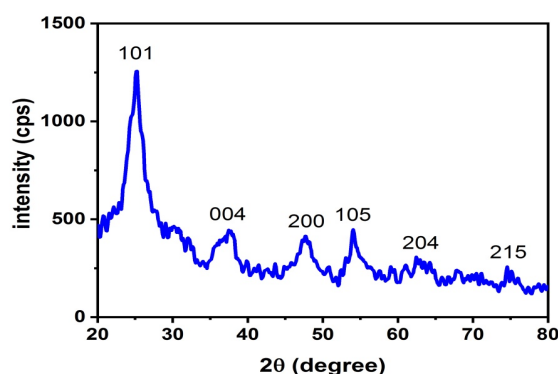


Figure 1. XRD spectrum of prepared TiO<sub>2</sub> nanoparticles.

The XRD pattern of the fabricated TiO<sub>2</sub> nanoparticles is depicted in Figure 1. The crystal planes of (101), (004), (200), (105), (204), and (215) are represented by diffraction peaks at 2θ values of 25.23°, 37.76°, 47.87°, 53.89°, 62.55°, and 74.87°, as observed in the XRD spectrum. The XRD pattern matches the standard reference XRD pattern of TiO<sub>2</sub> (JCPDS Card No.21-1272), thus verifying the successful synthesis of anatase-phase TiO<sub>2</sub> nanoparticles via the sol-gel method. The most intense peak, located at 2θ value of 25.23°, indicates the preferred crystal plane of (101) for anatase phase of titanium oxide.

### 3.2. AFM image

Performing atomic force microscope (AFM) analysis on  $\text{TiO}_2$  nanoparticles offers valuable insights into the surface morphology and properties of the nanoparticles. AFM image of  $\text{TiO}_2$  nanoparticles is shown in Figure 2. The surface of the fabricated titanium dioxide nanoparticles exhibits a rough and irregular texture, as evidenced by the root mean square (RMS) height of 122.4 nm. Furthermore, the mean particle size was measured to be 76.84 nm. These results provide valuable insights into the properties and potential applications of titanium dioxide nanoparticles in various fields, including nanotechnology, materials science, and biomedicine.

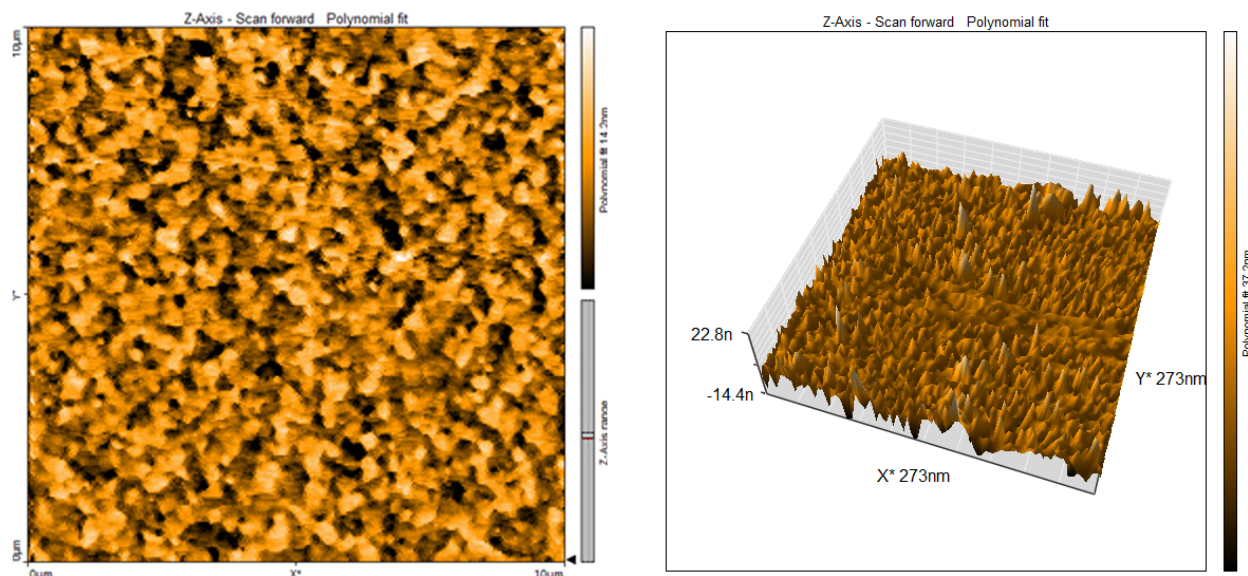


Figure 2. AFM image of synthesized  $\text{TiO}_2$  nanoparticles

### 3.3. SEM Images

Examining the surface morphology of materials, such as titanium dioxide nanoparticles and  $\text{TiO}_2$ -epoxy nanocomposites, can be effectively achieved through the use of SEM. The SEM image of prepared  $\text{TiO}_2$  nanoparticles and  $\text{TiO}_2$  (0.002 mg)-epoxy nanocomposite are shown in figure 3. Upon analyzing SEM images of  $\text{TiO}_2$  nanoparticles (Fig. 3a), it is evident that the surface is rough and irregular, with lumps of varying shapes and sizes present throughout. The existence of irregular lumps at the nanoparticle surface is particularly noteworthy, as it suggests that the surface is not homogeneous. This roughness and lack of uniformity is consistent with the results of atomic force microscopy, which also showed a non-uniform and rough surface for these nanoparticles. According to Figure 3b, the SEM image of the  $\text{TiO}_2$  (0.002 mg)-epoxy nanocomposite revealed a polished and almost uniform surface (Fig. 3b). The SEM image showed that the nanoparticles were distributed throughout the epoxy matrix, visible as small dots or clusters. Furthermore, the distribution of the nanoparticles appeared to be uniform throughout the sample.

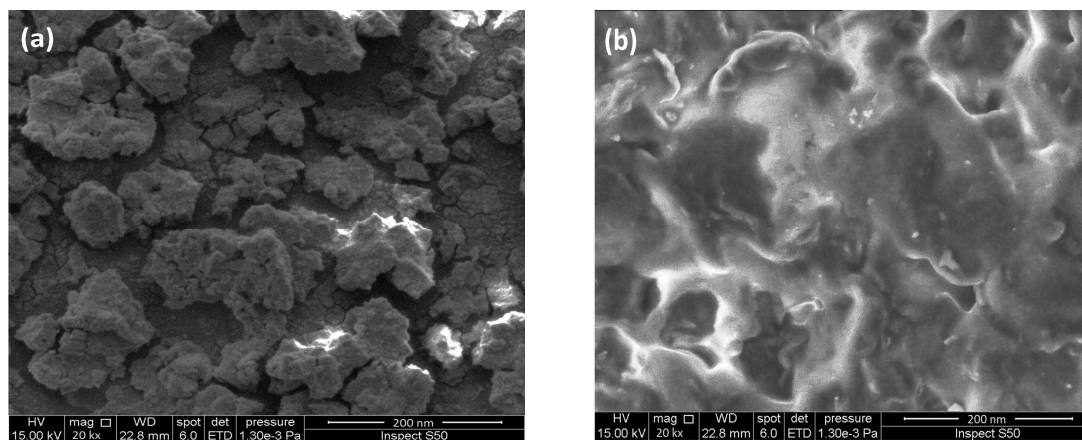


Figure 3. SEM micrographs of (a)  $\text{TiO}_2$  nanoparticles and (b)  $\text{TiO}_2$  (0.002 mg)-epoxy nanocomposite

### 3.4. UV-Vis spectroscopy

Titanium dioxide nanoparticles exhibit unique optical properties. In this study, the optical absorption properties of  $\text{TiO}_2$  nanoparticles were investigated by measuring their absorption spectrum using UV-Vis analysis. As illustrated in Figure 4, the absorption curve showed a sharp absorption edge at a wavelength of 350 nm, which is a significant factor

for understanding the optical response of TiO<sub>2</sub> nanoparticles. The absorption edge is the wavelength at which the material starts to absorb light due to valence-to-conduction band electronic transitions.

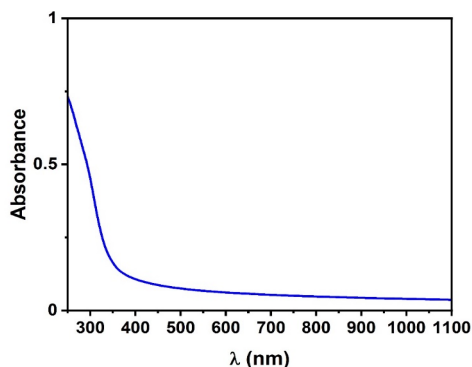


Figure 4. Optical absorption of synthesized TiO<sub>2</sub> nanoparticles

### 3.5. FTIR

Figures 5 and 6 depict the FTIR spectra of TiO<sub>2</sub> nanoparticles and an epoxy-TiO<sub>2</sub> (0.002 mg) nanocomposite, respectively. The FTIR spectrum for the anatase phase of TiO<sub>2</sub> nanoparticles displayed a broad vibration peak between 500 and 800 cm<sup>-1</sup>, which was attributed to vibrational mode associated with Ti-O bonds. The incorporation of TiO<sub>2</sub> nanoparticles into the epoxy resin resulted in overlapping spectral features between 500 and 800 cm<sup>-1</sup>, due to the presence of a minor concentration of TiO<sub>2</sub> nanoparticles in the epoxy resin matrix. The absorption band centered at 915 cm<sup>-1</sup> in the epoxy-TiO<sub>2</sub> nanocomposite is indicating the bending motion of the C-O bond in the epoxy structure.

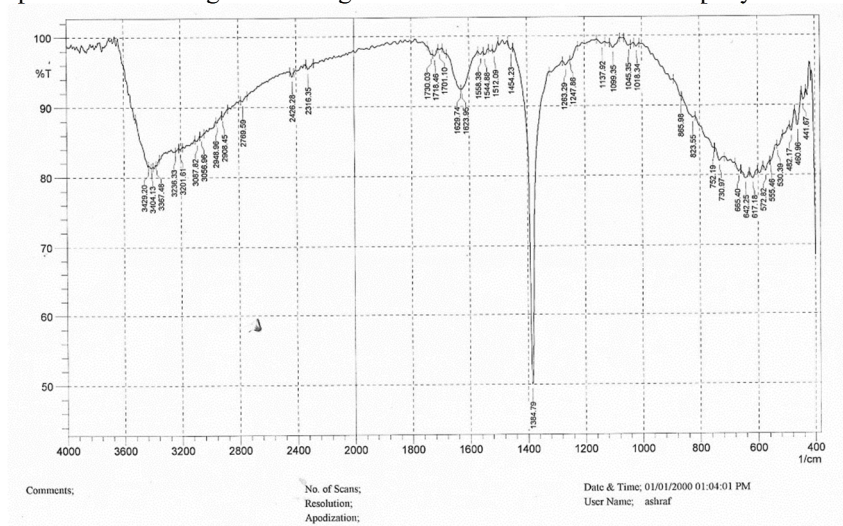


Figure 5. FTIR spectra TiO<sub>2</sub> nanoparticles

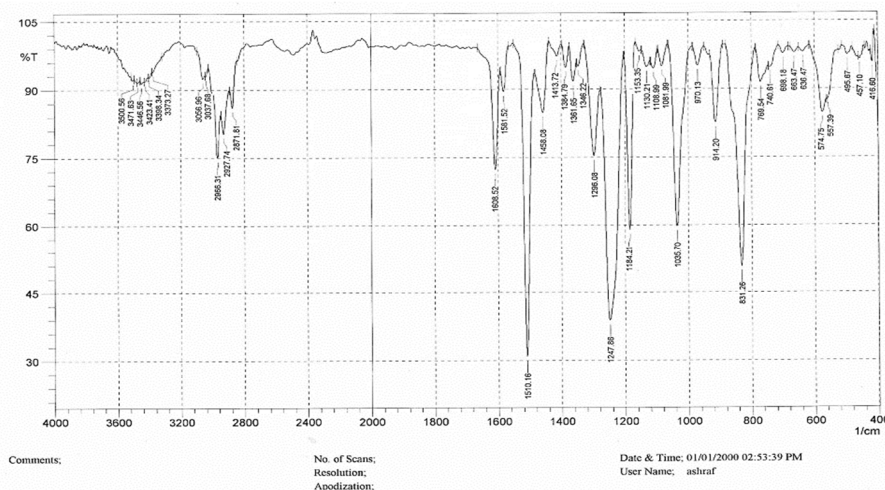


Figure 6. FTIR spectra of epoxy-TiO<sub>2</sub> (0.002 mg) nanocomposite

### 3.6. EIS

EIS is a potent method employed to analyze and evaluate the ability of various coatings to resist corrosion. Corrosion is a natural process that occurs when metals react with their environment, and it can lead to serious damage and deterioration of structures. EIS can be used to evaluate the effectiveness of coatings in preventing corrosion by measuring the electrical response of a coated metal sample to an alternating current (AC) signal. The process of conducting an EIS analysis involves applying an AC signal with a range of frequencies to a coated metal sample submerged in an electrolytic solution. The resulting electrical response is then measured and plotted on a graph called a Nyquist plot. The Nyquist diagram is a graphical representation in the complex plane that shows the relationship between the real and imaginary components of impedance. The curve obtained from the Nyquist plot is then analyzed to determine the coating's anti-corrosion performance. The Nyquist plot obtained from an EIS analysis typically shows a semicircle that corresponds to the impedance at the electrode/electrolyte interface. The semicircle observed in the Nyquist plot corresponds to the charge transfer resistance, which represents the level of resistance that the coating offers to electron transfer at the interface between the metal and electrolyte. By analyzing the shape and size of the semicircle, the coating's anti-corrosion properties can be determined.

To analyze the graphs obtained from EIS analysis, an electrical equivalent circuit (EEC) diagram is often used. The simplified electrical circuit diagram, also known as the equivalent circuit diagram, represents the physical mechanisms occurring at the interface between the metal and electrolyte. The parameters of the circuit can be established by matching the experimental quantities to the ECC diagram, which can then be employed to assess the anti-corrosive characteristics of the coating. The EIS test results for different samples of TiO<sub>2</sub>-epoxy nanocomposite coated pills with varying amounts of TiO<sub>2</sub> immersed to 1 M HCL for different time intervals were obtained by fitting an appropriate electrical equivalent circuit (R1(R2C1)(R3C2)), consisting of three elements: R1 (The resistance of the solution), R2C1 (The resistance to charge transfer at the external surface of the coating and its capacitance), and R3C2 (The resistance to charge transfer at the internal surface of the coating and its capacitance), as shown in Figure 7.

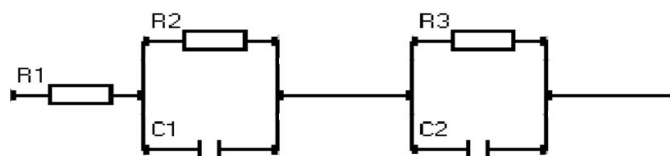


Figure 7. Equivalent electrical circuit (EEC)

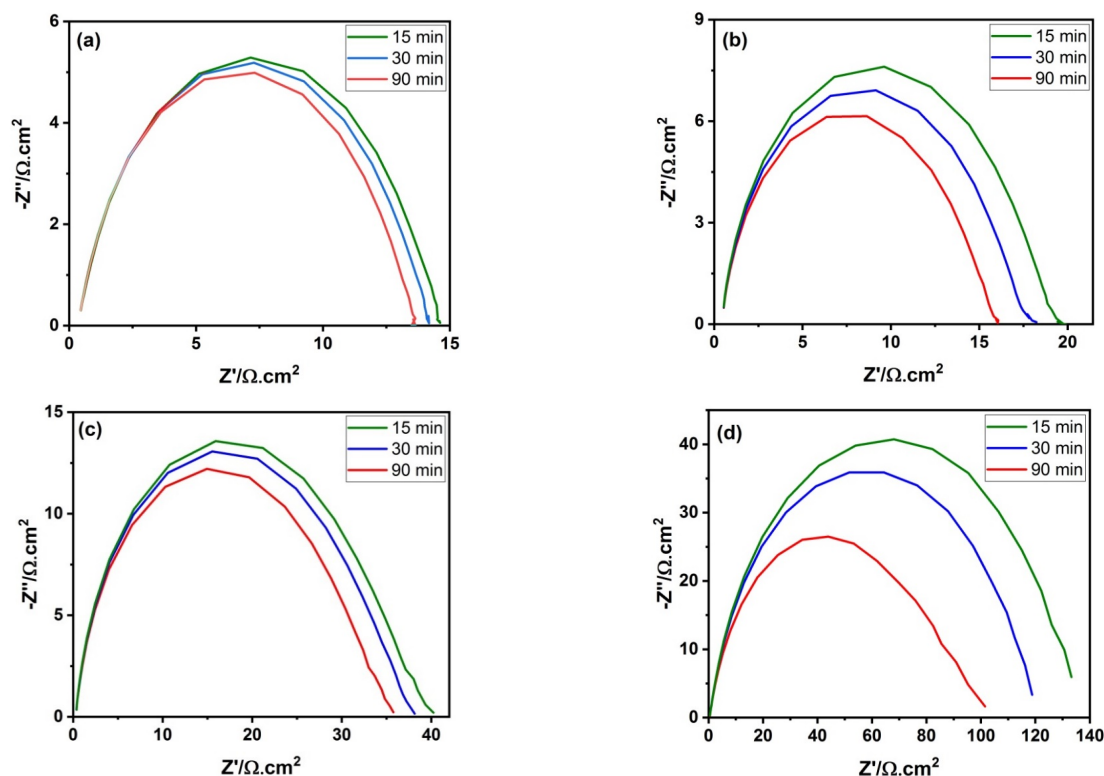
Following this, the information was examined and condensed into Table 1. The values of R1, R2, R3, C1, and C2 change with time and TiO<sub>2</sub> concentration, indicating the progression of the corrosion process and the influence of the TiO<sub>2</sub>-epoxy nanocomposite coating on the pills' susceptibility to corrosion, As indicated by Table 1.

Table 1. The EIS parameters of TiO<sub>2</sub>-epoxy nanocomposite coated pills after 15-, 30- and 90-minutes immersion time

| Sample                    | Immersion time (min) | R1 (Ω)   | R2 (Ω)   | R3 (Ω)   | C1 (f)   | C2 (f)   |
|---------------------------|----------------------|----------|----------|----------|----------|----------|
| 0.002 mg TiO <sub>2</sub> | 15                   | 4.66E-01 | 1.18E+01 | 1.63E+00 | 1.57E-04 | 1.10E-04 |
|                           | 30                   | 4.45E-01 | 1.10E+01 | 1.55E+00 | 1.47E-04 | 1.11E-04 |
|                           | 90                   | 4.55E-01 | 1.15E+01 | 1.58E+00 | 1.50E-04 | 1.11E-04 |
| 0.004 mg TiO <sub>2</sub> | 15                   | 3.74E-01 | 7.98E+00 | 2.43E+00 | 1.56E-04 | 8.51E-05 |
|                           | 30                   | 3.72E-01 | 9.08E+00 | 2.51E+00 | 1.44E-04 | 8.46E-05 |
|                           | 90                   | 3.72E-01 | 1.01E+01 | 2.48E+00 | 1.30E-04 | 8.58E-05 |
| 0.006 mg TiO <sub>2</sub> | 15                   | 3.93E-01 | 2.75E+01 | 4.63E+00 | 1.30E-04 | 8.99E-05 |
|                           | 30                   | 3.96E-01 | 2.86E+01 | 5.82E+00 | 1.37E-04 | 8.78E-05 |
|                           | 90                   | 3.97E-01 | 2.98E+01 | 5.94E+00 | 1.33E-04 | 8.73E-05 |
| 0.01 mg TiO <sub>2</sub>  | 15                   | 5.41E-01 | 6.91E+01 | 7.53E+00 | 2.99E-04 | 1.29E-04 |
|                           | 30                   | 5.69E-01 | 9.06E+01 | 8.74E+00 | 2.62E-04 | 1.17E-04 |
|                           | 90                   | 5.77E-01 | 1.02E+02 | 9.77E+00 | 2.64E-04 | 1.15E-04 |

The Nyquist diagram of all samples, as shown in Figure 8, exhibits a semi-circular shape. It is important to note that the diameter of the Nyquist diagram is directly related to the anti-corrosion properties of the sample, with larger diameters indicating better anti-corrosion properties. By increasing the amount of titanium dioxide from 0.002 mg to 0.01 mg, the impedance values increased. The pills with higher TiO<sub>2</sub> concentrations showed a slower rate of corrosion. Furthermore, the sample with 0.01 mg of titanium dioxide demonstrated the highest impedance value, indicating superior corrosion resistance and more effective corrosion protection compared to the others. The amount of titanium dioxide present in the sample has a notable impact on its impedance and corrosion inhibition capabilities. Increasing the amount of titanium dioxide results in higher impedance values, indicating better anti-corrosion properties. Incorporating TiO<sub>2</sub> into the epoxy nanocomposite enhances the pills' ability to resist corrosion by producing a dense and protective coating on the pills' surface, which impedes the penetration of acid and decelerates the corrosion process. TiO<sub>2</sub> is known for its excellent

chemical stability, high surface area, and photocatalytic properties. When added to the epoxy nanocomposite, TiO<sub>2</sub> particles act as physical barriers that limit the access of the acid to the pill's surface, which reduces the rate of corrosion and the amount of material that is corroded. In addition, the TiO<sub>2</sub> particles improve the adherence of the coating to the pill's exterior, thereby inhibiting the coating from peeling off and exposing the underlying metal to the corrosive environment. The presence of TiO<sub>2</sub> particles improves the mechanical characteristics of the coating, providing it with greater durability and strength against wear and abrasion. Furthermore, TiO<sub>2</sub> is known to have photocatalytic properties, which can lead to the development of a self-cleaning coating on the pills' surface. When exposed to UV light, TiO<sub>2</sub> particles generate reactive oxygen species that can break down organic contaminants and bacteria on the pills' surface, leading to an enhancement in the coating's anti-corrosion performance.



**Figure 8.** Nyquist plots of the TiO<sub>2</sub>-epoxy coated pills immersed in 1 M HCL with varying quantities of TiO<sub>2</sub>: (a) 0.002 mg, (b) 0.004 mg, (c) 0.006 mg and (d) 0.01 mg, after 15-, 30- and 90-minutes immersion time

Additionally, the effect of immersion time on impedance and anti-corrosion properties was also investigated. As seen in Figure 8, with an increase in the time of exposure to the solution, the impedance of all samples decreased, leading to a decrease in the diameter of the Nyquist diagram and, as a result decrease in anti-corrosion properties. The impact of immersion time on the anti-corrosive performance of coatings is an essential aspect of evaluating the durability and effectiveness of materials in real-world applications. Corrosion is a natural process that occurs when metals react with their environment, and it can cause significant damage and deterioration to structures and materials. Therefore, the ability of coatings to prevent or resist corrosion over time is crucial in ensuring their long-term performance. As materials are exposed to corrosive environments for extended periods, the effectiveness of coatings in preventing corrosion may decrease. This decrease in effectiveness can be attributed to a variety of factors, such as the breakdown of the coating or the depletion of its anti-corrosive agents. As a result, the anti-corrosive properties of the samples may weaken, leading to an increase in the rate of corrosion over time. Studying the influence of immersion time on the ability of coatings to inhibit corrosion can provide valuable insights into their long-term durability and effectiveness. By exposing coated materials to corrosive environments for varying durations, researchers can evaluate the speed of corrosion and the effectiveness of the protective film in preventing it. This information can then be used to improve the design and formulation of coatings, ensuring that they remain effective in preventing corrosion over extended periods.

Tafel analysis was performed for all samples to assess the corrosion performance of the coatings. Assessing the corrosion performance of metallic materials and coatings using this technique is a widely employed method. This analysis is based on measuring the current density of the sample in a corrosive environment ( $j_{\text{corr}}$ ) as a function of the applied potential. To conduct a Tafel analysis, the sample is submerged in an electrolyte solution, and a slight potential difference is introduced between the sample and a reference electrode. The current passing through the sample is computed and used to calculate the corrosion current density. The potential is then varied over a range of values and the corresponding corrosion current densities are recorded. The resulting data is then plotted in a Tafel diagram, which visually represents the polarization curves of the sample for both its anodic and cathodic behavior. The anode part of the diagram represents

the region where the sample is oxidized, and the cathode part represents the region where the sample is reduced. The slope of the anodic part of the diagram, known as the anodic Tafel slope ( $\beta_a$ ), represents the rate at which the anodic reaction increases with increasing potential. Similarly, the slope of the cathodic part of the diagram, known as the cathodic Tafel slope ( $-\beta_c$ ), represents the rate at which the cathodic reaction increases with decreasing potential. The direction of the anode and cathode parts of the diagram depends on the type of corrosion mechanism involved. In general, the anode part of the diagram is oriented towards more positive potentials, while the cathode part is oriented towards more negative potentials. The intersection points of the anode and cathode parts of the diagram, known as the corrosion potential ( $E_{corr}$ ), represents the equilibrium potential at which the anodic and cathodic reactions are balanced and no net current flows through the sample. The intersection points of the anode and cathode parts of the graph, which is known as the  $E_{corr}$ , represents the equilibrium potential where the anode and cathode reactions are balanced and no net current passes through the sample. The  $j_{corr}$  is obtained by using this point of intersection. The  $j_{corr}$  is a measure of the rate of corrosion on the surface of the sample, expressed in units relative to the area of the surface being evaluated. The results obtained from a Tafel diagram can yield valuable insights about the corrosion behavior of the sample. Lower values of  $j_{corr}$  indicate better corrosion resistance and slower corrosion rates, while higher values of  $j_{corr}$  indicate higher corrosion rates and poorer corrosion resistance.

Table 2 summarizes The Tafel parameters of TiO<sub>2</sub>-epoxy nanocomposite coated pills. Based on the data provided in this table, sample with 0.01 mg TiO<sub>2</sub> has the least  $j_{corr}$  among the all samples, with a value of 1.329E-07 mA/cm<sup>2</sup>. This indicates that this sample has the best corrosion resistance and lower resistance to corrosion compared to the other samples. This may be attributed to the creation of a protective oxide layer on the sample's surface, which functions as a protection to impede additional corrosion. The higher  $j_{corr}$  values of the other samples suggest that they are more susceptible to corrosion and may require additional protective coatings or surface treatments to improve their corrosion resistance. Sample with 0.006 mg TiO<sub>2</sub> has the second-lowest  $j_{corr}$  value of 3.643E-06 mA/cm<sup>2</sup>, which is lower than the  $j_{corr}$  values of Sample with 0.004 and 0.002 mg TiO<sub>2</sub>, but higher than that of 0.01 mg TiO<sub>2</sub>. The sample with 0.002 mg TiO<sub>2</sub> has the highest amount of corrosion  $j_{corr}$ , with a value of 1.98E-04 mA/cm<sup>2</sup>, which shows the low resistance of this sample against corrosion among all samples.

**Table 2.** The Tafel parameters of TiO<sub>2</sub>-epoxy nanocomposite coated pills.

| Sample                    | $E_{corr}/V$ | $(j_{corr})_{Tafel}/mA\ cm^{-2}$ | $\beta_a/V\ dec^{-1}$ | $-\beta_c/V\ dec^{-1}$ |
|---------------------------|--------------|----------------------------------|-----------------------|------------------------|
| 0.002 mg TiO <sub>2</sub> | -0.5476      | 1.98E-04                         | 0.178                 | 0.211                  |
| 0.004 mg TiO <sub>2</sub> | -0.5697      | 7.292E-05                        | 0.187                 | 0.178                  |
| 0.006 mg TiO <sub>2</sub> | -0.0971      | 3.643E-06                        | 0.159                 | 0.154                  |
| 0.01 mg TiO <sub>2</sub>  | -0.04391     | 1.329 E-07                       | 0.155                 | 0.146                  |

#### 4. CONCLUSION

The study aimed to explore the influence of varying quantities of titanium dioxide nanoparticles in epoxy resin on the anti-corrosion characteristics of the TiO<sub>2</sub>-epoxy nanocomposite coated pills. Epoxy-TiO<sub>2</sub> nanocomposite coated pills were prepared and subjected to EIS to evaluate their anti-corrosion properties. The results indicated that the sample containing 0.01 mg of TiO<sub>2</sub> exhibited the highest impedance value, indicating superior corrosion resistance and better anti-corrosion properties than the other samples. Additionally, this sample had the lowest corrosion current density among all samples, with a value of 1.329E-07 mA/cm<sup>2</sup>, indicating the best corrosion resistance and a slower rate of corrosion compared to the other samples. These findings have implications for the design of more efficient corrosion-resistant materials.

#### ORCID

©Ahmed Ibrahim Dawood, <https://orcid.org/0009-0005-6269-3361>; ©Ahmed Qasim Abdullah, <https://orcid.org/0000-0002-2464-5845>

#### REFERENCES

- [1] M. Czaban, "Aircraft corrosion - Review of corrosion processes and its effects in selected cases," *Fatigue Aircr. Struct.* **10**, 5-20 (2018). <https://doi.org/10.2478/fas-2018-0001>
- [2] H. Xu, and Y. Zhang, "A review on conducting polymers and nanopolymer composite coatings for steel corrosion protection," *Coatings*, **9**(12), 1-22 (2019). <https://www.mdpi.com/2079-6412/9/12/807#>
- [3] A. Shafaamri, R. Shafaghat, I.A.W. Ma, R. Kasi, and V. Balakrishnan, "Effects of TiO<sub>2</sub> Nanoparticles on the Overall Performance and Corrosion Protection Ability of Neat Epoxy and PDMS Modified Epoxy Coating Systems," *Front. Mater.* **6**, 1–19. (2020). <https://doi.org/10.3389/fmats.2019.00336>
- [4] X. Zhao, S. Liu, and B.R. Hou, "A comparative study of neat epoxy coating and nano ZrO<sub>2</sub>/epoxy coating for corrosion protection on carbon steel," *Appl. Mech. Mater.* 599-601, 3-6 (2014). <https://doi.org/10.4028/www.scientific.net/AMM.599-601.3>
- [5] F. Dolatzadeh, S. Moradian, and M.M. Jalili, "Influence of various surface treated silica nanoparticles on the electrochemical properties of SiO<sub>2</sub>/polyurethane nanocoatings," *Corros. Sci.* **53**, 4248-4257 (2011). <https://doi.org/10.1016/j.corsci.2011.08.036>
- [6] M. Heidarian, M. Shishesaz, S. Kassiriha, and M. Nematollahi, "Study on the effect of ultrasonication time on transport properties of polyurethane/organoclay nanocomposite coatings," *J. Coat. Technol. Res.* **8**, 265-274 (2011). <http://dx.doi.org/10.1007/s11998-010-9297-7>
- [7] S. Shen, and Y. Zuo, "The improved performance of Mg-rich epoxy primer on AZ91D magnesium alloy by addition of ZnO," *Corros. Sci.* **87**, 167-178 (2014). <https://doi.org/10.1016/j.corsci.2014.06.020>

- [8] E. Matin, M. Attar, and B. Ramezanzadeh, "Investigation of corrosion protection properties of an epoxy nanocomposite loaded with polysiloxane surface modified nanosilica particles on the steel substrate," *Prog. Org. Coat.* **78**, 395-403 (2015). <http://dx.doi.org/10.1016/j.porgcoat.2014.07.004>
- [9] Mohamad Saidi, N., Shafaamri, A. S., Wonnie Ma, I. A., Kasi, R., Balakrishnan, V., and Subramaniam, R. "Development of anti-corrosion coatings using the disposable waste material," *Pigment Resin Technol.* **47**, 478-484 (2018). <https://doi.org/10.1108/PRT-03-2018-0030>
- [10] S. Zheng, D.A. Bellido-Aguilar, Y. Huang, X. Zeng, Q. Zhang, and Z. Chen, "Mechanically robust hydrophobic bio-based epoxy coatings for anti-corrosion application," *Surf. Coat. Technol.* **363**, 43-50 (2019). <https://doi.org/10.1016/j.surfcoat.2019.02.020>
- [11] S. Ammar, K. Ramesh, B. Vengadaesvaran, S. Ramesh, and A. Arof, "A novel coating material that uses nano-sized SiO<sub>2</sub> particles to intensify hydrophobicity and corrosion protection properties," *Electrochim. Acta*, **220**, 417-426 (2016). <https://doi.org/10.1016/j.electacta.2016.10.099>
- [12] X. Shi, T.A. Nguyen, Z. Suo, Y. Liu, and R. Avci, "Effect of nanoparticles on the anticorrosion and mechanical properties of epoxy coating," *Surf. Coat. Technol.* **204**, 237-245 (2009). <https://doi.org/10.1016/j.surfcoat.2009.06.048>
- [13] M. Heidarian, M. Shishesaz, S. Kassirha, and M. Nematollahi, "Characterization of structure and corrosion resistivity of polyurethane/organoclay nanocomposite coatings prepared through an ultrasonication assisted process," *Prog. Org. Coat.* **68**, 180-188 (2010). <http://dx.doi.org/10.1016/j.porgcoat.2010.02.006>
- [14] A.M. Atta, N.H. Mohamed, M. Rostom, H.A. Al-Lohedan, and M.M. Abdullah, "New hydrophobic silica nanoparticles capped with petroleum paraffin wax embedded in epoxy networks as multifunctional steel epoxy coatings," *Prog. Org. Coat.* **128**, 99-111 (2019). <https://doi.org/10.1016/j.porgcoat.2018.12.018>
- [15] J. Liqiang, S. Xiaojun, C. Weimin, X. Zili, D. Yaoguo, and F. Honggang, "The preparation and characterization of nanoparticle TiO<sub>2</sub>/Ti films and their photocatalytic activity," *J. Phys. Chem. Solids*, **64**, 615-623 (2003). [https://doi.org/10.1016/S0022-3697\(02\)00362-1](https://doi.org/10.1016/S0022-3697(02)00362-1)
- [16] G. Fu, P.S. Vary, and C.-T. Lin, "Anatase TiO<sub>2</sub> nanocomposites for antimicrobial coatings," *J. Phys. Chem. B*, **109**, 8889-8898. (2005). <https://doi.org/10.1021/jp0502196>
- [17] P. Evans, and D. Sheel, "Photoactive and antibacterial TiO<sub>2</sub> thin films on stainless steel," *Surf. Coat. Technol.* **201**, 9319-9324 (2007). <https://doi.org/10.1016/j.surfcoat.2007.04.013>

#### ДОСЛІДЖЕННЯ ВПЛИВУ КОНЦЕНТРАЦІЇ НАНОЧАСТИНОК TiO<sub>2</sub> НА АНТИКОРОЗІЙНІ ХАРАКТЕРИСТИКИ TiO<sub>2</sub>-ЕПОКСИД НАНОКОМПОЗИТНИХ ПОКРИТТІВ

Ахмед Ібрагім Дауд, Ахмед Касім Абдулла

*Факультет фізики, Науковий коледж, Багдадський університет, Багдад, Ірак*

Вивчені антикорозійні властивості зразків покритих TiO<sub>2</sub>-епоксид наноконкомпозитами, від концентрації наночастинок TiO<sub>2</sub> в епоксидній смолі. Антикорозійні характеристики зразків досліджували за допомогою електрохімічної імпедансної спектроскопії (EIS). Згідно з результатами EIS, зразок, що містить 0,01 мг TiO<sub>2</sub>, продемонстрував найвище значення імпедансу, що вказує на кращу стійкість до корозії та кращі антикорозійні властивості, ніж інші зразки. Крім того, цей зразок має найнижчу щільність струму корозії серед усіх зразків, зі значенням 1,329E-07 мА/см<sup>2</sup>, що показує, що цей зразок має найкращу корозійну стійкість і нижчу швидкість корозії порівняно з іншими зразками.

**Ключові слова:** епоксидна смола; наночастинки TiO<sub>2</sub>; наноконкомпозит; електрохімічна імпедансна спектроскопія (EIS); покриття; золь-гель синтез

## THE EFFECT OF MULTI-WALL CARBON NANOTUBES ADDITION ON THE SHIELDING PROPERTIES AGAINST GAMMA RADIATION<sup>†</sup>

Moaz M. Altarawneh<sup>a,\*</sup>, Mutaz W. Aladailah<sup>a</sup>, Osama Y. Al-Madanat<sup>b,c</sup>

<sup>a</sup>Department of Physics, Mutah University, Alkarak 61710, Jordan

<sup>b</sup>Department of Chemistry, Mutah University, Alkarak 61710, Jordan

<sup>c</sup>Institute for Technical Chemistry Gottfried Wilhelm Leibniz Universität, Hannover  
Callinstrasse 5, Hannover, 30167, Germany

\*Corresponding Author e-mail: [moaz@mutah.edu.jo](mailto:moaz@mutah.edu.jo)

Received May 5, 2023; revised June 25, 2023; accepted June 26, 2023

In this work, the effect of Multi-Wall Carbon Nanotubes (MWCNTs) addition on the materials shielding properties against Gamma radiation with an energy of 662 keV from a <sup>137</sup>Cs source is investigated. The linear attenuation coefficient of MWCNTs-based materials (gelatin-water mixture) with MWCNTs concentrations of 0%, 5%, and 10% is measured. To isolate the contribution of the MWCNTs unique structure to the shielding capabilities, samples with the same concentrations of activated carbon were fabricated and their linear attenuation coefficients were obtained. Also, the linear and the mass attenuation coefficients are obtained theoretically for the same concentrations using the XCOM program and compared with measured values. It is found that the addition of MWCNTs by 5% or 10% has increased the linear attenuation coefficient by around 5% when compared to the same concentrations of activated carbon. This increase in the shielding capabilities against gamma radiation can be related to the interaction of gamma radiation with the extraordinary geometry and structure of MWCNTs.

**Keywords:** Radiation; Shielding; Attenuation coefficient; XCOM; Multi-wall carbon Nanotubes

**PACS:** 78.70.-g; 87.50.Gi; 87.52.-g

### 1. INTRODUCTION

Carbon nanotubes (CNTs), because of their outstanding physical and geometrical properties are considered one of the key materials for many of the current and future technologies [1, 2, 3, 4]. So far, there is a large number of studies focusing on the electrical, thermal, and mechanical properties of CNTs-based composites targeting vast technological applications [5, 6]. However, when it comes to the interaction of gamma ( $\gamma$ ) radiation with CNTs based composites there is a large number of studies that explore the effect of  $\gamma$  irradiation on the electrical and mechanical properties [7, 8]. Nevertheless, focusing on the shielding properties of CNTs-based composites against  $\gamma$  radiation has drawn less attention [9, 10]. One reason for this is related to the fact that shielding capability against radiation is mainly directly proportional to the atomic numbers of the elements in the used shielding material and their mass density [11]. However, engineering the shielding materials at the nano-scale level has proven to enhance the shielding properties in some applications. For example, in previous studies by Hassan et al. as in Ref.[12] and by El-Khatib et al. as in Ref.[13], aiming to fabricate better gamma radiation shields, materials (e.g., concrete, polymers) were doped with lead oxide nano-particles to enhance the shielding properties due to the existence of the lead (Pb) element. In fact, lead is known as one of the best elements to shield gamma radiation due to its large atomic number and its high mass density. In the X-ray range, in a work by Fujimori et al. [9], the shielding properties against X-ray radiation were enhanced when CNTs are used in comparison with other forms of carbon structures in highly oriented pyrolytic graphite (HOPG) and fullerenes (C<sub>60</sub>). This enhancement in the shielding properties could not be explained by the known theories, which raises the need for an alternative theoretical model to explain such enhancement. In a study by Zhang et al.[14], the shielding capabilities of carbon nanotube (CNT)-based film materials against gamma-ray are investigated for energies from <sup>241</sup>Am and <sup>137</sup>Cs. The study shows that CNT films have higher shielding capabilities against gamma radiation when compared with carbon fiber-reinforced composites, owing to the interaction of gamma radiation with the outstanding cylindrical structure on the nanoscale. In another work by Viegas et al.[15], an enhancement of X-ray shielding in the functionalized graphene oxide-based nanocomposites when compared to MWCNTs is reported for energies between 6.9 to 22.1 keV. The study showed that the structure of carbon used in the composite is an essential parameter to consider when studying the shielding properties. Moreover, the work has pointed out that a new interaction mechanism between the graphene structure and the incident  $\gamma$ -ray could be responsible for such enhancement.

<sup>†</sup> Cite as: M.M. Altarawneh, M.W. Aladailah, O.Y. Al-Madanat, East Eur. J. Phys. 3, 524 (2023), <https://doi.org/10.26565/2312-4334-2023-3-60>

© M.M. Altarawneh, M.W. Aladailah, O.Y. Al-Madanat, 2023

Since most studies did not focus on the shielding against gamma radiation when CNTs are utilized at least in the bulk case, it's worth searching for potential contributions to the shielding capability against gamma radiation due to the unique geometrical and structural properties of CNTs. Recently, there is an increasing interest in the medical applications of CNTs for treating cancer by dielectric heating of infected tissues by the application of microwave radiation [16]. In special cases, if gamma radiation therapy is used during the existence of CNTs in the tissue, it is important to estimate the shielding level of CNTs to give the correct dose of  $\gamma$  radiation [17].

When studying the shielding capability of any material after the addition of CNTs, there are key parameters to consider in such study, e.g., the geometry of CNTs (number of walls, diameter, and length), alignment and orientation of CNTs, and their concentration in the hosting material. Another important parameter to consider is the energy of the gamma radiation  $E_\gamma$  used, where  $E_\gamma$  is related to the wavelength  $\lambda$  of  $\gamma$ -ray as  $E_\gamma = hc/\lambda$  where  $h$  is the Planck's constant and  $c$  is the speed of light [11]. In the current study, we are considering the concentration of MWCNTs parameter only which can be investigated within the available resources.

To investigate the effect of MWCNTs addition on the radiation shielding properties, the linear attenuation coefficient ( $LAC$ ) will be measured for a gelatin-water mixture that is doped with different concentrations of MWCNTs against  $\gamma$ -radiation from  $^{137}\text{Cs}$  at 662 keV. Activated carbon is used in the current study as a control variable (in terms of structure) to isolate the effect of the unique structure of MWCNTs at such conditions. The chemical structure of activated carbon is very close to pure graphite structure in which carbon atoms are arranged as layers of connected hexagons [18]. To help understand the effect of MWCNTs addition on the shielding properties, the XCOM program will be used to calculate the mass attenuation coefficient  $\mu$  values and the  $LAC$  values theoretically [19]. The importance of the XCOM program in the current study stems from the fact that the XCOM program does not account for the structure of the shielding materials in general and for the MWCNTs structure specifically. Such calculations can help isolate the contribution of the MWCNTs structure when compared with the experimental measurements of the shielding properties.

One more important goal for the current work is to verify the need for a new theory to explain the mechanism of interaction between the  $\gamma$  radiation and the MWCNTs at such an energy range. For the  $\gamma$  rays at an energy of 662 keV from the  $^{137}\text{Cs}$ , the dominant mechanism of interaction is the Compton effect at which the  $\gamma$  rays scattered at different angles  $\theta$  with less energy (depending on the angle) [20].

## 2. THEORY

For a radiation of a single energy  $\gamma$  radiation with an intensity of  $I_0$  initially incident on the surface of a material that has a thickness of  $x$ , the intensity of the gamma radiation after traveling a distance  $x$  inside the material will drop according to the exponential attenuation law (Lambert-Beer law) as [21]:

$$I(x) = I_0 e^{-LACx} \quad (1)$$

Here  $LAC$  represents the linear attenuation coefficient in units of  $\text{cm}^{-1}$ . For a shielding material with a large  $LAC$  value, the intensity of  $\gamma$ -rays gets attenuated dramatically as it travels through the material [21]. The total mass attenuation coefficient  $\mu$  for any shielding material is given as  $\mu = LAC/\rho$ , where  $\rho$  is the mass density of the sample in units of  $\text{g}/\text{cm}^3$ . For any chemical compound or a mixture of elements the  $\mu$  value can be calculated theoretically using the following relation:

$$\mu = \sum_i w_i (LAC/\rho)_i \quad (2)$$

where the fractional weight of the  $i^{\text{th}}$  component is  $w_i$ . The value of  $\mu$  can be obtained theoretically using the XCOM program that is provided by the National institute of standards NIST (USA) [19]. Also, one can find the Half Value Thickness (HVT), which is the thickness of the shielding material at which the radiation intensity drops to one-half of its initial value, it can be calculated according to the following equation:

$$HVT = \frac{\ln 2}{LAC} \quad (3)$$

The HVT value is a key parameter to consider when comparing the shielding capability of different radiation-absorbing materials [22].

## 3. EXPERIMENTAL SETUP

### 3.1. Fabrication of the samples

In the current study, a mixture of gelatin and water was prepared as a hosting material for the MWCNTs due to the simplicity of casting the samples and due to the good dispersion of the MWCNTs into the mixture after curing [16]. The host material mixture is fabricated out of gelatin (gelatin from bovine skin type B, Sigma-Aldrich) and distilled water, as demonstrated in a work by Altarawneh et al.[23]. A small amount of p-toluic

acid and n-propanol were added to the distilled water and gelatin to enhance the bonding in the host material and to preserve it for longer periods of time [24]. Table 1 shows the percentage of the elements composing the host material used in this work. The MWCNTs (supplied by Cheap Tubes Co., with a length of 10-20  $\mu\text{m}$ , purity > 95 wt.% outer diameter 30-50 nm, and ash < 1.5 wt.%) or the activated carbon (supplied by Acros Organics BVBA Janssen Pharmaceutical, with grains size > 1  $\mu\text{m}$ ) of the desired concentrations were added to the distilled water initially and sonicated using an ultrasonic processor (UP100H- Hielscher Ultrasonics technology) for 30 minutes. Then, the gelatin and the rest of the components were added according to the procedure described in Altarawneh et al.[23]. The samples containing the MWCNTs or the activated carbon were fabricated with concentrations by weight of 0, 5%, and 10% for each of them.

**Table 1.** The percentage of the main components of the hosting material mixture

| p-toluic acid | n-propanol | deionized water | gelatin |
|---------------|------------|-----------------|---------|
| 0.080%        | 3.44%      | 81.84%          | 14.64%  |

The resultant mixtures with different concentrations and different fillers types were molded in 10 cm long glass tubes with a diameter of 1.2 cm. The glass tubes containing the samples were sealed with thin plastic sheets and left to cure at room temperature for five days. The final form of the samples is flexible cylindrical rods that can be easily cut by a sharp blade. The mass density for each sample was measured and tabulated to be used in the rest of the study. For each of the fabricated samples, the LAC value was measured as demonstrated in the following subsection.

### 3.2. Experimental setup for studying Gamma radiation shielding capabilities

The setup used in this work to measure the LAC values is as demonstrated in Figure 1. The setup is composed of a Sodium Iodide (NaI) detector (manufactured by Canberra, model: 2007P) that is housed in a 4.0 cm thickness lead shield to block radiation from background sources.

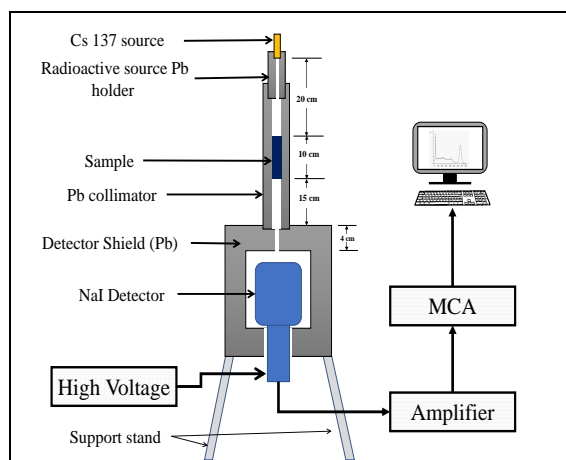


**Figure 1.** The schematic diagram of the setup used to measure the LAC values of each of the fabricated samples.

The NaI detector was connected to an operating high voltage source of 700V (manufactured by Canberra, model: 3102). The output signal was sent to an amplifier (manufactured by Ortec, model: 575A) where its output is connected to a Multi-Channel Analyzer (MCA). The data from the MCA was acquired and plotted on a computer monitor with the help of the MAESTRO Version 7.0 package (supplied by Ortec).

The fabricated samples were inserted in the custom-made lead housing with a 1.2 cm internal diameter, 40.0 cm length, and 2.0 cm thickness. The detector was placed at a large enough distance to ensure narrow beam geometry. The Cesium source ( $^{137}\text{Cs}$ ) has a pen shape with an outer diameter of 1.0 cm (supplied by Amersham) that was inserted in a custom-made lead holder with a length of 8.0 cm. The sample thickness was adjusted by pushing the sample out of the glass tube and by cutting it with a sharp blade. Inserting a small amount of oil between the glass tube and the sample can help slide the sample in and out of the glass tube during the adjustment of the thickness.

The fabricated samples were irradiated by gamma radiation from the  $^{137}\text{Cs}$  source where the intensity was collected for a time interval of 90 minutes. The values of the LAC were obtained by fitting Eq.1 using Igor Pro 9 data analysis software (provided by Wavemetrics). Suitable background subtraction was conducted for all collected intensity [25, 26].

### 3.3. Calculations of the mass attenuation coefficients using the XCOM program

In the theoretical part of this work, the XCOM program is used to calculate the mass attenuation coefficients of the fabricated samples at energies from 1 keV to 100 GeV. The XCOM program runs under the Windows operating system on the Google Chrome web browser [27]. The elements percentages in each sample were calculated initially and used in the XCOM program to calculate the mass attenuation coefficient for each sample. In Table 2, the net percentages of the elements (carbon, oxygen, hydrogen, and nitrogen) making up each of the fabricated samples were calculated.

**Table 2.** The elements percentage of the 0% host material, for the 5% additives of carbon, and for 10% additives of carbon either in the activated carbon form or the MWCNTs form.

| % of carbon additives | % C   | % H   | % N  | % O   |
|-----------------------|-------|-------|------|-------|
| 0%                    | 9.54  | 10.62 | 2.48 | 77.29 |
| 5%                    | 13.82 | 10.11 | 2.36 | 73.63 |
| 10%                   | 17.88 | 9.64  | 2.25 | 70.17 |

The output data generated by the XCOM program is tabulated and plotted for comparison. The theoretical mass attenuation coefficient values are found for the fabricated samples using the XCOM program and plotted as a function of energy as in Figure 2.

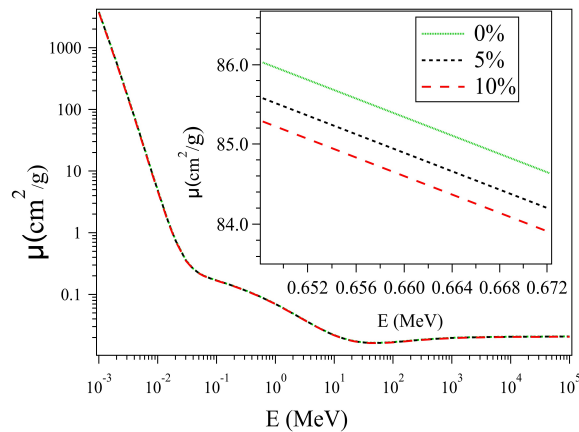


**Figure 2.** The mass attenuation coefficients as calculated by the XCOM program for the samples with 0%, 5%, and 10% of carbon additives. The inset shows the values of  $\mu$  around the  $^{137}\text{Cs}$  energy of 0.662 MeV.

## 4. RESULTS AND DISCUSSION

The gamma radiation intensity  $I$  from the  $^{137}\text{Cs}$  source at 662 keV was collected using the setup described earlier for different thicknesses of gelatin-water mixtures with no additives (0%), with the addition of MWCNTs (5% and 10%), and with the addition of activated carbon (5% and 10%). After suitable background subtraction, the intensities  $I$  for each of the five samples were plotted as a function of the sample's thickness, and the values of the LAC were obtained by fitting Eq.1. As it can be seen in Table 3 and in Figure 3-a., there is a small decrease in the measured LAC values from  $0.089\text{ cm}^{-1}$  down to  $0.085\text{ cm}^{-1}$  and  $0.087\text{ cm}^{-1}$  when the gelatin-water mixture was doped with 5% and 10% of activated carbon respectively.

**Table 3.** The Measured and calculated parameters related to the attenuation of gamma radiation for 0%, 5%, and 10% concentrations of carbon nanotubes and activated carbon.

|                                       | Host Material     | Activated carbon  | MWCNT             | Activated carbon  | MWCNT             |
|---------------------------------------|-------------------|-------------------|-------------------|-------------------|-------------------|
| concentration                         | 0                 | 5%                | 5%                | 10%               | 10%               |
| LAC ( $\text{cm}^{-1}$ )              | $0.089 \pm 0.001$ | $0.085 \pm 0.001$ | $0.089 \pm 0.001$ | $0.087 \pm 0.001$ | $0.091 \pm 0.001$ |
| HVT (cm)                              | $7.79 \pm 0.09$   | $8.16 \pm 0.09$   | $7.79 \pm 0.09$   | $7.97 \pm 0.09$   | $7.62 \pm 0.08$   |
| $\rho$ ( $\text{g}/\text{cm}^3$ )     | $1.06 \pm 0.01$   | $1.08 \pm 0.01$   | $1.09 \pm 0.01$   | $1.10 \pm 0.01$   | $1.12 \pm 0.01$   |
| $\mu$ ( $\text{cm}^2/\text{g}$ ) exp  | $0.084 \pm 0.001$ | $0.079 \pm 0.001$ | $0.082 \pm 0.001$ | $0.079 \pm 0.001$ | $0.081 \pm 0.001$ |
| $\mu$ ( $\text{cm}^2/\text{g}$ ) XCOM | 0.0854            | 0.0850            | 0.0850            | 0.0846            | 0.0846            |

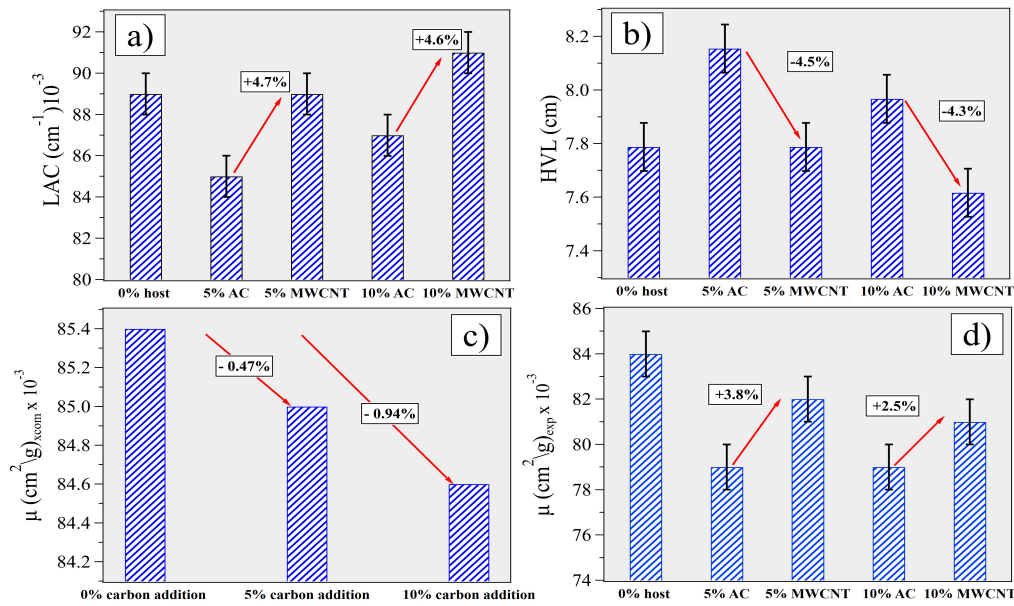


**Figure 3.** a) the LAC values for all the samples in this study, b) the HVT, c) the  $\mu$  values as obtained by XCOM, and d) comparison between values of  $\mu$  from the XCOM program and the experimental values for the different types and concentrations of carbon in the study.

In Figure 3-a, the decrease in the LAC values after the addition of activated carbon can be attributed to the fact that the LAC value is less for materials that are composed of elements of smaller atomic numbers. Particularly, increasing the concentration of carbon atoms in the sample results in reducing the concentrations of the rest of the elements in the sample like oxygen and nitrogen which each has slightly a larger atomic number (see Table 2 for the concentrations of the elements). However, the addition of MWCNTs to the gelatin-water mixture (by 5% and 10%) results in an increase of about  $\approx 4.7\%$  and  $4.6\%$  in the LAC values relative to the gelatin-water mixture with 5% and 10% of activated carbon respectively. Since the concentration of carbon (in the two forms, as activated carbon or MWCNTs) in the compared samples is the same, the extraordinary structure of the MWCNTs is the only factor that can be responsible for such an increase in the LAC values.

The HVT value of the gelatin-water mixture after the addition of 5% and 10% of MWCNTs decreases with 4.5% and 4.3 % respectively when compared with the addition of activated carbon as demonstrated in Figure 3-b. Such a decrease in the HVT is due to the extra shielding from the interaction between the  $\gamma$  radiation and the MWCNTs' cylindrical geometry. The increase in the HVT value after the addition of activated carbon is justified by the increase of carbon percentage in the mixture relative to oxygen and nitrogen.

The theoretical mass attenuation coefficients  $\mu$  for the gelatin-water mixture with the addition of 0%, 5%, and 10% carbon obtained using the XCOM program were presented in figure 3-c. It's evident in figure 3-c that the gelatin-water mixture has less  $\mu$  as the concentration of carbon is increased. However, the current experimental results show that the addition of carbon in the MWCNTs form has the opposite effect as demonstrated in Figure 3-d. Particularly, while the addition of the activated carbon (for both 5% and 10% concentrations) decreases the values of  $\mu$ , the addition of MWCNTs increases the values of  $\mu$  for the same concentrations. Based on this, it is clear that MWCNTs due to their unique structure add extra shielding strength to the gelatin-water mixture.

Since the MWCNTs geometry and structure appear to be the only factors enhancing the shielding properties, we should try to find a connection between the physical properties of the  $\gamma$  radiation and the main features of the MWCNTs structure and geometry. It's noteworthy that the wavelength of the  $\gamma$ -rays used in this study at an energy of 0.662 MeV is around 1.87pm, where the interlayer spacing between the walls of the MWCNTs is around 0.35 nm [28]. In this case, the ratio between the wavelength of  $\gamma$ -ray and interlayer spacing size is around 1:200. For such a small ratio between the wavelength and the interlayer spacing, one would expect less interaction between the  $\gamma$ -rays and the MWCNTs. The ratio between the wavelength of the X-ray and the interlayer spacing between the walls of MWCNTs can be calculated as 1:20 in Fujimori et al. work [9], where the used X-ray wavelength was 7.11 nm and the spacing between MWCNTs walls was 0.35 nm. The ratio in both cases can be correlated with the shielding capabilities where a stronger interaction is expected for the X-rays case. Based on the values of the two ratios above, it can be concluded as the ratio between the photon wavelength and the interlayer spacing is close to 1:1, the shielding capability against electromagnetic

radiation would be stronger. This can be observed in the achieved shielding enhancement due to the addition of MWCNTs against the X-ray radiation (50% enhancement, as in Ref.[9]) compared to the shielding enhancement against the  $\gamma$ -rays shielding in the current work (5% enhancement) when MWCNTs are used.

## 5. CONCLUSIONS

In the current study, the *LAC* values for the gelatin-water mixture, for the gelatin-water mixture with activated carbon addition (5% and 10%), and for MWCNTs addition (5% and 10%) are investigated experimentally and theoretically. In contrast to the theoretical prediction of the XCOM program of a decrease in the *LAC* values, the addition of MWCNTs has increased the *LAC* values by 5% when compared to the addition of activated carbon. The main reason for such an increase is only explained by the interaction of  $\gamma$  radiation with the unique structure of MWCNTs when compared with the activated carbon. It is recommended to use the MWCNTs to enhance the shielding properties in the X-ray range rather than in the  $\gamma$ -ray range due to stronger interaction when the wavelength of the radiation is close to the interlayer spacing of the MWCNTs. In the medical fields, if MWCNTs are introduced to enhance heating effects in living tissues due to the application of microwaves radiation as many studies have proposed [17],  $\gamma$  radiation therapy can be used too on the tissue without the need to dramatically increase the radiation doses.

## ORCID

Moaz M. Altarawneh, <https://orcid.org/0000-0001-9278-9907>; Mutaz W. Aladailah, <https://orcid.org/0000-0002-8675-0608>; Osama Y. Al-Madanat, <https://orcid.org/0000-0002-7107-9460>

## REFERENCES

- [1] Z. Shariatnia, "Applications of carbon nanotubes," in *Handbook of Carbon-Based Nanomaterials*, edited by S. Thomas, C. Sarathchandran, S. A. Ilangoan, and J. C. Moreno-Pirajan, (Elsevier, 2021). pp. 321-364.
- [2] P.S. R. Kumar, and S. J. Alexis, "Synthesized Carbon Nanotubes and Their Applications," in: *Carbon-Based Nanofillers and Their Rubber Nanocomposites*, edited by S. Yaragalla, R. Mishra, S. Thomas, N. Kalarikkal, and H. J. Maria, (Elsevier, 2019), Chapter Four, pp. 109-122.
- [3] A. D'Alessandro, and F. Ubertini, "Advanced Applications of Carbon Nanotubes in Engineering Technologies," in: *Handbook of Carbon Nanotubes*, edited by J. Abraham, S. Thomas, and N. Kalarikkal, (Springer, 2021), pp. 1-38. [https://doi.org/10.1007/978-3-319-70614-6\\_75-1](https://doi.org/10.1007/978-3-319-70614-6_75-1)
- [4] H. P. Wong, and D. Akinwande, *Carbon Nanotube and Graphene Device Physics*, (Cambridge University Press, 2010). Chapter 9, pp. 233-248.
- [5] A. Agarwal, A. Nieto, D. Lahiri, A. Bisht, and S. R. Bakshi, *Carbon nanotubes: Reinforced Metal Matrix Composites*, (CRC Press, 2021).
- [6] Q. Li, J. Liu, and S. Xu, "Progress in research on carbon nanotubes reinforced cementitious composites," *Advances in Materials Science and Engineering*, **2015**, 307-445 (2015). <https://doi.org/10.1155/2015/307435>
- [7] M. A. Tarawneh, S. A. Sarairoh, R. S. Chen, S. H. Ahmad, M. A. Al-Tarawni, and L. J. Yu, "Gamma irradiation influence on mechanical, thermal and conductivity properties of hybrid carbon nanotubes/montmorillonite nanocomposites," *Radiation Physics and Chemistry*, **179**, 109168 (2021). <https://doi.org/10.1016/j.radphyschem.2020.109168>
- [8] J. Naveen, S. Amizhtan, M. Danikas, T. Imai, and R. Sarathi, "Effect of gamma-ray irradiation on the electrical and mechanical properties of epoxy/TiO<sub>2</sub> nanocomposite," in: *2021 IEEE International Conference on the Properties and Applications of Dielectric Materials*, (2021). <https://doi.org/10.1109/ICPADM49635.2021.9493940>
- [9] T. Fujimori, S. Tsuruoka, B. Fugetsu, S. Maruyama, A. Tanioka, M. Terrones, M.S. Dresselhaus, M. Endo, and K. Kaneko, "Enhanced X-ray shielding effects of carbon nanotubes," *Materials Express*, **1**(4), 273-278 (2011). <https://doi.org/10.1166/mex.2011.1043>
- [10] A. Ambrosio, and C. Aramo, "Carbon nanotubes-based radiation detectors," in: *Carbon Nanotubes Applications on Electron Devices*, edited by J.M. Marulanda, (IntechOpen, 2011). <http://dx.doi.org/10.5772/18086>
- [11] J. E. Martin, *Physics for radiation protection*, Chapter 8, 3d edition, (WILEY-VCH, 2013), pp. 307-361.
- [12] H. Hassan, H. Badran, A. Aydarous, and T. Sharshar, "Studying the effect of nano lead compounds additives on the concrete shielding properties for  $\gamma$ -rays," *Nuclear Instruments and Methods in Physics Research Section B: Beam Interactions with Materials and Atoms*, **360**, 81-89 (2015). <https://doi.org/10.1016/j.nimb.2015.07.126>
- [13] A. M. El-Khatib, T. I. Shalaby, A. Antar, and M. Elsafi, "Improving gamma ray shielding behaviors of polypropylene using PBO nanoparticles: An experimental study," *Materials*, **15**(11), 3908 (2022). <https://doi.org/10.3390/ma15113908>
- [14] W. Zhang, H. Xiong, S. Wang, M. Li, Y. Gu, and R. Li, "Gamma-ray shielding performance of Carbon Nanotube Film material," *Materials Express*, **6**(5), 456-460 (2016). <https://doi.org/10.1166/mex.2016.1326>
- [15] J. Viegas, L. A. Silva, A. M. S. Batista, C. A. Furtado, J. P. Nascimento, and L. O. Faria, "Increased X-ray Attenuation Efficiency of Graphene-Based Nanocomposite," *Industrial and Engineering Chemistry Research*, **56**(41), 11782-11790 (2017). <https://doi.org/10.1021/acs.iecr.7b02711>

- [16] A. Mashal, B. Sitharaman, X. Li, P. K. Avti, A. V. Sahakian, J. H. Booske, and S. C. Hagness, "Toward carbon nanotube-based the ranostic agents for microwave detection and treatment of breast cancer: Enhanced dielectric and heating response of tissue-mimicking materials," *IEEE Transactions on Biomedical Engineering*, **57**(8), 1831-1834 (2010). <https://doi.org/10.1109%2FTBME.2010.2042597>
- [17] M. L. Taylor, and T. Kron, "Consideration of the radiation dose delivered away from the treatment field to patients in radiotherapy," *Journal of Medical Physics*, **36**(2), 59-71 (2011). <https://doi.org/10.4103%2F0971-6203.79686>
- [18] H. Itynowicz, P. Hodurek, J. Kaczmarczyk, M. Kula'zy'nski, and M. Lukaszewicz, "Hydrolysis of surfactin over activated carbon," *Bioorganic Chemistry*, **93**, 102896 (2019). <https://doi.org/10.1016/j.bioorg.2019.03.070>
- [19] M. Berger, J. Hubbell, S. Seltzer, J. Chang, J. Coursey, R. Sukumar, D. Zucker, and K. Olsen, "XCOM: photon cross database (section version 1.5) Gaithersburg, MD: The National Institute of Standards and Technology (NIST) (2010). <https://dx.doi.org/10.18434/T48G6X>
- [20] J. T. Bushberg, "The AAPM/RSNA physics tutorial for residents. X-ray interactions," *RadioGraphics*, **18**(2), 457-468 (1998). <https://doi.org/10.1148/radiographics.18.2.9536489>
- [21] Y. M. Tsipenyuk, *Physical methods, instruments and Measurements*, (Eolss Publishers Co Ltd, 2009).
- [22] H. Cember, T. E. Johnson, *Introduction to Health Physics*, 4th ed., (McGraw-Hill Education, 2008).
- [23] M. M. Altarawneh, G. A. Alharazneh, and O. Y. Al-Madanat, "Dielectric properties of single wall carbon nanotubes-based gelatin phantoms," *Journal of Advanced Dielectrics*, **8**(02), 1850010 (2018). <https://doi.org/10.1142/S2010135X18500108>
- [24] M. Lazebnik, E. L. Madsen, G. R. Frank, and S. C. Hagness, "Tissue-mimicking phantom materials for narrow-band and ultrawideband microwave applications," *Physics in Medicine and Biology*, **50**(18), 4245-4258 (2005). <https://doi.org/10.1088/0031-9155/50/18/001>
- [25] P. Worsfold, A. Townshend, C.F. Poole, and M. Manuel, *Encyclopedia of analytical science*, (Elsevier, 2019).
- [26] B. Irene, and C. Grupen, *Handbook of Particle Detection and Imaging*, (Springer, 2012).
- [27] L. Gerward, N. Guilbert, K. Jensen, and H. Levring, "WinXCom – a program for calculating X-ray attenuation coefficients," *Radiation Physics and Chemistry*, **71**(3-4), 653-654 (2004). <http://dx.doi.org/10.1016/j.radphyschem.2004.04.040>
- [28] O. V. Kharissova, and B. I. Kharisov, "Variations of interlayer spacing in carbon nanotubes," *RSC Adv.* **4**(58), 30807-30815 (2014). <https://doi.org/10.1039/C4RA04201H>

## ВПЛИВ ДОДАВАННЯ БАГАТОСТІННИХ ВУГЛЕЦЕВИХ НАНОТРУБОК НА ВЛАСТИВОСТІ ЕКРАНУВАННЯ ВІД ГАММА-ВИПРОМІНЮВАННЯ

Моаз М. Альтарауне<sup>a</sup>, Мутаз В. Аладайла<sup>a</sup>, Усама Й. Аль-Маданат<sup>b,c</sup>

<sup>a</sup>Кафедра фізики, Університет Мута, Алкарак 61710, Йорданія

<sup>b</sup>Кафедра хімії, Університет Мута, Алкарак 61710, Йорданія

<sup>c</sup>Інститут технічної хімії Університет імені Готфріда Вільгельма Лейбніца,  
Ганновер, Каллінштрассе 5, Ганновер Німеччина

У цій роботі розглядається вплив додавання багатостінних вуглецевих нанотрубок (MWCNT) на екрануючі властивості матеріалів. Досліджено гамма-випромінювання з енергією 662 кеВ від джерела <sup>137</sup>Cs. Виміряно коефіцієнт лінійного загасання матеріалів на основі MWCNT (суміш желатин-вода) з концентрацією MWCNT 0%, 5% і 10%. Щоб виділити внесок унікальної структури MWCNT в екрануючі можливості, були виготовлені зразки з такою ж концентрацією активованого вугілля та отримані їхні лінійні коефіцієнти ослаблення. Крім того, лінійний і масовий коефіцієнти ослаблення отримані теоретично для однакових концентрацій за допомогою XCOM програми та порівняно із вимірними значеннями. Виявлено, що додавання MWCNTs на 5% або 10% збільшило лінійний коефіцієнт ослаблення приблизно на 5% у порівнянні з тими ж концентраціями активованого вугілля. Це збільшення можливостей екранування від гамма-випромінювання може бути пов'язане із взаємодією гамма-випромінювання з геометрією та структурою MWCNTs.

**Ключові слова:** радіація; екранування; коефіцієнт ослаблення; XCOM; багатостінні вуглецеві нанотрубки

## COMPREHENSIVE INVESTIGATION OF NEOLITHIC CERAMIC SAMPLES: FIRING TECHNOLOGY AND AGE INSIGHTS<sup>†</sup>

 Sahib Mammadov\*,  Aybeniz Ahadova

*Institute of Radiation Problems, ANAS, Azerbaijan*

\*Corresponding Author e-mail: [mammadov.irp@gmail.com](mailto:mammadov.irp@gmail.com)

Received April 28, 2023; revised May 31, 2023; accepted June 5, 2023

Thermogravimetric (TG/DTG), thermoluminescence (TL), and X-ray powder diffraction (XRD) techniques were applied to characterize samples collected from the archaeological site of Polutepe in Azerbaijan, dating to the Neolithic period, and gave new information on the firing technology. The thermogravimetric analysis of ceramic shards from Polutepe revealed that the firing temperature of the samples was in the range of 700°C, based on the presence of calcite in the sample. XRD analysis confirmed the presence of quartz, feldspar, and clay minerals in the ceramic samples. According to XRD analysis the mineral composition of the ceramic sample from Polutepe site was as follows: Quartz-33.8 mass%, Feldspar (albite)-21.7 mass%, Muscovite- 33.6 mass%, and Calcite- 10.9 mass%. TL glow-curve intensity at 325°C was measured to estimate the historical dose of the sample, which was found to be 22.19±1.36 Gy. The concentration of U, Th, and K were 2.24±0.20 ppm, 8.31±0.80 ppm, 2.39±0.23% respectively. Dose rate and age calculation were conducted using the DRAC, version 1.2 and output results are as follows: Environmental dose rate: 3.46±0.19 mGy/a; Age of the sample: 4.400±530 BC years which are in line with the stratigraphically estimated age of this area and with the radiocarbon age (4270±160 BC) reported in our previous work. The results obtained from this multidisciplinary approach provide insights into the firing technology and age of the ceramic samples.

**Keywords:** Thermogravimetry; X-ray powder diffraction; Ancient ceramic; Firing temperature; Clay; Quartz; Feldspar

**PACS:** 78.60.Kn

### INTRODUCTION

Archaeology in modern times is adopting an interdisciplinary methodology that employs a range of instrumental techniques to examine ancient artifacts. The defining characteristic of the Neolithic period is pottery, and a detailed account of ancient pottery typically involves an explanation of its mineralogical, chemical, and thermal attributes. The outcomes of the analyses conducted through these methods can help make significant findings in studies of dating and the evolution of ancient technologies. Thermal analysis has been extensively employed to scrutinize ancient ceramics using a variety of approaches such as powder X-ray diffraction, thermogravimetry, simultaneous thermal analysis, and thermoluminescence.

To check the quality of ceramics, thermal analysis methods are widely used, allowing you to control the processes during firing [1][2]. The traditional approach is that if gas is released from the sample during heat treatment, then the thermal transformation of minerals in the clay composition is considered irreversible [3]–[7]. When reheating, i.e., when a ceramic product is analyzed, exothermic reactions with gas release occur only at temperatures above the first heating.

Thermogravimetric studies of ancient ceramics and pottery are based on these considerations. Based on these studies, the production conditions are reconstructed, and attempts are made to identify sources of raw clay, which enables archaeologists to guess the technological level of the ancient potters and restore ancient trade links between regions by comparing ceramics from different localities.

Ceramics usually consists of clay minerals and various additives like quartz, feldspars, calcite, etc. These minerals contain unique information about the firing conditions of raw materials. Because quartz and feldspars are thermally very stable, only clay and calcite constituent minerals undergo significant changes during firing. Clay minerals (smectites and kaolinite) transform into an amorphous phase, while calcite decomposes to form CO<sub>2</sub>. The powder X-ray diffraction (PXRD) [1] method provides adequate information on the mineral composition of ceramics, thereby allowing estimation of the firing temperatures of ancient ceramics. And the presence of certain minerals helps to establish the origin of ceramics. The possibility of measuring the TL luminescence properties of quartz in order to determine the firing temperature of archeological ceramic artifacts was also investigated in [8].

### MATERIALS AND METHODS

The Institute of Archeology, Ethnography, and Anthropology of ANAS provided samples of single fragments of ceramics found at the archeological site Polutepe. It is located on the eastern outskirts of Uchtepe village of Jalilabad region, Azerbaijan Republic, on the right (southern) bank of the Injachai river (39°19' 37. 67" N, 48° 27' 05.71" E) at 38 m above sea level. A ceramic sample for analysis was taken at the base of the furnace, at a depth of 6.3 m from the standard reference point, 5.3 m into the Neolithic layer, and 0.7 m above the base of the settlement. Most of these specimens are believed to be from the Neolithic period and may have been used for cooking or preserving food. The samples were air-dried overnight at 50°C before analysis and finely powdered in an agate mortar.

<sup>†</sup> Cite as: S. Mammadov, A. Ahadova, East Eur. J. Phys. 3, 531 (2023), <https://doi.org/10.26565/2312-4334-2023-3-61>

© S. Mammadov, A. Ahadova, 2023

PXRD was performed using a D2Phaser (Bruker) diffractometer with Ni-filtered CuK $\alpha$  radiation on randomly oriented samples. The samples were scanned at the region of  $5 \leq 2\theta \leq 75^\circ$  at a scanning speed of  $1.2^\circ/\text{min}$ . Semi-quantitative estimates of the abundance of the mineral phases were derived from the PXRD data, using the intensity of specific reflections, the density, and the mass absorption coefficients of the elements for CuK $\alpha$  radiation.

Thermogravimetric and differential thermal analysis of ceramic powders were carried out in a Perkin Elmer STA6000 Simultaneous Thermal Analyzer with the following parameters: heating range from ambient to  $950^\circ\text{C}$ , heating rate  $5^\circ\text{C}$ , balance sensitivity-  $0.1\mu\text{g}$ , and nitrogen gas flow- $20\text{ ml/min}$ .

The Harshaw TLD 3500 Manual Reader is used to measure the characteristics of TL samples. TL measurements were performed using a linear heating rate  $20^\circ\text{C/s}$  from  $50^\circ\text{C}$  to  $400^\circ\text{C}$ . Three aliquots of  $5\text{ mg}$  each of the samples were used for each measurement. TL data points represent the average of three different aliquots of the sample. A thin and uniform layer of feldspar grains was laid on the planchet surface in order to get full contact that ensures uniform TL signal from the sample.

In order to estimate the natural dose rate soil samples were collected from the site and U, Th, and K content analysis by gamma spectrometry Canberra GR4520 which has a low-level gamma spectrometry system with  $15\text{ cm}$  lead shielding and high-resolution GeHP hyper pure germanium detector, having  $43.5\%$  resolution efficiency for  $661.6\text{ keV}$ .

## RESULTS AND DISCUSSIONS

### Thermogravimetric analysis

The results of the TG and DTG analysis of the ceramic shred from Polutepe are presented in Fig. 1.

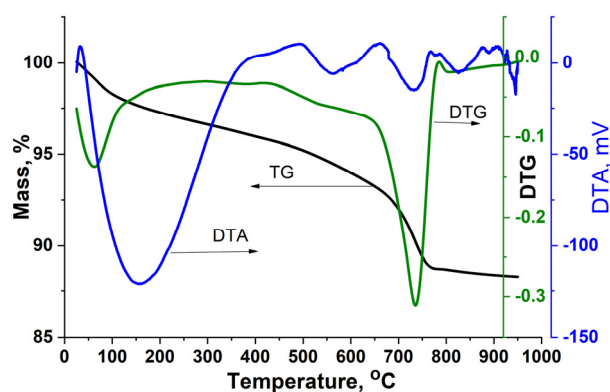
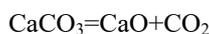


Figure 1. TG, DTG and DTA curves of ceramic shred from Polutepe

The DTG curve has a small peak at about  $100^\circ\text{C}$  and a deep peak at  $650\text{--}750^\circ\text{C}$ . A large peak in the temperature ranges from  $100$  to  $400^\circ\text{C}$  on the DTA curve indicates endothermic processes due to dehydration/dihydroxylation. Mass loss figures are summarized in Table 1. The total mass loss ( $m_3$ ) is  $11.8\%$ . Mass loss in the region  $\leq 350^\circ\text{C}$  occurs due to dehydration ( $m_1$ ) and is  $4.05\%$ , and mass loss due to dehydroxylation ( $m_2$ ) occurs in the region of  $350^\circ\text{C}\div 600^\circ\text{C}$  and is  $2.71\%$ . Mass loss above a temperature of  $600^\circ\text{C}$  can be attributed to the decomposition of calcite ( $m_3=5.12\%$ ) according to the reaction:



There are different approaches in the literature for determining the firing temperature of ancient pottery [9]. The basic idea of the thermogravimetric method is that only reversible thermal transformations will be detected if the sample is heated a second time. Upon reheating, transformations not observed in the previous heating will be detected only at temperatures above the upper-temperature limit of the first heating. The irreversibility of thermal transformations in clay occurs due to chemical transformations with the release of gaseous products, the formation of new minerals, or irreversible phase transformations.

Calcite is the most common “fingerprint” for determining the provenance of ceramics and, to some extent, for determining the firing temperature since it can be added to ceramic paste or found in the original clays as a natural impurity. The presence of calcite in ancient pottery is considered today the sign of low-temperature firing at about  $700^\circ\text{C}$  [4]. The concentration of calcite in the investigated sample determined by XRD method is  $5.12\%$ ; therefore, according to the traditional interpretation, the firing temperature of the samples was in the range of  $700^\circ\text{C}$ . The presence of calcite in ceramic samples from Polutepe was studied by exposing the ceramic powder to hydrochloric acid. The ceramic powder was kept in a  $10\%$  HCl solution for a week and periodically mixed. After that, the ceramic powder was thoroughly washed and dried at a temperature of  $50^\circ\text{C}$  for 48 hours. The results of the TG/DTG analysis of a ceramic sample treated in an HCl solution are shown in Figs. 2. The total mass loss ( $m_3$ ) is  $8.28\%$ . Mass loss in the region  $\leq 350^\circ\text{C}$  occurs due to dehydration ( $m_1$ ) and is  $5.42\%$ , and mass loss due to dehydroxylation ( $m_2$ ) occurs in the region of  $350^\circ\text{C}\div 600^\circ\text{C}$  and is  $2.01\%$ . Mass loss above a temperature of  $600^\circ\text{C}$  was  $0.81\%$ , indicating the decomposition of the significant part of calcite.

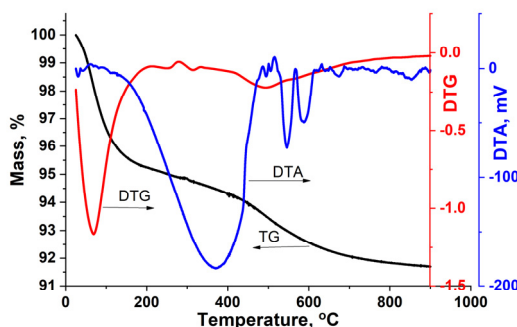


**Figure 2.** TG/DTG/DTA analysis of a ceramic sample treated in HCl solution X-ray phase analysis also reveals the calcite in the sample from Polutepe (Fig. 3).

**Table 1.** Mass-loss of ancient ceramic sample from Polutepe

| Sample             | Mass loss ≤350C, % | Mass loss ≤600C % | Mass loss ≤850C, % | m1 % | m2 % | m3 % | Total mass loss, % | m2/m1 |
|--------------------|--------------------|-------------------|--------------------|------|------|------|--------------------|-------|
| Polutepe, natural  | 95.95              | 93.24             | 88.12              | 4.05 | 2.71 | 5.12 | 11.8               | 0.67  |
| Polutepe, with HCl | 94.58              | 92.57             | 91.76              | 5.42 | 2.01 | 0.81 | 8.28               | 0.37  |

**Chemical and XRD analysis**

XRD analysis of ceramic shreds reveals that all investigated samples contain similar minerals: quartz, feldspar, and clay (Fig.3).

Feldspars (in our case, albite) can be introduced into the ceramic mass as a hardening or be present in the composition of the original clay as a natural admixture since the clays themselves are weathering products of feldspar. Quartz is a significant component of tempering materials and also exists in raw clay as a natural mixture. Quartz undergoes a phase transition around 573°C when heated, but this process is reversible, and no signs of previous heating could be detected after cooling.

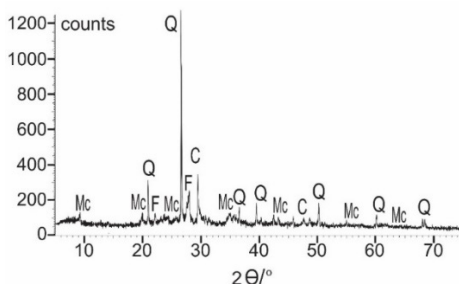


**Figure 3.** XRD patterns of ceramic shred from Polutepe. Mc-muscovite; Q-quartz; F-feldspar (albite); C-calcite.

According to XTD analysis the mineral composition of the ceramic sample from Polutepe site was as follows: Quartz-33.8 mass%, Feldspar (albite)-21.7 mass%, Muscovite- 33.6 mass%, and Calcite- 10.9 mass%.

*TL analysis*

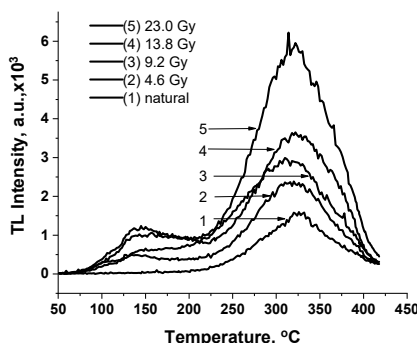


**Figure 4.** TL glow-curve of quartz samples extracted from ancient ceramic at different additional laboratory doses. (1) The TL glow curve of unirradiated quartz extracted from pottery sample. The four aliquots of quartz were irradiated with additional laboratory doses 4.6 (2); 9.2 (3); 13.8 (4); and 23 Gy (5) respectively. Dose rate- 0.194 Gy/s.

Fig. 4 illustrates the dose dependence of the TL glow curve from 0 to 24 Gy. Samples were irradiated with <sup>60</sup>Co gamma source then TL glow-curves measured after two days. Plotting the TL glow-curve intensity at 325°C against the dose adsorbed and backward extrapolation enables the estimation of historical dose equal to 22.19±1.36 Gy.

Soil sample collected from the close proximity of the pottery sample was air dried and kept in a closed environment for one month. The concentration of U, Th, and K were  $2.24 \pm 0.20$  ppm,  $8.31 \pm 0.80$  ppm,  $2.39 \pm 0.23$  % respectively. Dose rate and age calculation were conducted using the DRAC version 1.2 and output results are as follows: Environmental dose rate:  $3.46 \pm 0.19$  mGy/a and; Age of the sample:  $4.400 \pm 530$  BC years which are in line with the stratigraphically estimated age of this area and with the radiocarbon age ( $4270 \pm 160$  BC) reported in our previous work [10].

### CONCLUSIONS

TG and DTG analysis of the ceramic shred from Polutepe showed a total mass loss of 11.8%, with mass loss above  $600^\circ\text{C}$  attributed to the decomposition of calcite. The presence of calcite in the ceramic samples suggested a firing temperature of around  $700^\circ\text{C}$ . The studied ceramic shred from Polutepe consisted, as it was deduced from XRPD studies, mainly of quartz, calcite, feldspar (albite), and micas (muscovite).

The thermal properties of the studied ceramic sample from Polutepe obtained from the TG/DTG analysis were consistent with their mineralogical data.

The TL glow curve and dose rate calculations indicated an estimated historical dose of  $22.19 \pm 1.36$  Gy and an age of the sample of  $4.400 \pm 530$  BC years, respectively, which are in line with the stratigraphically estimated age of the area and previous radiocarbon dating results.

### ORCID IDs

● Sahib Mammadov, <https://orcid.org/0000-0002-4547-4491>; ● Aybeniz Ahadova, <https://orcid.org/0000-0001-9173-9537>

### REFERENCES

- [1] J.A. Stratis, M. Lalia-Kantouri, E.L. Charalambous, A. Charalambous, and N. Kantiranis, "Thermal, chemical, and mineralogical characterization of ceramic tobacco pipes from Cyprus," *J. Therm. Anal. Calorim.* **104**(2), 431-437 (2011). <https://doi.org/10.1007/s10973-010-1141-x>
- [2] D. Vlase, O. Rogozea, C. Moşoiu, G. Vlase, R. Lazău, and T. Vlase, "Thermoanalytical investigations of some ceramics dated from the Neolithic period, discovered at Oxenbricel, Sănanndrei, Romania," *J. Therm. Anal. Calorim.* **138**(3) 2145-2157 (2019). <https://doi.org/10.1007/s10973-019-08767-8>
- [3] S. Meyvel, P. Sathya, and G. Velraj, "Thermal characterization of archaeological pot sherds recently excavated in Nedunkur, Tamilnadu, India Caracterização térmica de fragmento cerâmico arqueológico," *Ceramica*, **58**(347), 338-341 (2012). <https://doi.org/10.1590/S0366-69132012000300009>
- [4] D.N. Papadopoulou, M. Lalia-Kantouri, N. Kantiranis, and J.A. Stratis, "Thermal and mineralogical contribution to the ancient ceramics and natural clays characterization," *J. Therm. Anal. Calorim.* **84**(1), 39-45 (2006). <https://doi.org/10.1007/s10973-005-7173-y>
- [5] V.A. Drebuschak, L.N. Mylnikova, and V.I. Molodin, "Thermogravimetric investigation of ancient ceramics: Metrological analysis of sampling," *Journal of Thermal Analysis and Calorimetry*, **90**(1), 73-79 (2007). <https://doi.org/10.1007/s10973-007-8478-9>
- [6] V.A. Drebuschak, L.N. Mylnikova, and T.N. Drebuschak, "The mass-loss diagram for the ancient ceramics," *J. Therm. Anal. Calorim.* **104**(2), 459-466 (2011). <https://doi.org/10.1007/s10973-010-1230-x>
- [7] V.A. Drebuschak, L.N. Mylnikova, and T.N. Drebuschak, "Thermoanalytical investigations of ancient ceramics," *J. Therm. Anal. Calorim.* **133**(1), 135-176 (2018). <https://doi.org/10.1007/s10973-018-7244-5>
- [8] G.S. Polymenis, A. Sakalis, D.N. Papadopoulou, G. Dallas, G. Kitis, and N.C. Tsirliganis, "Firing temperature of pottery using TL and OSL techniques," *Nucl. Instruments Methods Phys. Res. Sect. A Accel. Spectrometers, Detect. Assoc. Equip.* **580**(1), 747-750 (2007). <https://doi.org/10.1016/j.nima.2007.05.139>
- [9] V. Molodin, L. Mylinkova, N. Shtertser, I. Durakov, and V.A. Drebuschak, "Thermogravimetry in the Studies of Ancient Technical Ceramics," *Chem. Sustain. Dev.* **27**(1), 101-108 (2019). <https://doi.org/10.15372/csd20190116>
- [10] T.I. Akhundov, S.G. Mammadov, A.A. Ahadova, and A.N. Abdullayev, "Dating of Charcoal Samples from the Polutepe Archeological Site in Azerbaijan," *Asian J. Humanit. Soc. Stud.* **6**(4), 321-2799 (2018). <https://doi.org/10.24203/ajhss.v6i4.5459>

### КОМПЛЕКСНЕ ДОСЛІДЖЕННЯ ЗРАЗКІВ КЕРАМІКИ НЕОЛІТУ: ТЕХНОЛОГІЯ ВІДПАЛУ ТА ВІК

Сахіб Мамедов, Айбеніз Ахадова

*Інститут радіаційних проблем НАНА, Азербайджан*

Методи термогравіметрії (TG/DTG), термолюмінесценції (TL) і рентгенівської порошкової дифракції (XRD) були застосовані для характеристики зразків, зібраних з археологічної стоянки Полутепе в Азербайджані, що датуються періодом неоліту, і дали нову інформацію про технології відпалу. Термогравіметричний аналіз черепків кераміки з Полутепе показав, що температура відпалу зразків була в межах  $700^\circ\text{C}$ , виходячи з наявності кальциту в зразку. XRD аналіз підтвердив наявність кварцу, польового шпату та глинистих мінералів у зразках кераміки. За даними ХТД-аналізу, мінеральний склад зразка кераміки з стоянки Полутепе був таким: кварц – 33,8 мас.%, польовий шпат (альбіт) – 21,7 мас.%, мусковіт – 33,6 мас.%, кальцит – 10,9 мас.%. Інтенсивність кривої світіння TL при  $325^\circ\text{C}$  була виміряна для оцінки історичної дози зразка, яка виявилася  $22,19 \pm 1,36$  Гр. Концентрації U, Th і K становили  $2,24 \pm 0,20$  ppm,  $8,31 \pm 0,80$  ppm,  $2,39 \pm 0,23\%$  відповідно. Розрахунок потужності дози та віку було проведено за допомогою DRAC, версія 1.2, і отримані результати такі: потужність дози в навколишньому середовищі:  $3,46 \pm 0,19$  мГр/рік; вік зразка:  $4,400 \pm 530$  років до н.е., що відповідає стратиграфічно оціненому віку цієї території та радіовуглецевому віку ( $4270 \pm 160$  до н.е.), про які ми повідомляли в попередній роботі. Результати, отримані в результаті цього мультидисциплінарного підходу, дають змогу зрозуміти технологію випалу та вік зразків кераміки.

**Ключові слова:** термогравіметрія; рентгенівська порошкова дифракція; старовинна кераміка; температура відпалу; глина; кварц; польовий шпат

## ADVANCEMENTS IN THERMOLUMINESCENCE DATING: A CASE STUDY OF MEDIEVAL BRICK STRUCTURES IN AZERBAIJAN<sup>†</sup>

 Sahib Mammadov\*,  Aqshin Abishov

*Institute of Radiation Problems, ANAS, Azerbaijan*

\*Corresponding Author e-mail: [mammadov.irp@gmail.com](mailto:mammadov.irp@gmail.com)

Received June 15, 2023; revised July 6, 2023; accepted July 7, 2023

The study aimed to improve the precision of dating historical landmarks, specifically the Ballabur castle in Lenkaran, Azerbaijan Republic, using the thermoluminescence dating (TL) method. The annual dose rate, calculated with  $\gamma$ -spectrometer equipped with a hyper-pure germanium detector, was found to be  $2.98 \pm 0.19$  mGy/year. By employing an online dose rate and age calculator, the sample's age was determined to be  $920 \pm 50$  years, consistent with the historical estimates of this region.

**Keywords:** Ballabur castle; Thermoluminescence dating; Annual dose rate; Quartz

**PACS:** 78.60.Kn

### INTRODUCTION

Determining the age of archaeological artifacts poses a significant challenge in geological science and practice. This method exploits the accumulation of nonequilibrium charge carriers on defects in dielectric materials caused by ionizing radiation from natural radionuclides present in the objects being dated or their surroundings. The thermoluminescence (TL) method has proven to be a reliable technique for dating archaeological ceramics [1]–[3]. In the case of fired bricks, the determined age corresponds to the time elapsed between the firing of the product and their removal from the burial site [4], [5].

The age of brickwork in many standing buildings from Azerbaijan's late medieval and early modern periods (11<sup>th</sup> to 19<sup>th</sup> centuries AD) can only be determined through historical records or by analyzing their design and style. However, this typological dating method relies on the availability of written records. This research aims to establish a standardized procedure for dating medieval brick structures in Azerbaijan. We collected two brick samples from the Ballabur castle in Lankaran, Azerbaijan, which architectural experts have already estimated to be approximately 1000 years old.

### MATERIALS AND METHODS

Quartz, a commonly occurring mineral in raw ceramic paste, undergoes a significant change during the heat treatment (600–700°C). This change eliminates all previously accumulated charge carriers within the quartz, which have been building up since the mineral's formation. Consequently, when employing the thermoluminescence method for dating, a reset to a zero state occurs through the heating process during ceramics, bricks, or pottery manufacturing.

However, in solid materials like quartz crystals, there are traps at various energy levels for both electrons and holes. To determine the age of ceramics, the trapped electrons' (or holes') lifetime at room temperature should be at least 10–20 times longer than the age of the studied objects. In practical terms, the TL peaks with a luminescence maximum of 230–375°C in quartz and feldspars are well-suited for dating purposes.

The methodology for using thermoluminescence (TL) to determine the absolute age of artifacts is based on the observation that, up to a specific limit, the accumulation of TL in traps is roughly proportional to the radiation dose. This dose, in turn, depends on the intensity of irradiation and the duration of exposure [6]. The age of the studied material was calculated by experimentally determining the increase in TL per unit of absorbed radiation dose and the rate of natural radioactivity according to the protocol described in [2], [7].

The experiment utilized quartz samples extracted from two bricks sourced from Bellabur Castle through conventional chemical separation techniques [8]. The brick samples exhibit a light red color attributed to hematite ( $\text{Fe}_2\text{O}_3$ ), known for its strong coloring properties in pottery. Even a minimal concentration of 1% hematite was sufficient to produce a reddish hue during the firing process under oxidizing conditions [4]. The brick sample underwent a series of steps, including crushing and sieving, to obtain grain size fractions of 80 to 120  $\mu\text{m}$ . The targeted grain fraction was then treated with HCl, subjected to heavy liquid separation, and etched in 40% HF [9], [10]. Precipitated fluorides were subsequently dissolved using HCl. To ensure the purity of the quartz concentration, XRF analysis was performed, and the amount of  $\text{SiO}_2$  in the extracted samples was 98.5%.

As a result of methodological advancements, it was discovered that the most favorable measurement outcomes were achieved using powder samples weighing approximately 5 mg, with particle sizes ranging from 0.1 to 0.25 mm.

Before conducting the ED measurements, the grains underwent a preheating process to eliminate any influence from unstable traps on luminescence counts. Experimenting determined that preheating the grains at 200°C for 12 minutes

<sup>†</sup> Cite as: S. Mammadov, A. Abishov, East Eur. J. Phys. 3, 535 (2023), <https://doi.org/10.26565/2312-4334-2023-3-62>

© S. Mammadov, A. Abishov, 2023

yielded relevant results. The uncertainties in the measurements were calculated, taking into account the losses caused by anomalous fading.

The samples' natural TL (thermoluminescence) was recorded using the HarshawTLD 3500 Manual Reader. Each non-irradiated sample underwent five measurements. For accurate TL analysis, it is crucial to maintain linearity during the heating process. In this study, the sample was heated linearly up to 400°C at a rate of 5°C/s, which met the needs of the TL analysis instruments. A 3 mm heat-absorbing filter (Schott KG-1) was positioned in front of the tube.

To safeguard the photomultiplier tube against blackbody radiation. The irradiation process was conducted at room temperature using a  $^{60}\text{Co}$  source at various dose levels ranging from 5 to 25 Gy. The dose rate of the  $^{60}\text{Co}$  source was determined using the Magnetech Miniscope MS400 EPR Spectrometer. The dose was measured using individually wrapped BioMax Alanine Dosimeter Films with barcode labels developed by Eastman Kodak Company [11]. The irradiated samples, weighing approximately  $5\pm 0.5$  mg, were then read after two days in an N<sub>2</sub> atmosphere using a Harshaw 3500 manual reader, employing a linear heating rate of 5°C/s.

One of the fundamental steps in luminescence dating is calculating the annual dose rate, which represents the radiation dose received by the sample per year. In our study, this dose rate comprises three components: i) the beta dose contribution originating from the brick samples themselves, ii) the gamma dose contribution arising from the surrounding soil, and iii) a specific contribution from cosmic radiation. Soil samples were collected close to the pottery sample to determine the natural dose rate. The concentrations of Uranium, Thorium, and Potassium in the soil were measured using the Canberra GR4520 gamma spectrometry system. This system is equipped with a high-resolution GeHP (hyper-pure germanium) detector and 15 cm lead shielding, providing a resolution efficiency of 43.5% for 661.6 keV.

## RESULTS AND DISCUSSIONS

When irradiated quartz grains are heated from room temperature to 500°C, multiple TL (thermoluminescence) peaks can be observed [12]. In the case of quartz inclusions extracted from pottery, two peaks were identified above 300°C. The peak observed at the temperature of 375°C is considered more favorable compared to the lower shoulder peak of around 325°C. Another peak that emerges under laboratory irradiation is observed around 110°C, the basis for the "pre-dose dating" method. This method utilizes the peak height to monitor dose-dependent sensitivity changes after heating to 500°C. Fig. 1 depicts the dose-response of the TL glow curve, where samples were irradiated using a  $^{60}\text{Co}$  gamma source, and TL glow curves were measured two days after irradiation.

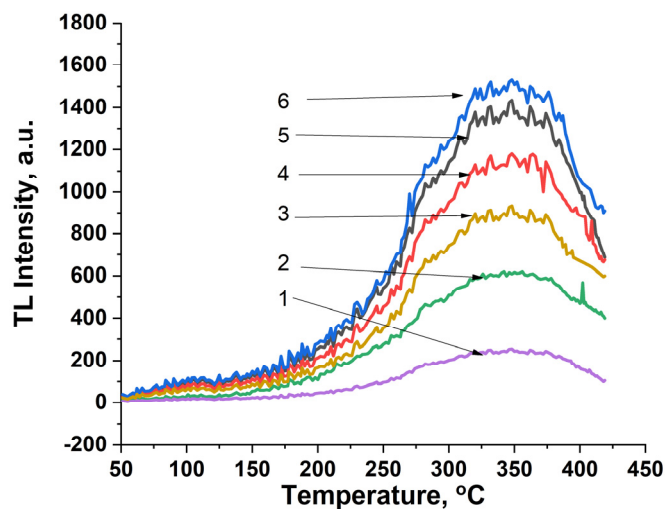


**Figure 1.** Dose-dependent TL intensity of irradiated quartz at various doses: (1) Natural quartz extracted from the brick; Quartz irradiated at (2) 5 Gy, (3) 10 Gy, (4) 15 Gy, (5) 20 Gy, and (6) 25 Gy

To assess the environmental dose rate, a soil sample collected near the pottery sample was air-dried and kept in a closed environment for one month. The determined concentrations of Uranium (U), Thorium (Th), and Potassium (K) were found to be  $2.21\pm 0.20$  ppm,  $9.71\pm 1.10$  ppm, and  $1.90\pm 0.10\%$ , respectively.

To identify a stable temperature range for the glow curve of the samples, the plateau test, as described by [12], was conducted. This procedure involved comparing the natural TL glow curve with the glow curve obtained after laboratory irradiation. The region exhibiting a plateau indicated thermal stability, as the ratio between the natural TL signal and the signal from the laboratory-irradiated sample remained constant. The archaeological dose was determined by integrating the plateau region of the respective glow curves and subtracting the background signals recorded after each measurement.

By plotting the intensity of the TL glow-curve at 350°C against the absorbed dose and extrapolating backward, the estimated historical dose was determined to be  $2.93\pm 0.30$  Gy (Fig. 2).

Precise determination of the environmental radiation dose rate is crucial for trapped charge datings methods like luminescence and electron spin resonance dating. While the calculation of the environmental radiation dose rate itself

may not be mathematically intricate, incorporating multiple variables and accounting for uncertainties can present challenges. The Dose Rate and Age Calculator (DRAC) has been developed as an accessible web-based tool [13] to address this issue. DRAC allows users to swiftly calculate environmental dose rates for various trapped charge dating applications by selecting a range of recently published attenuation and conversion factors that ensures robust and reproducible environmental radiation dose rate calculations, enhancing the accuracy of age estimations [13]. Using the DRAC version 1.2 software, dose rate and age calculations were performed. The output results are as follows: The environmental dose rate was determined to be  $2.98 \pm 0.19$  Gy/ka (gray per kilo annum), indicating the rate of radiation absorbed from the surroundings. The moisture content of a sample plays a significant role due to its impact on water dose absorption. When archaeological samples contain water, it absorbs a portion of the radiation, impeding the radiation energy from reaching the quartz grains. As a result, a dry sample's dose rate can be higher than a moist sample. This disparity can potentially lead to an underestimation of the sample's age. Hence, it is crucial to determine the percentage of water in the laboratory analysis of the samples and to consider when the dose rate is calculated.

Additionally, the cosmic dose rate, which refers to radiation from cosmic sources, was calculated to be  $0.10 \pm 0.01$  Gy/ka. Based on these calculations, the sample's age was estimated to be  $920 \pm 50$  years.

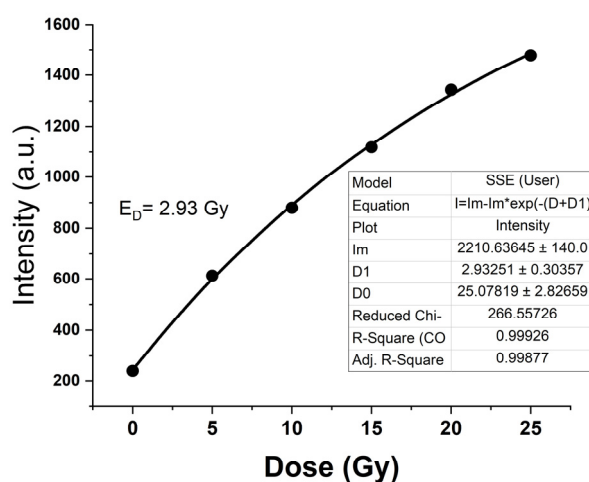


**Figure 2.** Relationship between TL signal intensity (in arbitrary units) and adsorbed dose in quartz extracted from bricks at Ballabur Castle

## CONCLUSION

Despite being in its preliminary stage and involving a limited range of samples, this study has successfully showcased the potential of utilizing the TL technique on quartz inclusions for obtaining luminescence ages of late medieval bricks. Applying the thermoluminescence (TL) dating method has provided valuable insights into the age determination of archaeological ceramics, specifically in the case of the Ballabur castle in Lenkaran, Azerbaijan Republic. By analyzing the TL peaks and conducting measurements on both irradiated and non-irradiated samples, significant progress has been made in establishing a standardized procedure for dating medieval brick structures.

The assessment of the environmental dose rate and cosmic dose rate, conducted with the help of software like DRAC, has provided vital information for age calculations. Considering factors such as the concentration of Uranium, Thorium, and Potassium in the soil, along with the historical dose estimation from TL glow-curve intensity, the age of the sample from the Ballabur castle was approximately  $920 \pm 50$  years.

These findings highlight the significance of TL dating methods in archaeological research, particularly for historical ceramics. The established methodology and measurements presented in this study contribute to the broader understanding and precise dating of medieval structures in Azerbaijan. Continued advancements in TL dating techniques will enhance our knowledge of ancient civilizations and aid in uncovering past mysteries.

## ORCID

© Sahib Mammadov, <https://orcid.org/0000-0002-4547-4491>; © Aqshin Abishov, <https://orcid.org/0000-0003-2467-4344>

## REFERENCES

- [1] E. Ekdal, A. Ege, T. Karali, and Z. Derin, "Luminescence dating studies of Yeşilova Hoyuk," *Geochronometria*, **39**(4), 268-275, (2012), <https://doi.org/10.2478/s13386-012-0013-5>
- [2] I.K. Bailiff and N. Holland, "Dating bricks of the last two millennia from Newcastle upon Tyne: a preliminary study," *Radiat. Meas.* **32**(5-6), 615-619 (2000), [https://doi.org/10.1016/S1350-4487\(99\)00286-3](https://doi.org/10.1016/S1350-4487(99)00286-3)
- [3] M. Altihan, T. Koray, and E. Sahiner, "Luminescence dating and mineralogical investigations of bricks from erikli basilica in Stratonikeia ancient city (SW-Turkey)," *Mediterr. Archaeol. Archaeom.*, **18**(1), 77-91 (2018), <https://doi.org/10.5281/zenodo.1069527>
- [4] R. Podoba, T. Kaljuvee, I. Štubňa, L. Podobník, and P. Bačík, "Research on historical bricks from a Baroque Church," *J. Therm. Anal. Calorim.* **118**(2), 591-595 (2014), <https://doi.org/10.1007/s10973-013-3417-4>

- [5] A. Zink, and E. Porto, "La datation par luminescence sur les objets de collection : une problématique spécifique," *Technè*, **24**(52), 12-13 (2021). <https://doi.org/10.4000/technè.9543>
- [6] C.X. Wang, et al., "Quartz OSL and TL dating of pottery, burnt clay, and sediment from Beicun archaeological site, China," *Quat. Geochronol.* **70**, 101281 (2022), <https://doi.org/10.1016/j.quageo.2022.101281>
- [7] A.G.A.G. Wintle, "Luminescence dating: Laboratory procedures and protocols," *Radiat. Meas.* **27**(5-6), 769-817 (1997). [https://doi.org/10.1016/S1350-4487\(97\)00220-5](https://doi.org/10.1016/S1350-4487(97)00220-5)
- [8] D. Mebhah, D. Imatoukene, F.Z. Abdelazziz, and Z. Lounis-Mokrani, "Evaluation of trap parameters associated with thermoluminescence peaks in fired quartz," *Radiat. Meas.* **41**(7-8), 813-818 (2006), <https://doi.org/10.1016/j.radmeas.2006.04.005>
- [9] A.K. Singh, I. Manna, P.P. Kumar, A. Dawar, P.P. Kumar, and M.K. Murari, "A new and effective method for quartz-feldspar separation for OSL and CRN dating," *Quat. Geochronol.* **72**, 101315 (2022), <https://doi.org/10.1016/j.quageo.2022.101315>
- [10] S. Woor, J.A. Durcan, S.L. Burrough, A. Parton, and D.S.G. Thomas, "Evaluating the effectiveness of heavy liquid density separation in isolating K-feldspar grains using alluvial sediments from the Hajar Mountains, Oman," *Quat. Geochronol.* **72**, 101368 (2022), <https://doi.org/10.1016/j.quageo.2022.101368>
- [11] S. Mammadov, A. Ahadova, A. Abishov, and A. Ahadov, "The Thermoluminescence Parameters of Irradiated K-Feldspar," *East Eur. J. Phys.* **2**, 182-186 (2023), <https://doi.org/10.26565/2312-4334-2023-2-18>
- [12] M.J. Aitken, *Thermoluminescence Dating*, (Academic Press INC., 1985).
- [13] J.A. Durcan, G.E. King, and G.A.T. Duller, "DRAC: Dose Rate and Age Calculator for trapped charge dating," *Quat. Geochronol.* **28**, 54-61 (2015), <https://doi.org/10.1016/J.QUAGEO.2015.03.012>

### УСПІХИ В ТЕРМОЛЮМІНЕСЦЕНТНОМУ ДАТУВАННІ: ПРИКЛАД СЕРЕДНЬОВІЧНИХ ЦЕГЛЯНИХ КОНСТРУКЦІЙ В АЗЕРБАЙДЖАНІ

Сахіб Мамедов, Акшин Абішов

*Інститут радіаційних проблем НАНА, Азербайджан*

Дослідження мало на меті покращити точність датування історичних пам'яток, зокрема замку Баллабур у Ленкорані, Азербайджанська Республіка, за допомогою методу термолюмінесцентного датування (TL). Річна потужність дози, розрахована за допомогою  $\gamma$ -спектрометра, оснащеного детектором надчистого германію, виявилася  $2,98 \pm 0,19$  мГр/рік. За допомогою онлайн-калькулятора потужності дози та віку було визначено, що вік зразка становить  $920 \pm 50$  років, що відповідає історичним оцінкам цього регіону.

**Ключові слова:** замок Баллабур; термолюмінесцентне датування; річна потужність дози; кварц

## INFLUENCE OF LEAD NANOPARTICLES ON STRUCTURAL, MORPHOLOGICAL, AND MECHANICAL CHARACTERISTICS OF (SiR-PU/Micro-Pb) COMPOSITES FOR RADIATION SHIELDING APPLICATIONS<sup>†</sup>

 Mousa Hawan Naeem<sup>a,\*</sup>,  Sameer Hassan Hadi Al-Nesrawy<sup>a</sup>,  Mohammed H. Al-Maamori<sup>b</sup>

<sup>a</sup>Department of Physics, College of Education for Pure Sciences, University of Babylon, Al-Hilla, 51001, Iraq

<sup>b</sup>Department of Bio-Medical Engineering, College of Engineering, University of Al-Mustaqbal, Babylon, Al-Hilla, 51001, Iraq

\*Corresponding Author e-mail: [mousahawannaem@gmail.com](mailto:mousahawannaem@gmail.com)

Received April 21, 2023; revised June 19, 2023; accepted June 19, 2023

This research includes the manufacture of a polymeric nanocomposite consisting of silicone rubber/polyurethane as a base, with the addition of the first filler of micro-lead with a ratio of 300 pphr and the second filler of nano-lead with different ratios (0, 0.2, 0.4, 0.6, 0.8 pphr). With the addition of hexane (liquid state) to the superposition using the casting technique at room temperature. The structural properties of the surfaces of the samples were measured using Fourier transformation spectroscopy (FT-IR) and the scanning electron microscope (SEM). In addition to studying the mechanical properties represented by each hardness, tensile, elongation, and elastic modulus. (FT-IR) showed the absence of a chemical reaction for all samples. While SEM measurements showed a homogeneous distribution of micro-lead and nano-lead in the presence of hexane equally, and there were no voids in the eyes of the prepared rubber equally. For the mechanical properties, we see that the hardness, tensile strength and modulus of elasticity continue to improve with the increase in the number of lead nanoparticles. And a decrease in elongation as a result of inverse proportion to the modulus of elasticity. From the results obtained, this composite can be used in gamma ray attenuation applications in shielding, especially in medical and industrial fields.

**Keywords:** Mechanical characteristics; Silicone rubber; Polyurethane; lead; Hexane; SiR-PU/micro-Pb/nano-Pb nanocomposites

**PACS:** 61.25.he, 68.35.B, 68.37.Hk, 68.60.Bs, 28.41.Qb

### 1. INTRODUCTION

A composite material is made of two or more different materials that are put together at a macroscopic level to create new qualities that can't be made by the parts working alone. Each material has its own chemical, physical, and mechanical qualities, unlike metal alloys [1]. Composites are made up of a reinforcing component and a matrix phase. Materials like polymers, ceramics, and metals can serve as the matrix phase, while fibers, flakes, or particles provide the reinforcing phase with the greater strength and stiffness. Most of the time, composite materials are put into four groups: fibrous composites, laminated composites, particle composites, and others [2]. The potential of composites as a strengthening material for many issues related to infrastructure deterioration has only recently become apparent to civil engineers and the building industry [3]. Composites are made by combining different materials that all have useful mechanical and physical characteristics [4]. In numerous engineering applications, the use of massive metals decreases the product's performance. Due to their high specific stiffness and strength, polymer-based synthetic fibre composites began to be used in numerous applications in 1930 to surmount this limitation [5]. The goal of making hybrid composites is to improve the composite characteristics by using multiple reinforcing agents in a single polymer matrix. The reinforcement impact can be enhanced or diminished depending on whether multiple reinforcing materials are used together [6]. Silicone rubber is a widely used manufactured elastomer because of its high quality and versatility. Silicone rubber can be subdivided into various kinds based on differences in monomer, vulcanization conditions, applicable environments, etc. [7]. Silicone rubber's molecular framework was built from Si-O links that alternated with one another. The primary cause of silicone rubber's deterioration with age was the breakdown of its molecular structure in a hot atmosphere. There were two major categories to the aging mechanism of silicone rubber in a thermal oxygen environment. A rearrangement process was initiated, on the one hand, due to the breaking of the Si-O-Si bond. However, the silicone rubber molecule chain structure was altered due to the oxidation of side groups [7]. Polyurethanes (PU) can be found in a wide variety of contemporary products. They are a type of polymer that has found extensive application in the healthcare, transportation, and manufacturing sectors. Polyurethanes can be found in a wide variety of goods, including furniture, coatings, adhesives, building materials, fibers, paddings, paints, elastomers, and synthetic skins [8]. Today's catheters are typically made from polyurethane or silicon elastomer. Catheter-related bloodstream infections and thrombotic complications happened significantly more frequently with polyurethane catheters in a study comparing 698 venous-access ports implanted at the forearm made of both materials. However, mechanical failures like disconnection and catheter breakage are on the rise in silicon. However, this finding only applies to devices and catheters inserted through a brachial port, which are subjected to distinct mechanical forces than those experienced through a chest port. Rubber may have an effect on catheter-related complications, as evidenced by the fact that significant differences were observed with regard to the used catheter material [9]. Because effective radiation protection materials are readily available, it is possible to use technologies that generate ionizing radiation, such as gamma rays and radioactive sources, without risking one's health. In this context, advancements in efficacious radiation shielding materials have

<sup>†</sup> Cite as: M.H. Naeem, S.H.H. Al-Nesrawy, M.H. Al-Maamori, East Eur. J. Phys. 3, 539 (2023), <https://doi.org/10.26565/2312-4334-2023-3-63>

© M.H. Naeem, S.H.H. Al-Nesrawy, M.H. Al-Maamori, 2023

gained a significant importance, which motivates the researchers working in the field of nuclear radiation to continuously search and fabricate new radiation, some of these studies are focused on developing composite materials by incorporation of various filler materials in various matrices so that the various properties of these materials will be merged and one effective composite radiation shield will be formed. In this respect, polymers are a good example because they are highly valued matrix materials that can be used to develop gamma-ray barriers that are light weight, resilient, and malleable [10,11]. Nano-particles due to extraordinary characteristics including a high surface-to-volume ratio, are incorporated into the polymer matrices to make polymer-nanocomposites that have a wide range of applications for dosimetry, calorimetric, and radiation protection purposes especially for diagnostic X-rays [12]. Silicon rubber matrix with nanomaterials can improve the gamma radiation attenuation characteristics of nanocomposites because nanomaterials are more uniform and exert less force in the composite, thereby enhancing the material's protective capacity [13]. Many fields, including manufacturing quality control, basic science, astronomy, astrophysics, nuclear engineering, medicine, and even space exploration, have made significant use of X-ray and gamma-ray technology. However, due to long-term exposure, ionizing radiation can be harmful to people working in the field, to equipment, and to the ecosystem. Shielding is the most efficient way to block harmful rays in radiation uses. Since lead is the most commonly used material for radiation shielding, its toxicity, weight, and disposal issues have severely constrained its application. As a result, alloys and glasses have been developed as progressively more suitable replacements [14]. In this present work, polymer nanocomposites were synthesized and its structural, mechanical and radiation properties were measured. From the unique results obtained, it can be used in shielding applications, especially in the medical and industrial fields.

## 2. MATERIALS AND METHODS

The materials used in the present work are silicone rubber and polyurethane as matrix, while micro-lead and nanoparticles are used as additives; a sensitive electrical scale for weighing small amounts of samples [15] with a hardness measuring instrument for measuring the rubber's hardness [16]; the (Shore-A) hardness tester (H-17A, Congenix-Wallac) tested hardness experimentally, English (Kingston) [17]. Silicone rubber is combined with a specific amount of (SiR<sub>80</sub>pphr-PU<sub>20</sub>pphr/micro-pb<sub>300</sub>pphr) nano-Pb powder (99.5% purity, 50 nm diameter) is then doped at quantities of (0, 0.2, 0.4, 0.6, 0.8 pphr) where the mixture was stirred for 15 minutes using a Stirrer (HT-120DX) and hexane to fill the gaps and homogenise the lead material by casting, to make nanocomposites of (SiR<sub>80</sub>/PU<sub>20</sub>/micro-pb<sub>300</sub>/nano-pb<sub>0.8</sub>). The rubber samples were tested by Fourier infrared spectroscopy (FT-IR) with the wavelength range (600-4000) cm<sup>-1</sup> [18]. Scanning Electron Microscope (SEM) and measuring some mechanical characteristics of rigidity represented by the hardness, tensile, elongation and modulus of elastic [19]. And radiation characteristics using two elements, Cs137 and Co60, by an American-made Geiger counter [20].

## 3. RESULT AND DISCUSSION

Figure 1 represents the FT-IR spectra of the rubber composite of (SiR<sub>80</sub>/PU<sub>20</sub>/micro-pb<sub>300</sub>/nano-pb<sub>0.8</sub>), with hexane in the rang (600-4000) cm<sup>-1</sup>, where it was observed that there are no apparent changes in the radiation spectrum. Infrared for the rubber composite [21].

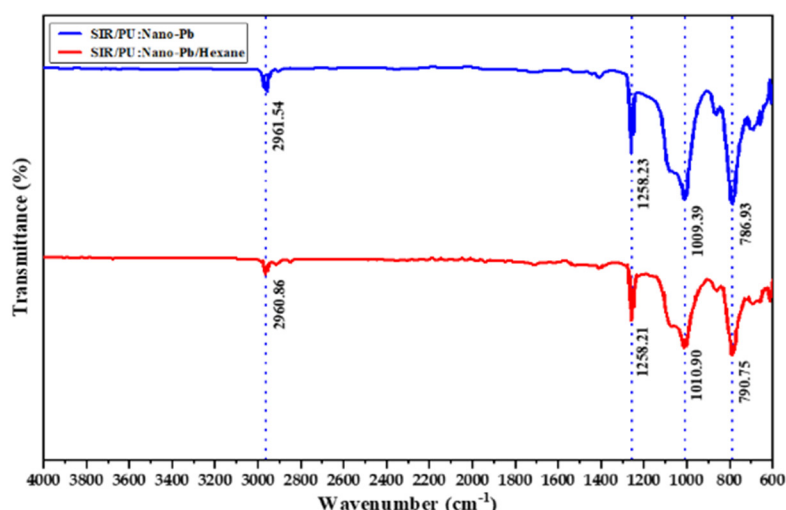


**Figure 1.** Plot of rubber composite (SiR<sub>80</sub>/PU<sub>20</sub>/micro-Pb<sub>300</sub>/nano-Pb<sub>0.8</sub>) of the sample without hexane and within hexane

Even when the loading ratios changed, the presence of hexane closed the gaps in the rubber composite, and the lead distribution was equally distributed. The FTIR spectra displayed the unique bonds of vibrations. The FTIR spectra displayed the distinctive bonds of vibrations. These spectra of silicone rubber's distinctive peaks stretch from the functional groups generated in the composites when the crosslinker weight ratio increased. Absorption peaks at 1258.4 cm<sup>-1</sup>, 790.75 cm<sup>-1</sup>, and 1010.90 cm<sup>-1</sup> were attributable to methyl groups and Si-O bonds, respectively. The results

suggested that methyl groups on the side-chain were degraded during the corona process and the polymer main-chain became decomposed [22].

Figure 2. The sample consisting of (SiR<sub>80</sub>/PU<sub>20</sub>/micro-pb<sub>300</sub>/nano-pb<sub>0.8</sub>) was viewed on a scanning electron microscope (SEM) (Hitachi, Japan) before mixing the hexane. Image (B) shows lead heterogeneity and voids in the composite sample, while image (A) shows nanoparticles evenly distributed and no voids after mixing hexane. The two images are the same and have the same components and amounts [23-25]. Figure 3 shows the distribution function in numbers (B, B1), the diameter and area of the nanolead volume without hexane, and (A, A1), the diameter and volume area of the nano lead with hexane. This shows that the nano lead is evenly distributed over the sample. The polymeric chains crosslinked in image (A, A1) [26-27].

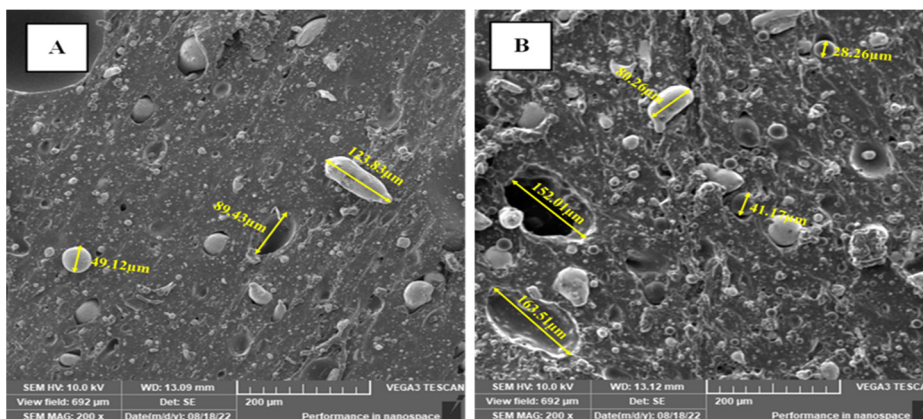


Figure 2. SEM image of: (A) when hexane is added, and (B) the sample without hexane

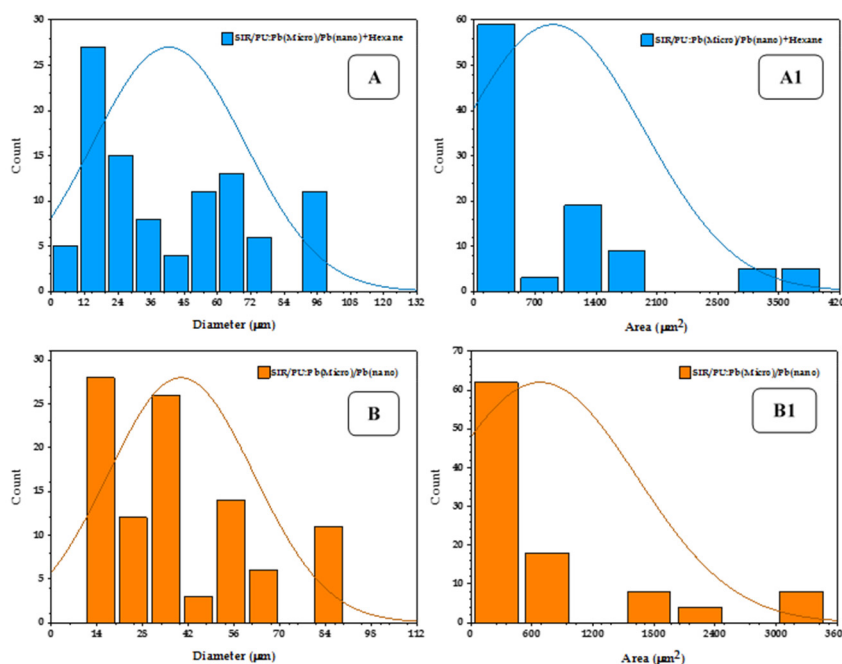


Figure 3. Plot of particles distributive function for (A, A1) represents the diameter and volume area of Nano-lead when hexane is added. (B, B1) represent the diameter and volume area of Nano-lead without adding hexane.

Table 1 represents the components of all batches of the composite (SiR<sub>80</sub>/PU<sub>20</sub>/micro-pb<sub>300</sub>) with different weight ratios of Nano-Pb (0, 0.2, 0.4, 0.6, 0.8 pphr). Table 2 represents the results of examining the mechanical properties of hardness, tensile strength, elongation, and modulus of elasticity.

Table 1. Represented by fixed weight ratios of (SiR/PU/micro-Pb) with different weight ratios of (nano-Pb)

| Sample No | SiR <sub>80</sub> (pphr) + PU <sub>20</sub> (pphr) | (micro-pb) (pphr) | (Nano-pb) (pphr) |
|-----------|--|-------------------|------------------|
| Sam 1     | 100  | 300               | 0                |
| Sam 2     | 100  | 300               | 0.2              |
| Sam 3     | 100  | 300               | 0.4              |
| Sam 4     | 100  | 300               | 0.6              |
| Sam 5     | 100  | 300               | 0.8              |

**Table 2.** Represents the results of the mechanical characteristics examination represented by hardness, tensile, elongation and modulus of elasticity.

| Sample No | Hardness (Shore A) | Tensile Strength (Mpa) | Elongation at % | Elastic Modulus (Mpa) |
|-----------|--------------------|------------------------|-----------------|-----------------------|
| Sam 1     | 29.7               | 0.544                  | 127.5           | $4.2 \times 10^{-3}$  |
| Sam 2     | 30.1               | 0.564                  | 125.5           | $4.4 \times 10^{-3}$  |
| Sam 3     | 32.5               | 0.577                  | 120.5           | $4.7 \times 10^{-3}$  |
| Sam 4     | 34.0               | 0.597                  | 117.5           | $5.0 \times 10^{-3}$  |
| Sam 5     | 34.7               | 0.614                  | 113.5           | $5.4 \times 10^{-3}$  |

Figure 4. It is clear that the measured hardness values for the surface of the rubber doughs increased gradually and irregularly with the increase in the amount of the additive (Nano-Pb). The reason for this is due to the interference that occurs between the supporting material and the base material, which increases the value of the hardness. The reason for this is due to the occurrence of some cross-linking between the rubber chains and the additive inside the prepared dough that is responsible for resisting the external forces applied to it, which increases the hardness of the surface of the prepared material and this agrees with previous research [28].

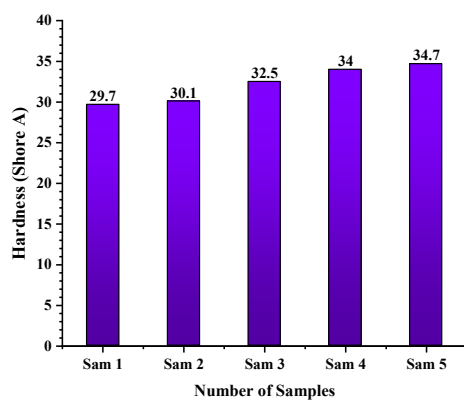


**Figure 4.** Plot of change the hardness for different blends samples

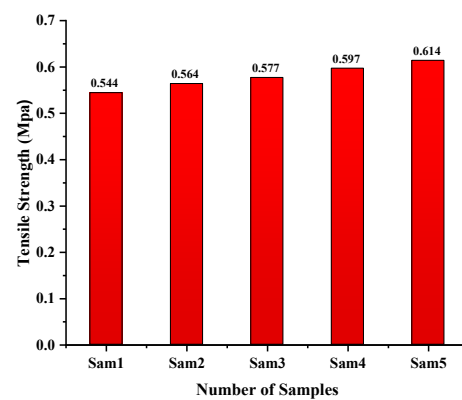


**Figure 5.** Plot of change the tensile strength for different blends samples

Figures 5, 6 and 7 show the effect of Nano-lead powder additive with loading ratios (0,0.2,0.4,0.6,0.8 pphr) on some mechanical characteristics such as tensile, modulus of elasticity and elongation of the rubber composite consisting of silicone rubber (80). and polyurethane (20) for rubber batches, and as a result of the comparison between the effects of mechanical tests (tensile resistance, modulus of elasticity and elongation) as well as the radiation characteristics of the batches models [29].

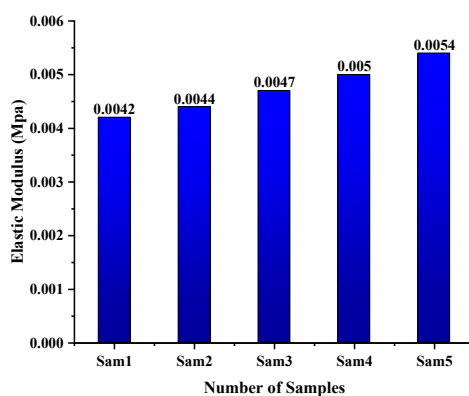


**Figure 6.** Plot of change the elastic modulus for different blends samples.

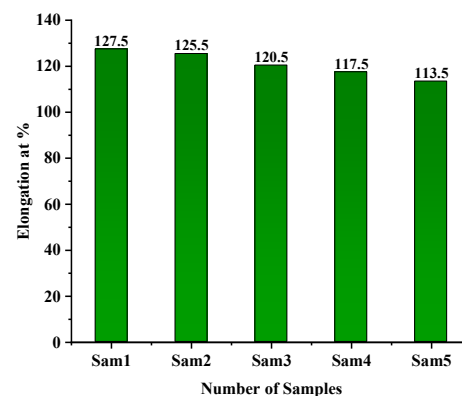


**Figure 7.** Represents change the elongation for different blends samples

The sample (5) with components (SiR<sub>80</sub>/PU<sub>20</sub>/micro-pb<sub>300</sub>) with (nano-pb<sub>0.8</sub>) pphr was more appropriate. It achieved the mechanical characteristics as we notice from the figures a slight increase in the tensile strength, modulus of elasticity and a decrease in the amount of elongation with the increase in the loading ratio of the Nano-lead powder [30]. This is due to the rise in the physical bonding and the cohesion of the filler with rubber. The Nano lead powder (Pb-nano) has a small granular size that increases the surface area for diffusion and, thus, the formation of a larger amount of crosslinking with the rubber chains, and this is consistent with previous research [31]. It is also noted from the numbers that the decrease in the elongation diagram is explained based on the material's arrival to the point of application, where the

material continues to resist until its resistance collapses as a result of the lack of space between the rubbers. The chains, as they are in a certain percentage, do not bear the added material, which leads to cracks and toxins in the sample. Flexibility, and this is consistent with previous research [32]. As for the increase in the modulus of elasticity, it can indicate a strong drop in elongation, and as a result of its inverse proportion to the modulus of elasticity property [33]. Due to the obvious increase in the modulus of elasticity and tensile strength, the loading percentage of the nano-additive material is increased.

Figure 8 shows the graphical relationship between thickness and penetrating radiation (N) when using a Cs<sup>137</sup> radiation source and different loading ratios of (Pb-nano). Where a decrease in the value of the thickness of the half X<sub>1/2</sub> and an increase in both linear and mass absorption coefficients were observed with increasing loading ratios. This is due to the efficiency of the prepared composite in absorbing and attenuating the rays used, and this efficiency increases with increasing the loading percentage of lead nano powder [34] (see Table 3.). From equations (1,2) we obtain the linear absorption coefficient (μ) and the mass (μ<sub>m</sub>).

$$\mu = \frac{\ln 2}{X_{1/2}} \tag{1}$$

$$\mu_m = \frac{\mu}{\rho} \tag{2}$$

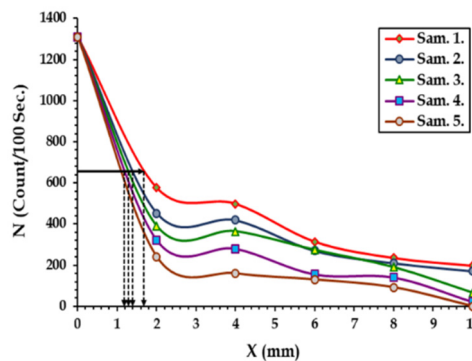


**Figure 8.** Graphical relationship between thickness and the number of penetrating radiation (N) when using a source (Cs<sup>137</sup>) for different loading ratios of (Pb-nano).

**Table 3.** Linear and mass absorption coefficient and half thickness of cesium source Cs<sup>137</sup> for different loading ratios of Pb-nano powder for rubber samples.

| Batch No | Nano-Pb | X <sub>1/2</sub> (mm) | μ (cm <sup>-1</sup> ) | μ <sub>m</sub> (cm <sup>2</sup> /gm) |
|----------|---------|-----------------------|-----------------------|--------------------------------------|
| A        | 0       | 1.678                 | 4.131                 | 1.487                                |
| B        | 0.2     | 1.390                 | 4.987                 | 1.622                                |
| C        | 0.4     | 1.288                 | 5.381                 | 1.723                                |
| D        | 0.6     | 1.178                 | 5.887                 | 1.877                                |
| E        | 0.8     | 1.186                 | 5.842                 | 1.861                                |

Figure 9 represents the results obtained for the Co<sup>60</sup> cobalt source. The second source of electromagnetic radiation, the Co<sup>60</sup> source, was used to examine the superimposed rubber models. We observed a decrease in the thickness of the half when the percentage of additive loading was increased. Basically about the number of particles in the radiation path [35], see Table 4.

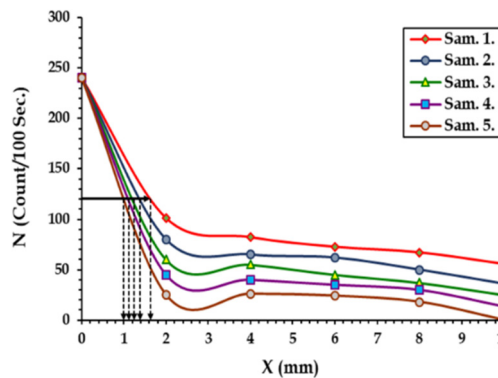


**Figure 9.** Graphical relationship between thickness and the number of penetrating radiation (N) when using a source (Co<sup>60</sup>) for different loading ratios of (Nano-Pb)

**Table 4.** Linear and mass absorption coefficient and half thickness of cobalt source Co<sup>60</sup> for different loading ratios of nano-Pb powder for rubber samples.

| Batch No | Nano-Pb | X <sub>1/2</sub> (mm) | μ (cm <sup>-1</sup> ) | μ <sub>m</sub> (cm <sup>2</sup> /gm) |
|----------|---------|-----------------------|-----------------------|--------------------------------------|
| A        | 0       | 1.624                 | 4.269                 | 1.537                                |
| B        | 0.2     | 1.389                 | 4.991                 | 1.623                                |
| C        | 0.4     | 1.234                 | 5.616                 | 1.799                                |
| D        | 0.6     | 1.108                 | 6.253                 | 1.994                                |
| E        | 0.8     | 0.985                 | 7.040                 | 2.243                                |

#### 4. CONCLUSIONS

The purpose of this research is to better understand the characteristics of (SiR<sub>80</sub>/PU<sub>20</sub>/micro-pb<sub>300</sub>/nano-pb<sub>0.8</sub>) nanostructures for use as radiation shielding in the medical and industrial fields. These findings from our study allow us to conclude:

1- When nano lead powder was added to the batch for the prepared composite of (SiR<sub>80</sub>/PU<sub>20</sub>/micro-Pb<sub>300</sub>) with a ratio of (0.8pphr) on the mechanical properties, it led to an increase in tensile strength, hardness modulus and modulus of elasticity with a decrease in elongation.

2- The prepared rubber batch samples were examined with the FTIR device, and it was noted that there was no change in the rubber composites and We gradually obtained a physical correlation in all the composites.

3- Also, the rubber batch samples examined by the (SEM) device were examined, as the lead was distributed evenly, and there were no voids on the samples prepared in the presence of hexane.

4- The lowest thickness and the largest linear and mass absorption coefficients were obtained at the loading ratio of 300 pphr and 0.8 pphr when using the Co<sup>60</sup> source.

5- The samples were tested for attenuation of radiation from the sources Cs<sup>137</sup> and Co<sup>60</sup> whose decay energy is 1.17563 MeV and 2.82307 MeV, respectively. The results indicated that the linear absorption coefficient (μ) and mass absorption coefficient (μ<sub>m</sub>) are continually growing, while the half-thickness (X<sub>1/2</sub>) is decreasing with ray attenuation.

6- The sample was selected (SiR<sub>80</sub>/PU<sub>20</sub>/micro-Pb<sub>300</sub>/nano-Pb<sub>0.8</sub>) it can be used in armor applications as an armor suit to protect workers in the medical and industrial fields.

#### Acknowledgements

We thank university of Babylon for their great support to complete this work.

#### ORCID

©Mousa Hawan Naeem, <https://orcid.org/0000-0002-3508-3606>; ©Sameer Hassan Hadi Al-Nesrawy, <https://orcid.org/0009-0001-2888-7980>; ©Mohammed H. Al-Maamori, <https://orcid.org/0009-0004-7543-9883>

#### REFERENCE

- [1] J. Cai, L. Qiu, S. Yuan, *et al.*, "Structural health monitoring for composite materials," in: Composites and Their Applications, edited by N. Hu, Intech, (2012). <https://doi.org/10.5772/3353>
- [2] T. Singh, and S. Sehgal, "Structural health monitoring of composite materials," Arch. Comput. Methods Eng. **29**, 1997-2017 (2022). <https://doi.org/10.1007/s11831-021-09666-8>
- [3] S.S. Pendhari, T. Kant, and Y.M. Desai, "Application of polymer composites in civil construction: A general review," Compos. Struct. **84**, 114-124 (2008). <https://doi.org/10.1016/j.compstruct.2007.06.007>
- [4] R. Hsissou, R. Seghiri, Z. Benzekri, M. Hilali, M. Rafik, and A. Elharfi, "Polymer composite materials: A comprehensive review," Compos. Struct. **262**, 113640 (2021). <https://doi.org/10.1016/j.compstruct.2021.113640>
- [5] S.O. Prakash, P. Sahu, M. Madhan, A.J. Santhosh, "A review on natural fibre-reinforced biopolymer composites: properties and applications," Int. J. Polym. Sci. **2022**, 7820731 (2022). <https://doi.org/10.1155/2022/7820731>
- [6] N.I.N. Haris, M.Z. Hassan, R.A. Ilyas, M.A. Suhot, S.M. Sapuan, R. Dolah, R. Mohammad, *et al.*, "Dynamic mechanical properties of natural fiber reinforced hybrid polymer composites: A review," J. Mater. Res. Technol. **19**, 167-182 (2022). <https://doi.org/10.1016/j.jmrt.2022.04.155>
- [7] R. Han, Y. Li, Q. Zhu, and K. Niu, "Research on the preparation and thermal stability of silicone rubber composites: A review," Compos. Part. C, **100249** (2022). <https://doi.org/10.1016/j.jcom.2022.100249>
- [8] G.T. Howard, "Biodegradation of polyurethane: a review," Int.. Biodeterior. Biodegradation, **49**, 245-252 (2002). [https://doi.org/10.1016/S0964-8305\(02\)00051-3](https://doi.org/10.1016/S0964-8305(02)00051-3)
- [9] U. Braun, E. Lorenz, C. Weimann, H. Sturm, I. Karimov, J. Ettl, R. Meier, *et al.*, "Mechanic and surface properties of central-venous port catheters after removal: A comparison of polyurethane and silicon rubber materials," J. Mech. Behav. Biomed. Mater. **64**, 281-291 (2016). <https://doi.org/10.1016/j.jmbbm.2016.08.002>
- [10] O. Kilicoglu, C.V. More, F. Akman, K. Dilsiz, H. Oğul, M.R. Kaçal, H. Polat, *et al.*, "Micro Pb filled polymer composites: Theoretical, experimental and simulation results for γ-ray shielding performance," Radiat. Phys. Chem. **194**, 110039 (2022). <https://doi.org/10.1016/j.radphyschem.2022.110039>
- [11] M.Ö. Kiliçoğlu, "Micro Pb filled polymer composites: Theoretical, experimental and simulation results for gamma-ray shielding performance," (2022). <https://openaccess.marmara.edu.tr/bitstreams/4c3b39bc-86a4-4e63-b3d5-59ed74fabd3b/download>
- [12] M.A. Hosseini, S. Malekie, F. Kazemi, "Experimental evaluation of gamma radiation shielding characteristics of polyvinyl alcohol/tungsten oxide composite: A comparison study of micro and nano sizes of the fillers," Nucl. Instruments. Methods Phys. Res. Sect. A, Accel. Spectrometers, Detect. Assoc. Equip. **1026**, 166214 (2022). <https://doi.org/10.1016/j.nima.2021.166214>
- [13] El-Khatib A.M., Abbas M.I., Hammoury S.I., *et al.*, "Effect of PbO-nanoparticles on dimethyl polysiloxane for use in radiation shielding applications," Sci. Rep. **12**, 15722 (2022). <https://doi.org/10.1038/s41598-022-20103-z>
- [14] J. Wu, J. Hu, K. Wang, Y. Zhai, Z. Wang, Y. Feng, H. Fan, *et al.*, "Flexible stretchable low-energy X-ray (30–80 keV) radiation shielding material: Laser-melting-point GaIn1Sn7Bi1 alloy/thermoplastic polyurethane composite," Appl. Radiat. Isot. **192**, 10603 (2023). <https://doi.org/10.1016/j.apradiso.2022.110603>

- [15] Román A.J., Qin S., Rodríguez J.C., L.D. González, V.M. Zavala, and T.A. Osswald, "Natural rubber blend optimization via data-driven modeling: The implementation for reverse engineering," *Polymers*, (Basel), **14**, 2262 (2022). <https://doi.org/10.3390/polym14112262>
- [16] A. Umanskii, K. Gogolinskii, V. Syasko, and A. Golev, "Modification of the Leeb Impact Device for Measuring Hardness by the Dynamic Instrumented Indentation Method," *Inventions*, **7**, 29 (2022). <https://doi.org/10.3390/inventions7010029>
- [17] Y. Wang, C. Feng, M. Zhao, C. Shan, F. Liu, Q. Lei, Z. Zhou, *et al.*, "Development of a high energy resolution and wide dose rate range portable gamma-ray spectrometer," *Appl. Radiat. Isot.* **192**, 110572 (2023). <https://doi.org/10.1016/j.apradiso.2022.110572>
- [18] Lilo T., Morais C.L.M., Shenton C., *et al.*, "Revising Fourier-transform infrared (FT-IR) and Raman spectroscopy towards brain cancer detection," *Photodiagnosis. Photodyn. Ther.* **102785** (2022). <https://doi.org/10.1016/j.pdpdt.2022.102785>
- [19] T. Marquardt, and A.W. Momber, "The assessment of fractal dimensions with the direct use of scanning electron microscopy (SEM) images from blast-cleaned steel substrates," *J. Adhes. Sci. Technol.* **37**, 16–37 (2023). <https://doi.org/10.1080/01694243.2021.2013057>
- [20] Libeesh N.K., Naseer K.A., Arivazhagan S., *et al.*, "Multispectral remote sensing for determination the Ultra-mafic complexes distribution and their applications in reducing the equivalent dose from the radioactive wastes," *Eur. Phys. J. Plus.* **137**, 267 (2022). <https://doi.org/10.1140/epjp/s13360-022-02473-5>
- [21] M.H. Naeem, and S.H.H. Al-Nesrawy, "Preparation of (Rubber Blend/Oyster Shell Powder) Composites and Study Rheological Properties," *J. Engineer. Appl. Sciences*, **14**(7), 10092-10097 (2019). <https://dx.doi.org/10.36478/jeasci.2019.10092.10097>
- [22] Y. Yang, Z. Wang, X. Peng, Z. Huang, and P. Fang, "Influence of Crosslinking Extent on Free Volumes of Silicone Rubber and Water Diffusion after Corona Discharge," *Materials* (Basel), **15**, 6833 (2022). <https://doi.org/10.3390/ma15196833>
- [23] S.H.K. Bahrain, N.R.N. Masdek, J. Mahmud, M.N. Mohammed, S.M. Sapuan, R.A. Ilyas, A. Mohamed, *et al.*, "Morphological, physical, and mechanical properties of Sugar-Palm (Arenga pinnata (Wurmb) Merr.)-Reinforced silicone rubber biocomposites," *Materials* (Basel), **15**, 4062 (2022). <https://doi.org/10.3390/ma15124062>
- [24] M.H. Meteab, A. Hashim, and B.H. Rabee, "Controlling the Structural and Dielectric Characteristics of PS-PC/Co2O3-SiC Hybrid Nanocomposites for Nanoelectronics Applications," *Silicon*, **15**, 251-261 (2023). <https://doi.org/10.1007/s12633-022-02020-y>
- [25] M.H. Meteab, A. Hashim, B.H. Rabee, "Synthesis and Characteristics of SiC/MnO2/PS/PC Quaternary Nanostructures for Advanced Nanodielectrics Fields," *Silicon*, **15**, 1609-1620 (2023). <https://doi.org/10.1007/s12633-022-02114-7>
- [26] T.L. Christiansen, S.R. Cooper, and K.M.Ø. Jensen, "There's no place like real-space: elucidating size-dependent atomic structure of nanomaterials using pair distribution function analysis," *Nanoscale Adv.* **2**, 2234-2254 (2020). <https://doi.org/10.1039/D0NA00120A>
- [27] H.S. Suhail, and A.R. Abdulridha, "Investigation of the Morphological, Optical, and D.C Electrical Characteristics of Synthesized (Bi<sub>2</sub>O<sub>3</sub>/ZnO) Nanocomposites, as Well as Their Potential Use in Hydrogen Sulfide Gas Sensor," *Trans. Electr. Electron. Mater.* **24**, 205–216 (2023) (2023). <https://doi.org/10.1007/s42341-023-00436-w>
- [28] C. Yang, C. Ren, Y. Jia, G. Wang, M. Li, and W. Lu, "A machine learning-based alloy design system to facilitate the rational design of high entropy alloys with enhanced hardness," *Acta Mater.* **222**, 117431 (2022). <https://doi.org/10.1016/j.actamat.2021.117431>
- [29] S.H. Al-Nesrawy, M. Al-Maamori, and H.R. Jappor, "Effect of mixed of industrial scraps and lamp black percent on the mechanical properties of NR70/SBR30 composite," *Int. J. Pharm. Tech. Res.* **9**, 207-217 (2016).
- [30] A.A. Abid, S.H. Al-Nesrawy, and A.R. Abdulridha, "New fabrication (PVA-PVP-C. B) nanocomposites: structural and electrical properties," *Journal of Physics: Conference Series*, IOP Publishing, **1804**, 012037 (2021). <https://doi.org/10.1088/1742-6596/1804/1/012037>
- [31] Y. Zeng, L. Tang, and Z. Xin, "Improved dielectric and mechanical properties of Ti<sub>3</sub>C<sub>2</sub>T<sub>x</sub> MXene/silicone rubber composites achieved by adding a few boron nitride nanoplates," *Ceram. Int.* **49**(6), 9026-9034 (2023).. <https://doi.org/10.1016/j.ceramint.2022.11.058>
- [32] A. Gupta, K.K. Saxena, A. Bharti, J. Lade, K. Chadha, and P.R. Paresi, "Influence of ECAP processing temperature and number of passes on hardness and microstructure of Al-6063," *Adv. Mater. Process Technol.* **8**, 1635-1646 (2022). <https://doi.org/10.1080/2374068X.2021.1953917>
- [33] A.M. Ajam, S.H. Al-Nesrawy, and M. Al-Maamori, "Effect of reclaim rubber loading on the mechanical properties of SBR composites," *Int. J. Chem. Sci.* **14**, 2439-2449 (2016). <https://www.tsijournals.com/articles/effect-of-reclaim-rubber-loading-on-the-mechanical-properties-of-sbr-composites.pdf>
- [34] E. Timakova, Ms.S. Thesis, "Characterization of Dosimeters for Small Field Applications Including Comparisons to Monte Carlo and Treatment Planning System Computed Doses," McMaster University, (2022). <http://hdl.handle.net/1828/14616>
- [35] H. Al-Ghamdi, M.I. Sayyed, and M. Elsaifi, A. Kumar, N. Al-Harbi, A.H. Almuqrin, S. Yasmin, *et al.*, "An experimental study measuring the photon attenuation features of the P<sub>2</sub>O<sub>5</sub>-CaO-K<sub>2</sub>O-Na<sub>2</sub>O-PbO glass system," *Radiat. Phys. Chem.* **200**, 110153 (2022). <https://doi.org/10.1016/j.radphyschem.2022.110153>

**ВПЛИВ НАНОЧАСТИНОК СВИНЦЮ НА СТРУКТУРНІ, МОРФОЛОГІЧНІ ТА МЕХАНІЧНІ  
ХАРАКТЕРИСТИКИ (SiR-PU/Micro-Pb) КОМПЗИТІВ ТА ЗАСТОСУВАННЯ  
ДЛЯ ЗАХИСТУ ВІД ВИПРОМІНЮВАННЯ**

**Муса Хаван Наем<sup>а</sup>, Самір Хасан Хаді Аль-Несраві<sup>а</sup>, Мохаммед Х. Аль Мааморі<sup>б</sup>**

<sup>а</sup>Кафедра фізики, Освітній коледж чистих наук, Вавилонський університет, Аль-Хілла, 51001, Ірак

<sup>б</sup>Кафедра біомедицинської інженерії, Інженерний коледж, Університет Аль-Мустакбал, Вавилон, Аль-Хілла, 51001, Ірак

Це дослідження включає виготовлення полімерного нанокompозиту, що складається із силіконового каучуку/поліуретану як основи, з додаванням першого наповнювача з мікросвинцю із співвідношенням 300 phr та другого наповнювача з наносвинцю з різними співвідношеннями (0, 0,2, 0,4, 0,6, 0,8 phr). З додаванням гексану (рідкий стан) до суперпозиції методом лиття при кімнатній температурі. Структурні властивості поверхонь зразків вимірювали за допомогою спектроскопії з перетворенням Фур'є (FT-IR) та скануючого електронного мікроскопа (SEM). Також вивчалися механічні властивості, а саме твердість, розтягування, відносно подовження та модуль пружності. (FT-IR) показав відсутність хімічної реакції для всіх зразків. У той час як SEM вимірювання показали рівномірний розподіл мікро- та нано-свинцю в присутності гексану, і відсутність пор в підготовленій гумі. Стосовно механічних властивостей спостерігалось, що твердість, межа міцності та модуль пружності покращувалися зі збільшення кількості наночастинок свинцю і зменшення подовження в результаті обернено пропорційно модулю пружності. З отриманих результатів видно що ця сполука може бути використана для ослаблення гамма-випромінювання, особливо в медицині та промисловості.

**Ключові слова:** механічні характеристики; силіконова гума; поліуретан; свинець; гексан; SiR-PU/мікро-Pb:нано-Pb нанокompозити

## ENHANCEMENTS OF STRUCTURAL AND OPTICAL PROPERTIES OF MgO: SnO<sub>2</sub> NANOSTRUCTURE FILMS<sup>†</sup>

 R.H. Ayoub<sup>a</sup>,  Muhammad H. Al-Timimi<sup>a\*</sup>,  M.Z. Abdullah<sup>b</sup>

<sup>a</sup>Department of Physics, College of Science, University of Diyala, Iraq

<sup>b</sup>Materials Research Directorate, Ministry of Science and Technology, Iraq

\*Corresponding Author e-mail: [muhammادتimimi@yahoo.com](mailto:muhammادتimimi@yahoo.com)

Received July 10, 2023; revised August 3, 2023; accepted August 5, 2023

This study uses the chemical precipitation method to investigate the structural and optical properties of MgO:SnO<sub>2</sub> nanoparticles. The thin films were deposited by the spin coating technique on glass substrates. X-ray diffraction analysis proved the crystalline structure of prepared thin films, with the peaks corresponding to the (110), (101), (200), (211), and (220) planes, with the tetragonal SnO<sub>2</sub> crystal structure. Fourier transforms infrared (FTIR), and scanning electron microscope (SEM) are used to characterize the functional groups, shape, and dimensions of synthesized metal oxide nanoparticles. The optical properties of the films were studied by UV-Vis spectroscopy. The bandgap energy was estimated to be in the range of (3.9-3.4 eV). The refractive index and extinction coefficient of the films were also determined, and the results indicated that the films had good transparency in the visible region. The study concludes that MgO:SnO<sub>2</sub> thin films obtained by the spin coating technique have potential applications in optoelectronics and gas sensors.

**Keywords:** MgO:SnO<sub>2</sub> films; Spin coating technique; Precipitation method; Structure; Optical properties

**PACS:** 73.20.At, 78.20.-e, 77.55.+f

### INTRODUCTION

MgO:SnO<sub>2</sub> nanoparticles are composite particles consisting of magnesium oxide (MgO) and tin dioxide (SnO<sub>2</sub>) in the form of nanoparticles. These nanoparticles can be synthesized using various methods, including sol-gel [1,2], co-precipitation [3], and hydrothermal methods [4]. MgO:SnO<sub>2</sub> nanoparticles have attracted significant attention due to their unique properties, such as high surface area, high reactivity, and good stability [5]. These properties make them suitable for various applications, including gas sensing, catalysis, energy storage, and biomedical applications. One of the main applications of MgO:SnO<sub>2</sub> nanoparticles is in gas sensing [6]. These nanoparticles have been shown to exhibit excellent sensitivity and selectivity towards various gases, such as CO, NO<sub>2</sub>, and H<sub>2</sub> [7]. The high surface area of the nanoparticles provides a large surface area for gas adsorption, while the SnO<sub>2</sub> component provides a high catalytic activity for gas oxidation. In addition, MgO:SnO<sub>2</sub> nanoparticles have been investigated for their catalytic activity in various reactions, such as CO oxidation, methanol synthesis, and photocatalysis [8]. The unique properties of the nanoparticles, such as their size and composition, can be tuned to optimize their catalytic activity [9]. MgO:SnO<sub>2</sub> nanoparticles also show promise in energy storage applications, such as in lithium-ion batteries [10,11]. The nanoparticles can be used as anode materials due to their high lithium-ion storage capacity and good cycling stability. Furthermore, MgO:SnO<sub>2</sub> nanoparticles have potential biomedical applications, such as in drug delivery and cancer therapy [12]. The nanoparticles can be functionalized with various ligands and drugs to target specific cells or tissues, and their high stability and biocompatibility make them suitable for in vivo applications. Overall, MgO:SnO<sub>2</sub> nanoparticles have a wide range of potential applications due to their unique properties and can be synthesized using various methods [13,14].

Spin coating is a popular method for depositing thin films, especially for research and development purposes, due to its ease of use, low cost, and compatibility with various materials. In this method, a liquid solution containing the desired precursor materials is first applied onto a spinning substrate, such as a glass or silicon wafer [15,16]. The centrifugal force generated by the spinning causes the solution to spread uniformly across the substrate and evaporate, leaving behind a thin film on the surface [17]. MgO:SnO<sub>2</sub> thin films obtained by spin coating have potential applications in various fields, including optoelectronics [18], and gas sensors [19]. The properties of the thin films, such as their thickness, composition, and morphology, can be tuned by adjusting the concentration and ratio of the precursor materials in the solution and the spin-coating parameters, such as spin speed, spin time, and temperature [20].

The study aimed to characterize MgO:SnO<sub>2</sub> by Co-Precipitation method and prepares thin films by spin coating and study the structural properties of the nanoparticles using XRD analysis, determine the surface morphology using SEM, investigate the optical properties of the thin films using UV-Vis spectroscopy, and study the properties of MgO:SnO<sub>2</sub> thin films obtained by spin coating.

### EXPERIMENTAL PART

1. **Materials.** Magnesium chloride MgCl<sub>2</sub>·6H<sub>2</sub>O, Tin chloride SnCl<sub>2</sub>·2H<sub>2</sub>O, Ammonium hydroxide solution, Deionized water

<sup>†</sup> Cite as: R.H. Ayoub, M.H. Al-Timimi, M.Z. Abdullah, East Eur. J. Phys. 3, 546 (2023), <https://doi.org/10.26565/2312-4334-2023-3-64>

© R.H. Ayoub, M.H. Al-Timimi, M.Z. Abdullah, 2023

2. **Equipment.** Magnetic stirrer (China-Wincom Co. Ltd.), Glass beaker, Centrifuge (China-Wincom Co. Ltd.), Drying oven (Germany -Mettler UE 500 Lab Oven), Spin coating device (Britain-Ossila co.).

3. **Procedure.** Weigh out the desired amounts of Magnesium chloride and tin (IV) chloride and dissolve them in deionized water separately, Slowly add the Magnesium chloride solution to the tin chloride solution while stirring continuously with a magnetic stirrer with percentages MgO<sub>1-x</sub>: SnO<sub>2</sub> x (x=0.2,0.3,0.4,0.5), adding Ammonium hydroxide solution to the mixture until the pH reaches around 9, The mixture will turn white and a precipitate will form, Continue stirring the mixture for another 2-3 hours to ensure complete precipitation of the nanoparticles, Centrifuge the mixture at a high speed (around 10,000 rpm) for 15-20 minutes to collect the precipitate, Washing the precipitate with deionized water to remove any impurities and residual reactants. Finally Drying the nanoparticles in an oven at a low temperature (around 80°C) for several hours until all the solvent is evaporated and the nanoparticles are fully dried and Calcination at 800°C.

The MgO<sub>1-x</sub>: SnO<sub>2</sub> x (x=0.2,0.3,0.4,0.5), thin films were prepared by the addition (the MgO<sub>1-x</sub>: SnO<sub>2</sub> nanoparticles dissolved in ethylene glycol with a mass ratio (0.1:10) at room temperature), the MgO, SnO<sub>2</sub>, and MgO:SnO<sub>2</sub> concentration was 0.1 g. Glass substrates were successively cleaned with acetone, ethanol, and deionized water. MgO, SnO<sub>2</sub>, and MgO:SnO<sub>2</sub> thin films were deposited on the glass substrates by spin coating at room temperature with a rate of 2000 rpm for 30 s, the spin-coating step, the films were heated on a hot plate at 30-50 °C in the air for 10 min to remove organic contaminations.

## RESULTS AND DISCUSSION

The X-ray diffraction (XRD) test was carried out on prepared samples to determine the crystal structure type and the crystalline size using an x-ray (Shimadzu-6000) diffractometer, with wavelength ( $\lambda=1.54060\text{\AA}$ ) and voltage (40 KV). Fig. 1 shows the obtained XRD patterns of prepared samples. The detected peaks at ( $2\theta = 36.98^\circ, 42.97^\circ, 62.39^\circ, 74.8^\circ$  and  $78.75^\circ$ ) of the crystalline planes (111), (002), (022), (113), and (222) demonstrated the formation of cubic MgO structure, space group (Fm-3m no. 225), with lattice parameters ( $a=b=c = 4.2060\text{\AA}$ ) and ( $\alpha=\beta=\gamma=90^\circ$ ), which well agreed with the standard data (JCPDS 98-016-9450). While the peaks at ( $2\theta = 26.59^\circ, 33.89^\circ, 37.96^\circ, 51.79^\circ, 54.77^\circ, 57.85^\circ, 61.9^\circ, 64.77^\circ, 65.99^\circ, 71.31^\circ$  and  $78.74^\circ$ ) of the planes (110), (011), (020), (121), (220), (002), (130), (112), (031), (002), and (231) attributed to the Cassiterite tetragonal SnO<sub>2</sub> structure, space group (P42/mnm no.136), with lattice parameters ( $a = b = 4.7360\text{\AA}$  and  $c = 3.1850\text{\AA}$ ) and ( $\alpha=\beta=\gamma=90^\circ$ ) corresponded to the standard data (JCPDS 98-003-9173). As shown in Fig. 1(a,b).

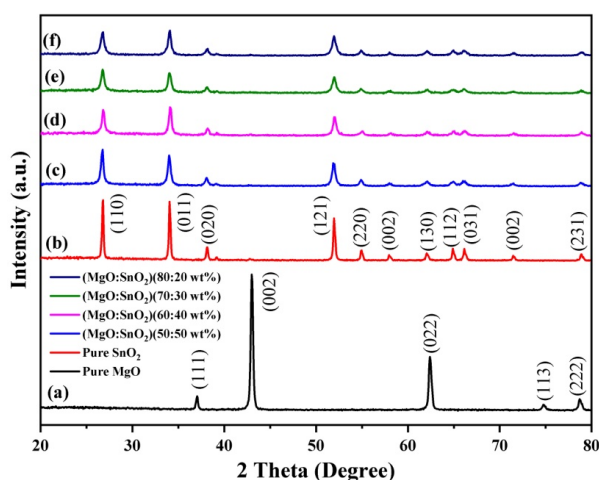


Figure 1. XRD patterns of synthesized samples

The XRD results revealed the highly pure crystalline structure of the synthesized MgO, SnO<sub>2</sub>, and MgO:SnO<sub>2</sub> nanoparticles, where there are no impurities peaks appearing in the obtained XRD patterns. After doping with MgO, observed that the crystal structure of SnO<sub>2</sub> has not changed in all MgO ratios (50, 60, 70 and 80 wt. %), suggesting that the Mg ions were incorporated within the SnO<sub>2</sub> crystalline lattice, cassiterite tetragonal structure of pure MgO:SnO nanoparticles with space group (P42/mnm no.136) obtained. The XRD patterns demonstrated that the peaks intensity of pure SnO<sub>2</sub> decreased after the doping process, while the full-width half maximum value (FWHM) increased, which can be attributed to the SnO<sub>2</sub> crystalline growth decreased by Mg ions doping as shown in Fig. 1(c,d,e,f), this is due to the smaller diameter of Mg ions (0.067 nm) compared to the tin ions (0.071 nm) [21, 22].

The crystalline sizes of the pure MgO, SnO<sub>2</sub> and different ratio (50, 60, 70 and 80 wt. %) of Mg ions doped SnO<sub>2</sub> were calculated depending on the highest XRD peak using Scherrer's equation [23], to be (24.5 nm), (35.42 nm), (19.89 nm), (18.97 nm), (14.55 nm), (14.11 nm) respectively. The results indicated a clear decrease in crystalline size with the doping Mg ions ratio, as a result of the difference in the ion size of Sn and Mg ions [24].

The samples have been investigated using the FTIR test to determine the functional groups within the prepared materials. The FTIR spectra of MgO, SnO<sub>2</sub>, and MgO:SnO<sub>2</sub> powder in the wavenumber range (500-4000 cm<sup>-1</sup>) are shown in Fig. 8. The stretching and bending vibrations of metal-oxygen (MgO and SnO<sub>2</sub>) bonds detected at the range

(1500-900  $\text{cm}^{-1}$ ), spectroscopic evidence points to the presence of Sn-O and Mg-O vibrations bonds at the broad peak centered around (616  $\text{cm}^{-1}$ ) [23].

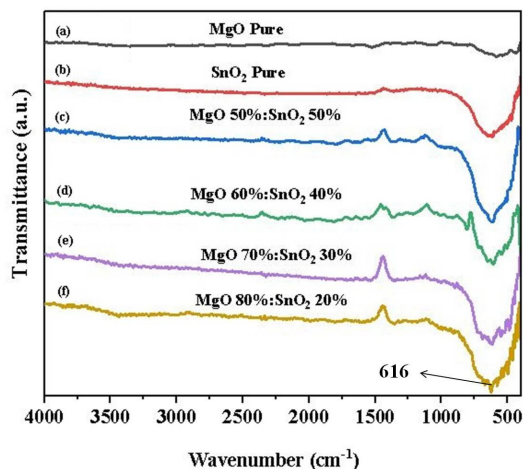


Figure 2. FTIR curve of synthesized samples

Figure 3 presents the results of Scanning Electronic Microscopy images and particle size distributions of prepared samples. The synthesized nanoparticles exhibited a semi-spherical nanoparticle of all samples, as shown in Fig. 3 (a,b,c,d,e,f). The results revealed that the average particle size of pure MgO is about (117.93 nm), while the smaller average particle size (90.07 nm) for pure SnO<sub>2</sub> nanoparticles. As presented in Fig. 3(a, b), the SEM images clearly show that the SnO<sub>2</sub> nanoparticles are approximately identical in size. Fig. 3(c,d,e,f) showed the morphology of MgO nanoparticles doped with different ratios of SnO<sub>2</sub>. The SEM images revealed the agglomeration of doped nanoparticles with semi-spherical shapes, and the MgO:SnO<sub>2</sub> nanoparticles gathered as clusters. Finally, the SEM image demonstrated that the average particle size significantly decreased with the doping with the SnO<sub>2</sub>, to be (48.71 nm), (48.5 nm), (50.05 nm) and (50.3 nm) of the SnO<sub>2</sub> ratio (50, 60, 70 and 80 wt. %) respectively, which can be attributed to the smaller ionic radius of Sn ions compared with Mg ions [24, 25].

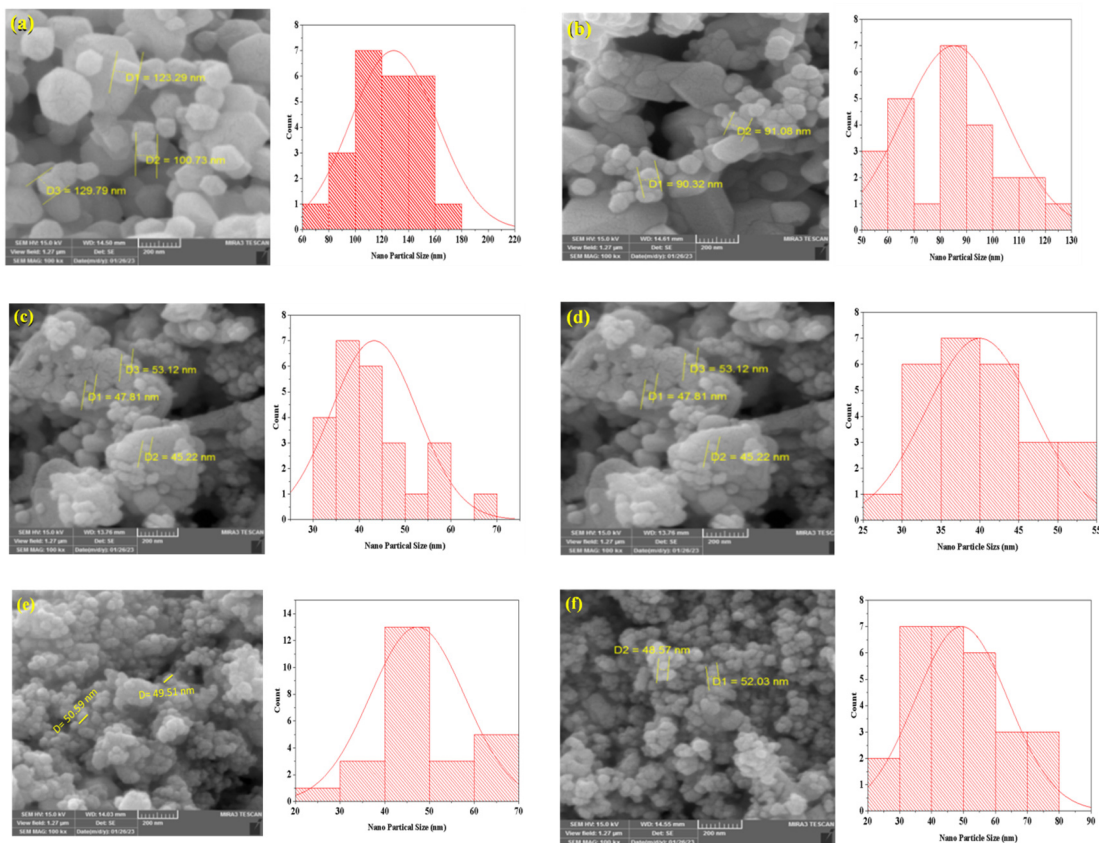


Figure 3. SEM images and particle size distribution of prepared samples (a) pure MgO, (b) pure SnO<sub>2</sub>, (c) MgO<sub>(0.5)</sub>: SnO<sub>2(0.5)</sub>, (d) MgO<sub>(0.6)</sub>: SnO<sub>2(0.4)</sub>, (e) MgO<sub>(0.7)</sub>: SnO<sub>2(0.3)</sub>, (f) MgO<sub>(0.8)</sub>: SnO<sub>2(0.2)</sub>

UV-Vis absorption spectroscopy is a useful technique to investigate the optical properties of prepared films. The films were deposited on glass substrates using the spin coating technique. Optical measurements are conducted in the range of 200-1200 nm to determine the optical parameters. The optical absorption and transmission spectra of the MgO nanoparticles revealed a change in the band gap transition as the concentration of SnO<sub>2</sub> is increased, with a higher percentage of dopant, there is a small shift toward the longer wavelength region. The sharp increase in the spectra at the absorption edge demonstrates highly crystalline nanoparticles with few surface defects within the films [26, 27]. Transmittance and reflectance were calculated separately, the transmittance spectra of the films are plotted as a function of the wavelength of incident light of all MgO:SnO<sub>2</sub> samples. The transmittance spectra is directly related to the concentration of SnO<sub>2</sub>, It is worth noting that the maximum value of reflectance occurs at a wavelength of 350 nm and decreases with the visible wavelength as shown in Fig. 4.

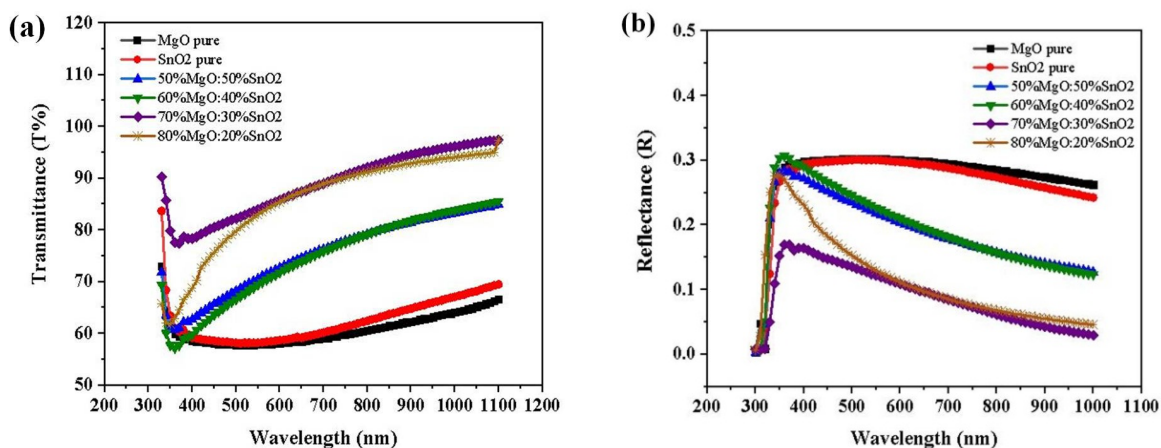


Figure 4. (a) Transmittance and (b) reflectance spectra of prepared MgO:SnO<sub>2</sub> films

The absorption coefficient ( $\alpha$ ) was determined using the following equation, which was derived from the absorbance spectrum [28]:

$$\alpha = 2.303 \frac{A}{t} \tag{1}$$

The absorbance (A) is used in the calculation of the absorption coefficient ( $\alpha$ ), As depicted in Fig. 5, the absorption coefficient ( $\alpha$ ) decreases as the concentration of MgO increases. This is attributed to the increase in the energy gap that occurs with higher concentrations of MgO.

The absorption coefficient ( $\alpha$ ) describes how well a material can absorb light at a particular wavelength. In the case of MgO: SnO<sub>2</sub> film, an increase in the concentration of MgO leads to a widening of the bandgap [29], which is the energy range where electrons are not available to absorb photons [30,31]. This means that fewer photons are absorbed by the film, resulting in a decrease in the absorption coefficient ( $\alpha$ ). Therefore, as the concentration of MgO increases, the film becomes less efficient in absorbing light, causing a decrease in the absorption coefficient, which agreed with the results [32, 33].

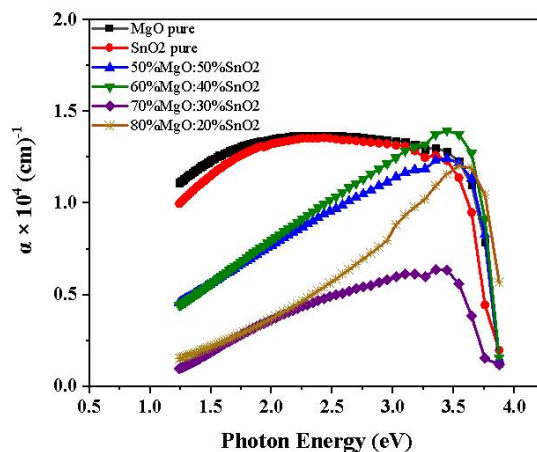
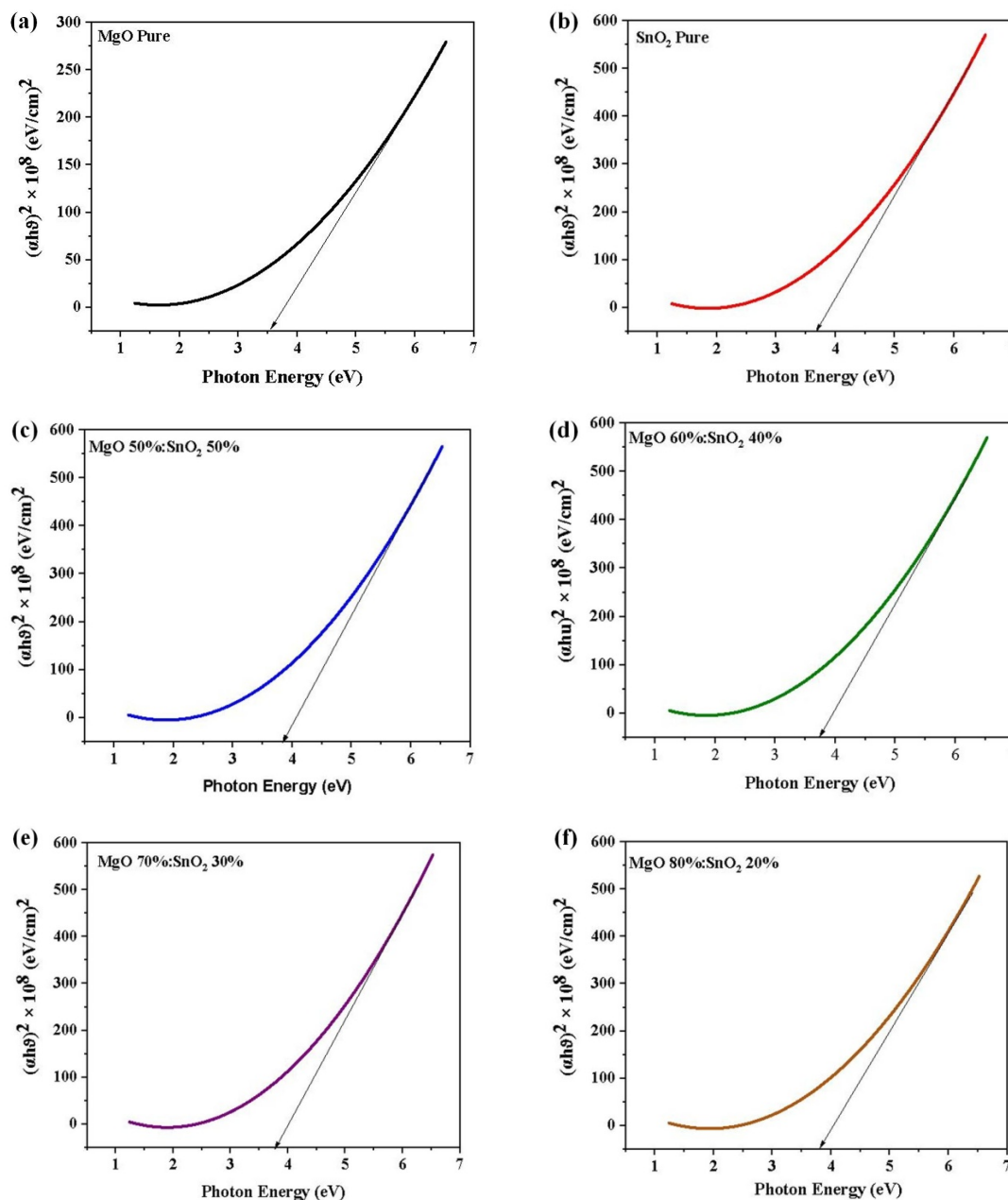


Figure 5. Absorption coefficient ( $\alpha$ ) of prepared MgO:SnO<sub>2</sub> films

Fig. 6 shows the bandgap energy of pure MgO film, pure SnO<sub>2</sub> film, and MgO:SnO<sub>2</sub> films. The bandgap energy of the sample can be determined using the formula [34,35] :

$$\alpha h\nu = C(h\nu - E_g)^{1/2} \tag{2}$$

Assuming a constant value (C) for the absorption coefficient ( $\alpha$ ), the bandgap energies of MgO: SnO<sub>2</sub> nanoparticles were approximately 3.9 eV, while those of tin oxides were around 3.6 eV. The bandgap energy of pure MgO was approximately 3.5 eV. These values were obtained for (MgO) (SnO<sub>2</sub>) (MgO: SnO<sub>2</sub>) films. When these two materials are combined in the form of a composite film, their bandgap energies are affected by several factors, including the concentration of the materials and the degree of crystallinity [36]. The addition of SnO<sub>2</sub> to MgO can cause the bandgap energy to decrease, as observed in the case of the MgO:SnO<sub>2</sub> films. This is due to the change in the electronic structure of the composite film, which arises from the interaction between the two materials [37,38].



**Figure 6.** Energy band gap curves of prepared samples (a) pure MgO, (b) pure SnO<sub>2</sub>, (c) 80%MgO:20%SnO<sub>2</sub>, (d) 80%MgO:20%SnO<sub>2</sub>, (e) 80%MgO:20%SnO<sub>2</sub>, (f) 80%MgO:20%SnO<sub>2</sub>

By using relation (3), the refractive index of both pure MgO, SnO<sub>2</sub> films, and (MgO: SnO<sub>2</sub>) films has been calculated [39].

$$n_o = \frac{1+R}{1-R} + \left( \frac{4R}{(1-R)^2} - k_o \right)^{1/2} \tag{3}$$

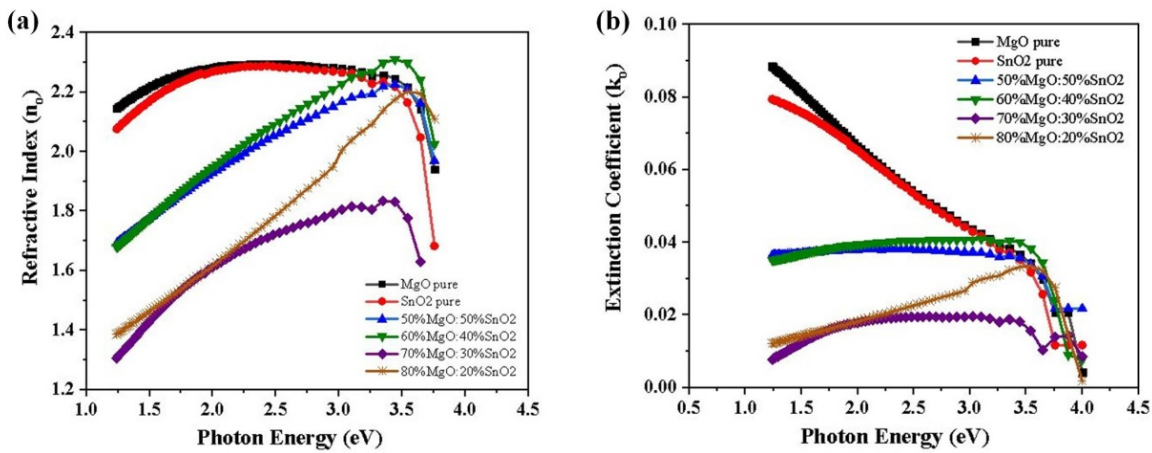


Figure 7. (a) Refractive index and (b) extinction coefficient curves of prepared films

The absorption spectra can be used to calculate the extinction coefficient from the equation (4) [40,41]:

$$k_o = \frac{\alpha\lambda}{4\pi} \tag{4}$$

The fundamental dielectric constant is shown in Figure 8. We can see that the value of 60% MgO:40%SnO<sub>2</sub> is maximum (5) at the photon Energy (3.5eV), while the value of 70% MgO:30% SnO<sub>2</sub> decreases to (3) at the wavelength. (3.5eV). The values of (n<sub>o</sub>) and (k<sub>o</sub>) are connected to the real (ε<sub>r</sub>) and imaginary (ε<sub>i</sub>) components of the dielectric constant, The formulae (5) and (6) were utilized to calculate the values of (ε<sub>r</sub>) and (ε<sub>i</sub>), respectively [42, 43]:

$$\epsilon_r = n_o^2 - k_o^2 \tag{5}$$

$$\epsilon_i = 2n_o.k_o \tag{6}$$

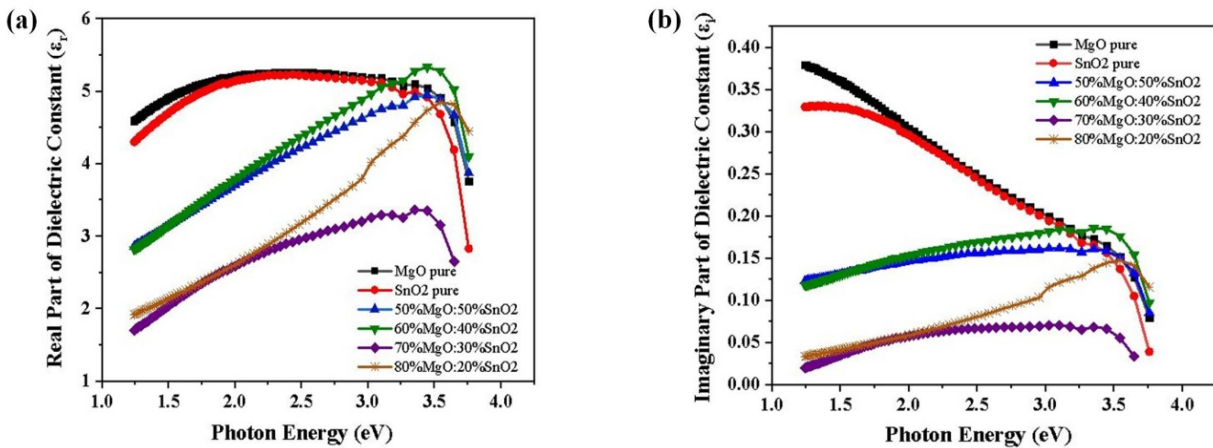


Figure 8. (a) Real part and (b) imaginary part of dielectric constant curves of prepared films

Figure 8(a) presents the real dielectric constant with the highest value of 5.21 observed at a photon energy of 3.5 eV of the 60%MgO:40%SnO<sub>2</sub> film, while the lowest value of 3.18 is observed at the photon energy of 3.25 eV of the 70%MgO:30%SnO<sub>2</sub> film. Figure 8(b) illustrates the imaginary dielectric constant, with the highest value of 0.384 observed at a photon energy of 1.3 eV for the Pure MgO film, and the lowest value of 0.023 observed at the photon energy of 0.384 eV for the 70%MgO:30%SnO<sub>2</sub> film. In general, both the real and imaginary dielectric constants exhibited a change in the behavior with an increase in the doping ratio [44,45].

### CONCLUSIONS

The co-precipitation method proved successful in synthesizing MgO, SnO<sub>2</sub>, and MgO:SnO<sub>2</sub> nanoparticles with distinct characteristics. X-ray diffraction analysis revealed an average crystallite size of 33 nm, while particle size analyzer results indicated an average particle size of 22 nm. The samples exhibited different crystal structures, with MgO having a cubic structure, SnO<sub>2</sub> nanoparticles showing a tetragonal structure, and MgO:SnO<sub>2</sub> displaying a tetragonal structure as well. SEM images provided further evidence of spherical and aggregated particles with a granular crystalline structure. The nanoparticles were further characterized using UV-Vis spectroscopy. It was observed

that increasing the SnO<sub>2</sub> concentration doping led to enhanced transmittance in the MgO:SnO<sub>2</sub> films. Moreover, the energy band gap increased with higher SnO<sub>2</sub> concentration, the refractive index, extinction coefficient, and real and imaginary dielectric constant components of the material also increased with rising SnO<sub>2</sub> concentration. The synthesized nanoparticles have potential applications in various fields, such as optoelectronics, and sensors.

## ORCID

© R.H. Ayoub, <https://orcid.org/0009-0002-6590-8258>; © Muhammad H. Al-Timimi, <https://orcid.org/0000-0002-9828-6945>  
© M.Z. Abdullah, <https://orcid.org/0000-0002-4087-7830>

## REFERENCES

- [1] J. Xiong, Y. Xue, Y.-D. Xia, F. Zhang, Y.-X. Zhang, L.-H. Li, X.-H. Zhao, and B.-W. Tao, "Fabrication of long-length ion beam-assisted deposited MgO templates for YBCO coated conductors," *Rare Met.* **32**, 574-578 (2013). <https://doi.org/10.1007/s12598-013-0164-4>
- [2] S. Stankic, M. Sterrer, P. Hofmann, J. Bernardi, O. Diwald, and E. Knozinger, "Novel optical surface properties of Ca<sup>2+</sup>-doped MgO nanocrystals," *Nano Lett.* **5**, 1889-1893 (2005). <https://doi.org/10.1021/nl0511418>
- [3] M.H. Al-Timimi, W.H. Albanda, and M.Z. Abdullah, "Influence of Thickness on Some Physical Characterization for Nanostructured MgO Thin Films," *East European Journal of Physics*, (2), 173-181 (2023). <https://periodicals.karazin.ua/ejpp/article/view/21350>
- [4] Y. Cai, D. Wu, X. Zhu, W. Wang, F. Tan, J. Chen, X. Qiao, and X. Qiu, "Sol-gel preparation of Ag-doped MgO nanoparticles with high efficiency for bacterial inactivation," *Ceram. Int.* **43**, 1066-1072 (2017). <https://doi.org/10.1016/j.ceramint.2016.10.041>
- [5] M.Z. Abdullah, M.H. Al-Timimi, W.H. Albanda, M. Dumitru, A.E. Balan, C. Ceaus, et al., "Structural and Electrochemical Properties of P3-Na<sub>0.67</sub>Mn<sub>0.3</sub>Co<sub>0.7</sub>O<sub>2</sub> Nanostructures Prepared by Citric-Urea Self-Combustion Route as Cathode for Sodium Ion Battery," *Digest Journal of Nanomaterials and Biostructures*, **14**(4), 1179-1193 (2019). [https://chalcogen.ro/1179\\_AbdullahMZ.pdf](https://chalcogen.ro/1179_AbdullahMZ.pdf)
- [6] A.M.E. Raj, L. Nehru, M. Jayachandran, and C. Sanjeeviraja, "Spray pyrolysis deposition and characterization of highly (100) oriented magnesium oxide thin films," *Crystal Research and Technology*, *J. Exp. Indust. Crystallogr.* **42**, 867-875 (2007). <https://doi.org/10.1002/crat.200710918>
- [7] J. Lee, T. Jeong, S. Yu, S. Jin, J. Heo, W. Yi, and J. Kim, "Secondary electron emission of MgO thin layers prepared by the spin coating method," *J. Vac. Sci. Technol. B: Microelectr. Nanometer Struct. Proc. Measure. Phenomena*, **19**, 1366-1369 (2001). <https://doi.org/10.1116/1.1383079>
- [8] I.M.I. Moustafa, and M.R. Abdelhamid, "Synthesis of MgO-ZrO<sub>2</sub> mixed nanoparticles via diferent precursors: identification of their destructive action for organic pollutants," *J. Chem. Eng. Process. Technol.* **9**(1), 372 (2018). <https://doi.org/10.4172/2157-7048.1000372>
- [9] M. Kiaei, Y.R. Moghdam, B. Kord, and A. Samariha, "The effect of nano-MgO on the mechanical and fammability properties of hybrid nano composites from wood four-polyethylene," *Maderas. Ciencia y Tecnología*, **19**(4), 471-480 (2017). <http://dx.doi.org/10.4067/S0718-221X2017005000701>
- [10] H.M. Hussein, and M.H. Al-Timimi, "Preparation and Study Some Physical Properties of (CMC/PAA: MgO) Nano Composites," *Eurasian Journal of Physics, Chemistry and Mathematics*, **8**, 47-55 (2022). <https://www.geniusjournals.org/index.php/ejpcm/article/view/1944>
- [11] Abdullah, M. Z., Hasan, H. M., Al-Timimi, M. H., Albanda, W. H., Alhussainy, M. K., & Dumitru, M. "Preparation And Characterization Of Carbon Doped Lithium Iron Phosphate Composite As Cathode For Rechargeable Battery" . *Journal of Ovonic Research* Vol, 15(3), 199-204 (2019). [https://chalcogen.ro/199\\_AbdullahMZ.pdf](https://chalcogen.ro/199_AbdullahMZ.pdf)
- [12] I.-C. Ho, Y. Xu, and J. D. Mackenzie, "Electrical and Optical Properties of MgO Thin Film Prepared by Sol-Gel Technique," *Journal of Sol-Gel Science and Technology*, **9**, 295-301 (1997). <https://doi.org/10.1023/A:1018315529408>
- [13] A.M.E. Raj, M. Jayachandran, and C. Sanjeevijaya, "Fabrication techniques and material properties of dielectric MgO thin films- A status review," *CIRP Journal of Manufacturing Science and Technology*, **2**(2), 92-113 (2010). <https://doi.org/10.1016/j.cirpj.2010.02.003>
- [14] A.D. Bhagwat, S.S. Sawant, B.G. Ankamwar, and C.M. Mahajan, "Synthesis of nanostructured tin oxide (SnO<sub>2</sub>) powders and thin flmsby sol-gel method," *J. Nano Electron. Phys.* **7**(4), 04037 (2015). [https://jnep.sumdu.edu.ua/en/component/content/full\\_article/1658](https://jnep.sumdu.edu.ua/en/component/content/full_article/1658)
- [15] A. Mariam, V.S. Vidhya, S. Sivaranjani, M. Bououdina, R. Perumalsamy, and M. Jayachandran, "Synthesis and characterizations of SnO<sub>2</sub> nanoparticles," *J. Nanoelectron. Optoelectron.* **8**, 273-280 (2013). <https://doi.org/10.1166/jno.2013.1471>
- [16] S. Vishniakou, R. Chen, Y.G. Ro, C.J. Brennan, C. Levy, E.T. Yu, and S.A. Dayeh, "Improved performance of zinc oxide thin film transistor pressure sensors and a demonstration of a commercial chip compatibility with the new force sensing technology," *Adv. Mater. Technol.* **3**(3), 1700279 (2018). <https://doi.org/10.1002/admt.201700279>
- [17] C.I. Priyadharsini, M. Sumathi, A. Prakasam, P.M. Anbarasan, R. Sathiyapriya, and V. Aroulmoji, "Effect of Mg doping on structural and optical properties of SnO<sub>2</sub> nanoparticles by chemical co-precipitation method," *Int. J. Adv. Sci. Eng.* **3**, 428-434 (2017). <https://doi.org/10.1016/j.phpro.2012.03.077>
- [18] B. Bendahmane, M. Tomić, N.E.H. Toudij, I. Gracia, S. Vallejos, and F. Mansour, "Influence of Mg doping levels on the sensing properties of SnO<sub>2</sub> films," *Sensors*, **20**(7), 2158 (2020). <https://doi.org/10.3390/s20072158>
- [19] K. Sujatha, T. Seethalakshmi, and O.L. Shanmugasundaram, "Synthesis, characterization of nano tin oxide via co-precipitation method," *Nanotechnology Research and Practice*, **11**(3), 98-105 (2016). <https://doi.org/10.13187/nrp.2016.11.98>
- [20] T.S. Vijayakumar, S. Karthikeyeni, S. Vasanth, A. Ganesh, G. Bupesh, R. Ramesh, M. Manimegalai, and P. Subramanian, "Synthesis of silver-doped zinc oxide nanocomposite by pulse mode ultrasonication and its characterization studies," *J. Nanosci.* **2013**, Article ID 785064 (2013). <https://doi.org/10.1155/2013/785064>

- [21] P.S. Shajira, M.J. Bushiri, B.B. Nair, and V.G. Prabhu, "Energy band structure investigation of blue and green light emitting Mg doped SnO<sub>2</sub> nanostructures synthesized by combustion method," *Journal of Luminescence*, **145**, 425-429 (2014). <https://doi.org/10.1016/j.jlumin.2013.07.073>
- [22] S. Vadivel, and G. Rajarajan, "Effect of Mg doping on structural, optical and photocatalytic activity of SnO<sub>2</sub> nanostructure thin films," *Journal of Materials Science: Materials in Electronics*, **26**, 3155-3162 (2015). <https://doi.org/10.1007/s10854-015-2811-z>
- [23] Md.M. Rashad, A. Ismail, I. Osama, I.A. Ibrahim, and A-H T. Kandil, "Photocatalytic decomposition of dyes using ZnO doped SnO<sub>2</sub> nanoparticles prepared by solvothermal method," *Arab. J. Chem.* **7**, 71-77 (2014). <https://doi.org/10.1016/j.arabjc.2013.08.016>
- [24] L.J.Q. Maia, C.R. Ferrari, V.R. Mastelaro, A.C. Hernandez, and A. Ibanez, "Raman and photoluminescence of Er<sup>3+</sup>-doped SnO<sub>2</sub> obtained via the sol-gel technique from solutions with distinct pH," *Solid State Sci.* **10**, 1935 (2008).
- [25] Y.C. Liang, and Y. Chao, "Enhancement of acetone gas-sensing responses of tapered WO<sub>3</sub> nanorods through sputtering coating with a thin SnO<sub>2</sub> coverage layer," *Nanomaterials*, **9**(6), 864 (2019). <https://doi.org/10.3390/nano9060864>
- [26] Mohammed, A. A., Ahmed, A. R., & Al-Timimi, M. H. Structural, "Optical and Thermal Properties of (PEG/PAA: MnO<sub>2</sub>) Nano Composites". *Technium BioChemMed*, 3(2), 107-119(2022). <https://doi.org/10.47577/biochemmed.v3i2.7116>
- [27] W.A. Aelawi, S. Alptekin, and M.H. Al-Timimi, "Structural, optical, and electrical properties of nanocrystalline CdS<sub>1-x</sub> CuS<sub>x</sub> thin films," *Indian Journal of Physics*, 1-8 (2023). <https://doi.org/10.1007/s12648-023-02736-6>
- [28] S. Balamurugan, J. Jainshaa, and S.A. Ashika, "Comparison of the synthesis of s, p, d, and f block simple oxides of MgO, SnO<sub>2</sub>, NiO, and CeO<sub>2</sub> nanostructured materials," *Results in Chemistry*, **5**, 100864 (2023). <https://doi.org/10.1016/j.rechem.2023.100864>
- [29] A. Velmurugan, and A.R. Warriar, "Production of biodiesel from waste cooking oil using mesoporous MgO-SnO<sub>2</sub> nanocomposite," *Journal of Engineering and Applied Science*, **69**(1), 92 (2022). <https://doi.org/10.1186/s44147-022-00143-y>
- [30] S. S. Mirtalebi, H. Almasi, & M. A. Khaledabad, "Physical, morphological, antimicrobial and release properties of novel MgO-bacterial cellulose nanohybrids prepared by in-situ and ex-situ methods," *International journal of biological macromolecules*, **128**, 848-857 (2019). <https://doi.org/10.1016/j.ijbiomac.2019.02.007>
- [31] H.S. Al-Rikabi, M.H. Al-Timimi, and W.H. Albanda, "Morphological and optical properties of MgO<sub>1-x</sub>ZnS<sub>x</sub> thin films," *Digest Journal of Nanomaterials & Biostructures (DJNB)*, **17**(3), (2022). <https://doi.org/10.15251/DJNB.2022.173.889>
- [32] M.H. Saeed, M.H. Al-Timimi, and O.A.A. Hussein, "Structural, morphological and optical characterization of nanocrystalline WO<sub>3</sub> thin films," *Digest Journal of Nanomaterials and Biostructures*, **16**(2), 563-569 (2021). [https://chalcogen.ro/563\\_SaeedMH.pdf](https://chalcogen.ro/563_SaeedMH.pdf)
- [33] H. Si, C. Xu, Y. Ou, G. Zhang, W. Fan, Z. Xiong, A. Kausar, et al., "Dual-passivation of ionic defects for highly crystalline perovskite," *Nano Energy*, **68**, 104320 (2020). <https://doi.org/10.1016/j.nanoen.2019.104320>
- [34] A.T. Abood, O.A.A. Hussein, M.H. Al-Timimi, M.Z. Abdullah, H.M.S. Al Aani, and W.H. Albanda, "Structural and optical properties of nanocrystalline SnO<sub>2</sub> thin films growth by electron beam evaporation," *AIP Conference Proceedings*, **2213**(1), 020036 (2020). <https://doi.org/10.1063/5.0000454>
- [35] J. Dagar, S. Castro-Hermosa, G. Lucarelli, F. Cacialli, and T.M. Brown, "Highly efficient perovskite solar cells for light harvesting under indoor illumination via solution processed SnO<sub>2</sub>/MgO composite electron transport layers," *Nano Energy*, **49**, 290-299 (2018). <https://doi.org/10.1016/j.nanoen.2018.04.027>
- [36] M.H. Abdul-Allah, S.A. Salman, and W.H. Abbas, "Annealing effect on the structural and optical properties of (CuO)(Fe<sub>2</sub>O<sub>3</sub>) x thin films obtained by chemical spray pyrolysis," *Journal of Thi-Qar Science*, **5**(1), 91-96 (2014). <https://www.iasj.net/iasj/pdf/a38620e9241bbe5a>
- [37] A.J. Kadham, D. Hassan, N. Mohammad, and A.H. Ah-Yasari, "Fabrication of (polymer blend-magnesium oxide) nanoparticle and studying their optical properties for optoelectronic applications," *Bulletin of Electrical Engineering and Informatics*, **7**(1), 28-34 (2018). <https://beei.org/index.php/EEI/article/view/839/518>
- [38] X. Wu, C. Zhou, W.R. Huang, F. Ahr, and F.X. Kärtner, "Temperature dependent refractive index and absorption coefficient of congruent lithium niobate crystals in the terahertz range," *Optics express*, **23**(23), 29729-29737 (2015). <https://doi.org/10.1364/OE.23.029729>
- [39] M.H. Abdullal, R.A. Jaseen, and A.H. Resan, "Annealing effect on the optical energy gap of (CdTe) thin films," *J. Pure Sciences*, **7**(3), 205-213 (2011). <https://www.iasj.net/iasj/pdf/ccf116d82c221e01>
- [40] J. Al-Zanganawee, M. Al-Timimi, A. Pantazi, O. Brincoveanu, C. Moise, R. Mesterca, ... & Enachescu, M. "Morphological and optical properties of functionalized SWCNTs: P3OT nanocomposite thin films, prepared by spincoating," *Journal of Ovonic Research*, **12**(4), 201-207 (2016). [https://www.chalcogen.ro/201\\_AlzanganaweeJ.pdf](https://www.chalcogen.ro/201_AlzanganaweeJ.pdf)
- [41] A. Manikandan, L.J. Kennedy, M. Bououdina, and J.J. Vijaya, "Synthesis, optical and magnetic properties of pure and Co-doped ZnFe<sub>2</sub>O<sub>4</sub> nanoparticles by microwave combustion method," *Journal of magnetism and magnetic materials*, **349**, 249-258 (2014). <https://doi.org/10.1016/j.jmmm.2013.09.013>
- [42] J.M. Rondinelli, and N.A. Spaldin, "Structure and properties of functional oxide thin films: insights from electronic-structure calculations," *Advanced materials*, **23**(30), 3363-3381 (2011). <https://doi.org/10.1002/adma.201101152>
- [43] S.S.H. Al-Mgrs, M.H. Al-Timimi, M.Z. Abdullah, and W.H. Al-Banda, "Structural and optical characterizations of synthesized CMC/PVP-SnO<sub>2</sub> nano composites," *AIP Conference Proceedings*, **2475**(1), 090018 (2023). <https://doi.org/10.1063/5.0102768>
- [44] A.J. Mawat, M.H. Al-Timimi, W.H. Albanda, AND M.Z. Abdullah, "Morphological and optical properties of Mg<sub>1-x</sub>Cd<sub>x</sub> nanostructured thin films," *AIP Conference Proceedings*, **2475**(1), 090019 (2023). <https://doi.org/10.1063/5.0103955>
- [45] Q.M. Jebur, A. Hashim, and M.A. Habeeb, "Structural, electrical and optical properties for (polyvinyl alcohol-polyethylene oxide-magnesium oxide) nanocomposites for optoelectronics applications," *Transactions on Electrical and Electronic Materials*, **20**(4), 334-343 (2019). <https://doi.org/10.1007/s42341-019-00121-x>

**ПОЛІПШЕННЯ СТРУКТУРНИХ ТА ОПТИЧНИХ ВЛАСТИВОСТЕЙ  
НАНОСТРУКТУРНИХ ПЛІВОК MgO: SnO<sub>2</sub>**

**Р.Х. Аюб<sup>а</sup>, Мухаммад Х. Аль-Тімімі<sup>а</sup>, М.З. Абдуллах<sup>б</sup>**

<sup>а</sup>*Департамент фізики, науковий коледж, університет Діяла, Ірак*

<sup>б</sup>*Управління досліджень матеріалів, Міністерство науки і технологій, Ірак*

У цьому дослідженні використовується метод хімічного осадження для дослідження структурних і оптичних властивостей наночастинок MgO:SnO<sub>2</sub>. Тонкі плівки були нанесені методом центрифугування на скляні підкладки. Рентгеноструктурний аналіз підтвердив кристалічну структуру отриманих тонких плівок з піками, що відповідають площинам (110), (101), (200), (211) і (220), з тетрагональною кристалічною структурою SnO<sub>2</sub>. Інфрачервона Фур'є спектроскопія (FTIR) і скануючий електронний мікроскоп (SEM), використовували для характеристики функціональних груп, форми та розмірів синтезованих наночастинок оксиду металу. Оптичні властивості плівок вивчали за допомогою спектроскопії UV-Vis. Енергія забороненої зони була оцінена в діапазоні (3,9-3,4 eV). Також було визначено показник заломлення та коефіцієнт екстинкції плівок. Результати показали, що плівки мають хорошу прозорість у видимій області. У дослідженні зроблено висновок, що тонкі плівки MgO:SnO<sub>2</sub>, технікою покриття методом центрифугування, мають потенційне застосування в оптоелектроніці та у газових датчиках.

**Ключові слова:** *плівки MgO:SnO<sub>2</sub>; техніка спінового покриття; метод осадження; структура; оптичні властивості*

## SCAPS NUMERICAL ANALYSIS OF GRAPHENE OXIDE/TiO<sub>2</sub> BULK HETEROJUNCTION SOLAR CELL SENSITIZED BY N719 RUTHENIUM DYE<sup>†</sup>

 **Hmoud Al Dmour**

*Department of Physics, Faculty of Science, Mutah University, Mutah, Jordan*

*E-mail: hmoud79@mutah.edu.jo*

Received July 13, 2023; revised August 6, 2023; accepted August 7, 2023

Solid-state dye-sensitized solar cells (SSDSC) have been fabricated using two different metal oxide materials, graphene oxide and titanium oxide, are used as hole and electron transport materials, respectively. The N719 dye ruthenium between the hole and electron transport materials to act as an absorber layer in your Go/N719dye/TiO<sub>2</sub> solar cells. Through the SCAPS-1D simulation, it was found that the Go/N719dye/TiO<sub>2</sub> solar cells have significantly improved the performance of the solar cells compared to the Go/TiO<sub>2</sub> solar cells. Specifically, the short circuit current (J<sub>sc</sub>) has increased from 0.17 mA/cm<sup>2</sup> to 1 mA/cm<sup>2</sup>, the open circuit voltage (V<sub>oc</sub>) has increased from 0.2 V to 1 V, and the power conversion efficiency (η) has increased from 0.02% to 2.5%. Additionally, Various factors that can affect the performance of Go/N719 dye/TiO<sub>2</sub> solar cells. It was found that the optimal dye thickness for achieving high short circuit current density, high power conversion efficiency, and high open circuit voltage is between 200nm and 300nm. Furthermore, the operating temperature of the solar cells also affects their performance. Increasing the operating temperature negatively affects the open circuit voltage and power conversion efficiency of the cells, while the short circuit current density is slightly enhanced. Finally, the efficiency of a solar cell can be affected by the type of metal used for the electrode and the type of semiconductor material used in the cell. In Ni and Cu electrodes solar cells ohmic contacts allow for efficient transfer of electrons, whereas Schottky barriers can impede electron flow and reduce efficiency in Mo and Ag electrodes solar cells.

**Keywords:** SCAPS; Graphene oxide; Operating temperature; Thickness; Work function; Parameter of solar cells

**PACS:** 42.79.Ek, 78.20.Bh, 72.80.Le, 73.30.y, 73.40.Kp

### 1. INTRODUCTION

Photovoltaic (PV) technology is used to convert sunlight into electricity, and it typically involves the use of solar cells made of semiconductor materials such as silicon [1,2] Hybrid photovoltaic cells have different semiconductor layers and junctions that allow them to create hole-electron pairs more efficiently, which leads to better performance such as Dye-sensitized solar cells (DSSCs). This device is a specific type of hybrid PV cell that uses a layer of organic dye to absorb light and create electron-hole pairs, which are then transported to an electrode by a layer of inorganic Nano-crystalline material [2-4]. They several advantages over traditional silicon-based solar cells, including lower production costs and the ability to generate electricity in low-light conditions. However, they also have some limitations, such as lower efficiency and shorter lifespan. Nevertheless, DSSCs are a promising technology that could help to make solar energy more accessible and affordable in the future [4].

The common hole conductor used in fabricating dye-sensitized MOSCs (Metal-Oxide-Semiconductor Cells) is an electrolyte composed of an iodine couple dissolved in an organic solvent [3,5]. This electrolyte plays a crucial role in the functioning of the MOSCs by providing the pathway for the transport of holes from the dye to the electrode. However, as known, there are certain problems associated with using electrolyte as the hole conductor. One of the main issues is the requirement for a good seal to prevent any leakage of the electrolyte, which can be challenging to achieve over long periods of time [5]. This leakage can not only affect the performance of the MOSCs but can also pose safety risks. To overcome this problem, researchers have been exploring alternative hole conductors, such as solid-state hole conductors or organic hole-transporting materials. These materials can offer improved stability and reliability compared to electrolytes, while also reducing the risk of leakage and increasing the lifetime of MOSCs. For example, solid-state materials such as PEDOT: PSS have been investigated as an alternative to electrolytes as the hole conductor in MOSCs. PEDOT:PSS has several advantages, such as high work function, high conductivity, high optical transmittance, easy solution process ability, and potential application on flexible substrates, which make it an attractive material for MOSCs and other solar cell application [6]. Recently m Yuhan Wu produced high efficiency solar cells of 18% utilizing bromide (KBr) into poly (3,4-ethylenedioxythiophene): polystyrene sulfonate) (PEDOT:PSS) to improve its own conductivity and interfacial charge transfer [7]. On other hand, there are also some drawbacks to using PEDOT:PSS as a hole transport layer. PEDOT:PSS can also be sensitive to moisture, leading to decreased performance and stability over time [8]. As a result, researchers are actively exploring alternative hole transport materials that can offer better performance, stability, and cost-effectiveness. Some promising options include metal oxides (such as TiO<sub>2</sub> or SnO<sub>2</sub>), conjugated polymers (such as PTB7 or P3HT), and carbon-based materials (such as graphene or carbon nanotubes). Graphene oxide (GO) has been investigated as a potential alternative to PEDOT:PSS as a hole transport material in solar cells. GO has several interesting properties, including a band gap energy of 3.5 eV, excellent transparency, low production cost, large scale production

<sup>†</sup> Cite as: Hmoud Al Dmour, East Eur. J. Phys. 3, 555 (2023), <https://doi.org/10.26565/2312-4334-2023-3-65>

© H. Al Dmour, 2023

capability, good solubility in many solvents, and high hole mobility [5,8]. Due to these properties, GO has been demonstrated to be a promising material for improving the efficiency of solar cells. Its high transparency allows for more light to pass through the cell and be absorbed by the active layer, while its high hole mobility can facilitate the transport of charge carriers and reduce the recombination of electrons and holes. Other important part in DSSCs is ruthenium dyes. It has indeed been extensively studied in photochemistry due to their remarkable properties such as chemical stability, excited state reactivity, luminescence, and long excited state lifetime [9,10].

This study aims to examine various factors that affect the performance of the solar cell, such as the presence of N719 Ruthenium dye, the thickness of the dye layer, the work function of the back contact, and the temperature. This information can provide insights into optimizing the design and performance of the solar cell. SCAPS-1D simulation package is a powerful tool for modeling the physical and electrical behavior of solar cells, including the absorption of light, generation and transport of charge carriers, and recombination processes [11]. It can simulate the effect of different parameters on the device performance, allowing for the optimization of the solar cell design.

## 2. NUMERICAL MODELING AND STRUCTURE DEVICE

Solar Cell Capacitance Simulator (SCAPS-1D) is a one-dimensional solar cell simulation program developed by the department of Electronics and Information Systems (ELIS) at the University of Gent, Belgium [11]. The purpose of SCAPS-1D is to simulate and evaluate the performance of Single-Step Deposition-Synthesized Solar Cells (SSDSC). It is also capable of modeling a variety of solar cell parameters and characteristics, including electrical and optical properties, interface and bulk recombination, and temperature and illumination dependence. SCAPS-1D uses a drift-diffusion approach to simulate carrier transport and considers the effects of doping, carrier lifetime, and surface recombination velocity on the cell's performance. The program has been validated against experimental data and has been used in various research studies to analyze the performance of different types of solar cells. Initially, the program was used to simulate the performance of solar cells made of CuInSe<sub>2</sub> and CdTe materials [11]. Later on, researchers began using the program to simulate the performance of crystalline solar cells and other types of materials [12].

This work has utilized SCAPS, a modeling software for solar cells, to investigate how certain parameters of the cells are affected by varying factors. Specifically, the thickness of the dye layer, operating temperature, and work function of the back contact were examined, and the efficiency, short circuit current density, and fill factor were extracted as parameters of interest. This was accomplished by analyzing the current density versus voltage of the solar cells under different experimental conditions. The SSDSC is a layered structure consisting of main layers): Graphen oxide (Go), nano crystalline Titanium oxide (TiO<sub>2</sub>), N719 Ruthenium Dye, back contact and front contact. Figure 1 show schematic diagrams of TiO<sub>2</sub>/dye/Go solar cells.

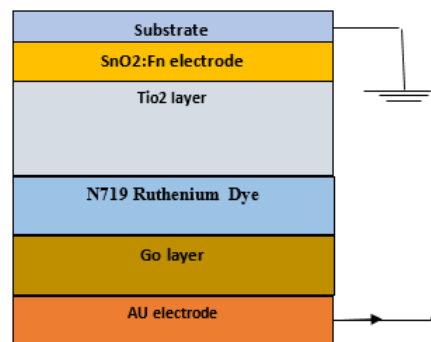


Figure 1. Schematic of the GO/N719dye/nc-TiO<sub>2</sub> solar cells

From previous literatures (13-15) Tables 1 and 2 present the input parameters used in SCAPS simulators for studying the performance of solar cells.

Table 1. Parameters for TiO<sub>2</sub>, Go and N719 Ruthenium Dye

| Material properties                                      | TiO <sub>2</sub> | Go      | N719 Ruthenium Dye |
|--|------------------|---------|--------------------|
| Thickness(nm)  | 2000             | 200     | Vary               |
| Bandgap (ev)   | 3.2              | 3.25    | 2.37               |
| Electron affinity(ev)                                    | 4.200            | 1.9     | 3.9                |
| dielectric permittivity(relative)                        | 10               | 3       | 30                 |
| CB effective density of states (1/cm <sup>3</sup> )      | 2.000E+17        | 2.2E+21 | 2.400E+20          |
| VB effective density of states (1/cm <sup>3</sup> )      | 6.000E+17        | 1.8E+21 | 2.500E+20          |
| Electron mobility (cm <sup>2</sup> /Vs)                  | 100              | 100     | 5                  |
| hole mobility (cm <sup>2</sup> /Vs)                      | 25               | 300     | 5                  |
| Shallow uniform donor density ND (1/cm <sup>3</sup> )    | 1.000E+17        | 0       | 0                  |
| Shallow uniform acceptor density NA (1/cm <sup>3</sup> ) | 0                | 1 E+16  | 1 E+17             |

**Table 2.** Parameters of back and front contacts

| Parameters                                  | Back contact | Front contact |
|---|--------------|---------------|
| Surface recombination velocity of electrons | 1.00E+5      | 1.00E+5       |
| Surface recombination velocity of holes     | 1.00E+7      | 1.00E+7       |
| Metal work function(ev)                     | 5.1          | 4.4           |

### 3. RESULTS AND DISCUSSION

#### 3-1 Simulation of TiO<sub>2</sub>/N719-dye/Go and TiO<sub>2</sub>/Go solar cells

The J-V characteristics and performance of two different types of solar cells, TiO<sub>2</sub>/N719-dye/GO (three layers) and TiO<sub>2</sub>/Go (two layers), have been studied using SCAPS simulations under standard simulated solar light of AM 1.5G (100mW/cm<sup>2</sup>). Based on the results in figure 1, the TiO<sub>2</sub>/N719-dye/Go solar cell exhibits the best performance with an open circuit voltage (V<sub>oc</sub>) of 1.02V, short current density (J<sub>sc</sub>) of 3.5mA/cm<sup>2</sup>, and a maximum output power (P<sub>max</sub>) of 0.9mW/cm<sup>2</sup>. The fill factor of the three-layer solar cells was around 0.67, calculated using equation 1 [16].

$$FF = \frac{I_m V_m}{I_{sc} V_{oc}} = \frac{P_{max}}{I_{sc} V_{oc}} \tag{1}$$

The power conversion efficiency (η) of a solar cell is given by the ratio of the maximum output power (P<sub>max</sub>) to the power of the incident light (P<sub>in</sub>). Mathematically, it can be expressed as:

$$\eta = \frac{P_{max}}{P_{in}} \tag{2}$$

The maximum output power (P<sub>max</sub>) can be obtained by multiplying the open-circuit voltage (V<sub>oc</sub>) and the short-circuit current density (J<sub>sc</sub>), and then multiplying the result by the fill factor (FF) of the solar cell. Therefore, we can express P<sub>max</sub> as:

$$P_{max} = V_{oc} \times J_{sc} \times FF \tag{3}$$

Substituting equation (2) into equation (1), we get:

$$\eta = \frac{V_{oc} \times J_{sc} \times FF}{P_{in}} \tag{4}$$

From equation (4), It is clear that the fill factor (FF) plays a crucial role in determining the power conversion efficiency (η) of a solar cell. A high fill factor indicates that the solar cell is able to convert a higher fraction of the incident light into electrical power, resulting in a higher efficiency. On the other hand, a low fill factor indicates that the solar cell is not able to utilize the incident light efficiently, resulting in a lower efficiency. It's important to note that no additional defects or recombination reactions were introduced in each layer during the simulation.

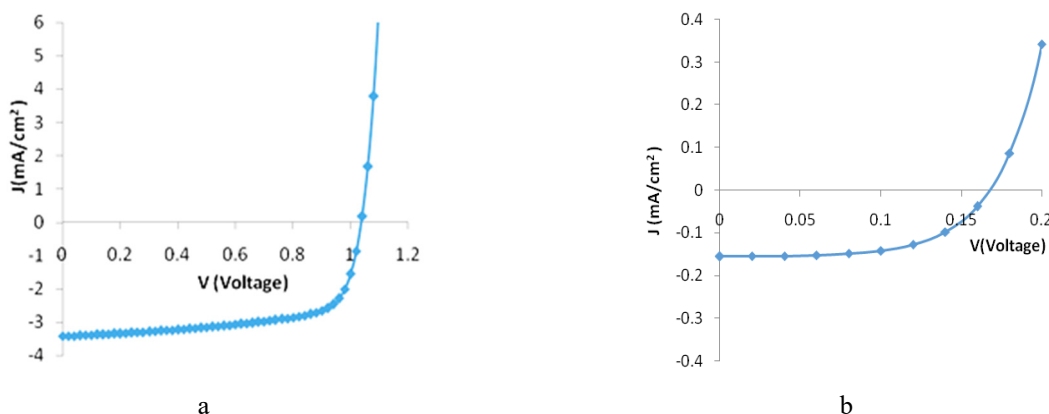


**Figure 2.** a) J -V characteristics of Go/DYE/TiO<sub>2</sub> solar cell and (b) J -V characteristics of Go /TiO<sub>2</sub> solar cell under illumination

The study found that a three-layer device composed of TiO<sub>2</sub>, dye, and Go showed an efficiency of 2.5% based on numerical simulations, which is higher than the reported 0.9% efficiency in recent literature [17]. Further investigations were conducted on three-layer solar cell by varying the thickness of the dye layer and the work function of the back contact and operating temperature, this could provide data on the relationship between these parameters and the efficiency of the solar cells. This data could then be analyzed to identify optimal values for these parameters that result in the highest efficiency. This process of optimizing the design of a solar cell is an important step in improving its performance and could lead to the development of more efficient and cost-effective solar energy technologies.

### 3-2. Effect of Thickness of N719 dye layer on solar cells

In dye-sensitized solar cells, the thickness of the dye layer plays an important role in the absorption of photons and the separation of photogenerated carriers at the interfaces between the dye layer and the metal oxide layer. The dye layer is responsible for absorbing light and transferring the energy to the metal oxide layer, where it generates electron-hole pairs. Figure 3 shows the dependence of various photovoltaic parameters on the thickness of dye, which was changed in the range of 10-300nm.

Figure 3a specifically shows the variation of  $V_{oc}$  with a change in the thickness of the dye layer. It appears that at 10 nm thickness,  $V_{oc}$  was initially around 0.94V, but as the thickness of the dye layer increased,  $V_{oc}$  also increased to reach 1.06V at 300 nm thickness. According to Figure 3b and c, the short-circuit current ( $J_{sc}$ ) and efficiency of the three-layer solar cells increased with an increase in the thickness of the dye layer. At a thickness of 200 nm, the  $J_{sc}$  and efficiency reached approximately 3.5 mA/cm<sup>2</sup> and 2.5%, respectively. However, as the thickness of the dye layer increased beyond 200 nm, the enhancement of  $J_{sc}$  and efficiency became very slow, indicating that there is an optimal thickness range for maximizing these parameters. This behavior can be explained by the fact that an increase in the thickness of the dye layer leads to the absorption of more light by the device, which generates more excitons (electron-hole pairs) that can contribute to the photocurrent. However, beyond a certain thickness, the additional dye molecules may not contribute significantly to the generation of excitons, leading to a plateau in the  $J_{sc}$  and efficiency values. A thinner dye layer may produce lower short-circuit current density and efficiency because of several factors. One of these factors is an increase in the recombination rate near the interfaces between the graphene oxide (GO)/dye and dye/ TiO<sub>2</sub> layers, which can limit the photocurrent generation. Additionally, a thinner dye layer may not absorb enough light, resulting in a lower photocurrent. Furthermore, the thickness of the dye layer should not be larger than the diffusion length of charge carriers, as a thick layer can reduce the short-circuit current density due to an increase in series resistance. In Figure 3d, the behavior of the fill factor was almost constant at the beginning, but it then declines for dye layers thicker than 100 nm, reaching a value of 67 at a thickness of 200 nm. This behavior indicates an increase in the series resistance, which can affect the fill factor. As the thickness of the dye layer increases, the series resistance also increases, leading to a decrease in the fill factor.

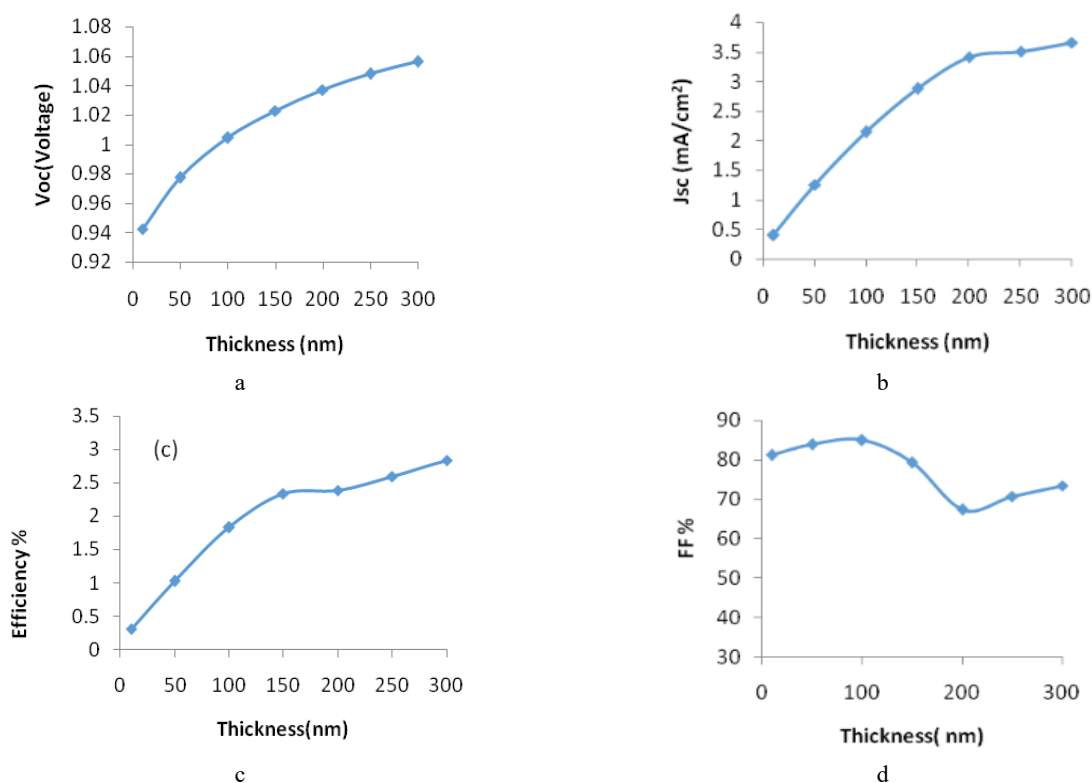


Figure 3. Photovoltaic performance parameters at various thickness of dye layer as: (a) Voc, (b) Jsc, (c) efficiency, and (d) FF

### 3-3. Effect of operating temperature on the performance of N719 dye layer on solar cells

The effect of temperature on the performance of solar cells is a crucial factor to consider for achieving optimal efficiency and durability. This section examines the effect of temperature on the performance of TiO<sub>2</sub>/dye/Go solar cell. Figure 4a shows the temperature of solar cells increases, the short circuit current density increases slightly due to improved light absorption and generation of electron and hole pairs. That is attributed to thermal energy breaks some of the bonds between the atoms or molecules in the material, causing the band gap to decrease. This allows electrons to absorb photons with lower energies, which results in improved light absorption and increased generation of electron and hole pairs [18].

As a result, the short circuit current density increases slightly at higher temperatures, reaching 0.35 mA/cm<sup>2</sup> at high temperature. As the temperature of solar cells increases, more electrons and/or hole carriers are generated, leading to an increase in the reverse saturation current density (J<sub>o</sub>). According to the Shockley diode equation (4) , there is an inverse relationship between the reverse saturation current density and the open circuit voltage [19].

$$V_{oc} = \frac{nK_B T}{q} \left[ \ln\left(1 + \frac{J_{sc}}{J_o}\right) \right]. \tag{5}$$

Where, Voc is the open circuit voltage, A is ideally factor , q is elementary charge, K<sub>B</sub> is Boltzman constant , Jo is reverse current.

This means that an increase in J<sub>o</sub> will lead to a decrease in the open circuit voltage. Therefore, as the temperature of solar cells increases, the open circuit voltage will decrease, as observed in Figure 4b. The operating temperature of a solar cell can have a significant impact on its power conversion efficiency (Figure 4 c). At higher temperatures, there can be changes in the properties of the semiconductor materials used in the solar cell, which can lead to a decrease in efficiency. This degradation in efficiency is due to changes in the physical and chemical properties of the semiconductor materials used in the solar cells [18,19]. That is attributed to change in the characteristics of semiconductors used in the solar cells. The high temperature causes to change in the electron and hole mobility, carrier concentrations and band gaps of the materials. For example, the band gap of semiconductor become narrow at high temperature which my lead the increase the recombination of electrons and holes while traveling across the region decrease of efficiency output power of the device ( J<sub>sc</sub> Voc ) [18]. The increase in fill factor (FF) of a solar cell from 67% to 72% with increasing temperature up to 450 k is likely due to a reduction in the series resistance within the bulk region of the solar cell. Series resistance is the sum of the resistances within a solar cell that limit the flow of current. As the temperature increases, the resistance of the bulk material of the solar cell decreases. This reduction in resistance can lead to a decrease in the voltage drop across the cell, resulting in an increase in the fill factor.

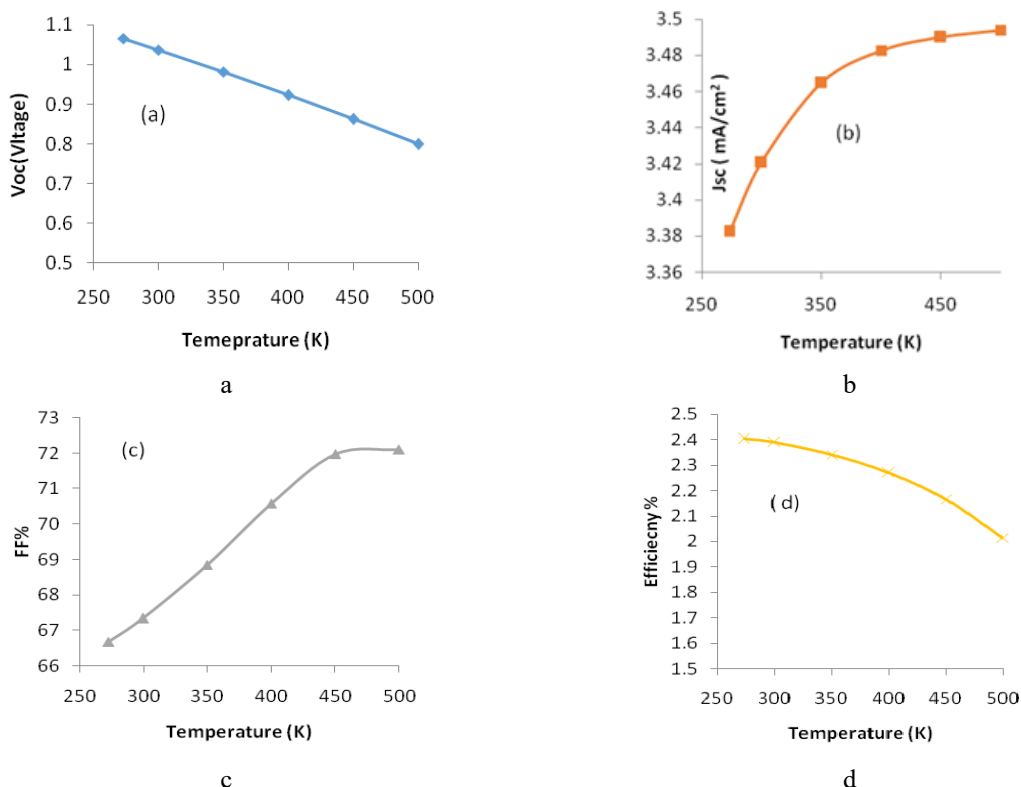
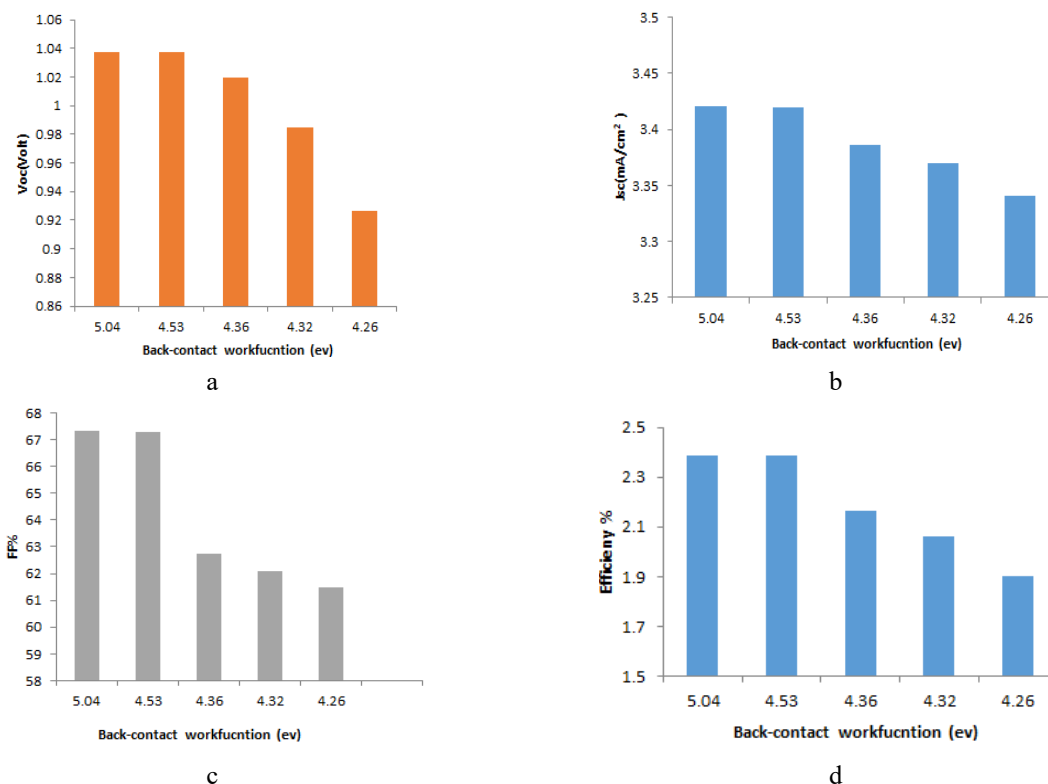


Figure 4. Photovoltaic performance parameters at various thickness of dye layer as: (a) Voc (b) Jsc, (c) efficiency and (d) FF

### 3.4 Effect of back-contact workfunction

In solar cells, it is important to optimize the alignment of energy levels of materials and work function of electrodes to ensure efficient charge transfer and minimize energy losses. To achieve this, the energy levels of the materials and electrodes must be aligned properly so that the charge carriers can flow efficiently from one to another without losing energy. It is desirable to have a small energy level offset between the electrodes and the hole transport layer in order to maximize the efficiency of the solar cell. A small offset can facilitate the injection of holes from the hole transport layer into the electrode, leading to efficient charge extraction and high photocurrent. Figure 5 demonstrates the impact of changing the back contact work function of a solar cell using different electrodes. Specifically, the back contact work

function is varied from 5.04 eV to 4.26 eV, and the electrodes used include nickel, silver, copper, molybdenum, and tungsten. According to the graph, the change in  $J_{sc}$  (short-circuit current density) is minimal, with only a 0.02 mA/cm<sup>2</sup> difference observed between the different electrodes. However, the open-circuit voltage decreases slightly from 1.03 V to 0.95 V. The more significant impact is observed in the efficiency and fill factor parameters, as indicated in Figure 5c and 5d. The efficiency of the solar cell decreases considerably with the change in back contact work function, with the maximum efficiency dropping from approximately 20% to 14%. Similarly, the fill factor parameter also decreases with the change in back contact work function, indicating that the cell's ability to convert light into electricity is reduced.



**Figure 5.** Photovoltaic performance parameters at various Back-contact workfunction (eV) as: (a) – Voc, (b) – Jsc, (c) – FF, and (d) – efficiency

The performance of solar cells is affected by the type of junction created at the interface between the electrode and HTM (hole transport material), as reported by studies [20]. The efficiency obtained in Ag, MO electrode, and Mo solar cells was low due to the large energy barrier at the interface that impedes the flow of the active layer to the electrode. This barrier is known as a Schottky barrier and arises from the difference in work function between the LUMO (lowest unoccupied molecular orbital) of graphene oxide (5.1 eV) and the work function of Ag and Mo (4.26, 4.36 eV). On the contrary, solar cells with Ni and Cu electrodes show high efficiency because an ohmic contact is formed between graphene oxide and the Ni and Cu electrodes. This is attributed to the small difference between the LUMO of GO and the work function of the electrodes, which facilitates efficient charge transfer and helps to form an ohmic contact.

#### 4. CONCLUSION

The SCAPS-1D simulation was utilized to investigate the impact of several parameters on the performance of TiO<sub>2</sub>/N719-dye/GO solar cells. These parameters included the thickness of the dye layer, operating temperature, and work function of the back contact. The simulation results indicated that the Go/N719dye/TiO<sub>2</sub> solar cells demonstrated higher  $J_{sc}$ ,  $V_{oc}$ , and  $\eta$  compared to the Go/TiO<sub>2</sub> solar cells. The  $J_{sc}$  increased from 0.17 mA/cm<sup>2</sup> to 1 mA/cm<sup>2</sup>, the  $V_{oc}$  increased from 0.2 V to 1 V, and the  $\eta$  increased from 0.02% to 2.5%. These enhancements were ascribed to the improved light absorption and charge transport through the interface due to the presence of the dye layer. Furthermore, it was found that the optimal dye layer thickness for achieving high  $J_{sc}$ ,  $V_{oc}$ , and  $\eta$  was between 200nm and 300nm. However, increasing the dye layer thickness resulted in a decrease in the fill factor. Moreover, the increase in operating temperature had a negative impact on the  $V_{oc}$  and  $\eta$ , while slightly enhancing the  $J_{sc}$ . This is due to changes in the electron and hole mobility, carrier concentrations, and band gaps of the materials at high temperatures. The type of electrode used also influences the efficiency of TiO<sub>2</sub>/dye/Go solar cells. Ni and Cu electrodes create low resistance at the interface with Go, while Ag and M electrodes create a high barrier that inhibits the flow of charge carriers across it.

#### ORCID

## REFERENCES

- [1] A. Blakers, N. Zin, K.R. McIntosh, and K. Fong, "High Efficiency Silicon Solar Cells," *Energy Procedia*, **33**, 1-10 (2013). <https://doi.org/10.1016/j.egypro.2013.05.033>
- [2] J. Niederhausen, K.A. Mazzi, and R.W. MacQueen, "Inorganic-organic interfaces in hybrid solar cells," *Electron. Struct.* **3**, 033002 (2021). <https://doi.org/10.1088/2516-1075/ac23a3>
- [3] B. O'Regan, and M. Grätzel, "A Low-Cost, High-Efficiency Solar Cell Based on Dye-Sensitized Colloidal TiO<sub>2</sub>Films," *Nature*, **353**, 737-740 (1991). <https://doi.org/10.1038/353737a0>
- [4] N. Saleh, S. Al-Trawneh, H. Al-Dmour, S. Al-Taweel, and J.P. Graham, "Effect of Molecular-Level Insulation on the Performance of a Dye-Sensitized Solar Cell: Fluorescence Studies in Solid State," *J. Fluoresc.* **25**, 59-68 (2015). <https://doi.org/10.1007/s10895-014-1479-8>
- [5] R. Harikisun, and H. Desilvestro, "Long-term stability of dye solar cells," *Sol. Energy*, **85**, 1179-1188 (2011). <https://doi.org/10.1016/j.solener.2010.10.016>
- [6] N. Touafek, R. Mahamdi, and C. Dridi, "The performance of planar inverted perovskite solar cells employing graphene oxide as HTL," *Digest Journal of Nanomaterials and Biostructures*, **16**, 705-712 (2021). [https://chalcogen.ro/705\\_TouafekN.pdf](https://chalcogen.ro/705_TouafekN.pdf)
- [7] Y. Wu, and G. Duan, "Inverted Planar Perovskite Solar Cells with High Electrical Conductivity and Efficiency by KBr-Doped PEDOT:PSS," *ECS J. Solid State Sci. Technol.* **11**, 025005 (2022). <https://doi.org/10.1149/2162-8777/ac4d81>
- [8] Y. Park, K.S. Choi, and S.Y. Kim, "Graphene oxide/PEDOT:PSS and reduced graphene oxide/PEDOT:PSS hole extraction layers in organic photovoltaic cells," *Phys. Status Solidi A*, **209**, 1363-1368 (2012). <https://doi.org/10.1002/pssa.201228040>
- [9] N. Tomar, A. Agrawal, V.S. Dhaka, and P.K. Suroliya, "Ruthenium complexes-based dye sensitized solar cells: Fundamentals and research trends," *Solar Energy*, **207**, 59-76 (2020). <https://doi.org/10.1016/j.solener.2020.06.060>
- [10] H. Al-Dmour, R.H. Alzard, H. Alblooshi, K. Alhosani, S. Al Madhoob, and N. Saleh, "Enhanced Energy Conversion of Z907-Based Solar Cells by Cucurbit[7]uril Macrocycles," *Frontiers in Chemistry*, **7**, 562 (2019). <https://doi.org/10.3389/fchem.2019.00561>
- [11] M. Burgelman, P. Nollet, and S. Degraeve, "Modelling polycrystalline semiconductor solar cells," *Thin Solid Films*, **361-362**, 527-532 (2000). [https://doi.org/10.1016/S0040-6090\(99\)00825-1](https://doi.org/10.1016/S0040-6090(99)00825-1)
- [12] H. Zerfaoui, D. Dib, M. Rahmani, K. Benyelloul, and C. Mebarkia, "Study by simulation of the SnO<sub>2</sub> and ZnO anti-reflection layers in n-SiC/p-SiC solar cells," *AIP Conference Proceedings*, **1758**, 030029 (2016). <https://doi.org/10.1063/1.4959425>
- [13] N. Touafek, R. Mahamdi, and C. Dridi, "Boosting the performance of planar inverted perovskite solar cells employing graphene oxide as HTL," *Digest Journal of Nanomaterials and Biostructures*, **16**, 705-712 (2021). [https://chalcogen.ro/705\\_TouafekN.pdf](https://chalcogen.ro/705_TouafekN.pdf)
- [14] N.S. Noorasid, F. Arith, A.Y. Firhat, A.N. Mustafa, and A.S.M. Shah, "SCAPS Numerical Analysis of Solid-State Dye Sensitized Solar Cell Utilizing Copper (I) Iodide as Hole Transport Layer," *Engineering Journal* **26** 1-12 2022. <https://doi.org/10.4186/ej.2022.26.2.1>
- [15] J.W. Lee, "Isothermal Electricity for Energy Renewal. PCT," International Patent Application Publication Number WO 2019/136037 A1, (11 July 2019).
- [16] J. Nelson, *Physics of Solar Cells, (The Properties of Semiconductor Materials)*, 1<sup>st</sup> edition, (Imperial College Press, 2003).
- [17] S. Daulay, A.F. Madsuha, E.S. Rosa, and A.H. Yuwono, "Fabrication of Titanium Dioxide-reduced Graphene Oxide (TiO<sub>2</sub>rGO) nanocomposites as the Photoanode in Dye Sensitized Solar Cells," *Journal of Physics: Conference Series*, **1402**, 055101 (2019). <https://doi.org/10.1088/1742-6596/1402/5/055101>
- [18] J. Xi, L. Zheng, S. Wang, J. Yang, and W. Zhang, "Temperature-dependent structural fluctuation and its effect on the electronic structure and charge transport in hybrid perovskite CH<sub>3</sub>NH<sub>3</sub>PbI<sub>3</sub>," *Journal of Computational Chemistry*, **42**, 2213-2220 (2021). <https://doi.org/10.1002/jcc.26750>
- [19] A. Husainat, W. Ali, P. Cofie, J. Attia, J. Fuller, and A. Darwish, "Simulation and Analysis Method of Different Back Metals Contact of CH<sub>3</sub>NH<sub>3</sub>PbI<sub>3</sub> Perovskite Solar Cell Along with Electron Transport Layer TiO<sub>2</sub> Using MBMT-MAPLE/PLD," *American Journal of Optics and Photonics*, **8**(1), 6-26 (2020). <http://dx.doi.org/10.11648/j.ajop.20200801.12>
- [20] P. Sawicka-Chudy, Z. Starowicz, G. Wisz, R. Yavorskyi, Z. Zapukhlyak, M. Bester, Ł. Głowa, *et al.*, "Simulation of TiO<sub>2</sub>/CuO solar cells with SCAPS-1D software," *Mater. Res. Express*, **6**, 085918 (2019). <https://doi.org/10.1088/2053-1591/ab22aa>

### SCAPS ЧИСЛОВИЙ АНАЛІЗ ОБ'ЄМНОГО ГЕТЕРОПЕРЕХОДУ СОНЯЧНОГО ЕЛЕМЕНТУ ОКСИД ГРАФЕНУ/ТІО<sub>2</sub>, СЕНСИБІЛІЗОВАНОГО БАРВНИКОМ РУТЕНІЮ n719

Хмуд Аль Дмур

*Кафедра фізики, Факультет природничих наук, Університет Мута, Мута, Йорданія*

Твердотільні сенсифілізовані до барвника сонячні елементи (SSDSC) були виготовлені з використанням двох різних металооксидних матеріалів, оксиду графену та оксиду титану, які використовуються як матеріали для транспортування дірок та електронів відповідно. Барвник Рутеній-N719 між матеріалами для транспортування дірок і електронів, діє як шар поглиначка у сонячних елементах Go/N719dye/TiO<sub>2</sub>. За допомогою моделювання SCAPS-1D було виявлено, що сонячні батареї Go/N719dye/TiO<sub>2</sub> значно покращили продуктивність сонячних елементів порівняно з сонячними елементами Go/TiO<sub>2</sub>. Зокрема, струм короткого замикання (J<sub>sc</sub>) збільшився з 0,17 mA/cm<sup>2</sup> до 1 mA/cm<sup>2</sup>, напруга холостого ходу (V<sub>oc</sub>) зросла з 0,2 В до 1 В, а ефективність перетворення потужності (η) зросла з 0,02 % до 2,5 %. Крім того, різноманітні фактори можуть впливати на продуктивність сонячних батарей Go/N719 dye/TiO<sub>2</sub>. Було виявлено, що оптимальна товщина барвника для досягнення високої щільності струму короткого замикання, високої ефективності перетворення потужності та високої напруги холостого ходу становить від 200 нм до 300 нм. Крім того, робоча температура сонячних батарей також впливає на їх продуктивність. Підвищення робочої температури негативно впливає на напругу холостого ходу та ефективність перетворення потужності елементів, у той час як щільність струму короткого замикання трохи підвищується. Нарешті, ефективність сонячної батареї може залежати від типу металу, який використовується для електрода, і типу напівпровідникового матеріалу, який використовується в комірці. У сонячних елементах з Ni та Cu електродами омичні контакти забезпечують ефективну передачу електронів, тоді як бар'єри Шотткі можуть перешкоджати потоку електронів і знижувати ефективність сонячних елементів із електродами Mo та Ag.

**Ключові слова:** SCAPS; оксид графену; робоча температура; товщина; робоча функція; параметри сонячних елементів

## NUCLEON-NUCLEON ELASTIC SCATTERING FOR MOTION IN THE SHIFTED DENG-FAN POTENTIAL<sup>†</sup>

 **Bidhan Khirali\***,  **S. Laha<sup>†</sup>**,  **Biswanath Swain<sup>§</sup>**,  **Ujjwal Laha<sup>#</sup>**

*Department of Physics, National Institute of Technology, Jamshedpur, 831014, India*

*\*Corresponding author: [b.khirali720@gmail.com](mailto:b.khirali720@gmail.com)*

*<sup>§</sup>e-mail: [lahas.bol@gmail.com](mailto:lahas.bol@gmail.com); <sup>§</sup>e-mail: [biswanathswain73@gmail.com](mailto:biswanathswain73@gmail.com); <sup>#</sup>e-mail: [ujjwal.laha@gmail.com](mailto:ujjwal.laha@gmail.com)*

*Received July, 5, 2023; revised July 22, 2023; accepted July 26, 2023*

The scattering theory's main objective is to comprehend an object by hurling something at it. One can learn details about an object by observing how it bounces off other objects. The potential that exists between the two particles is the thing that one seeks to comprehend. In a time-independent approach to scattering, one assumes that the incident beam has been activated for a very long time and that the entire system is in a stationary state. For short-range local potentials, the variable phase methodology is highly useful in solving quantum mechanical scattering problems. Variable phase methodology/phase-function technique has been explicitly utilized for non-relativistic nucleon-nucleon scattering phenomenon with the fundamental central local potential term and without spin-orbit force. Working under this methodology, scattering phase shifts, total scattering cross section, and Differential cross section have been investigated for a new nuclear potential model "Shifted Deng-Fan potential". Real nucleon-nucleon scattering systems (n-p) and (p-p) have been treated for this purpose with partial waves up to  $\ell = 2$  in the low and moderate energy region. For  $\ell > 0$  waves, interacting repulsive barrier potential has been incorporated with the existing central part. Our results for the considered potential model show a close contest with that of the experimental data.

**Keywords:** *Shifted Deng-Fan Potential; Phase function method; Scattering Phase shifts; Scattering cross sections; (n-p) and (p-p) systems*

**PACS:** 03.65.Nk; 21.30.Fe; 13.75.Cs; 24.10.-i

### INTRODUCTION

It is a well-known fact that the exact solution of the Schrödinger equation is significant in quantum mechanics as they enclose all necessary information regarding the quantum system under consideration. Most of the quantum systems can only be treated by approximation methodologies [1,2,3], as exact analytic solutions are feasible only for a few simple cases such as the hydrogen atom, the harmonic oscillator and others [4,5,6] in all partial waves and all energies. In a quest to find a suitable potential for diatomic interaction to describe the vibrational spectrum, Deng and Fan, in 1957, proposed a new molecular potential model [7] that is exponential in nature and was called Generalized Morse potential [8]. This potential is a modification of the Morse potential also known as Deng-Fan molecular potential (DF). Numerous studies were performed for this potential by researchers in various applications [9]. This potential has been adequately utilized in describing the nucleons' mobility in the mean field produced from the interactions of the nuclei [10]. Dong treated the Deng-fan potential as a pertinent alternative to the Morse potential for vibrational spectrum and electromagnetic transitions [11,12] of the diatomic molecules. Mesa [13] applied this potential for energy spectra studies of the diatomic molecules. Oyewumi [14] utilized the Nikiforov-Uvarov method to obtain bound state solutions of the Deng-Fan molecular potential for several diatomic molecules like HCl, LiH, H<sub>2</sub> and so on. Many of the other works have been accomplished with this potential via different quantum mechanical wave equations [15-22] by utilizing several standard approximation prescriptions to the solution in both relativistic and non-relativistic domains.

A modified form of the DF called Shifted Deng-Fan potential (SDF) was proposed by Hamzavi et al. in 2012 [23] for the calculation of ro-vibrational energy levels for few of the diatomic molecules. In the modified form, the DF potential is shifted by the dissociation energy (D). Ref. [23] also demonstrated that DF and Morse potential are qualitatively similar but SDF and Morse potentials are very much similar for large values of  $r$  i.e in the regions  $r \approx r_e$  and  $r > r_e$ , however, they differ at  $r \approx 0$ . Here,  $r_e$  is the equilibrium diatomic separation. Louis [24] solved the Dirac equation for the Manning-Rosen plus shifted Deng-Fan (MRSDF) potential in the presence of spin and pseudospin (pspin) symmetries and by including a Coulomb-like tensor potential. All of above works [7-24] pertains to molecular spectroscopy and molecular dynamics. Within the framework of the shifted Deng Fan potential (SDF), Sajedi [25] studied the cluster structure of astrophysically important <sup>19</sup>Ne nucleus. In recent past, working with the exponential class of potentials, our group obtained exact analytical solution of the elastic Deng Fan potential [26] scattering of a particle in S-wave and obtained the phase parameters using the Jost function methodology for the systems under consideration in the nuclear realm.

In this article, we present the study of the non-relativistic nuclear scattering treatment of the SDF potential in terms of the fundamental nucleon-nucleon scattering both charged and uncharged. In support of our justification, we present phase shift observables, total scattering cross section for proton-neutron (p-n) and proton-proton (p-p) scattering & differential cross section studies for proton-proton (p-p) scattering. A comparison is drawn for the obtained data against

<sup>†</sup> **Cite as:** B. Khirali, S. Laha, B. Swain, U. Laha, East Eur. J. Phys. 3, 562 (2023), <https://doi.org/10.26565/2312-4334-2023-3-66>

© B. Khirali, S. Laha, B. Swain, U. Laha, 2023

the well-established experimental data. This is indirect way of knowing how much the SDF potential model treatment is justified in nuclear realm. We make use of the standard Phase function approach (PFM) [27] for numerical solution of the Schrödinger wave equation for motion of a particle in the SDF potential. Our study on the selected systems reproduces well consistent data in phase parameters, elastic scattering cross section and differential cross section for partial wave calculations up to  $\ell=2$ .

## 2. METHODOLOGY

Computing scattering phase shifts  $\delta_\ell(k)$  as a function of centre of mass energy ( $E_{c.m} = k^2 > 0$  in the theoretical limit of  $\hbar^2/2m=1$ ) is one among the core problems of quantum scattering theory. Phase-function method (PFM) [27] is an alternative to the traditional Schrödinger equation approach. This technique is powerful for its capability in straightforward physical interpretation of its equations and basic quantities. Moreover, it introduces the same type of approach in the bound state problem. This methodology [27] arises from the fact in the theory that certain second order linear homogeneous differential equations can be reduced to their first order non-linear equations of Riccati type called Riccati equations. The Riccati equations are satisfied by the phase functions  $\delta_\ell(k, r)$  that is having the meaning of the phase shifts at each point of the wave function for scattering by the potential  $V(r)$  cut-off at that point. Similar investigations with PFM have been made by authors treating the local [28-34] and nonlocal [35-37] potentials. With the Shifted Deng Fan (SDF) [23-25] potential in all partial wave treatment, we incorporate a screened centrifugal barrier which is repulsive term. Thus, with a modified form of SDF potential [26], the effective potential becomes

$$V_{sDF}(r) = V_N(r) = v_0 + v_1 \frac{e^{-\alpha r}}{(1 - e^{-\alpha r})} + v_2 \frac{e^{-2\alpha r}}{(1 - e^{-\alpha r})^2} + \frac{\ell(\ell+1)}{r^2} \quad (1)$$

Where  $v_0$ ,  $v_1$  and  $v_2$  are the strength parameters with dimension of fm<sup>-2</sup> and  $\alpha$  is the inverse range parameter with dimension of fm<sup>-1</sup> and  $r$  is the inter nucleon distance between the particles.

For a local potential [1-3,6-33],  $\delta_\ell(k, r)$  satisfies a first-order non-linear differential equation [27] written as

$$\delta'_\ell(k, r) = -k^{-1}V(r) \left[ \cos \delta_\ell(k, r) \hat{j}_\ell(kr) - \sin \delta_\ell(k, r) \hat{\eta}_\ell(kr) \right]^2, \quad (2)$$

where  $\hat{j}_\ell(kr)$  and  $\hat{\eta}_\ell(kr)$  are the Riccati-Bessel and Riccati Neuman functions [38].

The resulting Phase equations for S, P and D waves and corresponding  $\ell = 0, 1 \& 2$  values

$$\delta'_0(k, r) = -k^{-1}V(r) \left[ \sin(\delta_0(k, r) + kr) \right]^2, \quad (3)$$

$$\delta'_1(k, r) = -\frac{V(r)}{k^3 r^2} \left[ \sin(\delta_1(k, r) + kr) - kr \cos(\delta_1(k, r) + kr) \right]^2 \quad (4)$$

and

$$\delta'_2(k, r) = -k^{-1}V(r) \left[ \left( \frac{3}{k^2 r^2} - 1 \right) \sin(\delta_2(k, r) + kr) - \frac{3}{kr} \cos(\delta_2(k, r) + kr) \right]^2. \quad (5)$$

The quantity  $k$  represents the momentum of the scattering particle (center of mass momentum) and is related to the centre of mass energy by the relation  $k = \sqrt{2mE} / \hbar$ . Thus,  $k^2$  is the energy of the scattering particle in the limit of  $\hbar = 1$  and  $2m = 1$  where  $m$  is the mass of the particle (reduced mass of the two particle system) scattering off the considered potential. Phase equation is solved initializing from the origin up to the asymptotic region, given the initial condition  $\delta_\ell(k, 0) = 0$ . In the course of solving the phase equation, the phase  $\delta_\ell(k, r)$  is built up by the potential in additive manner as one moves away from the origin to its asymptotic value which implies  $\delta_\ell(k) = \lim_{r \rightarrow \infty} \delta_\ell(k, r)$ . One can also calculate the amplitude function  $A_\ell(k, r)$  by utilizing the phase function  $\delta_\ell(k, r)$ ,

## 3. RESULTS AND DISCUSSIONS

Nuclear shifted Deng Fan potential (SDF) (Eq. (1)) is parameterized for the standard phase shifts [39, 40] of different states of the (n-p) and (p-p) systems by solving the differential equations (3)-(5) numerically. Proper optimization to the step size of the 'r' value is significant in the phase accumulation calculation within the range of the interaction. Thus, one has to judiciously optimize the step size in order to have proper phase parameters. The parameters for different states

of the (n-p) system are given in Table 1. For stated states of the (p-p) system, we have utilized the same corresponding (n-p) states' parameters as it is an established fact that for nuclear force, (n-p) and (p-p) interactions are equivalent. But with (p-p), a Coulombic repulsion force is associated. To take care of this Coulomb force in (p-p) interaction, a Coulombic potential term is added to the existing nuclear SDF (Eq.1).

**Table 1.** List of parameters for states of (n-p) scattering system

| System  | States  | $\alpha(\text{fm}^{-1})$ | $v1(\text{fm}^{-2})$ | $v2(\text{fm}^{-2})$ | $v0(\text{fm}^{-2})$ |
|---------|---------|--------------------------|----------------------|----------------------|----------------------|
| n-p/p-p | $^1S_0$ | 0.868                    | -0.7174              | -0.050               | 0.014                |
|         | $^3S_1$ | 0.874                    | -2.000               | 1.760                | -0.235               |
|         | $^1P_1$ | 0.756                    | -2.165               | 2.980                | -0.006               |
|         | $^3P_0$ | 0.874                    | -3.430               | 2.500                | -0.045               |
|         | $^3P_1$ | 0.756                    | -2.250               | 3.550                | -0.010               |
|         | $^3P_2$ | 0.756                    | -2.410               | 1.300                | -0.010               |
|         | $^1D_2$ | 0.350                    | -1.700               | 0.005                | -0.060               |
|         | $^3D_1$ | 0.017                    | -0.550               | 5.800                | -0.0102              |
|         | $^3D_2$ | 0.400                    | -1.682               | 0.050                | -0.011               |
|         | $^3D_3$ | 0.350                    | -2.865               | 0.003                | -0.008               |

Solving the equations (3)-(5), with the substitution of the values of the parameters from Table 1, we calculate the scattering phase shifts for neutron-proton (n-p) and (p-p) systems up to partial waves  $\ell=2$ . We have used the calculated reduced mass to be  $m_{np} = 0.5039 \text{ amu}$  for the n-p system, and the value of  $\hbar^2/2m = 41.47 \text{ MeV fm}^2$ . In our numerical routine, the parameters are given free running to fit the desired phase shifts for the various states of the concerned systems. The (n-p) scattering phase shifts are presented in the Figures 1-3.

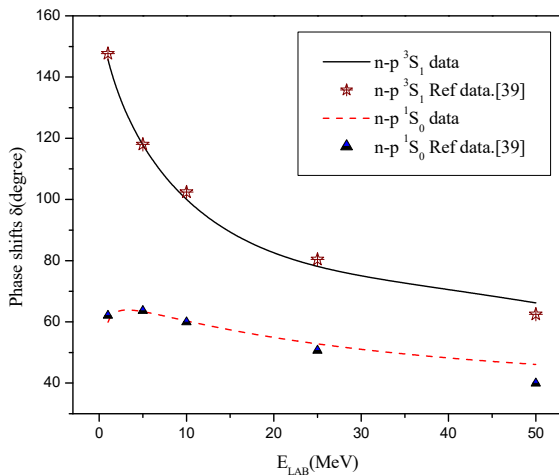


**Figure 1.** (n-p) S-wave scattering phase shifts as a function of laboratory energy

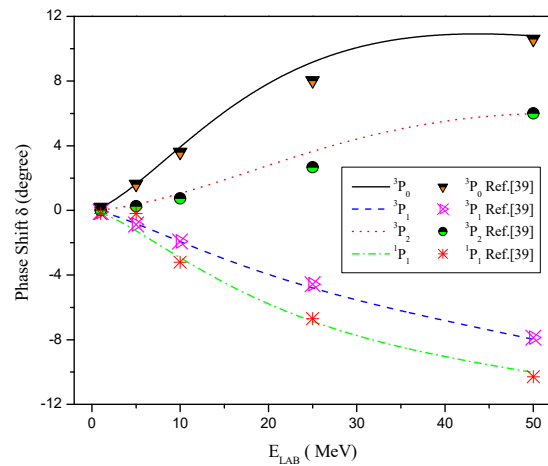


**Figure 2.** (n-p) P-wave scattering phase shifts as a function of laboratory energy

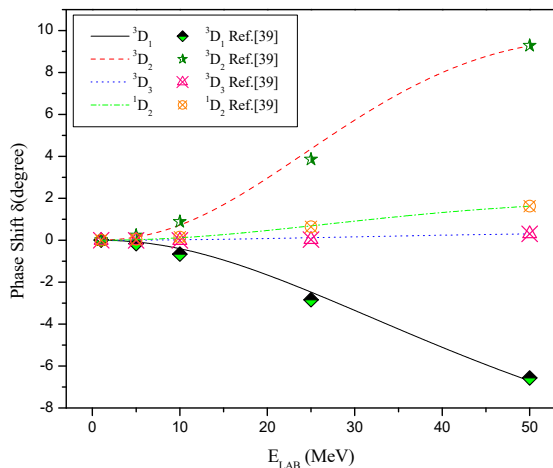


**Figure 3.** (n-p) D-wave scattering phase shifts as a function of laboratory energy

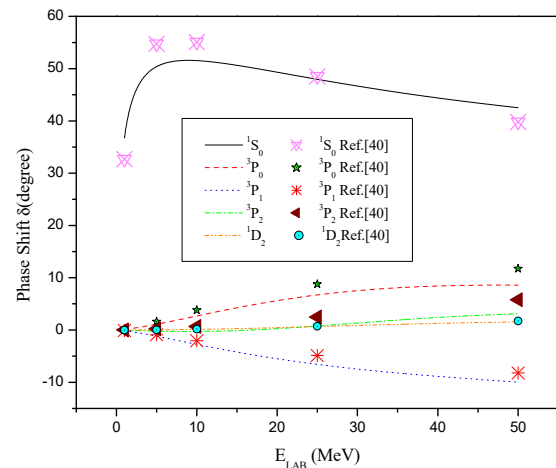


**Figure 4.** (p-p) S-P- and D-wave scattering phase shifts as a function of laboratory energy

And the (p-p) scattering phase shifts are presented in the Figure 4. From the figures of obtained results, one can see that our obtained phase shifts are in close agreement with the experimental results of Gross and Stadler [39] and Wiringa [40] data. Fig. 1 shows that the parameters for the  $^3S_1$  and  $^1S_0$  states from Table 1 for (n-p) system reproduces the close experimental phase parameter results of Ref. [39] up to laboratory energy 50 MeV. Similarly, Figs. 2 & 3 depict the phase shift values for the P- and D- wave states and show close agreement with the results of Ref. [39]. However, the P-wave states  $^3P_0$  and  $^3P_1$  show some deviation in phase shift around the laboratory energy of 25 MeV although the trend is exactly matching. Beyond 50 MeV, the phase shifts start differing significantly with the energy for the reason that with increasing energy, the reaction channels come into effect dominantly over the elastic channel. Also, for (p-p) scattering in Fig. 4, shows correct trend for different states with some deviation in the phase shift results with increasing laboratory energy. The difference in their numerical values is for the reason that nuclear potentials are highly state dependent and cannot be generated properly from any known interaction unlike atomic cases. And in our case, the potential is only the spherical central term without spin-dependence and tensor potential.

For the Shifted Deng Fan Potential (SDF) model scattering of the (n-p) and (p-p) systems, the interacting potential forms for all the partial wave states have been presented in Figs. 5- 8. It is an well-established fact that nuclear potentials are highly state dependent and therefore potentials for each different states of S-, P- and D- waves are shown in Figs. 5-8, against the variable 'r' for the (n-p) and (p-p) systems. From these figures, one can notice that the potentials are fully consistent with the phase shifts produced.

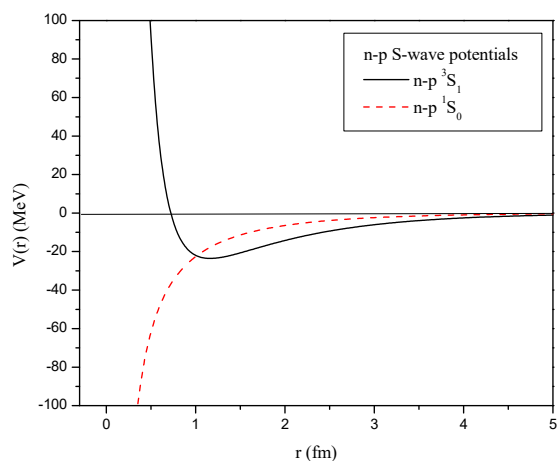


Figure 5. n-p S-wave potentials as a function of r

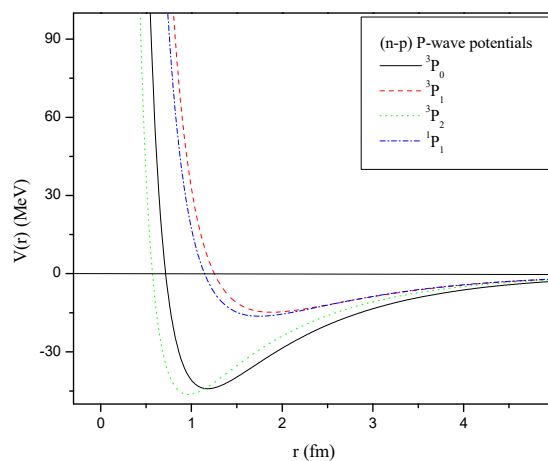


Figure 6. (n-p) P- wave potentials as a function of r

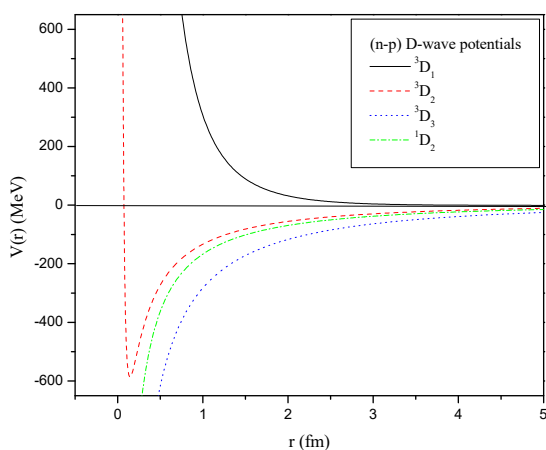


Figure 7. D- wave (n-p) potentials as a function of r

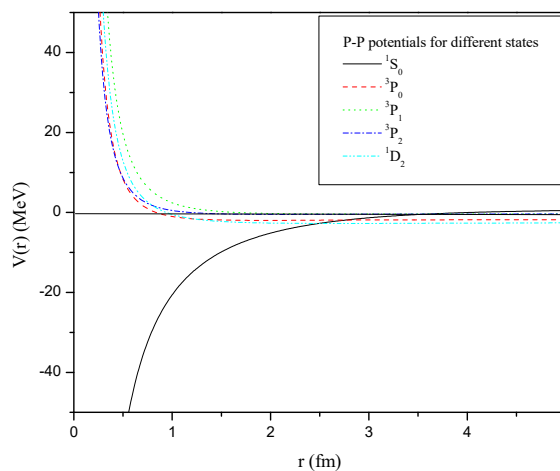


Figure 8. (p-p) potentials for different states as a function of r

#### 4. SCATTERING CROSS SECTION

In general, two particle interactions, a beam of particles is directed at a layer of matter. The effect of this layer is composed additively of the effects of the individual units and the individual nuclei act as independent scattering centers. Upon scattering, scattered current is uniformly distributed over a sphere of radius  $r$ . The cross section of a scattering is then defined as the ratio of number of events of a given type per unit time per nucleus to the number of incident particles per unit area per unit time [41,42]. The concept of cross section cannot be used if many scattering centers are taken to act coherently with incident ones. Scattering cross section in core of its idea is an effective area proportional to the intrinsic

rate at which a given radiation-target interaction occurs. Dimensionally cross section is an area with the base unit of barn ( $10^{-28}$  meter). We desire to investigate to what extent our SDF model calculations will be able to reproduce realistic cross section data in view of small discrepancies between the results of our phase shift analysis and of other calculations.

For combined coulomb and nuclear potential scattering as for charged particle interaction, the differential scattering amplitude is expressed as

$$f_{nC}(\theta) = f_C(\theta) + f_n(\theta), \tag{6}$$

where

$$f_C(\theta) = - \left\{ \frac{\eta}{2\chi \sin^2 \theta / 2} \right\} \exp \left[ -i\eta \ln \sin^2(\theta / 2) + 2i\sigma_0(\eta) \right], \tag{7}$$

and

$$f_n(\theta) = \frac{1}{2i\chi} \sum_{\ell=0}^{\infty} (2\ell + 1) \exp(2i\sigma_\ell(\eta)) P_\ell(\cos \theta) (\exp(2i\delta_\ell^n) - 1). \tag{8}$$

The quantity  $\delta_\ell^n$  is the Coulomb-distorted nuclear phase shift. The negative sign in front of Eq. (7) originates from the fact that the Coulomb force between two protons is repulsive. The Coulomb-distorted nuclear cross section  $\sigma_{nC}(\theta)$  is given by

$$\sigma_{nC}(\theta) = |f_C(\theta) + f_n(\theta)|^2 = |f_{nC}(\theta)|^2. \tag{10}$$

For identical particle, like (p-p), scattering

$$\sigma(\theta) = |f(\theta) + f(\pi - \theta)|^2. \tag{11}$$

One may calculate the total scattering cross section by integrating the differential cross section  $\sigma(\theta)$  over the entire solid angle and the angle integrated cross section is

$$\sigma_s = \frac{4\pi}{k^2} \sum_{L=0}^{\infty} (2L + 1) \sin^2 \delta_L, \tag{12}$$

where  $\delta_\ell$  is the total scattering phase shift.

Note that this integrated cross section is sometimes called the total cross section because it is the total after integration over all angles. The elastic scattering of neutrons by proton and proton by proton have been investigated by a number of researchers [43-48]. In the present text we calculate differential and total scattering cross sections for the (p-p) & (n-p) systems and compare them with the data [47- 48] available in the literature by exploiting Eqs. (7)- (12). The (p-p) differential cross sections are portrayed in Figs. 9 & 10 together with the Ref. [47] over the whole angular range. However, the experimental results [47] are available only up to angle  $50^\circ$ . We have obtained satisfying data from our calculation for two different laboratory energies of 6.141MeV and 9.918 MeV as shown in Figs. 9 &10 consecutively.

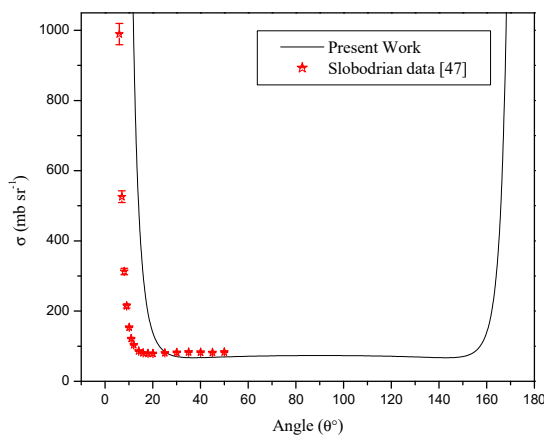


**Figure 9.** Differential p-p scattering cross section as a function of  $\theta$  at  $E_{\text{Lab}}=6.141$  MeV

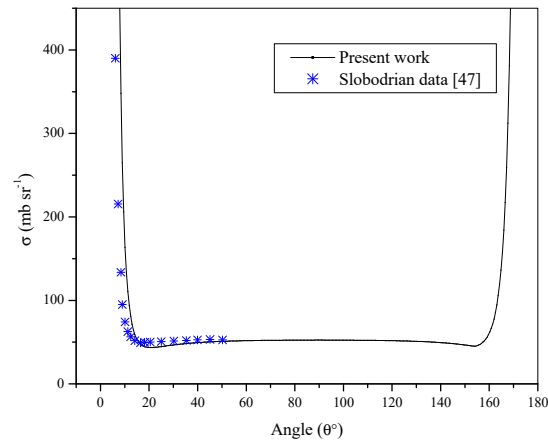


**Figure 10.** Differential p-p scattering cross section as a function of  $\theta$  at  $E_{\text{Lab}}=9.918$  MeV

The angular distributions for 6.141 MeV differ quantitatively in a narrow margin with those of Slobodrian et al. [47] up to angle  $20^\circ$  while for larger energy 9.918 MeV our results are in good conformity with Ref. [47]. Total cross section

results for both the systems (n-p) and (p-p) have been obtained up to laboratory energies of 50 MeV (Figs. 11 & 12) and compared with the experimental data [48].

The total cross section calculations are performed including the contributions of S, P and D waves for neutron-proton (n-p) and proton-proton (p-p) scattering systems. Our (n-p) cross sectional data are in excellent agreement with the Arndt data [48] while for (p-p) system it shows qualitative agreement but with a slight quantitative disagreement in the energy range 2- 20 MeV.

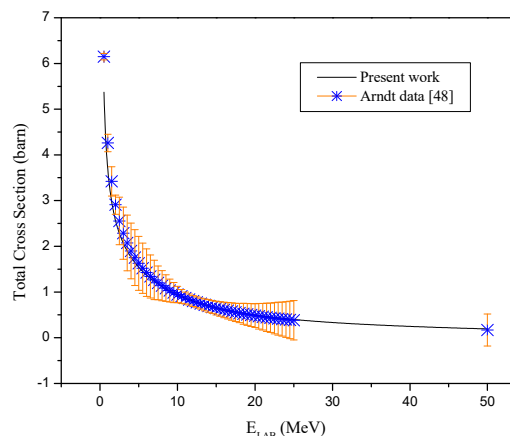


**Figure 11.** (n-p) total scattering cross section as a function of laboratory energy

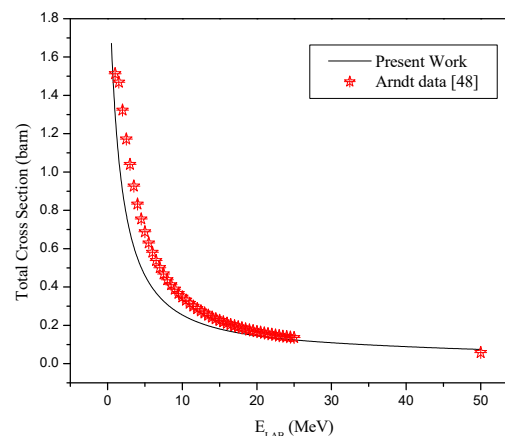


**Figure 12.** Total p-p scattering data with laboratory energy

## 5. CONCLUSIONS

We have parameterized the Shifted Deng Fan potential [23-25] for the phase shift parameters of the (n-p) and (p-p), spin independent, non-relativistic quantum nuclear scattering. Thus, obtained phase shifts along with the parameters are used to obtain total scattering cross section and differential scattering cross section values. Having obtained close agreements for scattering phase parameters with standard data of Gross and Stadler [38] & Wiringa [39], differential cross section data with Slobodrian [47], total cross section results with Arndt et al. [48], it is vivid that under standard PFM [27], Shifted Deng Fan potential (SDF) model scattering has the capability of producing the correct nature of phase shifts of respective states. And this simple minded, only three parameter attractive potential suffices to reproduce the most of the low energy nuclear interaction environment. In future, our group is aiming to explore this potential with other standard methodologies and several newer real scattering systems. We are hopeful that the present representation of the SDF potential in nuclear domain in the context of non-relativistic quantum scattering physics is expected to explore new possibilities.

## ORCID

© Bidhan Khirali, <https://orcid.org/0000-0001-7200-1828>; © Biswanath Swain, <https://orcid.org/0000-0002-9149-8857>  
 © Ujjwal Laha, <https://orcid.org/0000-0003-4544-2358>

## REFERENCES

- [1] C.L. Pekeris, “The Rotation-Vibration Coupling in Diatomic Molecules”, *Phys. Rev.* **45**, 98(1934), <https://doi.org/10.1103/PhysRev.45.98>
- [2] W.C. Qiang, and S.H. Dong, “Analytical approximations to the solutions of the Manning-Rosen potential with centrifugal term”, *Phys. Lett. A*, **363**, 169 (2007), <https://doi.org/10.1016/j.physleta.2007.03.057>
- [3] B. Khirali, A.K. Behera, J. Bhoi, and U. Laha, “Scattering with Manning-Rosen potential in all partial waves”, *Ann. Phys.* **412**, 168044 (2020), <https://doi.org/10.1016/j.aop.2019.168044>
- [4] L.D. Landau and E.M. Lifshitz, *Quantum Mechanics, Non-Relativistic Theory*, 3rd ed. (Pergamon, 1977).
- [5] R.L. Liboff, *Introductory Quantum Mechanics*, 4th ed. (Addison Wesley, San Francisco, 2003).
- [6] M.M. Nieto, “Hydrogen atom and relativistic pi-mesic atom in N-space dimensions”, *Am. J. Phys.* **47**, 1067 (1979), <https://doi.org/10.1119/1.11976>
- [7] Z.H. Deng, and Y.P. Fan, “A Potential Function of Diatomic Molecules”, *J. Shandong Univ. (Natural Sci.)* **1**, 162 (1957)
- [8] A.N. Ikot, H. Hassanabadi, B.H. Yazarloo, M.I. Umo, and S. Zarrinkamar, Dirac-Deng-Fan Problem with Coulomb-Hulthen Tensor Interactions, *Acta Phys. Polonica A*, **126**, 656 (2014), <https://doi.org/10.12693/APhysPolA.126.656>
- [9] K.J. Oyewumi, O.J. Oluwadare, K.D. Sen, and O.A. Babalola, “Bound state solutions of the Deng-Fan molecular potential with the Pekeris-type approximation using the Nikiforov-Uvarov (N-U) method”, *J. Math. Chem.* **51**(3), 976-991 (2013), <https://doi.org/10.1007/s10910-012-0123-6>
- [10] E. Maghsoodi, H. Hassanabadi, and S. Zarrinkamar, “Spectrum of Dirac equation under Deng-Fan scalar and vector potentials and a Coulomb tensor interaction by SUSYQM”, *Few-Body Syst.* **53**(3-4), 525-538 (2012), <https://doi.org/10.1007/s00601-012-0314-5>
- [11] S.H. Dong, *Factorization method in quantum mechanics Fundamental Theories in Physics*.150 (Springer, Netherlands, 2007). pp. 187-213.
- [12] O.J. Oluwadare, K.J. Oyewumi, C.O. Akoshile, and O.A. Babalola, “Approximate analytical solutions of the relativistic equations with the Deng-Fan molecular potential including a Pekeris-type approximation to the (pseudo) centrifugal term”, *Phys. Scr.* **86**, 035002 (2012), <https://doi.org/10.1088/0031-8949/86/03/035002>

- [13] A.D.S. Mesa, C. Quesne, and Y.F. Smirnov, “Generalized Morse potential: Symmetry and satellite potentials”, *J. Phys. A*, **31**, 321 (1998), <https://doi.org/10.1088/0305-4470/31/1/028>
- [14] K.J. Oyewumi, O.J. Oluwadare, K. D. Sen, and O.A. Babalola, “Bound state solutions of the Deng-Fan molecular potential with the Pekeris-type approximation using the Nikiforov-Uvarov (N-U) method”, *J. Math. Chem.* **51**, (2012) 976, <https://doi.org/10.1007/s10910-012-0123-6>
- [15] H. Hassanabadi, B.H. Yazarloo, S. Zarrinkamar, and H. Rahimov, “Deng-Fan potential for relativistic spinless particles - An ansatz solution”, *Commun. Theor. Phys.* **57** 339 (2012), <https://doi.org/10.1088/0253-6102/57/3/02>
- [16] S.H. Dong, “Relativistic Treatment of Spinless Particles Subject to a Rotating Deng-Fan Oscillator Relativistic Treatment of Spinless Particles Subject to a Rotating Deng-Fan Oscillator”, *Commun. Theor. Phys.* **55**, 969 (2011), <https://doi.org/10.1088/0253-6102/55/6/05>
- [17] J. Oluwadare, K.J. Oyewumi, and O.A. Babalola, “Exact s-wave solution of the Klein-Gordon equation with the Deng-Fan molecular potential using the Nikiforov-Uvarov (NU) Method”, *Afr. Rev. Phys.* **7**, 16 (2012). <http://aphysrev.ictp.it/index.php/aphysrev/article/download/543/236>
- [18] B.H. Yazarloo, L. Lu, G. Liu, S. Zarrinkamar, and H. Hassanabadi, “The nonrelativistic scattering states of the Deng-Fan potential”, *Adv. High Energy Phys.* **2013**, 317605 (2013), <https://doi.org/10.1155/2013/317605>
- [19] S.H. Dong, and X.Y. Gu, “Arbitrary l state solutions of the Schrödinger equation with the Deng-Fan molecular potential”, *J. Phys. Conf. Ser.* **96**, 012109 (2008), <https://doi.org/10.1088/1742-6596/96/1/012109>
- [20] Z. Rong, H.G. Kjaergaard, and M.L. Sage, “Comparison of the Morse and Deng-Fan potentials for X-H bonds in small molecules”, *Mol. Phys.* **101** 2285 (2003), <https://doi.org/10.1080/0026897031000137706>
- [21] L.H. Zhang, P. Li, and C.S. Jia, “Approximate analytical solutions of the Dirac equation with the generalized Morse potential model in the presence of the spin symmetry and pseudo-spin symmetry”, *Phys. Scr.* **80**, 035003 (2009), <https://doi.org/10.1088/0031-8949/80/03/035003>
- [22] S.M. Ikhdaïr, “An approximate  $\kappa$  state solutions of the Dirac equation for the generalized Morse potential under spin and pseudospin symmetry”, *J. Math. Phys.* **52** 052303 (2011), <https://doi.org/10.1063/1.3583553>
- [23] M. Hamzavi, S.M. Ikhdaïr, and K.E. Thylwe, “Equivalence of the empirical shifted Deng-Fan oscillator potential for diatomic molecules”, *J. Math. Chem.* **51**(1), 227-238 (2013), <https://doi.org/10.1007/s10910-012-0075-x>
- [24] H. Louis, B.I. Ita, P.I. Amos, O.U. Akakuru, M.M. Orosun, N.A. Nzeata-Ibe, and M. Philip, “Solutions to the Dirac Equation for Manning-Rosen Plus Shifted Deng-Fan Potential and Coulomb-Like Tensor Interaction Using Nikiforov-Uvarov Method”, *Int. J. Chem.* **10**, 3(2018), <https://doi.org/10.5539/ijc.v10n3p99>
- [25] M. Sajedi, and Z. Kargar, “Shifted Deng-Fan potential and cluster structure in  $^{19}\text{Ne}$ ”, *Nucl. Phys. A*, **1015**, 122314 (2021), <https://doi.org/10.1016/j.nuclphysa.2021.122314>
- [26] D. Saha, B. Khirali, B. Swain, and J. Bhoi, “Jost states for the Deng-Fan potential”, *Phys. Scr.* **98**, 015303 (2023), <https://doi.org/10.1088/1402-4896/aca1e6>
- [27] F. Calogero, *Variable Phase Approach to Potential Scattering* (New York: Academic 1967).
- [28] U. Laha, and J. Bhoi, “Higher partial-wave potentials from supersymmetry-inspired factorization and nucleon-nucleus elastic scattering”, *Phys. Rev. C - Nucl. Phys.* **91**, 034614(2015), <https://doi.org/10.1103/PhysRevC.91.034614>
- [29] J. Bhoi, R. Upadhyay, and U. Laha, “Parameterization of Nuclear Hulthén Potential for Nucleus-Nucleus Elastic Scattering”, *Commun. Theor. Phys.* **69**, 203–210 (2018), <https://doi.org/10.1088/0253-6102/69/2/203>
- [30] U. Laha, and J. Bhoi, “Parameterization of the nuclear Hulthén potentials”, *Phys. At. Nucl.* **79**, 62-66 (2016), <https://doi.org/10.1134/S1063778816010129>
- [31] A.K. Behera, U. Laha, M. Majumder, and J. Bhoi, “Energy-Momentum Dependent Potential and np Scattering”, *Research and Reviews: J. Phys.* **8**, 2265 (2019). <https://sciencejournals.stmjournals.in/index.php/RRJoPHY/article/view/2139>
- [32] A. K. Behera, J. Bhoi, U. Laha, and B. Khirali, “Study of nucleon – nucleon and alpha-nucleon elastic scattering by the Manning-Rosen potential”, *Commun. Theor. Phys.* **72**, 075301 (2020), <https://doi.org/10.1088/1572-9494/ab8a1a>
- [33] P. Sahoo, A. K. Behera, B. Khirali, and U. Laha, “Nuclear Hulthén potentials for F and G partial Waves”, *Research & Reviews: J. Phys.* **10**, 31-37 (2021), <https://doi.org/10.37591/RRJoPHY>
- [34] A.K. Behera, U. Laha, M. Majumder, and J. Bhoi, “Applicability of Phase-Equivalent Energy-Dependent Potential. Case Studies”, *Phys. At. Nucl.* **85**, 124-138 (2020), <https://doi.org/10.1134/S1063778822010057>
- [35] B. Talukdar, D. Chattarji, and P. Banerjee, “A generalized approach to the phase amplitude Method”, *J. Phys. G: Nucl. Phys.* **3**, 813–820 (1977), <https://doi.org/10.1088/0305-4616/3/6/012>
- [36] G.C. Sett, U. Laha, and B. Talukdar, “Phase function method for Coulomb -distorted nuclear Scattering”, *J. Phys. A: Math. Gen.* **21**, 3643-3657 (1999), <https://doi.org/10.1088/03054470/21/18/017>
- [37] U. Laha, A.K. Jana, and T.K. Nandi, “Phase-function method for Hulthén -modified Separable potentials”, *Pramana - J. Phys.* **37**(5), 387-393 (1991), <https://doi.org/10.1007/BF02848506>
- [38] J.M. Watson, *A Treatise on the Theory of Bessel Functions*, (Cambridge University Press, London, 1922).
- [39] F. Gross, and A. Stadler, “Covariant spectator theory of np scattering: Phase shifts obtained from precision fits to data below 350 MeV”, *Phys. Rev. C*, **78**, 014005 (2008), <https://doi.org/10.1103/PhysRevC.78.014005>
- [40] R.B. Wiringa, V.G.J. Stoks, and R. Schiavilla, “Accurate nucleon-nucleon potential with charge-independence breaking”, *Phys. Rev. C*, **51**, 38 (1995). <https://doi.org/10.1103/PhysRevC.51.38>
- [41] J.R Taylor, *Scattering Theory: The Quantum Theory of Nonrelativistic Collisions* (Dover Publications INC, New York, 2006).
- [42] R.G. Newton, *Scattering theory of Waves and Particles* (McGraw-Hill, New York, 1982).
- [43] C.L. Bailey, W.E. Bennett, T. Bergstrahl, R.G. Nuckolls, H.T. Richards, and J.H. Williams, “The neutron-proton and neutron-carbon scattering cross sections for fast Neutrons”, *Phys. Rev.* **70**, 583 (1946), <https://doi.org/10.1103/PhysRev.70.583>
- [44] F.F. Chen, C.P. Leavitt, and A.M. Shapiro, “Total p-p and “p-n” cross sections at cosmotron Energies”, *Phys. Rev.* **103**, 211 (1956), <https://doi.org/10.1103/PhysRev.103.211>
- [45] B.H. Daub, V. Henzl, M.A. Kovash, J.L. Matthews, Z.W. Miller, K. Shoniyozov, and H. Yang, “Measurements of the neutron-proton and neutron-carbon total cross section from 150 to 800 keV”, *Phys. Rev. C*, **87**, 014005 (2013), <https://doi.org/10.1103/PhysRevC.87.014005>

- [46] J.D. Jackson, and J.M. Blatt, “The interpretation of low energy proton-proton scattering”, Rev. Mod. Phys, **22**, 77 (1950), <https://doi.org/10.1103/RevModPhys.22.77>
- [47] R. J. Slobodrian, H.E. Conzett, E. Shield, and W.F. Tivol, “Proton-proton elastic scattering between 6 and 10 MeV”, Phys. Rev. **174**, 1122 (1968), <https://doi.org/10.1103/PhysRev.174.1122>
- [48] R.A. Arndt, W.J. Briscoe, A.B. Laptev, I.I. Strakovskiy, and R.L. Workman, “Absolute total np and pp cross-section determinations”, Nucl. Sci. Eng. **162**, 312 (2009), <https://doi.org/10.13182/NSE162-312>

**НУКЛОН-НУКЛОННЕ ПРУЖНЕ РОЗСІЯННЯ ПРИ РУСІ У ЗМІЩЕНОМУ ПОТЕНЦІАЛІ ДЕНГА-ФАНА**  
**Бідхан Хіралі, С. Лаха, Бісванат Суйейн, Уджвал Лаха**

*Факультет фізики, Національний технологічний інститут, Дзамшедпур, 831014, Індія*

Основна мета теорії розсіювання полягає в тому, щоб зрозуміти об'єкт, якщо щось в нього кинути. Можна дізнатися подробиці про об'єкт, спостерігаючи, як він відскакує від інших об'єктів. Потенціал, який існує між двома частинками, - це те, що ми прагнемо зрозуміти. У незалежному від часу підході до розсіювання передбачається, що падаючий промінь був активований протягом дуже тривалого часу і що вся система перебуває в стаціонарному стані. Для короткодіючих локальних потенціалів методологія змінної фази дуже корисна при розв'язанні задач квантово-механічного розсіювання. Методологія змінної фази/техніка фазової функції була явно використана для нерелятивістського явища нуклон-нуклонного розсіювання з фундаментальним центральним локальним потенційним членом і без спіно-орбітальної сили. Працюючи за цією методологією, фазові зсуви розсіювання, загальний переріз розсіювання та диференціальний переріз були досліджені для нової моделі ядерного потенціалу «зміщений потенціал Денга-Фана». Реальні нуклон-нуклонні системи розсіювання (n-p) і (p-p) були оброблені для цієї мети парціальними хвилями  $\ell = 2$  до в області низьких і помірних енергій. Для хвиль  $\ell > 0$  взаємодіючий бар'єрний потенціал відштовхування було включено в існуючу центральну частину. Наші результати для розглянутої потенційної моделі показують близьку конкуренцію з результатами експериментальних даних.

**Ключові слова:** *зміщений потенціал Денга-Фана; метод фазової функції; фазовий зсув розсіювання; перерізи розсіювання; (n-p) і (p-p) системи*

MODEL OF RADIATION-INDUCED MOTION OF LIQUID INCLUSIONS IN CRYSTAL<sup>†</sup>

 Oleksandr P. Kulyk<sup>a\*</sup>,  Oksana V. Podshyvalova<sup>b</sup>,  Mykhailo Yu. Shevchenko<sup>a,c</sup>,  
 Victor I. Tkachenko<sup>a,c,†</sup>,  Iryna V. Hariachevska<sup>a</sup>,  Toru Aoki<sup>d</sup>

<sup>a</sup>V.N. Karazin Kharkiv National University, 4 Svobody Sq., Kharkiv 61022, Ukraine

<sup>b</sup>National Aerospace University "Kharkiv Aviation Institute", 17 Chkalov St., Kharkiv 61070, Ukraine

<sup>c</sup>National Science Center "Kharkiv Institute of Physics and Technology", 1 Akademichna St., Kharkiv 61108, Ukraine

<sup>d</sup>Research Institute of Electronics, Shizuoka University, 3-5-1 Johoku, Naka-ku, Hamamatsu 432-8011, Japan

\*Corresponding author e-mail: [kulykop@gmail.com](mailto:kulykop@gmail.com)

<sup>†</sup>E-mail: [tkachenko.vikiv52@gmail.com](mailto:tkachenko.vikiv52@gmail.com)

Received July 10; revised August 19, 2023; accepted August 23, 2023

A physical model is formulated for the motion of liquid inclusions in a crystal in the field of forces caused by the presence of radiation point defects. The model is based on a statistical approach to the processes of induced transitions of structural elements of a crystalline matrix at the interfacial boundary with its solution. From the energy principle, an analytical dependence of the velocity of a spherical azimuthally symmetric inclusion on its size is obtained, considering the threshold nature of the motion. It is shown that the theoretical dependence correlates well with experimental results obtained for inclusions of aqueous saturated solution in potassium chloride crystals irradiated by high-energy electrons. The proposed model of the radiation-induced motion of a liquid inclusion is dynamic and allows us to interpret the nature of inclusion velocity changes in the crystal over time to determine the characteristic energy parameters of point defects.

**Keywords:** Crystal matrix; Point defects; Solution inclusion; Radiation-induced motion; Interfacial boundary; Statistical approach

**PhySH:** Surface & interfacial phenomena

The problem of radiation defect formation remains one of the most important topics in radiation damage physics and radiation materials science. Understanding the mechanisms of radiation defect formation in solids is necessary to increase the resistance of materials used in power generation or radioactive material storage, and to develop new materials (including nanostructured materials) with special properties that cannot be achieved by conventional synthesis methods (see [1] and references therein).

The problem of radiation defect formation also remains relevant for further improvement of technologies and methods for increasing the radiation resistance of semiconductor materials for various critical applications [2, 3], including the creation of X/γ-ray detectors (see [4, 5] and references in them).

At the same time, the problem of radiation defect formation has not been solved even for the simplest in-structure alkali halide crystals [6]. Although for more than a hundred years, alkali halide crystals, ionic systems with a simple electronic and crystal structure, have been model objects for studying radiation damage in materials caused by various types of radiation. It is known that irradiation of alkali metal halide crystals can produce Frenkel defect pairs in both the anionic and cationic sublattices. However, particular shockless formation mechanisms of Frenkel cation pairs (associated with the decay of various electronic excitations) remain unclear even today.

For many decades, alkali halide crystals have been topical objects not only for fundamental research but also for various applications. Optical media for recording and storing information, laser media, near-infrared light filters, thermoluminescent dosimeters, etc., have been proposed on their basis. [7]. One application of lithium fluoride, for example, is its use in the biological shielding of neutron-powered nuclear reactors. There are prospects for using lithium as an active element in thermonuclear fusion.

Our interest in the problem of the radiation defects formation and their subsequent dynamics during the thermal activation of alkali halide crystals in the medium temperature range (~300–600 K) is primarily due to the previously discovered effects of mass transfer on singular crystal faces modified by electron irradiation in vacuum [8] and in the process spontaneous migration of saturated solution inclusions in electron-irradiated water-soluble crystals (see [9] and references therein).

Study of surface mass transfer processes leading to elementary steps bunching is topical due to the need to obtain substrates for the production of low-dimensional structures (see [10–12] and references therein). And a study of motion and transformation of the shape of saturated solution inclusions in water-soluble crystals in the field of thermodynamic driving forces of various nature is of interest, in particular, for elucidating the mechanisms of crystallization under terrestrial conditions that exclude convective heat and mass transfer, which negatively affects the perfection of obtained crystals (see [13, 14] and references therein).

The purpose of this work is to construct a physical model of the motion of liquid inclusions in a crystal in the field of forces caused by the inhomogeneous distribution of radiation-induced point defects. As was shown earlier (see [9]

<sup>†</sup> **Cite as:** O.P. Kulyk, O.V. Podshyvalova, M.Yu. Shevchenko, V.I. Tkachenko, I.V. Hariachevska, T. Aoki, East Eur. J. Phys. 3, 570 (2023), <https://doi.org/10.26565/2312-4334-2023-3-67>

© O.P. Kulyk, O.V. Podshyvalova, M.Yu. Shevchenko, V.I. Tkachenko, I.V. Hariachevska, T. Aoki, 2023

and references therein), the presence of such thermodynamic nonequilibrium defects at a certain difference in their concentration can cause a chaotic inclusion motion at room temperatures under isothermal conditions. The presence of a dynamic model that adequately interprets the experimental data (including the time dependence of the inclusion velocity) may allow a better understanding of the radiation defect formation processes in alkali halide crystals.

**PROBLEM STATEMENT**

One of the experimentally detected features of the radiation-induced motion of liquid inclusions in crystals is the conservation of a rounded shape close to the equilibrium shape during their motion (see [9] and references therein).

Let us consider the case when the inclusion in the matrix has a spherical shape with a radius  $R_0$  (see Fig. 1). To describe such an inclusion shape, a spherical coordinate system is introduced:

$$x = r \sin(\theta) \cos(\varphi), \quad y = r \sin(\theta) \sin(\varphi), \quad z = r \cos(\theta), \tag{1}$$

where  $r = \sqrt{x^2 + y^2 + z^2}$ ,  $\cos(\theta) = zr^{-1}$ ,  $\text{tg}(\varphi) = yx^{-1}$ ,  $0 \leq r < \infty, 0 \leq \theta \leq \pi, 0 \leq \varphi \leq 2\pi$ .

For an azimuthal-symmetric inclusion, all unknown quantities do not depend on the angle  $\varphi$ , therefore one can assume  $\varphi = 0$  anywhere. Variables  $r$  and  $\theta$  remain independent. The gradient of inhomogeneity in the radiation defects density  $\rho(\vec{r})$  (see Fig. 1) is directed at a polar angle  $\theta = 0$ . Thus, on opposite hemispheres of the inclusion, the radiation defect density differs by a small amount  $\frac{\rho_2 - \rho_1}{\rho_2} \approx ((2\vec{R}_0)\vec{v}) \ll 1$ , that is, the following inequality can be considered valid:

$$\frac{\rho_2 - \rho_1}{\rho_2} \approx \frac{((\vec{R}_0)\vec{v}) \rho_2}{\rho_2} \ll 1.$$

On the other hand, one assumes that the density of defects is so high that the distance between them is small compared to the size of the inclusion in the direction of the crystal inhomogeneity. This condition is equivalent to inequality  $R_0 \sqrt[3]{\bar{\rho}} \gg 1$ , where  $\bar{\rho} = W_D^{-1} 2\pi \int_0^{\bar{R}} \int_0^\pi \rho(\vec{r}) r^2 dr \sin \theta d\theta$  is the average density of radiation defects in the crystal volume with radius  $\bar{R} \gg R_0$ .

Thus, to consider the macroscopic inclusion motion along the direction of radiation defect inhomogeneous distribution, the conditions have the following form:

$$(\sqrt[3]{\bar{\rho}})^{-1} \ll R_0 \ll \left( \frac{((\vec{R}_0)\vec{v}) \rho_2}{R_0 \rho_2} \right)^{-1}. \tag{2}$$

Figure 1 shows a schematic diagram of the inclusion in a crystal.

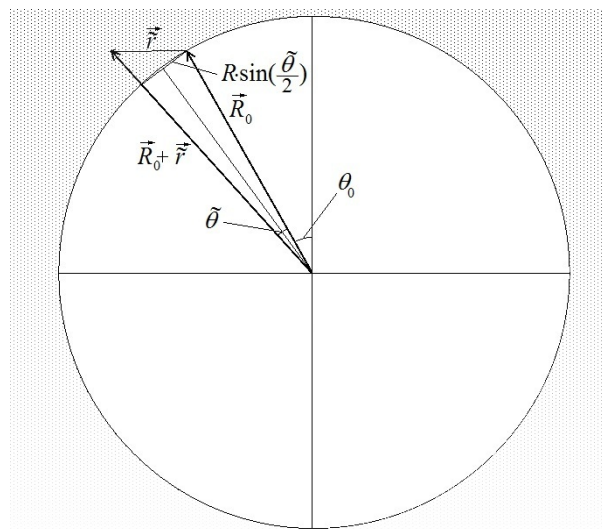


**Figure. 1.** Location diagram of a spherical azimuthally symmetric inclusion in a crystalline matrix.

The velocity of the spherical inclusion is assumed to be  $\vec{V}_0$ . To simplify the calculations, let us move to the reference frame where the inclusion is at rest. Then the velocities of the crystal matrix and the radiation defects are given in the form  $\vec{U}(R) = \vec{V}(R) - \vec{V}_0$ ,  $|\vec{V}_0| \geq |\vec{V}(R)|$ , where  $\vec{V}(R) = \vec{V}(R_0 + (R - R_0)\vartheta(R - R_0))$  is the velocity of

the spherical inclusion of radius  $R$ ,  $\vec{V}(R_0) = \vec{V}_0$  is the inclusion velocity corresponding to the inclusion size threshold value  $R_0$ , at which  $\vec{U} = 0$ . Here  $\vartheta(x)$  is a unit function of the form  $\vartheta(x < 0) = 0$ ;  $\vartheta(x \geq 0) = 1$ .

Thus, in the chosen reference frame, the crystal matrix with radiation defects either is at rest at  $R \leq R_0$  or moves in the negative axis  $\theta$  direction ( $\theta = \pi$ ) when the inclusion size is larger than the critical:  $R > R_0$ .

In the new frame of reference the crystal matrix moves with a velocity  $\vec{U}(R_0) = (U_r(R_0); U_\theta(R_0))$ , where  $U_r(R_0) = U_{r0} = \vec{U}(R_0)\vec{e}_r$ ,  $U_\theta(R_0) = U_{\theta0} = \vec{U}(R_0)\vec{e}_\theta$ ,  $\vec{e}_r, \vec{e}_\theta$  are unit vectors along the radial  $\vec{r}$  and polar  $\theta$  axes, respectively.

The inclusion in the crystal contains a solvent that facilitates stress relaxation in the crystal due to accelerated diffusion and transfer of the matrix material in the solvent from the front hemisphere to the back. At that, the experimental fact of the inclusion motion without a significant change in its shape indicates the transition of matrix atoms into solution from the front inclusion surface, and an equal to it deposition of atoms from the solution onto the matrix on the back inclusion surface.

Such processes of matrix atom dissolution and crystallization are observed only in the field of forces of inhomogeneously stressed crystal, to which radiation defect inhomogeneous distribution can be referred. Therefore, the inhomogeneous distribution of point defects can be considered as a force that initiates inclusion displacement.

The processes of matrix atom transitions into solution and back have a probabilistic nature. Therefore, a two-level system can be used to describe such transitions.

### STATISTICAL APPROACH

The processes occurring on the front and back surfaces of a spherical inclusion are similar to those observed when a crystal grows from a supersaturated solvent (vapor or liquid), or when it is dissolved in an unsaturated solvent [15-17]. Therefore, the previously developed models for describing such processes are also applicable to the description of the crystal inclusion motion, since they are based on the processes of crystal growth and dissolution.

The presence of a high defect density on the front inclusion surface makes the solvent unsaturated, and this surface dissolves. In turn, on the spherical inclusion back surface, where the defect density is lowered and the solvent is supersaturated, the growth is observed. Thus, the presence of a radiation defect density gradient causes the inclusion displacement in the direction of this gradient.

Let us consider a model that can explain the inclusion motion along the defect density gradient in a radiation-damaged crystal. In accordance with the above, the inclusion motion occurs in the direction of the axis  $\theta$ . In this model, the following statistical approach is used to describe the process of inclusion motion in the matrix.

The elementary processes of the matrix atom transitions into solution and back on the front inclusion surface will be considered in the concept of a two-level system shown in Fig. 2.

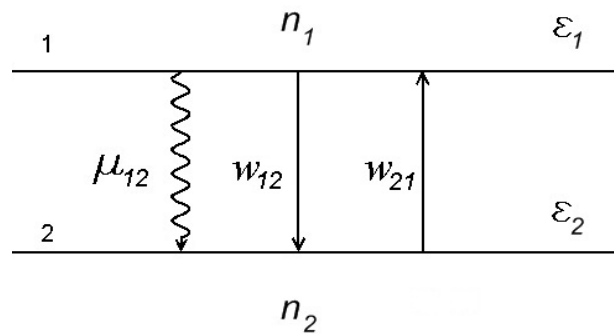


**Figure 2.** Scheme of a two-level system with populations  $n_1$  and  $n_2$ , energies  $\epsilon_1$  and  $\epsilon_2$ , transition probabilities:  $\mu_{12}$  – spontaneous,  $w_{12}$  and  $w_{21}$  – induced

In Fig. 2, the arrows show the directions of atom transitions from one level to another: spontaneous transitions with probability  $\mu_{12}$ , induced transitions with probabilities  $w_{12}$  and  $w_{21}$ . In Fig. 2, level 1 corresponds to the matrix atoms in the solvent, and level 2 corresponds to those held on the matrix surface.

In a stable crystal, when the difference in defect densities is less than the critical one, there is no inclusion motion. In this state, the difference between the free energies of an atom in the solvent and on the matrix surface is positive [18], i.e.  $\epsilon_1 > \epsilon_2$ .

Spontaneous transitions reduce the free energy of an atom in solution. Therefore, atoms spontaneously move from level 1 to level 2. The probability of spontaneous transitions  $\mu_{12}$  determines the probability of a spontaneous transition of an atom in 1 second. Spontaneous transitions from the upper level to the lower level ( $\epsilon_1 \rightarrow \epsilon_2$ ) are described by equations:

$$\frac{dn_1(t)}{dt} = -\mu_{12}n_1(t), \quad \frac{dn_2(t)}{dt} = \mu_{12}n_1(t), \quad (3)$$

where  $n_{1,2}(t)$  are the populations of levels 1, 2 as functions of time  $t$ ,  $\mu_{12}$  is the probability of spontaneous transition. Since the inclusion displacement is observed only when the defect density difference on its front and back surfaces is higher than the critical one, it is assumed that the probability of the induced transition  $w_{im}$  also depends on the externally created difference between the point defect densities on the front and back inclusion surfaces. Then the probability of induced transitions can be represented as:

$$w_{im} = \alpha_{im}(\rho(z_0 + c) - \rho(z_0)) = \frac{\alpha_{im}\beta}{a^2} W = \bar{w}_{im}N, \tag{4}$$

where indices  $i, m$  take values 1, 2, ( $i \neq m$ ),  $\alpha_{im}$  are constant values,  $W$  is the inclusion volume,  $\bar{w}_{im} = \frac{\alpha_{im}\beta}{a^2} W_0$  is the proportionality factor,  $W_0$  is the characteristic volume of a solvent molecule,  $N$  is the number of solvent atoms (molecules) in the inclusion volume.

At the initial moment, the number of solvent atoms is denoted by the value  $N(t)|_{t=0} \equiv N_0$ , and it is assumed to be sufficiently large, i.e.  $N_0 \gg n_{10}, n_{20}$ , where  $n_{10} = n_1(t)|_{t=0}$ ,  $n_{20} = n_2(t)|_{t=0}$ .

Consideration of induced processes caused by inhomogeneity of point defect density changes the form of the initial equations (4):

$$\frac{dn_1(t)}{dt} = -(\mu_{12} + \bar{w}_{12}N)n_1 + \bar{w}_{21}Nn_2, \quad \frac{dn_2(t)}{dt} = (\mu_{12} + \bar{w}_{12}N)n_1 - \bar{w}_{21}Nn_2. \tag{5}$$

Equation (6) should be supplemented by the equation for changing the solvent atom number  $N(t)$ , providing induced processes in the two-level system:

$$\frac{dN(t)}{dt} = -(\mu_{12} + \bar{w}_{12}N(t))n_1(t) + \bar{w}_{21}N(t)n_2(t). \tag{6}$$

From the condition of statistical equilibrium in a two-level system the Einstein relation follows  $-\mu_{12} = \bar{w}_{12} = \bar{w}_{21}$  [19, 18]. This relation, for the case when induced processes dominate over spontaneous ones ( $N_0 \gg n_{10}, n_{20}$ ), greatly simplifies the initial system of equations (5), (6):

$$\frac{dn_1(t)}{dt} = \mu_{12}(n_2(t) - n_1(t))N(t), \quad \frac{dn_2(t)}{dt} = -\mu_{12}(n_2(t) - n_1(t))N(t), \quad \frac{dN(t)}{dt} = -\mu_{12}(n_2(t) - n_1(t))N(t). \tag{7}$$

For spherically symmetric inclusions, the unknown quantities  $n_1, n_2, N, \mu_{12}$  in equations (7) become dependent on the coordinates  $R_0 + \tilde{r}, \theta_0 + \tilde{\theta}$ , where  $\tilde{r}$  and  $\tilde{\theta}$  correspond to a small ( $|\tilde{r}| \ll R_0, |\tilde{\theta}| \ll |\theta_0|$ ) deviation of the radius and polar angle from  $R_0$  and  $\theta_0$ , respectively.

Under these conditions, equations (7) are transformed to the form:

$$\begin{aligned} \frac{\partial n_1}{\partial t} + U_{r0} \frac{\partial n_1}{\partial \tilde{r}} + \frac{U_{\theta 0}}{R_0 + \tilde{r}} \frac{\partial n_1}{\partial \tilde{\theta}} &= \mu_{12}(n_2 - n_1)N, \\ \frac{\partial n_2}{\partial t} + U_{r0} \frac{\partial n_2}{\partial \tilde{r}} + \frac{U_{\theta 0}}{R_0 + \tilde{r}} \frac{\partial n_2}{\partial \tilde{\theta}} &= -\mu_{12}(n_2 - n_1)N, \\ \frac{\partial N}{\partial t} + U_{r0} \frac{\partial N}{\partial \tilde{r}} + \frac{U_{\theta 0}}{R_0 + \tilde{r}} \frac{\partial N}{\partial \tilde{\theta}} &= -\mu_{12}(n_2 - n_1)N, \end{aligned} \tag{8}$$

where  $\mu_{12}(R_0 + \tilde{r}, \theta_0 + \tilde{\theta})$  is the function of  $\tilde{r}$  and  $\tilde{\theta}$ .

Let us find solutions to equations (8) in the simple case when the probability of induced transitions  $\mu_{12}$  can be represented as an expansion in a Taylor series in small displacements  $\tilde{r}$  and  $\tilde{\theta}$  [20]:

$$\mu_{12}(R_0 + \tilde{r}, \theta_0 + \tilde{\theta}) \approx \mu_{12}(R_0, \theta_0) \times \left( 1 + \frac{1}{\mu_{12}(R_0, \theta_0)} \sum_{n=1}^{\infty} \frac{1}{n!} (\vec{\tilde{r}} \vec{\nabla})^n \mu_{12}(R_0, \theta_0) + \tilde{\theta} \lambda_{\theta} \right), \tag{9}$$

where  $\vec{\tilde{r}} = \tilde{r} \cdot \vec{e}_r + \tilde{r}_{\theta} \cdot \vec{e}_{\theta}$ ,  $\vec{\nabla} = \vec{e}_r \frac{\partial}{\partial \tilde{r}} + \vec{e}_{\theta} \frac{1}{R_0 + \tilde{r}} \frac{\partial}{\partial \tilde{\theta}}$ ,  $\tilde{r}_{\theta} = R_0 \cdot 2 \sin\left(\frac{\tilde{\theta}}{2}\right) \approx R_0 \cdot \tilde{\theta}$  (see Fig. 1). Further, in the calculations, the sign "  $\sim$  " is omitted.

Consider the case when expansion (9) contains only odd powers  $r$ . Then expression (9) takes the form:

$$\mu_{12}(R_0 + r, \theta_0 + \theta) \approx \mu_{12}(R_0, \theta_0) \times \left( 1 + \sum_{n=1}^2 \lambda_{r,2n-1} r^{2n-1} + \theta \lambda_{\theta} \right), \tag{10}$$

where  $\lambda_{r,2n-1} = \frac{1}{\mu_{12}(R_0, \theta_0)} \frac{1}{(2n-1)!} \frac{\partial^{2n-1} \mu_{12}(R_0, \theta_0)}{\partial r^{2n-1}}$ ,  $\lambda_\theta = \frac{1}{\mu_{12}(R_0, \theta_0)} \frac{\partial \mu_{12}(R_0, \theta_0)}{\partial \theta}$ . Choosing such a power dependence of the induced transition probability on  $r$  under the condition  $\lambda_{r,2n-1} > 0$  corresponds to the inclusion front surface, where the density of radiation defects increases with rising  $r$ . In this case, the matrix material dissolution is observed because the induced transition probability in the matrix is greater compared to the induced transition probability in the solution. This follows from the fact that the terms in (10) proportional to odd powers change sign, because in the solution  $r < 0$ .

On the back inclusion surface  $\lambda_{r,2n-1} < 0$ , and therefore the deposition of the dissolved crystal atoms on the matrix surface is observed, since the value of the probability of induced transitions in the matrix is less than in the solution.

Based on the type of expansion chosen in (10), a new variable is introduced  $\xi(t, r, \theta) = t + \frac{r^2 \lambda_{r,1}}{2U_{r0}} + \frac{r^4 \lambda_{r,3}}{4U_{r0}} + \frac{R_0 \theta^2 \lambda_\theta}{2U_{\theta0}}$ . Then equations (8) can be transformed to the form:

$$\frac{\partial n_1}{\partial \xi} = \mu(n_2 - n_1)N, \quad \frac{\partial n_2}{\partial \xi} = -\mu(n_2 - n_1)N, \quad \frac{\partial N}{\partial \xi} = -\mu(n_2 - n_1)N, \tag{11}$$

where, for simplification, the following notation is used  $\mu = \mu_{12}(R_0, \theta_0)$ .

The form of equation system (11) completely coincides with the form of equation system (7), with the only difference that the argument of system (11) is the function  $\xi(r, \theta, t)$ . Therefore, the solutions of system (11) coincide with the solutions of (7), where argument  $t$  must be replaced by argument  $\xi(r, \theta, t)$ , and  $\mu_{12}$  must be replaced by  $\mu$ .

### VELOCITY OF THE SPHERICAL AZIMUTHAL-SYMMETRIC INCLUSION

To determine the inclusion velocity  $V$ , the plane of constant phase is set. This plane is defined by:

$$\xi(t, r, \theta) = D \tag{12}$$

where  $D$  is the constant.

It follows from equation (12) that for a given time  $t = t_R$  and  $D = D_R$  it is possible to construct a second-order azimuthal-symmetric surface, which determines the dependence of its radial coordinate on  $r$  the polar angle  $\theta$ .

If one fixes  $D = D_R$ , then over time the azimuthal-symmetric surface of the second order moves in space together with the matrix with a velocity of  $U_R$ . This velocity is determined from the expression for the total time derivative of the equation (12):

$$1 + \frac{r \lambda_{r,1}}{U_{r0}} U_R + \frac{r^3 \lambda_{r,3}}{U_{r0}} U_R + \frac{R_0 \theta \lambda_\theta}{U_{\theta0}} \frac{1}{r} U_\theta = 0, \tag{13}$$

where  $U_R = \frac{dr}{dt}$  is the radial velocity of a constant phase surface,  $U_\theta = r \frac{d\theta}{dt}$  is the polar velocity of a constant phase surface.

The angular velocity of the constant phase surface is expressed in terms of the surface radial velocity, based on the following considerations. Since the matrix moves as a whole, and the spherical inclusion is at rest and does not change its shape, the polar velocity  $U_\theta$  of a point on its surface at  $\theta = \frac{\pi}{2}$  is equal to the radial velocity of a point on its surface at  $\theta = 0$ , i.e.  $U_\theta = U_R$ .

On this basis, it follows from (13):

$$U_R = - \frac{Ax}{B+x^2+Cx^4} \tag{14}$$

where  $x = \frac{r}{R_0}$ ,  $A = \frac{U_{r0}}{R_0 \lambda_{r,1}}$ ,  $B = \frac{\pi U_{r0} \lambda_\theta}{2 U_{\theta0} R_0 \lambda_{r,1}}$ ,  $C = \frac{R_0^2 \lambda_{r,3}}{\lambda_{r,1}}$ .

Assuming  $r = R$  in (14), the dependence of the matrix velocity on the spherical inclusion radius is obtained:

$$U_R = - \frac{Ax_R}{B+x_R^2+Cx_R^4}, \tag{15}$$

where  $x_R = R/R_0$ .

Expression (15) determines the matrix velocity in the frame of reference where the inclusion is at rest. In the laboratory frame of reference, where the matrix is at rest, the inclusion velocity has the opposite sign:

$$U'_R = \frac{Ax_R}{B+x_R^2+Cx_R^4}, \tag{16}$$

where the sign "-" already determines the inclusion velocity. Further, the sign "-" is omitted.

Since the inclusion motion is observed only at radii exceeding the threshold value of the inclusion radius  $R_0$ , it is possible to replace  $x_R \rightarrow x_R - 1$  in (16), which corresponds to the transition to the calculation of velocity dependence not on the inclusion radius  $R$ , but on its exceeding the threshold value.

Thus, taking into account the above replacement and equation (16), it follows that for small inclusion radii, when  $|x_R - 1| \ll 1$  and  $A > 0, B > 0$ , its velocity linearly increases as  $V_R \approx V_0 + \frac{A}{B}(x_R - 1)$  with increasing inclusion radius. As the inclusion radius increases, the velocity reaches a maximum value and then, at  $|x_R - 1| \gg 1$ , decreases as  $V_R \approx V_0 + \frac{A}{Cx_R^3}$ , where  $A > 0, C > 0$ .

### ENERGY INTERPRETATION OF THE INCLUSION VELOCITY

The spherical inclusion velocity  $U_R$  can be related to the matrix velocity  $U_{r0}$  using the energy relations.

The flow of point radiation defects with density  $\rho(z)$  creates a "wind" moving at speed  $U_R = U_{r0}$ . The wind pressure force of radiation defects on the inclusion is equal to the difference in pressure forces on its front and back hemispheres with an area of the order of  $S = \pi R_0^2$ :

$$F_D = C_w \frac{1}{2} (\rho_2 - \rho_1) m_D S U_{r0}^2 = C_w \frac{1}{2} \beta m_D W U_{r0}^2, \quad (17)$$

where  $m_D$  is the effective mass of a point defect,  $W = \pi R_0^3$  is the volume of the order of inclusion volume,  $C_w$  is the dimensionless resistance coefficient,  $\beta = \frac{\rho_2 - \rho_1}{R_0}$  is the density gradient of radiation defects,  $\rho_2, \rho_1$  are the radiation defect densities at the front and back poles of the spherical inclusion, respectively.

If the inclusion moves with velocity  $V'$  in the direction of the force (17), its velocity  $U_R$  is lower, and therefore the pressure force decreases:

$$F'_D = C_w \frac{1}{2} \beta m_D W (U_{r0} - V')^2. \quad (18)$$

The power produced by the pressure force (17) is equal to:

$$P_D = C_w \frac{1}{2} \beta m_D W (U_{r0} - V')^2 V'. \quad (19)$$

It follows from (19) that the maximum power is achieved at  $V' = \frac{U_{r0}}{3}$  [21], and is equal to:

$$P_D^{max} = \frac{4}{27} C_w \frac{1}{2} \beta m_D W U_{r0}^3. \quad (20)$$

The maximum power (20) is chosen based on the principle of least action, which determines the way of optimal stress relief in the crystal: the radiation stress of the crystal must be reset in the minimum time. The maximum power of the inclusion motion corresponds to the minimum time of stress relaxation in the crystal.

Thus, expression (20) determines the maximum power, which the inclusion gains by the wind of radiation defects blowing over it.

On the other hand, this power is spent on overcoming the resistance force  $F_R$ , which opposes the inclusion motion. The power expended to move an inclusion over a distance  $r(t + \Delta t) - r(t)$  in little time  $\Delta t$  is determined by the following expression:

$$P_R = F_R \lim_{\Delta t \rightarrow 0} \left( \frac{r(t + \Delta t) - r(t)}{\Delta t} \right) = F_R \left. \frac{dr}{dt} \right|_{\Delta t \rightarrow 0} = F_R \frac{Ax}{B + x^2 + Cx^4}, \quad (21)$$

where  $F_R = \kappa(U_{r0} - V') = \frac{2}{3} \kappa U_{r0}$  is the resistance force created by the inhomogeneity of the radiation defect density distribution and  $\kappa$  is the coefficient of proportionality.

From the equality  $P_D = P_R$ , the velocity of inclusion motion  $U_{r0}$  is defined, assuming that the coordinate  $r$  is equal to the coordinate of the front inclusion face  $r = R_0$ :

$$V = V_0 + F(x_R), \quad (22)$$

where  $F(x_R) = \frac{\delta x_R}{B + x_R^2 + Cx_R^4}$ ,  $\delta = \frac{4}{3} \frac{\kappa}{\beta m_D W R_0 \lambda_{r,1}}$ .

To determine the parameters  $V_0, A, B, C$  in (22), the experimental data [22] are used.

In Fig. 3, the solid line corresponds to the graph constructed using the analytical expression (22) and experimental data are shown with a marker  $\circ$ .

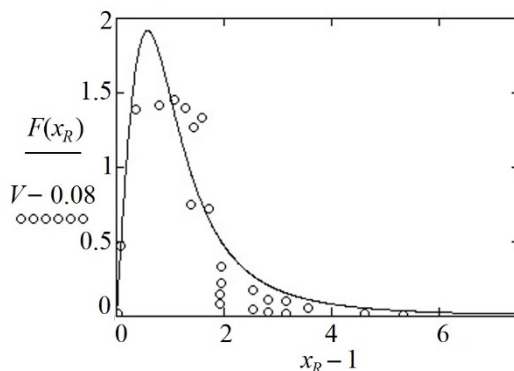


**Figure 3.** Dependence of the inclusion velocity on its longitudinal size (markers  $\circ$  correspond to experimental points),  $V_0 = 0.08 \cdot 10^{-10}$  m/s [22],  $\delta = 2.8$ ,  $B = 0.5$ ,  $C = 0.5$ .

Comparison of theoretical calculations with experimental data indicates an adequate description of the experiment by the proposed theoretical model.

### CONCLUSIONS

In the present work, a physical model of the liquid inclusion motion in the field of forces due to the inhomogeneous distribution of radiation point defects has been developed based on the statistical approach to the processes of induced transitions of matrix atoms into solution and back. The analytical dependence of the velocity of a spherical azimuthally symmetric inclusion on its size is obtained from the energy principle. It is shown that the analytical expression for the inclusion velocity describes the experimental results quite well. The proposed model of radiation-induced inclusion motion can be used to estimate the characteristic energy parameters of point defects inhomogeneously distributed in a crystalline medium.

### Acknowledgements

This research was partly supported by the 2023 (grants 2074 and 2076) Cooperative Research Projects at Research Institute of Electronics, Shizuoka University, Japan.

### ORCID

Oleksandr P. Kulyk, <https://orcid.org/0000-0002-7389-3888>; 
 Oksana V. Podshyvalova, <https://orcid.org/0000-0001-9680-9610>  
 Victor I. Tkachenko, <https://orcid.org/0000-0002-1108-5842>; 
 Iryna V. Hariachevska, <https://orcid.org/0000-0002-4630-9519>  
 Toru Aoki, <https://orcid.org/0000-0002-6107-3962>; 
 Mykhailo Yu. Shevchenko, <https://orcid.org/0009-0007-5811-0113>

### REFERENCES

- [1] N.A. Azarenkov, V.N. Vojevodin, V.G. Kirichenko, G.P. Kovtun, The Journal of Kharkiv National University, Physical series "Nucleus, Particles, Fields". 1(45) 887, 4 (2010), [http://nuclear.univer.kharkov.ua/lib/887\\_1\(45\)\\_10\\_p04-24.pdf](http://nuclear.univer.kharkov.ua/lib/887_1(45)_10_p04-24.pdf)
- [2] L.I. Barabash, I.N. Vishnevsky, A.A. Groza, A.Ya. Karpenko, P.G. Litovchenko, M.I. Starchik, Problems of Atomic Science and Technology. 2, 182 (2007), <https://vant.kipt.kharkov.ua/TABFRAME2.html>
- [3] A. Karmakar, J. Wang, J. Prinzie, V. Smedt, P. Leroux, Radiation. 1(3), 194 (2021), <https://doi.org/10.3390/radiation1030018>
- [4] V. Gnatyuk, O. Maslyanchuk, O. Kulyk, S. Shishiyanu, T. Aoki, Proceedings of SPIE, 12241, 122410M-1-8 (2022), <https://doi.org/10.1117/12.2633410>
- [5] V. Gnatyuk, S. Levytskyi, O. Maslyanchuk, O. Kulyk, T. Aoki, Proceedings of SPIE, 12126, 1212614-1-8 (2021), <https://doi.org/10.1117/12.2615569>
- [6] A. Lushchik, Ch. Lushchik, E. Vasil'chenko, A.I. Popov, Low Temperature Physics/Fizika Nizkikh Temperatur, 44(4), 357 (2018), <https://doi.org/10.1063/1.5030448>
- [7] N. Itoh, A.M. Stoneham, *Materials Modification by Electronic Excitation*, (Cambridge University Press, 2000), 520 p.
- [8] O.P. Kulyk, O.V. Podshyvalova, Bulletin of Kharkiv National Automobile and Highway University, 36, 91 (2007). (In Russian).
- [9] A.P. Kulik, O.V. Podshyvalova, and I.G. Marchenko, Problems of Atomic Science and Technology, 2(120), 13 (2019), [https://vant.kipt.kharkov.ua/ARTICLE/VANT\\_2019\\_2/article\\_2019\\_2\\_13.pdf](https://vant.kipt.kharkov.ua/ARTICLE/VANT_2019_2/article_2019_2_13.pdf)
- [10] O.P. Kulyk, V.I. Tkachenko, O.V. Podshyvalova, V.A. Gnatyuk, and T. Aoki, J. Cryst. Growth, 530, 125296-1-7 (2020), <https://doi.org/10.1016/j.jcrysgro.2019.125296>
- [11] O.L. Andrieieva, V.I. Tkachenko, O.P. Kulyk, O.V. Podshyvalova, V.A. Gnatyuk, T. Aoki, East European Journal of Physics, 4, 59 (2021), DOI: 10.26565/2312-4334-2021-4-06
- [12] O.P. Kulyk, O.V. Podshyvalova, O.L. Andrieieva, V.I. Tkachenko, V.A. Gnatyuk, T. Aoki, Problems of Atomic Science and Technology, 1(137), 154 (2022), <https://doi.org/10.46813/2022-137-154>
- [13] O.P. Kulyk, L.A. Bulavin, S.F. Skoromnaya, and V.I. Tkachenko, in: *Engineering for Sustainable Future. Inter-Academia 2019. Lecture Notes in Networks and Systems(LNNS)*, vol. 101, edited by A.R. Varkonyi-Koczy (Springer, Cham, 2020) pp. 326-339, [https://doi.org/10.1007/978-3-030-36841-8\\_32](https://doi.org/10.1007/978-3-030-36841-8_32)

- [14] O.P. Kulyk, V.I. Tkachenko, O.L. Andrieieva, O.V. Podshyvalova, V.A. Gnatyuk, T. Aoki, in: *Research and Education: Traditions and Innovations. INTER-ACADEMIA 2021. Lecture Notes in Networks and Systems*, vol. 422 (Springer, Singapore, 2022) pp. 141-158, [https://doi.org/10.1007/978-981-19-0379-3\\_14](https://doi.org/10.1007/978-981-19-0379-3_14)
- [15] Ya.E. Geguzin, and N.N. Ovcharenko, *Sov. Phys. Uspekhi*, **5**(1), 129 (1962), <https://dx.doi.org/10.1070/PU1962v005n01ABEH003403>
- [16] W.W. Mullins, *Journal of Applied Physics*, **30**(1), 77 (1959), <https://doi.org/10.1063/1.1734979>
- [17] Ya.E. Geguzin, Yu.S. Kaganovskij. *Diffusion Processes on a Crystal Surface*, (Ehnergoatomizdat, Moscow,1984), 128 p. (In Russian).
- [18] V.M. Kuklin, *The Journal of Kharkov National University, Physical series: Nuclei, Particles, Fields*, **933**(4/48), 4 (2010). (In Russian).
- [19] A. Einstein, *Physikalische Gesellschaft Zürich, Mitteilungen* **18**, 47 (1916).
- [20] H.B. Dwight, *Tables of Integrals and Other Mathematical Data*, 4th edition, (The Macmillan Company, 1961).
- [21] A. Betz, *Die Naturwissenschaften*, **XV**(46) 905 (1927).
- [22] V.S. Kruzhanov, O.V. Podshyvalova, *Sov. Solid State Physics*, **32**(2) 373 (1990). (In Russian).

#### МОДЕЛЬ РАДІАЦІЙНО-ІНДУКОВАНОГО РУХУ РІДКИХ ВКЛЮЧЕНЬ У КРИСТАЛІ

Олександр П. Кулик<sup>a</sup>, Оксана В. Подшивалова<sup>b</sup>, Михайло Ю. Шевченко<sup>a,c</sup>,

Віктор І. Ткаченко<sup>a,c</sup>, Ірина В. Гарячевська<sup>a</sup>, Тору Аокі<sup>d</sup>

<sup>a</sup>Харківський національний університет імені В.Н. Каразіна, Харків, Україна

<sup>b</sup>Національний аерокосмічний університет "Харківський авіаційний інститут", Харків, Україна

<sup>c</sup>ІНЦ "Харківський фізико-технічний інститут" НАН України, Харків, Україна

<sup>d</sup>Науково-дослідний інститут електроніки, Університет Шизуоки, Хамамацу, Японія

Сформульовано фізичну модель руху рідких включень у кристалі у полі сил, спричинених наявністю точкових дефектів радіаційного походження. В основу моделі покладено статистичний підхід до процесів індукованих переходів структурних елементів кристалічної матриці на міжфазній границі з власним розчином. З енергетичного принципу отримано аналітичну залежність швидкості сферичного азимутально-симетричного включення від його розміру, що враховує пороговий характер руху. Показано, що теоретична залежність добре корелює з експериментальними результатами, отриманими для включень насиченого водного розчину в кристалах хлориду калію, опромінених високоенергетичними електронами. Запропонована модель радіаційно-індукованого руху рідкого включення є динамічною і дозволяє інтерпретувати характер зміни швидкостей включень у кристалі у часі для визначення характерних енергетичних параметрів точкових дефектів.

**Ключові слова:** кристалічна матриця; точкові дефекти; включення розчину; радіаційно-індукований рух; міжфазна межа; статистичний підхід

## AMPLITUDES OF ${}^3\text{H}$ , ${}^3\text{He}$ TWO-PARTICLE PHOTO-BREAKUP IN NON-LOCAL QED APPROACH<sup>†</sup>

 Pylyp Kuznietsov<sup>a,b</sup>,  Yuriy A. Kasatkin<sup>b</sup>,  Vyacheslav F. Klepikov<sup>a,b</sup>

<sup>a</sup>*O.I. Akhiezer Department for Nuclear and High Energy Physics, V.N. Karazin Kharkiv National University,  
4 Svobody Sq., Kharkiv, 61022, Ukraine*

<sup>b</sup>*Institute of Electrophysics & Radiation Technologies National Academy of Sciences of Ukraine  
61002, Ukraine, Kharkiv, Chernyshevsky St, 28, P.O. Box 8812*

\*Corresponding Author e-mail: [kuznietsov@karazin.ua](mailto:kuznietsov@karazin.ua)

Received July 11, 2023; revised August 20, 2023; accepted August 25, 2023

Three-nucleon systems are essential for the investigation of many-body forces in nuclear physics. Well-grounded parametrization of their vertex functions with further application for the calculation of cross-sections in nonlocal QED approach provides the ground for investigation of the variety of multi-particle systems. In present paper we describe the process of parametrization of two-particle photo-breakup amplitudes of three-nucleon systems ( ${}^3\text{H}$ ,  ${}^3\text{He}$ ). We provide the general description of the wave function construction for three-nucleon systems as well as the parametrization of their vertex functions accounting two- and three-nucleon interactions based on meson exchange current formalism. In our calculations we account first and second order one-pion exchange terms and the term related to the exchange of  $\omega$  and  $\rho$  mesons. The three-nucleon interaction potential is given as a sum of attraction (two-pion exchange) term and appropriate repulsive part. Based on the variational "Urbana + Model VII" amplitudes we provide the results for energy dependence of differential cross-section of  ${}^3\text{He}(\gamma, p)d$  reaction at proton angle  $\theta = 90^\circ$  from the threshold up to  $E_\gamma = 40$  MeV and compare theoretical predictions with the available experimental data. The investigation is also provided for angular cross-section distributions at high photon energies ( $E_\gamma = 305 \pm 5$  MeV;  $365 \pm 5$  MeV;  $450 \pm 10$  MeV and  $675 \pm 50$  MeV). Correct description of  ${}^3\text{H}$ ,  ${}^3\text{He}$  photo-disintegration processes in a unified approach based on the gauge nature of the electromagnetic field implies application of this model for other multi-particle systems.

**Keywords:** *Three-nucleon system; Photo-breakup; Cross-section; Amplitude; Many-body force; Meson-exchange current*

**PACS:** 24.10.Cn, 25.20.-x

### 1. INTRODUCTION

The main goal of studying multi-particle systems in nuclear physics is to obtain the most complete description of the interactions between nucleons. This question is still open, while the charge independence of nuclear forces is a well-established fact both at low and high energies. In most cases, theoretical methods applied to multi-particle systems are extensions of the well-studied two-body problem. The most sensitive candidate for obtaining information about pure nuclear interactions is the binding energy of the tritium and helium-3 nuclei. Such information can be obtained through the study of three-nucleon systems in the presence of electromagnetic and weak interactions. In other words, one of the sources of information about sub-nuclear interactions is the electromagnetic breakup processes and the investigation of momentum distributions of constituent sets corresponding to different structural levels of matter. It's worth noting that a satisfactory analytical expression for the nuclear potential, covering the entire energy scale inside the nucleus, currently does not exist. At this stage, questions arise about the construction of the wave function components, which can be addressed based on the meson-exchange current (MEC) formalism.

Three-body systems are the simplest multi-particle systems. Essentially, they don't have a simple analytical solution (as in the two-body case) and their behavior cannot be predicted using statistical methods (as in the multi-particle case). Extending the two-body approximation to the three-body case can provide qualitative information about the importance and nature of three-body forces. The idea that there might exist a force between three bodies that cannot be represented as a sum of two-body interactions has no analogy in classical physics. However, there are indications that three-body forces might play an important role in nuclear physics. For instance, Brown and Green [1] in 1969 suggested that about 2 MeV of nuclear binding energy arises due to the presence of a specific multi-particle force. There are indications that the contribution of three-body forces to the behavior of strongly interacting three-nucleon systems must be significant, particularly proportional to the magnitude of the recoil in the ground state when the emitted particle has electromagnetic nature.

<sup>†</sup>*Cite as:* P. Kuznietsov, Yu.A. Kasatkin, V.F. Klepikov, East Eur. J. Phys. 3, 578 (2023), <https://doi.org/10.26565/2312-4334-2023-3-68>

## 2. CONSTRUCTING THE WAVE FUNCTION OF A THREE-NUCLEON SYSTEM

The usual spin and isospin dependence of nuclear forces in three-particle systems introduces algebraic issues that can be easily overcome. On the other hand, the short-range nature of nuclear interactions incorporates a more complex problem, which involves approximating complex wave functions with trial functions that have a simple analytical expression.

The presence of non-central forces significantly complicates the wave function of a three-nucleon system. In reality, for such systems, there are only three absolute quantum numbers. These are the quantum number of total angular momentum ( $J = 1/2$ ), parity ( $\uparrow\uparrow$ ), and isospin ( $T = 1/2$ ). However, if central forces are represented as a "mixture" of usual (Wigner) and spatial-exchange (Majorana) forces, then permutations of spatial positions of particles within the nucleus are allowed. These generate additional quantum numbers associated with the invariance of the wave function with respect to such permutations. A three-nucleon system can have only three such quantum numbers (three irreducible representations of the permutation group of three objects). There are completely symmetric, completely anti-symmetric, and one "mixed" representation.

Thus, the charge independence of nuclear forces yields three possible states  $^2S_{1/2}$ . The dominant state for a three-nucleon system under the influence of central forces is the symmetric  $S$ -state (with a probability of around 90%), such that  $L = 0$ ,  $S = 1/2$  and the wave function is fully symmetric. In this work, we will limit our consideration to this state. In turn, the "mixed" state is typically denoted as  $S'$ . The probability of this state does not exceed 1-2%.

For three-particle systems, the theory starts with 9 coordinates describing the position of each of the three particles  $\mathbf{r}_1(x_1, y_1, z_1)$ ,  $\mathbf{r}_2(x_2, y_2, z_2)$ ,  $\mathbf{r}_3(x_3, y_3, z_3)$ . The center-of-mass symmetry reduces the task to 6 coordinates. These coordinates are defining the size and shape of the triangle formed by the three nucleons. For instance, these could be the three sides of the triangle ( $r_{12}, r_{23}, r_{31}$ ) and the three Euler angles ( $\alpha, \beta, \gamma$ ), determining the orientation of this triangle in space relative to some standard orientation. Invoking symmetry groups eliminates the need to write explicit angular dependence in wave functions. This leads to transitioning from a set of six independent partial differential equations to a set of sixteen coupled equations involving only three independent variables. It's evident, that finding the solution for such a set of equations inevitably leads to the application of variational calculus.

Based on the above, the wave function of the ground state should be written as a sum of products, each containing three factors: inner wave function (A factor depending on the lengths of the triangle sides); angular" part of the wave function ( factor depending on the Euler angles, determining the triangle's position in space); "spin-isospin" part of the wave function (A factor depending on the spin and isospin functions of each nucleon). At present paper we attempt to define the first two parts of the total wave function, as long as the second and third factors can be combined using Clebsch-Gordan coefficients into a single term.

For the triangle sides, the following notations can be used:  $x_1 = r_{23}$ ;  $x_2 = r_{31}$ ;  $x_3 = r_{12}$ . Permutation of particles 1 and 2 leads to the permutation of  $x_1 \rightarrow r_{31} = x_2$ ,  $x_2 \rightarrow r_{23} = x_1$ , while leaving unchanged  $x_3 \rightarrow r_{12} = x_3$ . Thus, the permutation of particles corresponds to the permutations between  $x_1; x_2; x_3$ . An arbitrary function  $f(x_1, x_2, x_3)$  can be symmetric, antisymmetric, or can belong to a mixed representation of the permutation group of three objects. In the simplest case, when there's only one function  $u(x)$ , we can create only a symmetric function of the product  $f(x_1, x_2, x_3) = u(x_1)u(x_2)u(x_3)$ . Having two functions  $u(x)$  and  $v(x)$  allows creating both symmetric and "mixed" states. An example of such a state can be found in [19]. Finally, with 3 functions, one can create a state:

$$f(x_1, x_2, x_3) = \det \begin{bmatrix} u(x_1) & u(x_2) & u(x_3) \\ v(x_1) & v(x_2) & v(x_3) \\ w(x_1) & w(x_2) & w(x_3) \end{bmatrix} \quad (1)$$

which refutes the assertion that there is no antisymmetric  $S$ -function for three-nucleon systems. However, there is an evidence [2] that such a state is not observed in the ground state of a three-nucleon system.

## 3. PARAMETERIZATION OF THREE-NUCLEON SYSTEM VERTEX FUNCTIONS

To parameterize the vertices of strong interaction, we follow the works [4], [5] where for the nuclei  $^3\text{H}$  and  $^3\text{He}$  the results of variational calculations are presented for "Urbana+Model VII" and "Argonne+Model VII", as well as Faddeev calculations for the "Argonne+Model VII".

We start from the solution of 3-body Schrödinger equation:

$$H\Psi = E\Psi \quad (2)$$

$$H = \sum_{i=1,3} -\frac{\hbar^2}{2m} \nabla_i^2 + \sum_{i<j\leq 3} v_{ij} + \sum_{i<j<k\leq 3} V_{ijk} \quad (3)$$

where the potentials  $v_{ij}$  and  $V_{ijk}$  describe the two- and three-nucleon interactions, respectively. In many-body calculations for nuclei and nuclear matter, two-nucleon interactions are commonly expressed in the form of an operator:

$$v_{ij} = \sum_p v^p(r_{ij})O_{ij}^p \tag{4}$$

where  $v^p(r_{ij})$  are functions of distances between particles, and  $O_{ij}^p$  is represented as a set of operators. The model currently takes into account fourteen different operators. For the radial functions, we use the expansion:

$$v^p(r_{ij}) = v_\pi^p(r_{ij}) + v_I^p(r_{ij}) + v_S^p(r_{ij}) \tag{5}$$

which includes one-pion exchange in the first and second-order (terms  $v_\pi^p(r_{ij}); v_I^p(r_{ij})$ ) as well as exchange of  $\omega$  and  $\rho$  mesons (term  $v_S^p(r_{ij})$ ). For one-pion exchange in the first order the non-zero terms are related only to  $(\sigma_i\sigma_j)(\tau_i\tau_j)$  and  $\mathbf{S}_{ij}(\tau_i\tau_j)$  operators. They are chosen as:

$$v_\pi^{(\sigma_i\sigma_j)(\tau_i\tau_j)}(r) = 3.488 \frac{e^{-\mu r}}{\mu r} (1 - e^{-cr^2}) \tag{6}$$

$$v_\pi^{\mathbf{S}_{ij}(\tau_i\tau_j)}(r) = 3.488 \left(1 + \frac{3}{\mu r} + \frac{3}{(\mu r)^2}\right) \frac{e^{-\mu r}}{\mu r} (1 - e^{-cr^2})^2 \tag{7}$$

where  $\mu = 0.7 fm^{-1}$ . We note that selecting the multiplier  $(1 - e^{-cr^2})^2$  stimulates the  $\rho$ -meson exchange effect. Denoting  $\frac{e^{-\mu r}}{\mu r} (1 - e^{-cr^2})^2 = Y_\pi(r)$  and  $(1 + \frac{3}{\mu r} + \frac{3}{(\mu r)^2}) \frac{e^{-\mu r}}{\mu r} (1 - e^{-cr^2})^2 = T_\pi(r)$  the potentials for one-pion exchange in the first order can be rewritten as:

$$v_\pi^{(\sigma_i\sigma_j)(\tau_i\tau_j)}(r) = 3.488 Y_\pi(r) \tag{8}$$

$$v_\pi^{\mathbf{S}_{ij}(\tau_i\tau_j)}(r) = 3.488 T_\pi(r) \tag{9}$$

One-pion exchange in the second order is chosen in form:

$$v_I^P(r) = I_i^p T_\pi^2(r) \tag{10}$$

Such a choice of  $v_I^P$  facilitates accounting of three-nucleon interactions.

The exchange of  $\omega$  and  $\rho$  mesons is taken as a sum of two Woods-Saxon potentials. This choice is dictated by the fact that the size of nucleons must be at least of the order of the Compton wavelength of  $\omega$  and  $\rho$  mesons. Thus:

$$v_S^P(r) = S^p W(r) + S'^p W'(r) \tag{11}$$

where  $W(r) = \frac{1}{1+e^{\frac{r-R}{a}}}$  and  $W'(r) = \frac{1}{1+e^{\frac{r-R'}{a'}}}$ . The values of parameters  $c, I^p, S^p, S'^p$  are obtained from phase shift analysis and presented in [7].

Three-nucleon interactions are described by the potential  $V_{ijk}$ . It's expressed as:

$$V_{ijk} = V_{ijk}^{FM} + V_{ijk}^R \tag{12}$$

where  $V_{ijk}^{FM}$  is the Fujita-Miyazawa three-nucleon interaction potential due to a two-pion exchange. It describes attraction and can be written as:

$$V_{ijk}^{FM} = \sum_{cyc} -0.0333 \{(\tau_i\tau_j), (\tau_i\tau_k)\} \{x_{ij}, x_{ik}\} + \frac{1}{4} [(\tau_i\tau_j), (\tau_i\tau_k)] [x_{ij}, x_{ik}] \tag{13}$$

where  $x_{ij} = S_{ij} T_\pi(r_{ij}) + (\sigma_i\sigma_j) Y_\pi(r_{ij})$ . In turn,  $V_{ijk}^R$  describes repulsion and is expressed as:

$$V_{ijk}^R = \sum_{cyc} U_0 T_\pi^2(r_{ij}) T_\pi^2(r_{ik}) \tag{14}$$

where the coefficient  $U_0 = 0.0038$ .

All calculations are performed using the Monte Carlo simulation method based on realistic Hamiltonians that consider both two-nucleon and three-nucleon interactions. These Hamiltonians provide satisfactory binding energies and densities for light nuclei and nuclear matter. We mark that the results of calculations for  $d + p$  momentum distributions in  ${}^3\text{He}$  nucleus at low momentum transfers are in good agreement with the results of electron scattering analysis in the plane-wave impulse approximation. However, the values observed at high momentum transfers are slightly larger for the chosen approach.

The variational wave function  $\Psi_v$  is expressed as a symmetric product of correlation operators. Indeed, in the case of central forces, the ground state is the S-state, which is described by a spherically symmetric wave function. The ground  ${}^2S_1$  state is symmetric with respect to the spatial coordinates of the nucleon pair and anti-symmetric with respect to their spins. It has the form:

$$\Psi_v = \{S \prod_{i<j} f^c(r_{ij})(1 + \sum_p (\prod_{k \neq j} f_{ijk}^p) u^p(r_{ij}) O_{ij}^p)\} \Phi \quad (15)$$

where  $S$  is symmetrizer, and the factor  $\prod_{k \neq j} f_{ijk}^p$  reflects the effect from other particles in  $u^p$ . Correlations induced by the Coulomb potential are neglected, so  $F_{ij} = f^c(r_{ij})(1 + \sum_p u^p(r_{ij}) O_{ij}^p)$  are identical for  ${}^3\text{He}$  and  ${}^3\text{H}$  nuclei. The pair correlation  $F_{ij}$  can be rewritten as:

$$F_{ij} = f_{ij}^c(1 + u^\sigma(r_{ij})\sigma_i\sigma_j + u^{t\tau}(r_{ij})S_{ij}\tau_i\tau_j). \quad (16)$$

It contains central  $f_{ij}^c$ , tensor  $u^{t\tau}(r_{ij})$ , and spin  $u^\sigma(r_{ij})$  correlations.

The behavior of correlation functions at large  $r$  in three-nucleon systems is determined by considering the decay of the investigated nucleus. For instance, denoting  $R$  as the distance between selected nucleon and the center of mass of the system and considering the wave function in the region where  $R$  is large, the wave function for  ${}^3H \rightarrow d + n$  is determined from the formula:

$$\Psi(d+n; R \rightarrow \infty) = \frac{e^{-k'R}}{R} [Y_{0\frac{1}{2}}^{\frac{1}{2}\frac{1}{2}} + x(1 + \frac{3}{K'r} + \frac{3}{(K'r)^2})Y_{2\frac{3}{2}}^{\frac{1}{2}\frac{1}{2}}] \quad (17)$$

where  $x$  is asymptotic ratio of  $D$ -wave and  $S$ -wave,  $K'$  can be found from the equation  $\frac{3\hbar}{4m}K'^2 = E_d - E_t$  and  $Y_{JM}^{LS}$  represent spin and angular wave functions.

The dependence of the variational wave function at large  $R$  is given by:

$$\Psi_v(d+n; R \rightarrow \infty) = [f^c(R)]^2 \{ [1 - 4u^\sigma(R)]Y_{0\frac{1}{2}}^{\frac{1}{2}\frac{1}{2}} + u^{t\tau}(R)Y_{2\frac{3}{2}}^{\frac{1}{2}\frac{1}{2}} \} \quad (18)$$

assuming three-particle  $f_{ijk}^p$  factor to be unity.

By comparing (17) and (18) we finally obtain  $f^c(r \rightarrow \infty)$ ,  $u^\sigma(r \rightarrow \infty)$  and  $u^{t\tau}(r \rightarrow \infty)$ . The explicit forms of the spin and angular wave functions:  $Y_{0\frac{1}{2}}^{\frac{1}{2}\frac{1}{2}}$  and  $Y_{3\frac{3}{2}}^{\frac{1}{2}\frac{1}{2}}$  are taken from [2].

#### 4. RESULTS AND DISCUSSION

Denoting  $\Psi_2(m_d, \mathbf{r}_1)$  as the wave function of the deuteron with spin projection  $m_d$ , and  $\Psi_3(m_3, t_3)$  as the ground state of the three-nucleon system with spin and isospin projections  $m_3$  and  $t_3$  we can define the two-particle amplitude  $A_{dp}(m_d, m_p, m_3, \mathbf{k})$  as follows:

$$A_{dp}(m_d, m_p, m_3, \mathbf{k}) = \sqrt{\frac{3}{N_1 N_2}} \int d\mathbf{r}_1 \dots d\mathbf{r}_3 \Psi_2^\dagger(m_d, \mathbf{r}_{12}) \chi^\dagger(3, m_p, \frac{1}{2}) e^{-i\mathbf{k}(\mathbf{r}_3 - \mathbf{R}_{12})} \Psi_3(m_3, \frac{1}{2}) \quad (19)$$

The square of the amplitude gives the probability of the deuteron and proton to be in states  $m_d$  and  $m_p$  and a relative momentum  $\mathbf{k}$  in the ground state of  ${}^3\text{He}$ . In formula (19) the effect of antisymmetrization of the  $d+p$  state is contained in the multiplier  $\sqrt{3}$ . Antisymmetrization introduces a factor  $\sqrt{\frac{1}{3}}$  for the normalization and a factor of 3, which takes into account that any nucleon number can act as a proton. Expanding plane waves using Bessel functions, we obtain:

$$A_{dp}(m_d, m_p, m_3, \mathbf{k}) = \sum_{l,m} (-i)^l A_{dp}^{lm}(m_d, m_p, m_3, k) Y_{lm}(\mathbf{k}) \quad (20)$$

The angle averaged  $d+p$  momentum distribution in  ${}^3\text{He}$  is given by:

$$N_{dp}(k) = \frac{1}{4\pi} \sum_{m_d, m_p, l, m} |A_{dp}^{lm}(m_d, m_p, m_3, k)|^2 \quad (21)$$

The results of the calculations of the two-particle amplitudes are taken from [4]. In general, it's evident that variational and Faddeev calculations yield quite similar results. This fact points to the equivalence of Faddeev and variational calculations. However, we note that a slight difference in momentum distributions obtained from the Urbana and Argonne models is primarily due to the difference in radii obtained in these models. Nevertheless, the binding energy is not very sensitive to changes in radius, and therefore the accuracy

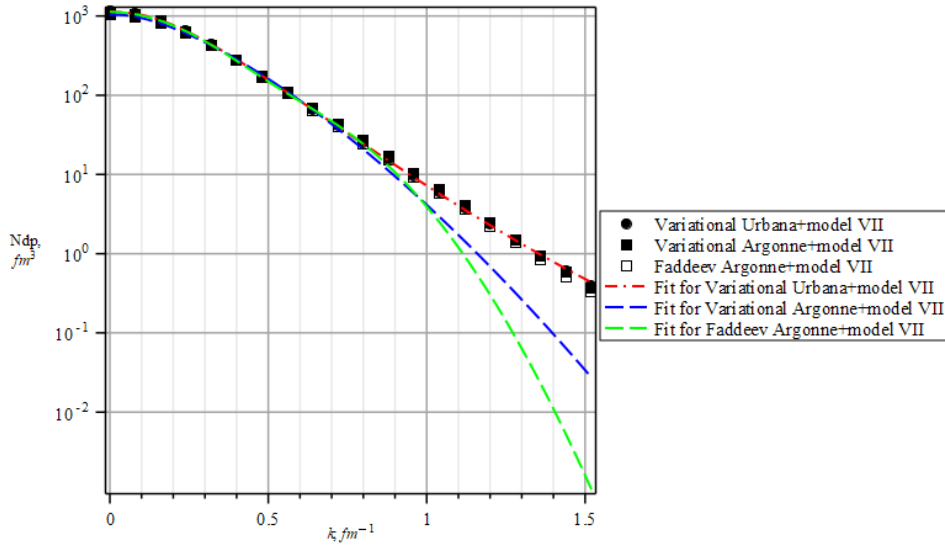


Figure 1.  ${}^3\text{He}$  two-body  $N_{dp}$  amplitudes in  $\text{fm}^3$ .

of variational calculations for computed radius is not very high. The error in the calculations is comparable to the difference between the radii obtained from different models, which suggests that differences in results between the two models are only related to approximation in the calculations. Here we present the results of calculations with the variational "Urbana+Model VII" and "Argonne+Model VII" and for Faddeev calculations in "Argonne+Model VII" amplitude  $N_{dp}$  of  ${}^3\text{He}$  plotted on Figure 1.

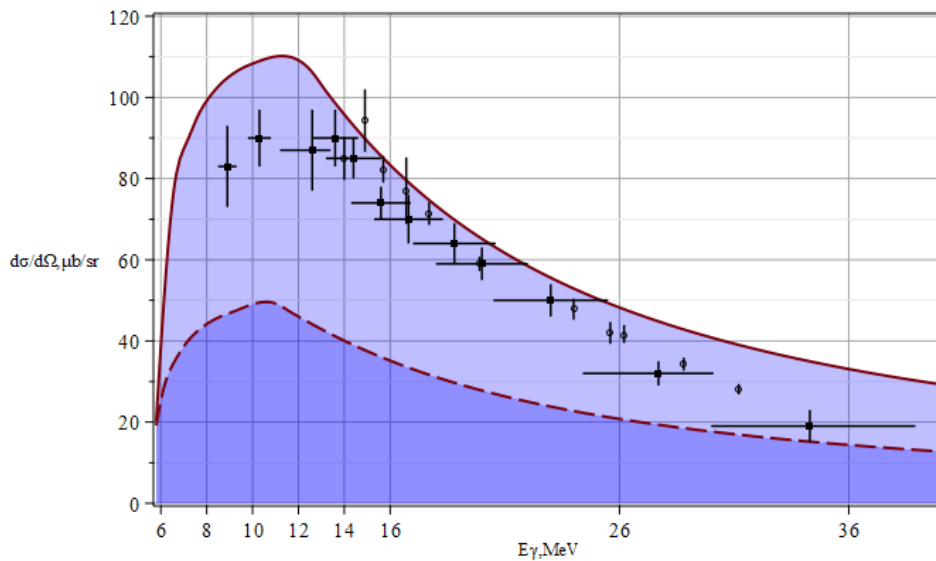
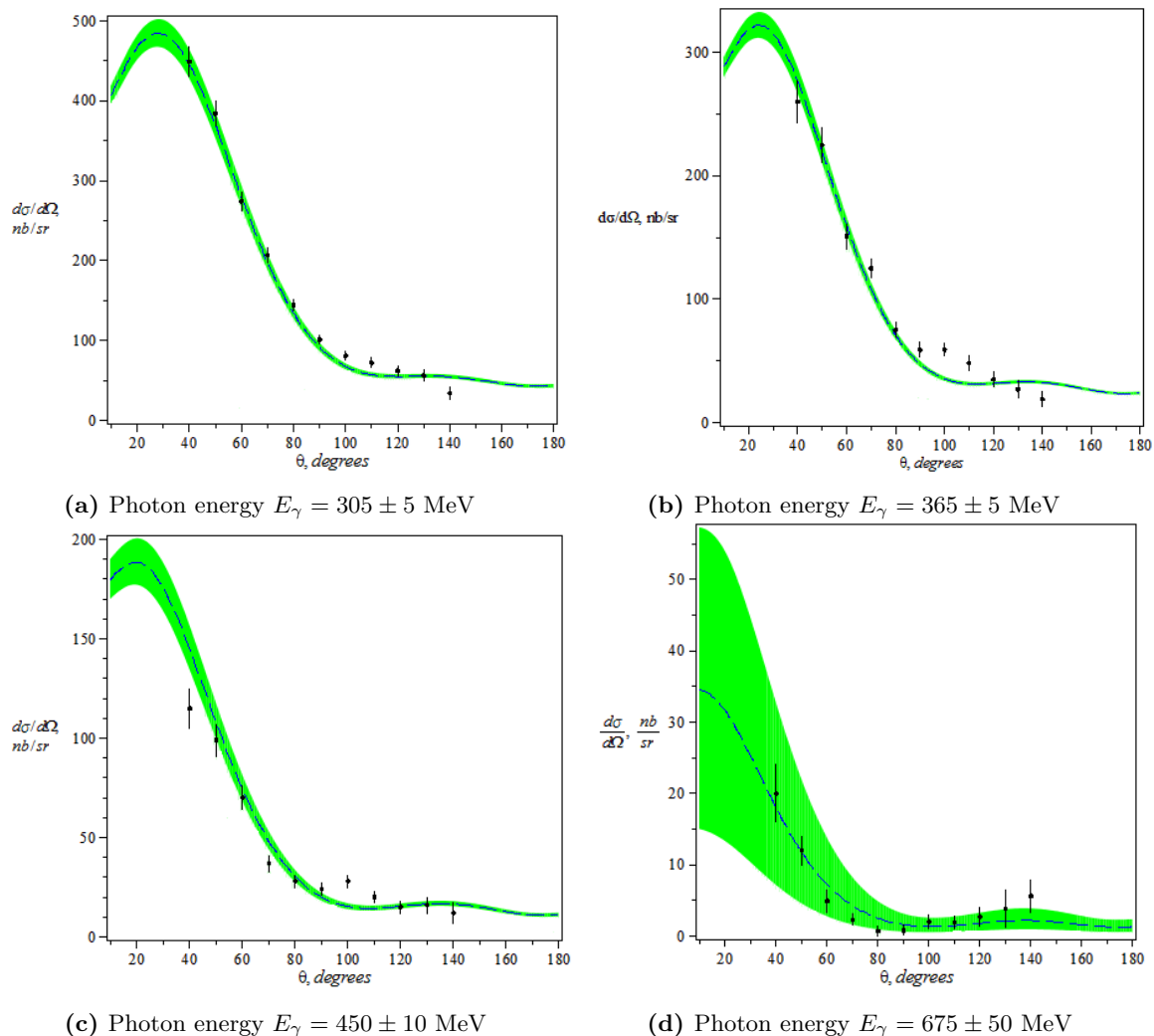


Figure 2. The energy ( $\theta = 90^\circ$ ) dependence of the differential cross-section of the process  $\gamma + {}^3\text{He} \rightarrow p + d$  from the threshold up to 40 MeV in photon energy. Experimental data are taken from [13], [14].

On Figure 2 the energy dependence of the differential cross-section is shown for the helium-3 nucleus with the proton's emission angle in the center-of-mass system equal to 90 degrees. The solid line represents the results of theoretical calculations. The dashed line represents calculations without accounting the non-local contact part of the diagram [10]. We provide the comparison of calculations for the approach, developed by authors in [8] with the experimental data on the cross-section energy dependence at a fixed angle of emitted nucleon [13], [14]. It can be seen that the theoretical curve is in satisfactory agreement with the experimental data from the disintegration threshold to a photon energy of 40 MeV. The peak cross-section is represented by different data sets [12], [13], [14] in the range from 80 to 120  $\mu\text{b}/\text{sr}$ . The process may be described if only the gauge invariance is preserved strictly and is brought into agreement with the law of conservation of the

four-momentum in the amplitude while applying the requirement of the general covariant scheme. As can be seen in this figure, there is a satisfactory agreement between the theoretical curve and experimental data from the threshold of splitting up to 40 MeV in photon energy.



**Figure 3.** Angular distributions of differential cross-sections for  $^3\text{He}(\gamma, p)d$  reaction in the center of mass system for different energies.

By expanding the cross-section with respect to the proton's emission angle at a fixed photon energy, it's possible to trace the evolution of the cross-section's shape as the energy increases. In this work we present theoretical distributions of cross-sections at high photon energies ( $E_\gamma = 305 \pm 5$  MeV;  $365 \pm 5$  MeV;  $450 \pm 10$  MeV and  $675 \pm 50$  MeV) and compare them with experimental data from [15]. The calculations are conducted for the two-particle breakup of helium-3 nuclei yield to the angular distributions of cross-sections shown on Figure 3. It can be seen that the proton peak does not disappeared at high energies except the energy  $E_\gamma = 675 \pm 50$  MeV. Using the explicit relativistic formulation of the theory [11] removes the question of the role of relativistic corrections and imposes no limitations on its use in various energy regimes and different kinematic conditions. As a result, it provides broad possibilities for conducting research on the structure of non-local fields of matter based on unified requirements.

#### ORCID

Pylyp Kuznietsov, <https://orcid.org/0000-0001-8477-1395>; Yuriy A. Kasatkin, <https://orcid.org/0000-0003-3824-8354>; Vyacheslav F. Klepikov, <https://orcid.org/0000-0002-3250-185X>

#### REFERENCES

- [1] G.E. Brown, A.M. Green, "Three-body forces in nuclear matter," Nuclear Physics A, **137**(1), 1-19 (1969). [https://doi.org/10.1016/0375-9474\(69\)90068-2](https://doi.org/10.1016/0375-9474(69)90068-2)

- [2] G. Derrick, D. Mustard, and J.M. Blatt, "Binding energy of the triton," Phys. Rev. Lett. **6**, 69 (1961). <https://doi.org/10.1103/PhysRevLett.6.69>
- [3] H. Wita, J. Golak, R. Skibiski, K. Topolnicki, and V. Urbanevych, "Investigation of the interaction of circularly and linearly polarized photon beams with a polarized  $^3\text{He}$  target," Phys. Rev. C, **101**, 2 (2020). <https://doi.org/10.1103/PhysRevC.101.024003>
- [4] R. Schiavilla, V.R. Pandharipande, and R.B. Wiringa, "Momentum distributions in A=3 and 4 nuclei," Nuclear Physics A, (449)(2), 219-242 (1986). [https://doi.org/10.1016/0375-9474\(86\)90003-5](https://doi.org/10.1016/0375-9474(86)90003-5).
- [5] W.W. Buck, and F. Gross, "Family of relativistic deuteron wave functions," Phys. Rev. D, **20**(9), 2361-2379 (1979). <https://doi.org/10.1103/PhysRevD.20.2361>.
- [6] Lovato, A. and Bombaci, I. and Logoteta, D. and Piarulli, M. and Wiringa, R. B., Benchmark calculations of infinite neutron matter with realistic two- and three-nucleon potentials Phys. Rev. C, **105**, 5 (2022). <https://link.aps.org/doi/10.1103/PhysRevC.105.055808>
- [7] I.E. Lagaris, V.R. Pandharipande, "Phenomenological two-nucleon interaction operator," Nuclear Physics A, **359**, 331-348 (1981). [https://doi.org/10.1016/0375-9474\(81\)90240-2](https://doi.org/10.1016/0375-9474(81)90240-2)
- [8] Y.A. Kasatkin, V.P. Klepikov, P.E. Kuznietsov, "Two-particle photodisintegration of the  $^3\text{He}$  and  $^3\text{H}$  nuclei in a relativistic approach with a strictly conserved EM current," Phys. Part. Nuclei Lett. **12**, 481-493 (2015). <https://doi.org/10.1134/S1547477115040172>
- [9] G. Laskaris, W. Ji, et al., "First measurement of the asymmetry and the Gerasimov-Drell-Hearn integrand from the  $^3\text{He}(\gamma, p)^2\text{H}$  reaction at an incident photon energy of 29 MeV," Phys. Rev. C, **103**, 3 (2021). <https://doi.org/10.1103/PhysRevC.103.034311>
- [10] Yu.A. Kasatkin, V.F. Klepikov, and P.E. Kuznietsov, "Two-particle photodisintegration of light nuclei with conserved EM current," Problems of Atomic Science and Technology, 93(5), 18-25 (2014). [https://vant.kipt.kharkov.ua/ARTICLE/VANT\\_2014\\_5/article\\_2014\\_5\\_18.pdf](https://vant.kipt.kharkov.ua/ARTICLE/VANT_2014_5/article_2014_5_18.pdf)
- [11] P.E. Kuznietsov, "Unified Description of Photo and Electro Processes on Light Nuclei in Covariant Approach with Exactly Conserved EM Current," East European Journal of Physics, 2(1), 88-92 (2015). <https://doi.org/10.26565/2312-4334-2015-1-13>
- [12] W. Schadow, O. Nohadani, and W. Sandhas, "Photonuclear reactions of three-nucleon systems," Phys. Rev. C, **63**, 044006 (2000). <https://doi.org/10.1103/PhysRevC.63.044006>.
- [13] M. Karlsson, et al. "Measurement of the differential cross section for the two-body photodisintegration of  $^3\text{He}$  at  $\theta^{\text{LAB}} = 90^\circ$  using tagged photons in the energy range 14 – 31 MeV," Phys. Rev. C, **80**, 4 (2009). <https://doi.org/10.1103/PhysRevC.80.044001>
- [14] J.R. Stewart, R.C. Morrison, and J.S. O'Connell, "Photodisintegration of  $\text{He}^3$ ," Phys. Rev. **138**, 2B (1965). <https://doi.org/10.1103/PhysRev.138.B372>
- [15] V. Isbert, G. Audit, N. d'Hose, et al., "Two body photodisintegration of  $^3\text{He}$  between 200 and 800 MeV // Nucl. Phys. A, **578**, 525-541 (1994). [https://doi.org/10.1016/0375-9474\(94\)90759-5](https://doi.org/10.1016/0375-9474(94)90759-5).
- [16] J. Golak, H. Witała, R. Skibiński, K. Topolnicki, Y. Volkotrub, A. Grassi, V. Soloviov, V. Urbanevych, "Theoretical investigations of three-nucleon systems," Acta Physica Polonica. B, Proceedings Supplement, **13**(4), 609-618 (2020). <https://doi.org/10.5506/APhysPolBSupp.13.609>

## АМПЛІТУДИ ДВОЧАСТИНКОВОГО ФОТО РОЗЩЕПЛЕННЯ ЯДЕР $^3\text{H}$ , $^3\text{He}$ В НЕЛОКАЛЬНОМУ КЕД ПІДХОДІ

Пилип Кузнецов<sup>a,b</sup>, Юрій А. Касаткін<sup>b</sup>, В'ячеслав Ф. Клепиков<sup>a,b</sup>

<sup>a</sup> Харківський національний університет ім. В.Н. Каразіна, майдан Свободи, 4, 61022, Харків, Україна

<sup>b</sup> Інститут електрофізики та радіаційних технологій Національної академії наук України,  
вул. Чернишевська, 28, п/с 8812, 61022, Харків, Україна

Трьохнуклонні системи відіграють важливу роль у вивченні багаточастинкових сил в ядерній фізиці. Обґрунтована параметризація їх вершинних функцій з подальшим застосуванням для обчислення перерізів реакцій в нелокальному КЕД підході дає основу для дослідження широкого спектру багаточастинкових систем. У данній статті ми проводимо параметризацію амплітуд двохчастинкового фото-розпаду тринуклонних систем ( $^3\text{H}$ ,  $^3\text{He}$ ). Ми надаємо загальний опис конструкції хвильової функції для систем з трьома нуклонами, а також параметризацію її вершинних функцій з урахуванням дво- та трьохнуклонних взаємодій на основі формалізму обміну мезонами. У наших обчисленнях ми враховуємо взаємодії за рахунок одно піонного обміну у першому та другому порядках та терм, пов'язаний з обміном  $\omega$  та  $\rho$  мезонами. Потенціал трьохнуклонної взаємодії розраховано як суму потенціалу притягання (за рахунок обміну двома піонами) та відповідної частини, яка відповідає за відштовхування. На основі варіаційних амплітуд "Urbaan + Model VII" отримано результати для енергетичної залежності диференціального перерізу реакції  $^3\text{He}(\gamma, p)d$  при куті протону  $\theta = 90^\circ$  від порогу до  $E_\gamma = 60$  MeV. Теоретичні передбачення порівняно з наявними експериментальними даними. Також проведено дослідження для кутових розподілів перерізів при високих енергіях фотонів ( $E_\gamma = 305 \pm 5$  MeV;  $365 \pm 5$  MeV;  $450 \pm 10$  MeV та  $675 \pm 50$  MeV). Корректний опис процесів фото-розщеплення  $^3\text{H}$ ,  $^3\text{He}$  в єдиному підході на основі каліброваної природи електромагнітного поля передбачає застосування цього підходу для інших багаточастинкових систем.

**Ключові слова:** тринуклонна система; фоторозпад; переріз; амплітуда; багаточастинкова сила; мезон-обмінний струм

## MULTIPLE LIGAND SIMULTANEOUS DOCKING OF ANTIVIRAL DRUGS AND CYANINE DYES WITH PROTEINS<sup>†</sup>

**Olga Zhytniakivska\***, **Uliana Tarabara**, **Kateryna Vus**, **Valeriya Trusova**, **Galyna Gorbenko**

*Department of Medical Physics and Biomedical Nanotechnologies, V.N. Karazin Kharkiv National University  
4 Svobody Sq., Kharkiv, 61022, Ukraine*

*\*Corresponding Author e-mail: [olga.zhytniakivska@karazin.ua](mailto:olga.zhytniakivska@karazin.ua)*

Received July 07, 2023; revised August 21, 2023; accepted August 24, 2023

Protein nanoparticles are currently regarded as promising biocompatible and biodegradable systems for targeted delivery of different types of pharmacological agents. Prior to fabricating such kind of drug nanocarriers it is reasonable to evaluate the drug-protein binding affinity and possible interaction modes using the computational tools, particularly, the molecular docking technique. The present study was undertaken to evaluate the possibility of creating the protein nanoparticles carrying the antiviral drugs and cyanine dyes as visualizing agents. The components of the examined systems included endogenous functional proteins cytochrome c, serum albumin, lysozyme and insulin, antiviral drugs favipiravir, molnupiravir, nirmatrelvir and ritonavir, mono- and heptamethinecyanine dyes. Using the multiple ligand simultaneous docking technique, it was demonstrated that: i) the drugs and the dyes occupy different binding sites on the protein molecule and do not interfere with each other; ii) the heptamethines AK7-5 and AK7-6 possess the highest affinity for the proteins; iii) among the examined systems the strongest complexes are formed between the heptamethine dyes and serum albumin. Taken together, the results obtained indicate that albumin-based nanoparticles functionalized by the heptamethine cyanine dyes can be used for targeted delivery of the explored antiviral agents.

**Keywords:** *Antiviral agents; Protein nanoparticles; Drug nanocarriers; Cyanine dyes; Molecular docking*

**PACS:** 87.14.C++c, 87.16.Dg

During the last decades the nanostructured drug delivery systems (DDS) such as liposomes, polymeric, lipidic, protein and inorganic nanoparticles, nanotubes, fullerenes, dendrimers and many others, have become a subject of considerable research interest in biomedical field [1-3]. Particular attention is devoted to protein nanoparticles which have numerous advantages among which are: i) biocompatibility and biodegradability; ii) a weak or negligible immune response; iii) controlled size and stability; iv) a possibility of drug protection from enzymatic degradation and renal clearance; v) mild preparation and drug encapsulation conditions; vi) an opportunity for surface modification and functionalization with tissue-specific ligands; vii) protein abundance in natural sources; viii) easy synthesis process and cost-effectiveness [4-6]. The use of proteins makes it possible to deliver the drugs with low aqueous solubility. The first endogenous protein utilized for preparing the nanoparticles was the blood serum albumin. A remarkable ability of human serum albumin to reversibly bind hydrophobic molecules provided a basis for obtaining the albumin-bound formulation of the antitumor low soluble drug paclitaxel (Abraxane) [7]. Due to their amphiphilic nature, proteins can interact with both hydrophilic and hydrophobic drugs. Along with albumin, the nanoparticles were fabricated from a variety of animal (gelatin, collagen, casein, silk fibroin) and plant (zein, gliadin, lectin, soy protein) [4,8]. Protein nanoparticles are currently used in cancer therapy, lung treatment, vaccine production, etc [9]. To create the protein-based drug delivery system it is necessary to ascertain whether the protein can simultaneously interact with a drug and functionalizing molecules, such as targeting, stabilizing or visualizing agents. The cyanine dyes fluorescing in the near-infrared region, in the optical windows of biological samples are among the most promising visualizing agents for DDS. In view of this, it seems of interest to evaluate the possibility of concurrent binding of antiviral drugs and cyanine fluorescent dyes. A series of the examined endogenous proteins included cytochrome c (Ct), serum albumin (SA), lysozyme (Lz), insulin (Ins). These proteins play important roles in the electron transport (Ct), blood circulation (SA), innate immune (Lz) and endocrine (Ins) systems. The antiviral drugs were represented by favipiravir, molnupiravir, nirmatrelvir and ritonavir. The aim of in the present study was to characterize the ternary complexes protein-drug-dye using the technique of multiple ligand simultaneous docking (MLSD).

### MATERIALS AND METHODS

#### Molecular docking studies

The set of the investigated pharmaceuticals included favipiravir, molnupiravir, nirmatrelvir and ritonavir [10]. The examined drug structures as well as monomethine and heptamethine cyanine dyes (Figure 1) were built in MarvinSketch (version 18.10.0) and optimized in Avogadro (version 1.1.0) using the Universal Force Field with the steepest descent algorithm [11,12]. The counterions were not added to the dye structures in order to save the molecular charges. The three-dimensional X-ray crystal structures of the examined proteins were obtained from the Protein Data Bank using the PDB IDs 1REX, 3I40, 3ZCF, 6M4R for lysozyme, insulin, cytochrome c and serum albumin, respectively. The proteins were

<sup>†</sup> *Cite as:* O. Zhytniakivska, U. Tarabara, K. Vus, V. Trusova, G. Gorbenko, East Eur. J. Phys. 3, 585 (2023), <https://doi.org/10.26565/2312-4334-2023-3-69>

© O. Zhytniakivska, U. Tarabara, K. Vus, V. Trusova, G. Gorbenko, 2023

taken in the native monomeric form. The SA structural model was prepared using the DockPrep module of UCSF Chimera molecular software by removing the water molecules and addition of polar hydrogen atoms and Kollman charges [13]. The blind docking of the drugs with the proteins was performed using the PatchDock server (<http://bioinfo3d.cs.tau.ac.il/PatchDock/php.php>) in which the molecular docking algorithm is focused on the finding of maximal surface shape complementarity along with the minimal amounts of steric clashes [14]. Subsequently, the top-scored docked drug-protein complexes were considered as a receptor for docking of the second ligand, one representative of the monomethine or heptamethine cyanine dyes, using the PatchDock server. The control dye-protein systems were also considered. In order to identify the amino acid residues constituting the binding sites and to analyse the types of the drug-protein and the dye-protein contacts, the protein-ligand interaction profiler (PLIP, <https://plip-tool.biotec.tudresden.de/plip-web/plip/index>) was employed [15]. The selected docking poses were visualized with the UCSF Chimera software (version 1.14) in which the docking models with the best geometric shape complementary were combined in the same picture to achieve the best visibility of the binding sites [16].

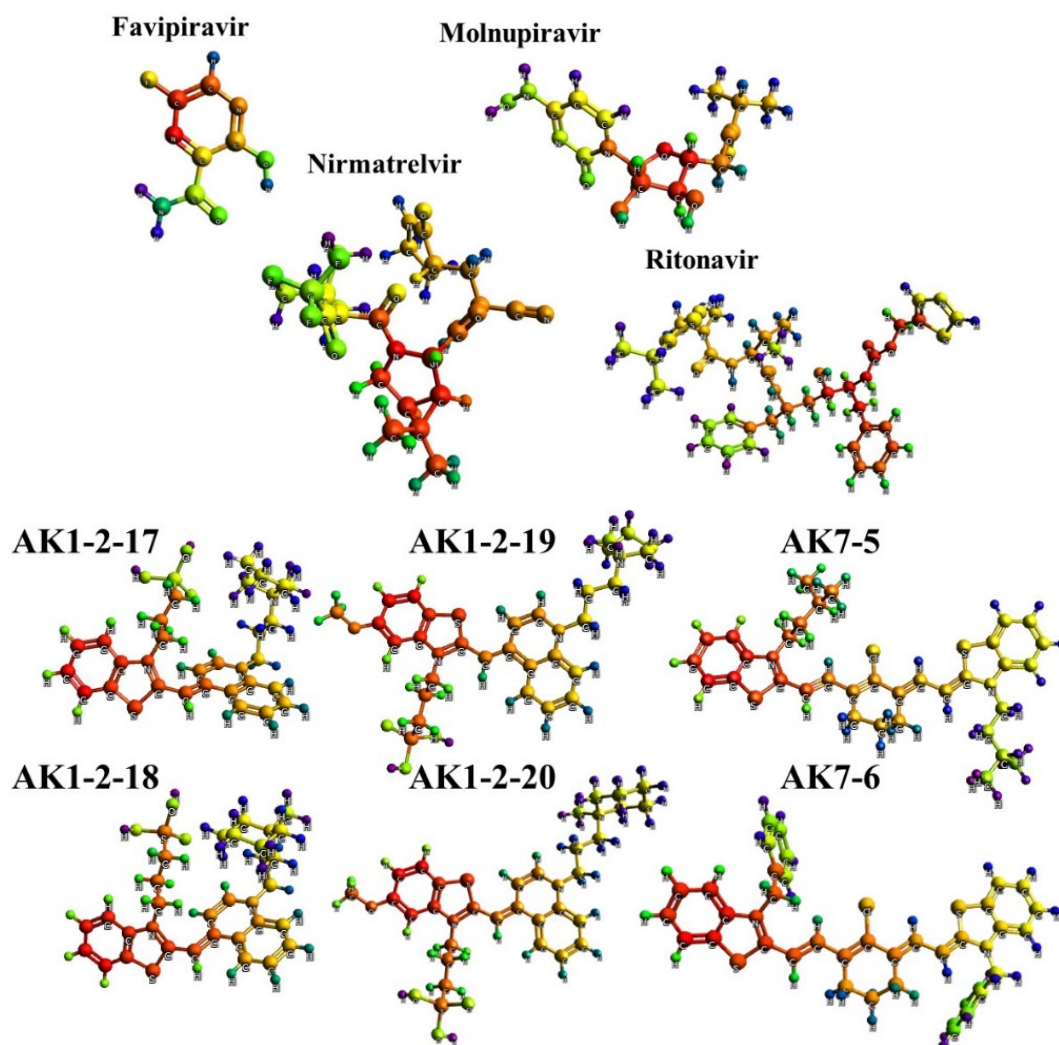


**Figure 1.** Structural formulas of the examined antiviral drugs and cyanine dyes

## RESULTS AND DISCUSSION

Shown in Figs 2-5 are the highest-score ternary complexes protein-drug-dye recovered for cytochrome *c* (Fig.2), albumin (Fig. 3), lysozyme (Fig. 4) and insulin (Fig. 5). It can be seen that in the cases of Ct, Lz and Ins the binding sites for the investigated mono- and heptamethines are located rather close to each other in the vicinity of the protein surface. Meanwhile, the drugs penetrate deeper into the interior of Ct, Lz and Ins, occupying the sites different from that of the cyanine dyes. In the case of albumin, the antiviral agents and the dyes reside in the distinct protein pockets.

The analysis of the geometric shape complementarity scores and approximate interface areas derived for the cytochrome *c*-drug-dye complexes (Table 1) revealed that: i) the drugs do not exert influence only on the dye-protein affinity and interface area, only in the cases of AK-1-2-20 for all drugs and AK7-6 for molnupiravir these parameters

slightly decrease; ii) the dye-protein affinity follows the order: AK7-5 > AK7-6 > AK-1-2-20 > AK-1-2-19 > AK-1-2-17 > AK-1-2-18; iii) the interface area decreases in the order: AK7-6 > AK7-5 > AK-1-2-19 > AK-1-2-20 > AK-1-2-17 > AK-1-2-18 for all drugs except molnupiravir for which AK7-5 has higher area than AK7-6.

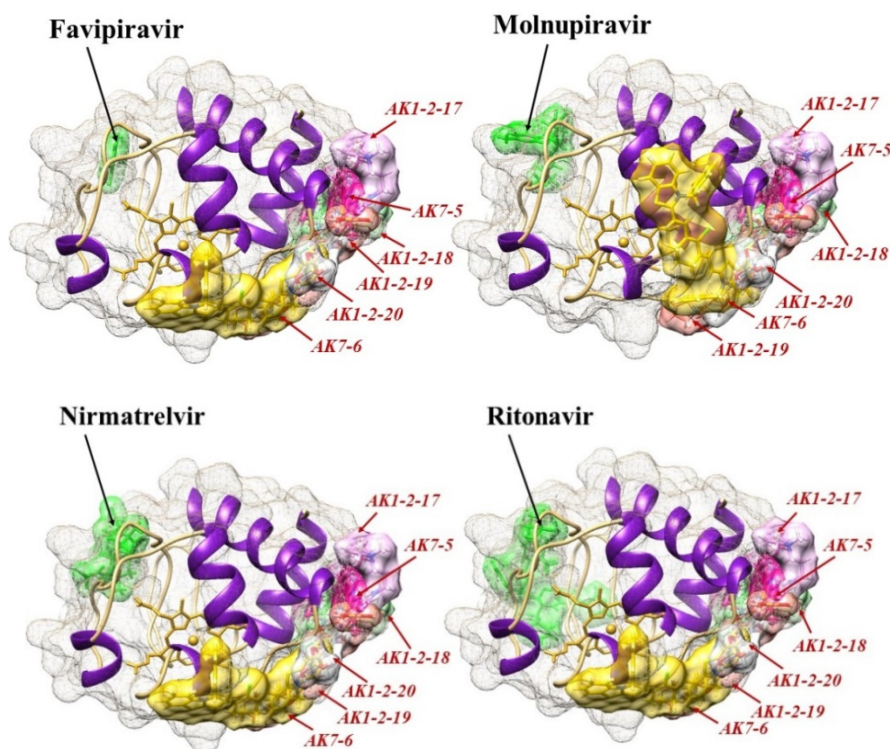


Figure 2. The highest-score docking positions obtained for cytochrome c using the MLSD in PatchDock.

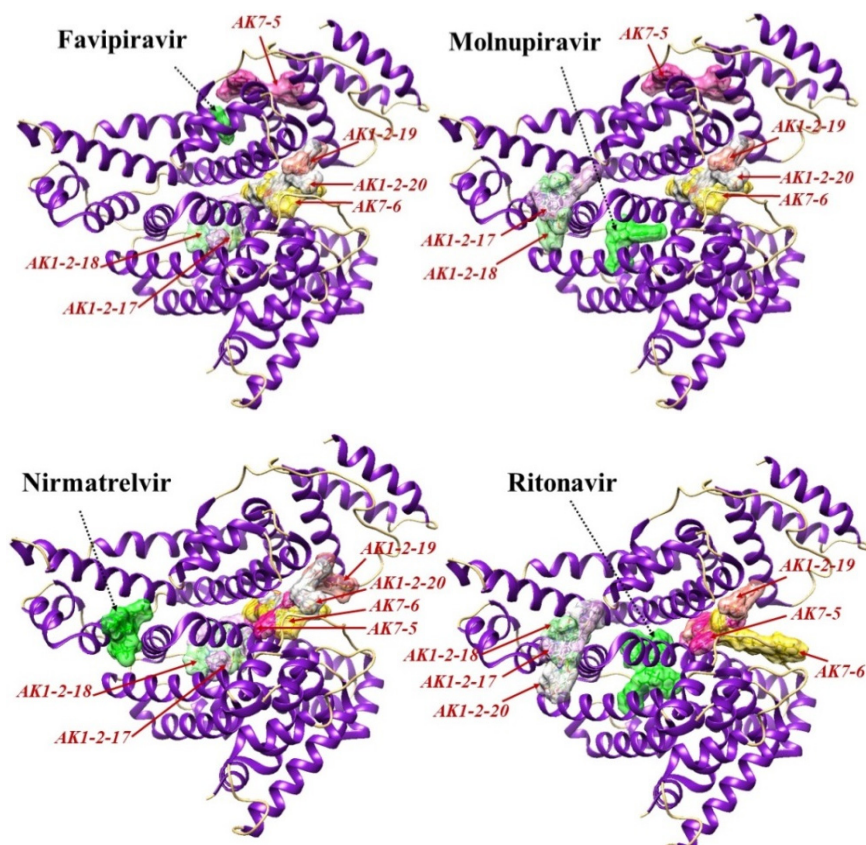


Figure 3. The highest-score docking positions obtained for albumin using the MLSD in PatchDock.

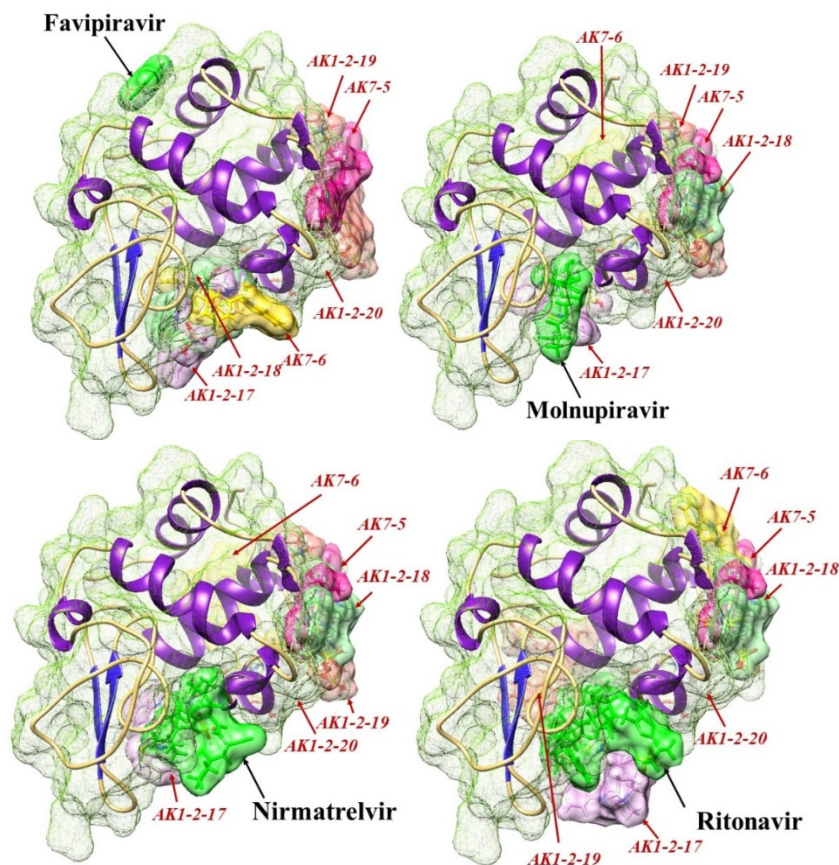


Figure 4. The highest-score docking positions obtained for lysozyme using the MLSD in PatchDock.

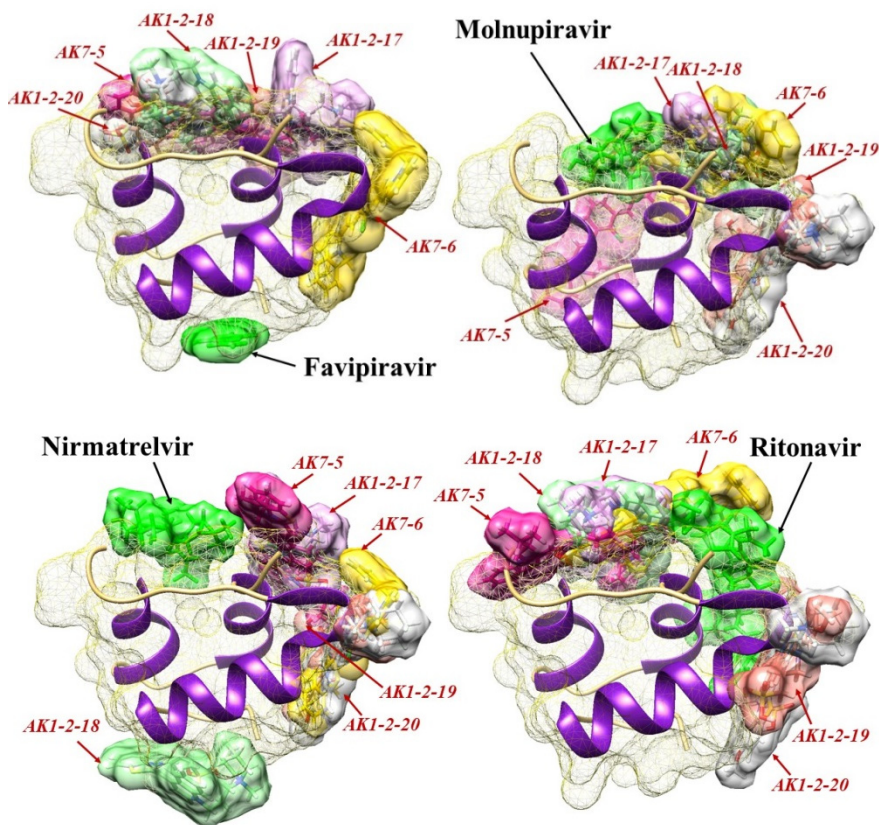


Figure 5. The highest-score docking positions obtained for insulin using the MLSD in PatchDock.

**Table 1.** The geometric shape complementarity score and approximate interface area of the complex derived for the cytochrome *c*-drug-dye systems (F- Favipiravir, M – Molnupiravir, N - Nirmatrelvir, R – Ritonavir).

| Cytochrome <i>c</i> |       |      |      |      |      |   |        |        |        |        |
|---------------------|-------|------|------|------|------|---|--------|--------|--------|--------|
| Dye                 | Score |      |      |      |      | Approximate interface area of the complex, A <sup>2</sup> |        |        |        |        |
|                     | F     | M    | N    | R    | -    | F   | M      | N      | R      | -      |
| -                   | 2220  | 3648 | 4292 | 6062 |      | 237.40  | 384.30 | 576.30 | 797.80 |        |
| AK-1-2-17           | 4642  | 4642 | 4642 | 4642 | 4642 | 608.50  | 608.50 | 608.50 | 608.50 | 608.50 |
| AK-1-2-18           | 4572  | 4544 | 4572 | 4572 | 4572 | 580.00  | 544.00 | 580.00 | 580.00 | 580.00 |
| AK-1-2-19           | 5414  | 5414 | 5414 | 5414 | 5414 | 744.10  | 744.10 | 744.10 | 744.10 | 744.10 |
| AK-1-2-20           | 5476  | 5476 | 5476 | 5476 | 5582 | 716.20  | 716.20 | 716.20 | 716.20 | 757.70 |
| AK7-5               | 6174  | 6174 | 6174 | 6174 | 6174 | 819.80  | 819.80 | 819.80 | 819.80 | 819.80 |
| AK7-6               | 5842  | 5716 | 5842 | 5842 | 5842 | 846.40  | 732.90 | 846.40 | 846.40 | 846.40 |

The data acquired for the albumin-drug-dye complexes (Table 2) show a greater variability. The dye-protein affinity remains the same for the systems AK-1-2-17 + F/N, AK-1-2-18 + F/N, AK-1-2-19 + N, AK-1-2-20 + F/M/N, AK7-5 + N, AK7-6 + F/M/N; decreases in the systems AK-1-2-18 + M/R, AK-1-2-20 + R, AK7-5 + F/M/R, AK7-6 + R; and increases in the systems AK-1-2-19 + F/M/R. The highest albumin-dye affinity was observed for AK7-6 (F, M, N) and AK7-5 (N, R).

**Table 2.** The geometric shape complementarity score and approximate interface area of the complex derived for the albumin-drug-dye systems (F- Favipiravir, M – Molnupiravir, N - Nirmatrelvir, R – Ritonavir).

| Serum albumin |       |      |      |      |      |   |        |        |         |        |
|---------------|-------|------|------|------|------|---|--------|--------|---------|--------|
| Dye           | Score |      |      |      |      | Approximate interface area of the complex, A <sup>2</sup> |        |        |         |        |
|               | F     | M    | N    | R    | -    | F   | M      | N      | R       | -      |
| -             | 2900  | 5054 | 6212 | 8412 |      | 343.60  | 553.10 | 719.50 | 1036.60 |        |
| AK-1-2-17     | 6444  | 6052 | 6444 | 6058 | 6444 | 747.70  | 756.70 | 747.70 | 754.60  | 747.70 |
| AK-1-2-18     | 6522  | 6420 | 6522 | 6420 | 6522 | 740.90  | 758.00 | 740.90 | 758.00  | 740.90 |
| AK-1-2-19     | 6936  | 6936 | 6790 | 6932 | 6790 | 886.60  | 886.60 | 867.40 | 885.60  | 867.40 |
| AK-1-2-20     | 6924  | 6924 | 6924 | 6804 | 6924 | 935.80  | 935.80 | 930.40 | 766.70  | 930.40 |
| AK7-5         | 6942  | 6940 | 7204 | 7016 | 7204 | 768.80  | 768.20 | 950.10 | 920.10  | 950.10 |
| AK7-6         | 7022  | 7022 | 7022 | 6954 | 7022 | 891.80  | 891.80 | 891.80 | 916.90  | 891.80 |

In the lysozyme-drug-dye systems (Table 3) the dye-protein affinity was found to follow the order: AK7-5 > AK-1-2-20 > AK7-6 > AK-1-2-19 > AK-1-2-18 > AK-1-2-17, while in the case of insulin (Table 4) the highest affinity for the protein was observed for AK-1-2-19 (F), AK7-6 (M), AK7-5 (N, R). The PLIP analysis of the driving forces of the cyanine-protein binding revealed essential role of hydrophobic interactions for all dye-protein complexes under study. The other types of interactions involve hydrogen bonds, salt and water bridges, as well as more rarely occurring  $\pi$ -stacking and  $\pi$ -cation interactions. Notably, the strongest complexes formed by heptamethines with Cyt, SA, Lz and Ins are stabilized exclusively by hydrophobic interactions.

**Table 3.** The geometric shape complementarity score and approximate interface area of the complex derived for the lysozyme-drug-dye systems (F- Favipiravir, M – Molnupiravir, N - Nirmatrelvir, R – Ritonavir).

| Lysozyme  |       |      |      |      |      |   |        |        |        |        |
|-----------|-------|------|------|------|------|---|--------|--------|--------|--------|
| Dye       | Score |      |      |      |      | Approximate interface area of the complex, A <sup>2</sup> |        |        |        |        |
|           | F     | M    | N    | R    | -    | F   | M      | N      | R      | -      |
| -         | 2184  | 3628 | 4690 | 5922 |      | 245.40  | -54.84 | 522.30 | 702.70 |        |
| AK-1-2-17 | 4986  | 4636 | 4612 | 4668 | 4986 | 527.70  | 553.60 | 518.20 | 527.40 | 527.70 |
| AK-1-2-18 | 5366  | 4874 | 4874 | 4874 | 5366 | 600.10  | 555.30 | 555.30 | 555.30 | 600.10 |
| AK-1-2-19 | 5432  | 5432 | 5432 | 5314 | 5432 | 666.10  | 666.10 | 666.10 | 691.30 | 666.10 |
| AK-1-2-20 | 5760  | 5760 | 5760 | 5752 | 5760 | 789.00  | 789.00 | 789.00 | 789.00 | 789.00 |
| AK7-5     | 5886  | 5886 | 5886 | 5886 | 5886 | 739.30  | 739.30 | 739.30 | 739.30 | 739.30 |
| AK7-6     | 5734  | 5472 | 5472 | 5492 | 5734 | 663.80  | 692.80 | 692.80 | 727.10 | 663.80 |

**Table 4.** The geometric shape complementarity score and approximate interface area of the complex derived for the insulin-drug-dye systems (F- Favipiravir, M – Molnupiravir, N - Nirmatrelvir, R – Ritonavir).

| Insulin   |       |      |      |      |      |   |        |        |        |        |
|-----------|-------|------|------|------|------|---|--------|--------|--------|--------|
| Dye       | Score |      |      |      |      | Approximate interface area of the complex, A <sup>2</sup> |        |        |        |        |
|           | F     | M    | N    | R    | -    | F   | M      | N      | R      | -      |
| -         | 1944  | 2826 | 3544 | 4582 |      | 244.40  | 327.80 | 410.40 | 619.30 |        |
| AK-1-2-17 | 3888  | 3802 | 3784 | 4030 | 3888 | 443.20  | 416.20 | 457.90 | 472.30 | 443.20 |
| AK-1-2-18 | 4000  | 3898 | 3862 | 4130 | 4022 | 454.80  | 489.00 | 493.20 | 490.90 | 475.10 |
| AK-1-2-19 | 5022  | 4954 | 4954 | 5102 | 5022 | 652.60  | 578.70 | 578.70 | 601.90 | 652.60 |
| AK-1-2-20 | 4886  | 4920 | 4920 | 5024 | 4886 | 613.70  | 591.30 | 591.30 | 578.50 | 613.70 |
| AK7-5     | 4816  | 5096 | 5048 | 5554 | 4816 | 613.00  | 638.00 | 570.80 | 708.70 | 613.00 |
| AK7-6     | 4858  | 5274 | 4858 | 4738 | 4858 | 649.40  | 688.10 | 649.40 | 557.00 | 649.40 |

### CONCLUSIONS

To summarize, in the present study the multiple ligand simultaneous docking technique was used to investigate the interactions between four functionally important proteins (cytochrome c, serum albumin, lysozyme and insulin), four antiviral drugs (favipiravir, molnupiravir, nirmatrelvir and ritonavir) and cyanine dyes (four monomethines and two heptamethines). It was found that: i) in most systems the drugs and the dyes interact with different binding sites on the protein molecule suggesting that there is no marked interference between the drugs and the dyes; ii) the heptamethines AK7-5 and AK7-6 form the strongest complexes with the proteins; iii) among the examined proteins the highest affinity binding of heptamethines is observed for albumin molecule where the dyes are located within the protein cavities. Overall, our findings suggest that the systems containing albumin and heptamethines are the most prospective for fabricating the protein nanoparticles for targeted delivery of the investigated antiviral drugs.

### Acknowledgements

This work was supported by the Ministry of Education and Science of Ukraine (the project “Development of novel means of medical diagnostics by biomedical nanotechnologies and modern ultrasonic and fluorescence methods”).

### ORCID

- Olga Zhytniakivska, <https://orcid.org/0000-0002-2068-5823>; • Uliana Tarabara, <https://orcid.org/0000-0002-7677-0779>
- Kateryna Vus, <https://orcid.org/0000-0003-4738-4016>; • Valeriya Trusova, <https://orcid.org/0000-0002-7087-071X>
- Galyna Gorbenko, <https://orcid.org/0000-0002-0954-5053>

### REFERENCES

- [1] A. Sultana, M. Zare, V. Thomas, T.S. Kumar, S. Ramakrishna, *Med. Drug Discov.* **15**, 100134 (2022). <https://doi.org/10.1016/j.medidd.2022.100134>
- [2] T. Fazal, B.N. Murtaza, M. Shah, S. Iqbal, M. Rehman, F. Jaberf, A.A. Dera, et al., *RSC Adv.* **13**, 23087-23121 (2023). <https://doi.org/10.1039/D3RA03369D>
- [3] J.A. Finbloom, C. Huynh, X. Huang, and T.A. Desai, *Nature Reviews Bioengineering*, **1**, 139–152 (2023). <https://doi.org/10.1038/s44222-022-00010-8>
- [4] E. Kianfar, *J. Nanobiotechnol.* **19**, 159 (2021). <https://doi.org/10.1186/s12951-021-00896-3>
- [5] A.L. Martínez-López, C. Pangua, C. Reboredo, R. Campión, J. Morales-Gracia, and J.M. Irache, *Int. J. Pharm.* **581**, 119289 (2020). <https://doi.org/10.1016/j.ijpharm.2020.119289>
- [6] A. Jain, S.K. Singh, S.K. Arya, S.C. Kundu, and S. Kapoor, *ACS Biomater. Sci. Eng.* **4**, 3939–3961 (2018). <https://doi.org/10.1021/acsbomaterials.8b01098>
- [7] E. Miele, G.P. Spinelli, E. Miele, F. Tomao, S. Tomao, *Int. J. Nanomedicine* **4**, 99–105 (2009). <https://doi.org/10.2147/ijn.s3061>
- [8] J.A. Carvalho, A.S. Abreu, V.T. Ferreira, E.P. Gonçalves, A.C. Tedesco, J.G. Pinto, J. Ferreira-Strixino, et al., *J. Biomater. Sci. Polym. Ed.* **29**, 1287–301 (2018). <https://doi.org/10.1080/09205063.2018.1456027>
- [9] S. Hong, D.W. Choi, H.N. Kim, C.G. Park, W. Lee, and H.H. Park, *Pharmaceutics*, **12**, 604 (2020). <https://doi.org/10.3390/pharmaceutics12070604>
- [10] V.M. Trusova, O.A. Zhytniakivska, U.K. Tarabara, K.A. Vus, and G.P. Gorbenko, *J. Pharm. Biomed. Anal.* **233**, 115448 (2023). <https://doi.org/10.1016/j.jpba.2023.115448>
- [11] P. Csizmadia, in: *Proceedings of ECSOC-3, the third international electronic conference on synthetic organic chemistry*, (1999), pp. 367-369. <https://doi.org/10.3390/ECSOC-3-01775>
- [12] M.D. Hanwell, D.E. Curtis, D.C. Lonie, T. Vandermeersch, E. Zurek, and G.R. Hutchison, *J. Cheminform.* **4**, 17 (2012). <https://doi.org/10.1186/1758-2946-4-17>
- [13] E. Pettersen, T. Goddard, C. Huang, G. Couch, D. Greenblatt, E. Meng, T. Ferrin, *J. Comput. Chem.* **25**, 1605–1612(2004). <https://doi.org/10.1002/jcc.20084>
- [14] D. Schneidman-Duhovny, Y. Inbar, R. Nussinov, and H.J. Wolfson, *Nucl. Acids. Res.* **33**, W363 (2005). <https://doi.org/10.1093/nar/gki481>
- [15] M.F. Adasme, K.L. Linnemann, S.N. Bolz, F. Kaiser, S. Salentin, V.J. Haupt, and M. Schroeder, *Nucl. Acids. Res.* **49**, W530-W534 (2021). <https://doi.org/10.1093/nar/gkab294>

- [16] E.F. Pettersen, T.D. Goddard, C.C. Huang, G.S. Couch, D.M. Greenblatt, E.C. Meng, and T.E. Ferrin, J. Comput. Chem. **25**, 1605 (2004). <https://doi.org/10.1002/jcc.20084>

### ОДНОЧАСНИЙ ДОКІНГ ПРОТИВІРУСНИХ АГЕНТІВ ТА ЦІАНІНОВИХ БАРВНИКІВ З БІЛКАМИ

Ольга Житняківська, Уляна Тарабара, Катерина Вус, Валерія Трусова, Галина Горбенко

*Кафедра медичної фізики та біомедичних нанотехнологій, Харківський національний університет імені В.Н. Каразіна  
м. Свободи 4, Харків, 61022, Україна*

Білкові наночастинки наразі розглядаються як перспективні біосумісні та біодеградовні системи для цілеспрямованої доставки фармакологічних агентів різних класів. Перед створенням наносів ліків такого типу доцільно здійснити оцінку спорідненості лікарських препаратів до білків та охарактеризувати можливі способи взаємодії з використанням комп'ютерних підходів, зокрема, методу молекулярного докінгу. Дане дослідження було проведене з метою оцінки можливості створення білкових наночастинок, навантажених противірусними препаратами та ціаніновими барвниками у якості візуалізуючих агентів. Компоненти досліджуваних систем були представлені ендogenous функціональними білками цитохромом с, сироватковим альбуміном, лізоцимом та інсуліном; противірусними агентами фавіпіравіром, молнупіравіром, нірматрелвіром і рітонавіром; моно- та гептаметиновими ціаніновими барвниками. З використанням методу одночасного молекулярного докінгу багатьох лігандів було продемонстровано, що: i) лікарські препарати та барвники займають різні центри зв'язування на білковій молекулі; ii) гептаметини АК7-5 та АК7-6 мають найвищу спорідненість до білків; iii) серед досліджених систем найміцніші комплекси утворюються між гептаметиновими барвниками та сироватковим альбуміном. В цілому, отримані результати свідчать про те, що наночастинки на основі альбуміну, функціоналізовані гептаметиновими ціаніновими барвниками, можуть бути застосовані для таргетної доставки досліджуваних противірусних агентів.

**Ключові слова:** *противірусні агенти; білкові наночастинки; наноносії ліків; ціанінові барвники; молекулярний докінг*

## CHAOS SYNCHRONIZATION OF InGaAsP LASERS<sup>†</sup>

 **Mohammed H.H. Al-Jassani<sup>a</sup>, Aqeel I. Faris<sup>b</sup>, Hussein H. Khudhur<sup>b</sup>**

<sup>a</sup>Physics Department, Science College, University of Kufa, Najaf, Iraq

<sup>b</sup>The General Directorate of Education in Al\_Najaf Al\_Ashraf, Ministry of Education, Najaf, Iraq

Corresponding author: [aljassani86@gmail.com](mailto:aljassani86@gmail.com)

Received May 18, 2023; revised June 28, 2023; accepted June 28, 2023

The optical output of a semiconductor laser can fluctuate chaotically by modulating its direct current in limited conditions of the modulated current signal parameters in terms of modulation frequency and modulation index. In this work, single, double, and chaotic pulses of an InGaAsP laser with direct current modulation, are numerically presented through a bifurcation diagram. Numerically, the unidirectional optical coupling system realizes chaotic synchronization between two identical InGaAsP lasers with direct current modulation, as the transmitter/receiver configuration. The transmission time for transmitting light from the transmitted laser to the received laser is essential for controlling the quality of chaos synchronization. The transmission time applies on the order of nanoseconds. Chaos synchronization quality is estimated by a correlation plot and calculated by the cross-correlation coefficient. This study observed the best synchronization quality (complete chaos synchronization) when the two lasers are identical. On the other hand, the chaotic synchronization between two non-identical InGaAsP lasers was investigated. In this case, complete chaos synchronization is not found, and the quality of chaotic synchronization was observed to decrease as the mismatch between the parameters of the two lasers increased.

**Keywords:** InGaAsP laser; Chaos synchronization; Direct current modulation; Optical coupling; Cross-correlation coefficient

**PACS:** 05.45.Xt, 05.45.Vx, 42.79.Sz, 05.45.-a, 42.65.Sf

### 1. INTRODUCTION

After the great success in the late last century in realizing chaos synchronization [1], chaos synchronization has been extensively investigated in various nonlinear dynamical systems [2-7]. Chaos synchronization represents the key to the success of chaotic communication systems, as the quality of the recovered message depends on the quality of synchronization between the transmitter and the receiver in chaotic communication systems [8-14]. Many studies have focused on the synchronization in chaotic systems of semiconductor lasers (SLs) with optical feedback [8,9,14-17], optical injection [10,11,18], and optoelectronic feedback [12,13,19,20]. In contrast, a few investigations have been published on the chaos synchronization and communication of SLs with direct current modulation [21,22]. The scant investigations of SLs with direct current modulation because the SLs have chaotic oscillations only under limited conditions. Also, it may be because the oscillation frequency of relaxation determines the modulation in direct current modulation, where the modulation efficiency decreases, and the intensity modulation becomes difficult as the modulation frequency is larger than the oscillation frequency of relaxation [23].

A solitary semiconductor laser (SL) is a very stable system. SL is easy to be destabilized by adding an extra degree of freedom when the SL is subjected to an external perturbation. Indeed, perturbed lasers show a chaotic oscillation. SL can be destabilized by the direct modulation of its current [24-28]. The direct current modulation exhibits doubled-period and chaos in some range of the modulation frequency and the modulation current [29,30]. The direct current modulation provides a third degree of freedom, which is responsible for making the nonlinear system non-autonomous [31].

In this paper, we numerically investigate the synchronization of a chaotic optical system consisting of two InGaAsP lasers with direct current modulation, which are unidirectionally coupled. Chaos synchronization can occur between two InGaAsP lasers (one the transmitter and the other the receiver) when a small proportion of the transmitter laser output power is optically coupled with the receiver laser. This synchronization method has been numerically investigated by Jones et al. They showed the synchronization of their optical model of self-pulsed semiconductor lasers with direct current modulation can be achieved by optical coupling [32]. In this study, the chaotic region of InGaAsP laser output with modulation index is shown by a bifurcation diagram. More importantly, the transmission time between the transmitter and the receiver was taken into account. The transmission time is executed on the order of nanoseconds. Also, the quality of the synchronization in this chaotic optical system is examined, where the cross-correlation coefficient is calculated between the output powers of the two identical and non-identical lasers.

### 2. SYNCHRONIZATION MODEL

The schematic diagram for the unidirectional optical coupling system, as transmitter/receiver configuration, is given in Fig. 1. The two semiconductor lasers are modulated with a sinusoidal current of GHz frequency. An optical isolator (OI) is ordinarily utilized to achieve one-way optical coupling between the two lasers. This optical coupling system can be modeled via the normalized rate equation of the photon density,  $S$ , and the carrier density,  $N$ , which is based on

<sup>†</sup> Cite as: M.H.H. Al-Jassani, A.I. Faris, H.H. Khudhur, East Eur. J. Phys. 3, 592 (2023), <https://doi.org/10.26565/2312-4334-2023-3-70>

© M.H.H. Al-Jassani, A.I. Faris, H.H. Khudhur, 2023

Agrawal's model of the InGaAsP laser with direct current modulation [30]. The rate equations of the optical coupling system are given by:

$$\frac{dS_t}{dt} = \frac{1}{\tau_{ph}} \left( \frac{N_t - \delta}{1 - \delta} (1 - \epsilon S_t) S_t - S_t + \beta N_t \right) S_t, \tag{1}$$

$$\frac{dS_r}{dt} = \frac{1}{\tau_{ph}} \left( \frac{N_r - \delta}{1 - \delta} (1 - \epsilon S_r) S_r - S_r + \beta N_r \right) S_r + k S_t(t-T), \tag{2}$$

$$\frac{dN_{t,r}}{dt} = \frac{1}{\tau_c} \left( \frac{I}{I_{th}} - N_{t,r} - \frac{N_{t,r} - \delta}{1 - \delta} S_{t,r} \right). \tag{3}$$

Where  $\tau_c$ , and  $\tau_{ph}$  are the electron and photon lifetimes.  $\delta = n_{th}/n_0$  where  $n_{th}$ , and  $n_0$  are the threshold carrier density and the carrier density for transparency respectively,  $\beta$  is the spontaneous emission factor, and  $\epsilon$  is the nonlinear gain reduction factor.

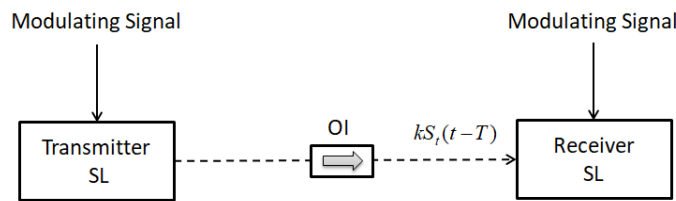


Figure 1. Schematic diagram for unidirectionally optical coupling system.

The modulating signal for the two lasers is given by [30]:

$$I = I_{b(t,r)} + I_m \sin(2\pi f_m t) \tag{4}$$

Where  $I_b$  is the bias current, and  $m, f_m$  are the index and frequency of modulation, respectively. Here,  $t$ , and  $r$  of the sub-position in the equations denote the transmitter and the receiver respectively. Eq.2 is written for the receiver only to effect synchronization between the two lasers by the term of delayed optical coupling from the transmitter. The coupling term is denoted in Eq.2 as  $k S_t(t-T)$ , where  $S_t(t-T)$  is the photon density of the transmitter laser, which is optically injected into the receiver laser after the time-delayed for the transmission,  $T$  is the transmission time for transmitting light from the transmitted laser to the received laser, and  $k$  is the optical coupling given as [32]:

$$k = x \frac{(1-R)}{\tau_{in} \sqrt{R}} \tag{5}$$

Where  $x$  is the portion of the transmitter optical power coupled into the receiver, is referred to as the optical coupling level, the mirror reflectivity of the receiver laser facing the transmitter laser,  $R = 0.32$ , and the round-trip time inside the laser cavity,  $\tau_{in} = 2l/v_g$ , where the cavity length of InGaAsP laser,  $l = \ln(R)/(1/\tau_{ph} v_g - \alpha)$ , the group velocity,  $v_g = c/\eta_e$ ,  $c$  is the speed of light in vacuum, the effective refractive index of InGaAsP laser,  $\eta_e = 4$ , and for simplicity the losses factor of InGaAsP laser,  $\alpha = 0$  [23]. Matlab program is used to solve the model of the optical coupling system as a delay differential equations. The parameter values of InGaAsP lasers used in the numerical simulations of the chaotic optical coupling system are listed in Table 1.

Table 1. The parameter values of the two InGaAsP lasers used for simulation [30].

| Symbol      | Value              |
|-------------|--------------------|
| $\tau_{ph}$ | 6 ps               |
| $\tau_c$    | 3 ns               |
| $\delta$    | 0.692              |
| $\epsilon$  | $10^{-4}$          |
| $\beta$     | $5 \times 10^{-5}$ |
| $m$         | 0.57               |
| $I_m$       | $m I_{th}$         |
| $I_b$       | $1.5 I_{th}$       |
| $f_m$       | 0.8 GHz            |

### 3. RESULTS AND DISCUSSION

In the beginning, attention is paid to the generation of chaos in the InGaAsP laser. By the modulation frequency of the laser close to the relaxation oscillation frequency with large values of the modulation index, the dynamics of the laser becomes chaotic, as shown in the bifurcation diagram in Fig.2.

Figure 2, shows the bifurcation diagram of the peak series of laser pulses against the modulation index for a modulation frequency fixed at 0.8 GHz. It indicates the regions of single, doubled, and chaotic pulses which have been numerically published by Agrawal in Ref. 30.

To effect chaos synchronization between two InGaAsP lasers, the receiver laser is coupled to the transmitter laser by it is receiving a portion of the transmitter output power with the transmission time  $T$ .  $T$  is executed in the order of nanoseconds (similar to the order of the modulation time  $\tau_m = 1/f_m = 1.25$  ns). The time series of the chaotic outputs of the transmitter and the receiver lasers are plotted to highlight how well the chaotic outputs are synchronized, and the output power of the transmitter laser and the output power of the receiver laser are used to estimate the quality of chaos synchronization by the correlation plot.

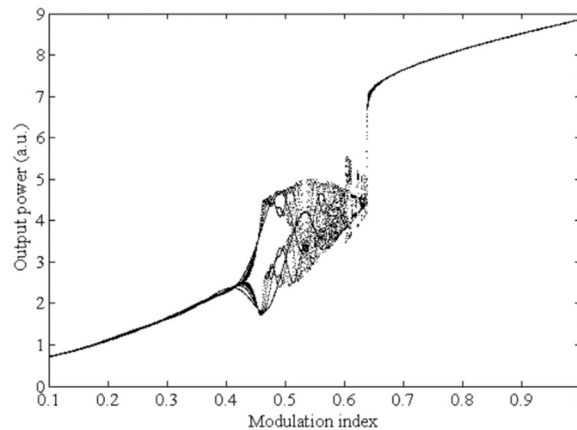


**Figure 2.** Bifurcation diagram of the laser output power against modulation index. The laser bias current is  $1.5I_{th}$ , and the modulation frequency is 0.8 GHz.

The chaotic time series and the correlation plot of the output powers for the transmitter and the receiver lasers at the same modulation conditions for both lasers  $I_{b(t,r)} = 1.5I_{th}$ ,  $m_{t,r} = 0.57$ ,  $f_m = 0.8$  GHz, and the optical coupling conditions are  $x = 1\%$ , and  $T$  varies in the order of nanoseconds, are shown in Fig. 3, and Fig. 4, respectively.

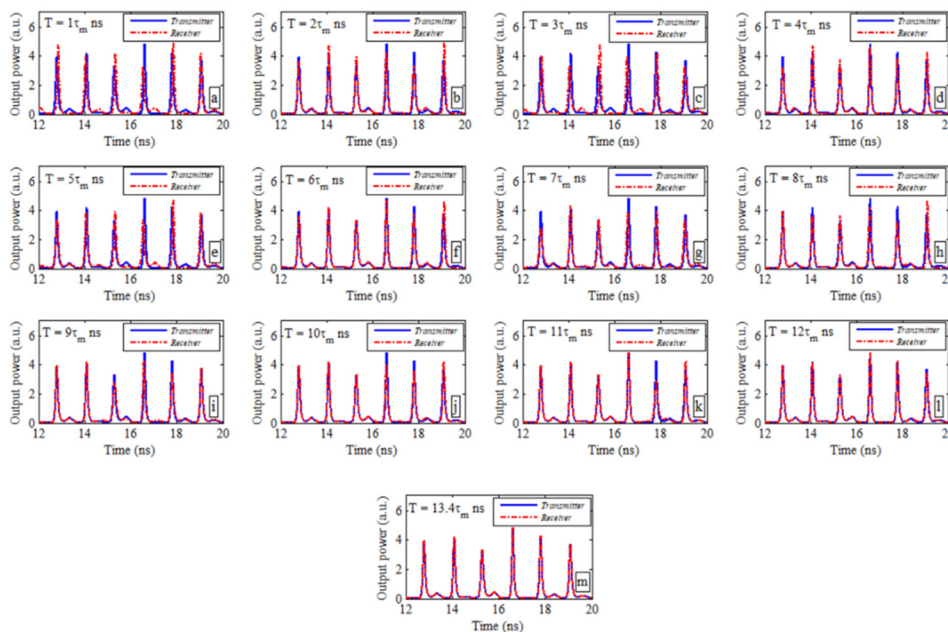


**Figure 3.** Chaotic fluctuations time series of transmitter and receiver for different transmission times (a)  $1\tau_m$  ns, (b)  $2\tau_m$  ns, (c)  $2\tau_m$  ns, (d)  $4\tau_m$  ns, (e)  $5\tau_m$  ns, (f)  $6\tau_m$  ns, (g)  $7\tau_m$  ns, (h)  $8\tau_m$  ns, (i)  $9\tau_m$  ns, (j)  $10\tau_m$  ns, (k)  $11\tau_m$  ns, (l)  $12\tau_m$  ns, and (m)  $13.4\tau_m$  ns. The optical coupling level is fixed at 1%. All modulation conditions and the parameters values of the two lasers are identical

In Fig. 3(a–i) when the transmission time is an odd integer number of the modulation time, the receiver's chaotic outputs are poor copies of the transmitter's chaotic outputs, as there is a large shifting between the chaotic fluctuations time series of the transmitter and receiver. This explains the poor quality estimation of synchronization as shown by the correlation plots in Fig. 4(a,c,e,g,i). While, the receiver's chaotic outputs are good copies of the transmitter's chaotic outputs. This is because the very small shifting between the chaotic fluctuations time series of the transmitter and receiver when the transmission time is an even integer number of the modulation time as shown in Fig. 3(a–i). So, the estimation of the good quality of synchronization as

shown by the correlation plots in Fig. 4(b,d,f,h). When the transmission time is increased, the shifting between the chaotic fluctuations time series of the transmitter and the receiver decreases, as shown in Fig. 3(j-l). Therefore, the receiver's chaotic outputs are excellent copies of the transmitter's chaotic outputs, and this explains the estimation of the excellent quality of synchronization as shown by the correlation plots in Fig. 4(j-l). The best case for synchronization is observed when the transmission time reaches  $13.4\tau_m$ , as shown in Fig. 3(m), where the receiver's chaotic output is an exact copy of the transmitter's chaotic output. Therefore, the distribution of all data points is a  $45^\circ$  diagonal line as shown by the correlation plot in Fig. 4(m), which indicates the receiver is completely driven by the transmitter.

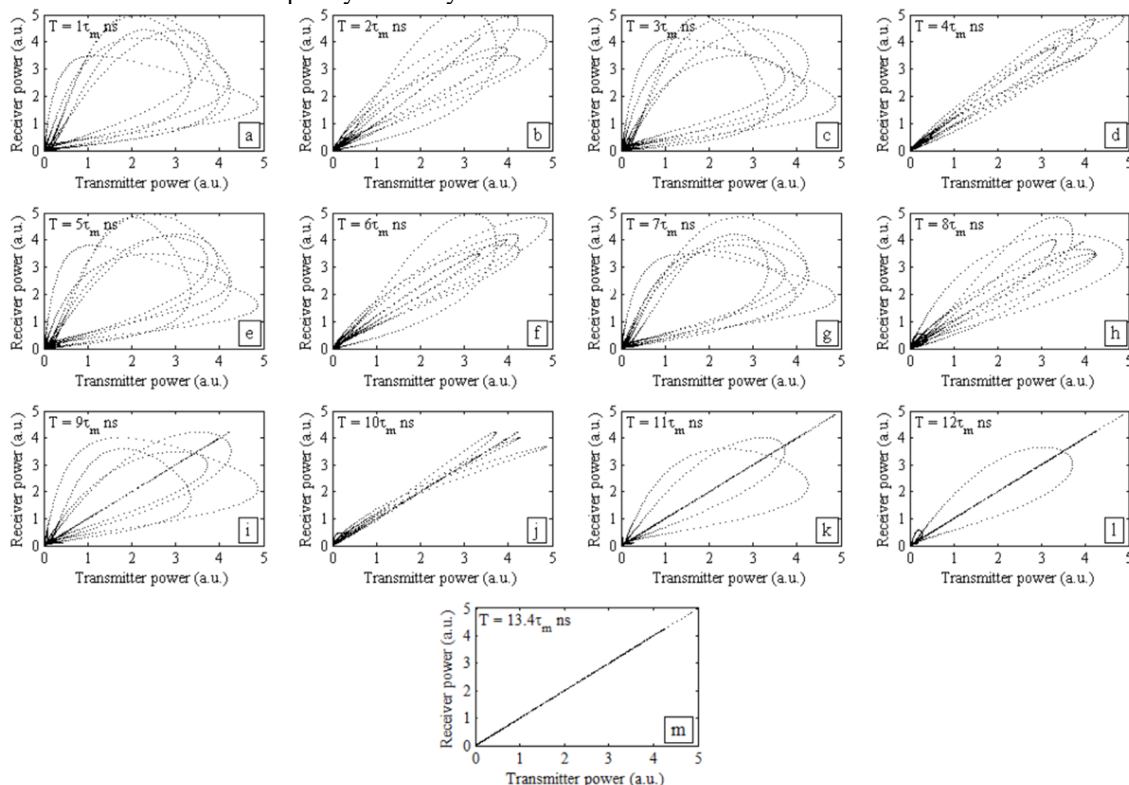


**Figure 4.** Transmitter output power against receiver output power. All modulation conditions and the parameters values of the two lasers are the same as in Fig. 3

To calculate the chaos synchronization quality between the two lasers, a method similar to that used in Ref. 5. A cross-correlation coefficient,  $C$ , is calculated between the transmitter and the receiver output powers, which, for better synchronization, would give a large value of  $|C|$  close to unity sometimes reaching unity. The cross-correlation coefficient against the transmission time for the case in Fig. 3, and Fig. 4, and for more optical coupling up to 20%, is shown in Fig. 4.

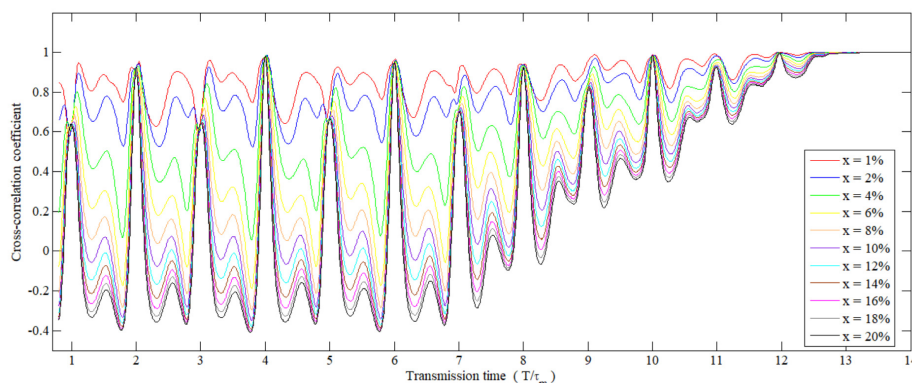


**Figure 5.** The cross-correlation coefficient against transmission time for optical coupling levels extends from 1% to 20%. Here, the transmission time on the order of nanoseconds. All modulation conditions and the parameters values of the two lasers are identical

In Fig. 5, before the best chaos synchronization quality ( $T = 13.4\tau_m$ ), the chaos synchronization quality decreases when the optical coupling level increases. Importantly, it can be seen that the chaos synchronization quality for each optical coupling level has a somewhat periodic behavior as a function of the transmission time. This behavior, in turn leads to synchronization quality being equal for each optical coupling level especially when all transmission times are an

even integer of modulation time and also at some transmission times are an odd integer of modulation time (see the intersection points of the curves in the figure). Although the model is not described in terms of the electric field and phase of the two lasers, this behavior of the chaos synchronization quality and the intersection points of the curves are a consequence of the optical coherence nature between the two lasers, which is achieved because the transmission time is on the same order as the modulation time (in other words, the same order as the time series of the output oscillations of the two lasers). The intersection points of the curves are not observed when the transmission time is applied on the order of picoseconds (no the same order as the modulation time) as shown in Fig. 6, and this confirms that the intersection points in Fig. 5 are attributable to the optical coherence between the chaotic output of two lasers.

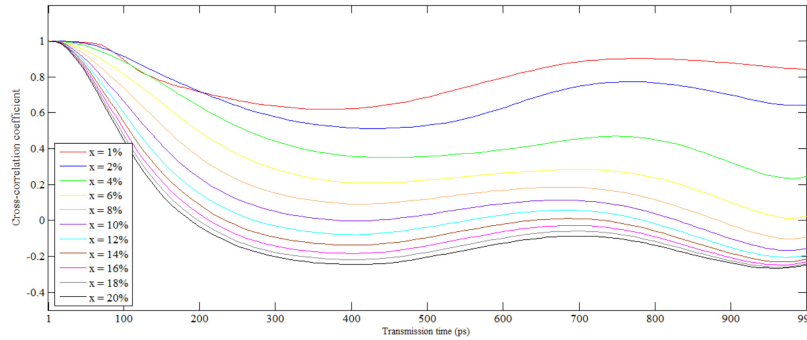


**Figure 6.** The cross-correlation coefficient against transmission time for optical coupling levels extends from 1% to 20%. Here, the transmission time on the order of picoseconds. All modulation conditions and the parameters values of the two lasers are identical

Moreover, for all-optical coupling levels, the best synchronization quality can be seen in Fig. 5 when the transmission time is equal to  $T = 13.4\tau_m$  and beyond, where the cross-correlation coefficient is equal to  $C = 1$ . This confirms the estimation of the chaos synchronization quality of the correlation plot in Fig. 4(m). In this situation of synchronization quality is called complete synchronization.

In Fig. 6 for each optical coupling level and the transmission time is very small about (1ps-10ps), complete chaos synchronization is observed, where the cross-correlation coefficient is about  $C = 1$ . This result is similar to when the transmission time is neglected. It is not included here; the optical coupling system has been its carry out without taking into account the transmission time and applied coupling levels are the same as in Fig. 6. Here, the model of an optical coupling system is solved as ordinary differential equations.

Now, the synchronization between the two lasers for non-identical parameter values will be verified by changing the values of some parameters of one laser, such as changing the bias current and the modulation index, which are the two most experimentally changeable parameters. Figure 7, shows the chaotic time series and the correlation plot of the output powers for the transmitter and the receiver when 1% of the optical output of the transmitter is coupled to the receiver with a transmission time of  $T = 13.4\tau_m$  for three different receiver bias currents. The transmitter bias current is fixed at  $I_{b(t)} = 1.5I_{th}$ , and the other modulation conditions for both lasers are  $m_{t,r} = 0.57, f_m = 0.8$  GHz.

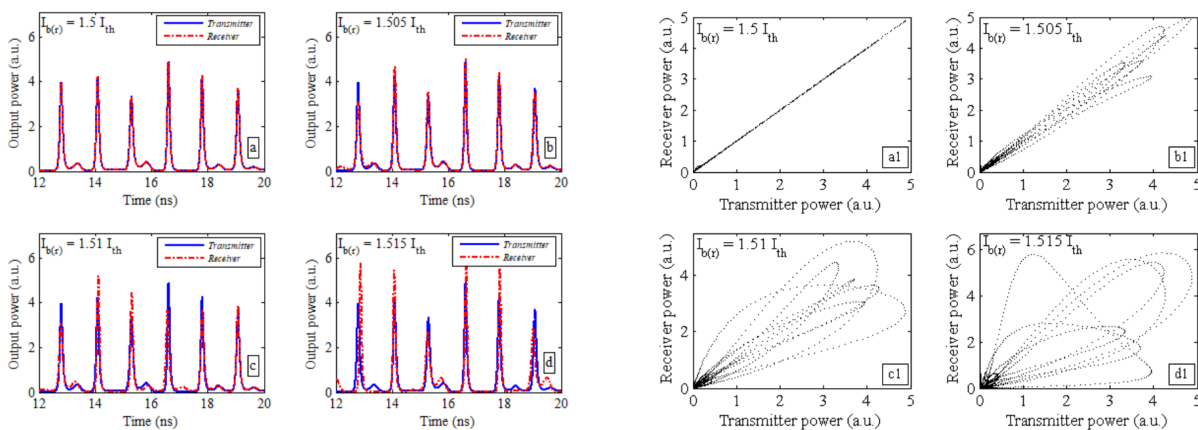


**Figure 7.** Chaotic fluctuations time series of transmitter and receiver (lift side), and transmitter output power against receiver output power for different laser bias currents of the receiver (right side): (a,a1)  $1.5I_{th}$ , (b,b1)  $1.505I_{th}$ , (c,c1)  $1.51I_{th}$ , and (d,d1)  $1.515I_{th}$ . The bias current of the transmitter laser is fixed at  $1.5I_{th}$ . The optical coupling level and the transmission time are fixed at 1% and  $13.4\tau_m$  respectively. The other modulation conditions and the parameters values of the two lasers are identical

In Fig. 7(b-d) the small change in the bias current affects the relaxation oscillation frequency of the receiver laser which determines the modulation frequency of the laser subject to the direct current modulation, resulting in a frequency mismatch between the two lasers. Therefore, when the receiver's bias current increases and at the same time the transmitter's bias current is kept constant, the receiver's chaotic outputs become poor copies of the transmitter's chaotic

outputs. This deteriorates the estimation of synchronization quality as shown by the correlation plots in Fig. 7(b1-d1). Figure 8, shows the chaotic time series and the correlation plot of the output powers for the transmitter and the receiver when 1% of the optical output of the transmitter is coupled to the receiver with a transmission time of  $T = 13.4\tau_m$  for three different modulation indexes of the receiver. The modulation index of the transmitter is fixed at  $m_t = 0.57$ , and the other modulation conditions for both lasers are  $I_{b(t,r)} = 1.5I_{th}$ , and  $f_m = 0.8$  GHz.

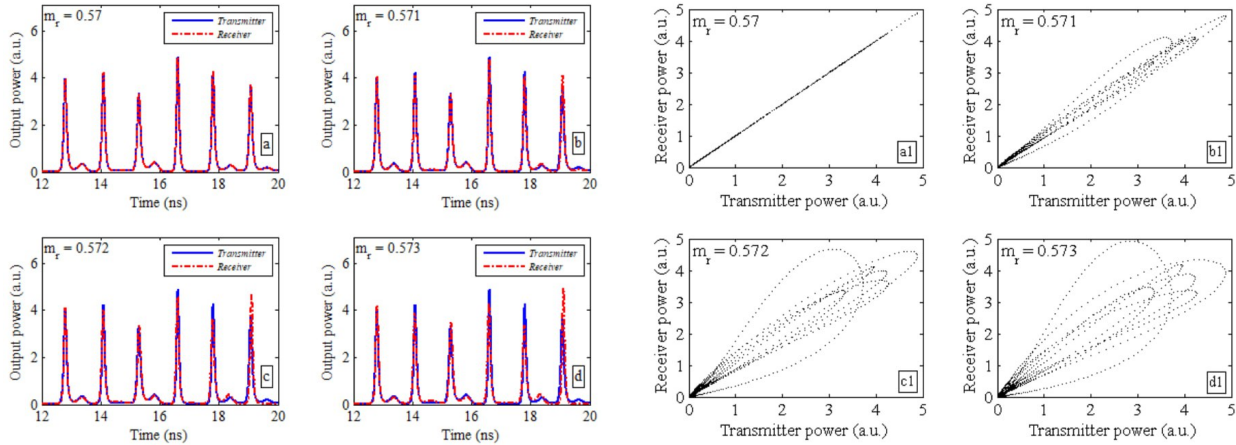


**Figure 8.** Chaotic fluctuations time series of transmitter and receiver (lift side), and transmitter output power against receiver output power for different laser modulation indexes of the receiver (right side): (a, a1)  $m_r = 0.57$ , (b, b1)  $m_r = 0.572$ , (c, c1)  $m_r = 0.574$ , and (d, d1)  $m_r = 0.576$ . The transmitter laser modulation index is fixed at  $m_t = 0.57$ . The optical coupling level and the transmission time are fixed at 1% and  $13.4\tau_m$  respectively. The other modulation conditions and the parameters values of the two lasers are identical

In Fig. 8(b-d) a slight change in the modulation index affects the amplitude of chaotic output with the keep the frequency of the receiver laser, resulting in a mismatch of the chaotic output amplitudes between the two lasers. Therefore, the increases of receiver's modulation index and at the same time the transmitter's modulation index is kept constant, the chaotic outputs of the receiver become poor copies of the transmitter's chaotic outputs. This deteriorates the estimation of synchronization quality as shown by the correlation plots in Fig. 8 (b1-d1). The cross-correlation coefficient against non-identical parameters for the case in Fig. 7, and Fig. 8, and for more values of non-identical parameters and optical coupling level up to 20%, are shown in Fig. 9.

From Figs. 9(a), and (b), for each optical coupling level, the chaos synchronization quality is calculated to be constant for each value of non-identical parameters. This is because the coupling between the two lasers was done optically (see Eq.2), and this does not affect the electrical non-identical parameters (bias current and modulation index, see Eq.4). Also, it's evident, since the modulation frequency is not as sensitive to the modulation index as to the bias current, so the drop in synchronization in the case of mismatching modulation indexes is seen as less than in the case of mismatching bias currents between the two lasers.

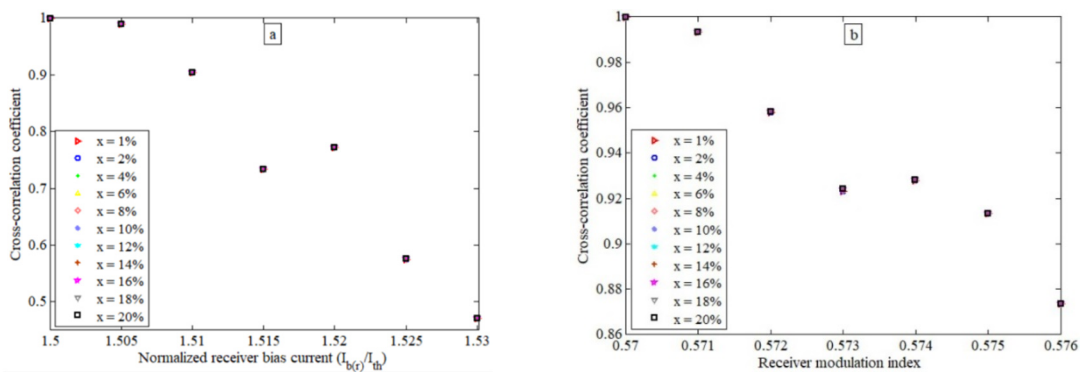


**Figure 9.** The cross-correlation coefficient against: (a) receiver bias current, and (b) receiver modulation index. The transmission time is fixed at  $13.4\tau_m$ , and the optical coupling level extends from 1% to 20%. The other modulation conditions and the parameters values of the two lasers are identical.

#### 4. CONCLUSION

Chaos synchronization is numerically investigated using two InGaAsP lasers with direct current modulation. The cross-correlation coefficient between the transmitter's output powers and the receiver's output powers is calculated when a few percent of the optical power of the transmitter is optically coupled to the receiver. The transmission time played an important role in the chaos synchronization quality. The transmission time is equal to  $T = 13.4\tau_m$  that achieves the best quality of the chaos synchronization, complete synchronization, as the synchronization quality is calculated by the cross-correlation coefficient which is equal to  $C = 1$ . On the other hand, the quality of synchronization between two non-

identical lasers is investigated. Here, the quality of synchronization decreases as the mismatch between the parameters of the two lasers increases.

## ORCID

© Mohammed H.H. Al-Jassani, <https://orcid.org/0000-0003-1463-2474>

## REFERENCES

- [1] L.M. Pecora, and T.L. Carroll, Physical review letters, **64**, 821 (1990). <https://doi.org/10.1103/PhysRevLett.64.821>
- [2] L. Kocarev, and U. Parlitz, Physical review letters, **74**, 5028 (1995). <https://doi.org/10.1103/PhysRevLett.74.5028>
- [3] H.D. Abarbanel, and M.B. Kennel, Physical review letters, **80**, 3153 (1998). <https://doi.org/10.1103/PhysRevLett.80.3153>
- [4] S.F. Abdalah, F.T. Arecchi, F. Marino, K. Al-Naimee, M. Ciszak, and R. Meucci, in: *Optoelectronic Devices and Properties*, edited by O. Sergiyenko, (InTech, 2011), pp. 651-660. <https://doi.org/10.5772/14197>
- [5] G. Yuan, X. Zhang, and Z. Wang, Optik, **125**, 1950 (2014). <https://doi.org/10.1016/j.ijleo.2013.11.007>
- [6] J. Yang, and F. Zhu, Communications in Nonlinear Science and Numerical Simulation, **18**, 926-937 (2013). <https://doi.org/10.1016/j.cnsns.2012.09.009>
- [7] S. Moon, J.J. Baik, and J.M. Seo, Communications in Nonlinear Science and Numerical Simulation, **96**, 105708 (2021). <https://doi.org/10.1016/j.cnsns.2021.105708>
- [8] C.R. Mirasso, P. Colet, and P. Garcia-Fernández, IEEE Photonics Technology Letters, **8**, 299 (1996). <https://doi.org/10.1109/68.484273>
- [9] A. Sanchez-Diaz, C.R. Mirasso, P. Colet, and P. Garcia-Fernandez, IEEE journal of quantum electronics, **35**, 292 (1999). <https://doi.org/10.1109/3.748833>
- [10] H.F. Chen, and J.M. Liu, IEEE journal of quantum electronics, **36**, 27 (2000). <https://doi.org/10.1109/3.817635>
- [11] J.M. Liu, H.F. Chen, and S. Tang, IEEE Transactions on Circuits and Systems I: Fundamental Theory and Applications, **48**, 1475 (2001). <https://doi.org/10.1109/TCSI.2001.972854>
- [12] S. Tang, and J.M. Liu, Optics letters, **26**, 596 (2001). <https://doi.org/10.1364/OL.26.000596>
- [13] S. Tang, H.F. Chen, S.K. Hwang, and J.M. Liu, IEEE Transactions on Circuits and Systems I: Fundamental Theory and Applications, **49**, 163 (2002). <https://doi.org/10.1109/81.983864>
- [14] N. Jiang, A. Zhao, S. Liu, C. Xue, and K. Qiu, Optics express, **26**, 32404 (2018). <https://doi.org/10.1364/oe.26.032404>
- [15] A. Murakami, and J. Ohtsubo, Physical Review A, **65**, 033826 (2002). <https://doi.org/10.1103/PhysRevA.65.033826>
- [16] E.M. Shahverdiev, and K.A. Shore, Optics Communications, **282**, 3568 (2009). <https://doi.org/10.1016/j.optcom.2009.05.068>
- [17] I. Oowada, H. Ariizumi, M. Li, S. Yoshimori, A. Uchida, K. Yoshimura, and P. Davis, Optics express, **17**, 10025-10034 (2009). <https://doi.org/10.1364/OE.17.010025>
- [18] L. Yu-Jin, Z. Sheng-Hai, and Q. Xing-Zhong, Chinese Physics, **16**, 463 (2007). <https://doi.org/10.1088/1009-1963/16/2/029>
- [19] S. Tang, and J.M. Liu, IEEE journal of quantum electronics, **39**, 708 (2003). <https://doi.org/10.1109/JQE.2003.810775>
- [20] M.H. Al-Lamye, and B.A. Ghalib, "High quality of generalized chaos synchronization in quantum-dot laser diode," AIP Conference Proceedings, **2386**, 080005 (2022). <https://doi.org/10.1063/5.0066864>
- [21] Y. C. Kouomou, and P. Woafu, Optics communications, **223**, 283 (2003). [https://doi.org/10.1016/S0030-4018\(03\)01683-3](https://doi.org/10.1016/S0030-4018(03)01683-3)
- [22] S.T. Kingni, C. Ainamon, V. Kamdoun, and J.C. Orou, Chaos Theory and Applications, **2**, 31-39 (2020). <https://dergipark.org.tr/en/download/article-file/1154899>
- [23] O. Junji, *Semiconductor lasers: stability, instability and chaos*, (Springer, 2017).
- [24] Y. Hori, H. Serizawa, and H. Sato, JOSA B, **5**, 1128 (1988). <https://doi.org/10.1364/JOSAB.5.001128>
- [25] E. Hemery, L. Chusseau, and J.M. Lourtioz, IEEE journal of quantum electronics, **26**, 633 (1990). <https://doi.org/10.1109/3.53379>
- [26] S. Bennett, C.M. Snowden, and S. Iezekiel, (1995). "Chaos in directly modulated laser diodes under two-tone modulation," in: *LEOS '95. IEEE Lasers and Electro-Optics Society 1995 Annual Meeting. 8th Annual Meeting. Conference Proceedings*, **2**, pp. 143-144, (1995). <https://doi.org/10.1109/LEOS.1995.484637>
- [27] S. Bennett, C.M. Snowden, and S. Iezekiel, IEEE journal of quantum electronics, **33**, 2076 (1997). <https://doi.org/10.1109/3.641323>
- [28] G. Carpintero, and H. Lamela, Journal of applied physics, **82**, 2766 (1997). <https://doi.org/10.1063/1.366108>
- [29] C.H. Lee, T.H. Yoon, and S.Y. Shin, Applied Physics Letters, **46**, 95 (1985). <https://doi.org/10.1063/1.95810>
- [30] G.P. Agrawal, Applied physics letters, **49**, 1013 (1986). <https://doi.org/10.1063/1.97456>
- [31] M. Tang, and S. Wang, Applied physics letters, **48**, 900 (1986). <https://doi.org/10.1063/1.96652>
- [32] R.J. Jones, P. Rees, P.S. Spencer, and K.A. Shore, JOSA B, **18**, 166-172 (2001). <https://doi.org/10.1364/JOSAB.18.000166>

## СИНХРОНІЗАЦІЯ ХАОСУ В InGaAsP ЛАЗЕРАХ

Мохаммед Х.Х. Аль-Джассані<sup>а</sup>, Акіл І. Фаріс<sup>б</sup>, Хусейн Х. Худхур<sup>б</sup>

<sup>а</sup>Фізичний факультет Наукового коледжу Куфського університету, Наджаф, Ірак

<sup>б</sup>Головне управління освіти в Аль-Наджаф Аль-Ашраф, Міністерство освіти, Наджаф, Ірак

Оптичний вихідний сигнал напівпровідникового лазера може хаотично коливатися шляхом модуляції його постійного струму в обмежених умовах параметрів сигналу модульованого струму з точки зору частоти модуляції та індексу модуляції. У даній роботі одиничні, подвійні та хаотичні імпульси лазера на InGaAsP з модуляцією постійного струму чисельно представлені через біфуркаційну діаграму. Чисельно, система односпрямованого оптичного сполучення реалізує хаотичну синхронізацію між двома ідентичними лазерами InGaAsP з модуляцією постійного струму, як конфігурація передавача/приймача. Час передачі світла від лазера є важливим для контролю якості синхронізації хаосу. Час передачі становить наносекунди. Якість синхронізації хаосу оцінюється кореляційним графіком і розраховується за коефіцієнтом крос-кореляції. У дослідженні спостережено найкращу якість синхронізації (повна хаотична синхронізація), коли два лазери ідентичні. З іншого боку, досліджувалася хаотична синхронізація між двома неідентичними лазерами на InGaAsP. У цьому випадку повна хаотична синхронізація не виявлена, і спостерігалось зниження якості хаотичної синхронізації зі збільшенням невідповідності між параметрами двох лазерів.

**Ключові слова:** InGaAsP лазер; синхронізація хаосу; модуляція постійного струму; оптичний зв'язок; коефіцієнт крос-кореляції

## TO STUDY THE CADMIUM SULPHIDE THIN FILMS SYNTHESIS BY SIMPLE SPIN COATING METHOD FOR ENERGY APPLICATION<sup>†</sup>

✉ **Jagmohan Lal Sharma**<sup>a</sup>, ✉ **S.K. Jain**<sup>b</sup>, ✉ **Balram Tripathi**<sup>c</sup>, ✉ **M.C. Mishra**<sup>d\*</sup>

<sup>a</sup>Raj Rishi Bhartrihari Matsya University, Alwar-301001, India

<sup>b</sup>Department of physics, Manipal University Jaipur, Jaipur-302017, India

<sup>c</sup>Department of Physics, S.S. Jain Subodh college, Jaipur-302004, India

<sup>d</sup>Department of Physics, R.R. Government College, Alwar -301001, India

\*Correspondence Author e-mail: [mahmishra11@gmail.com](mailto:mahmishra11@gmail.com)

Received July 12, 2023; revised August 15, 2023; accepted August 21, 2023

The paper examines the properties of CdS thin film, which is used for window material of solar cells and optical devices. The cadmium sulfide (CdS) thin film was prepared by sol-gel method on glass and ITO substrate. Prepared thin film dried in a vacuum oven at 70°C. Thin film and powder of CdS characterized for structural, optical, and electrical properties by X-ray Diffractometer (XRD), UV-Visible spectrometer, and Keithley spectrometer. The average crystallite sizes, micro strain and dislocation density of the samples were calculated by the Debye Scherrer formula. The optical band gap of CdS calculated by the Tauc-plot method and obtained 2.40 and 2.41eV for powder and film. The absorption wavelength of CdS is decreased near 280nm and becomes flat in the higher wavelength region. The FTIR spectrometer is used to identification of unknown materials and bond formation. The bond formation, imperfections and impurities were observed by the PL spectrometer. Keithley spectrometer is used for I-V characteristics and calculates electrical resistivity by Ohms law.

**Keywords:** Ultra-Sonication; CdS; XRD; UV-Visible; Electrical Properties

**PACS:** 43.35.Zc; 61.10.Nz; 87.64.Cc; 73.61.-r

### 1. INTRODUCTION

The cadmium sulphide (CdS) is II-VI group material. This is one of the most investigated semiconductors in the form of thin film. The creation and utilization of energy have been a cornerstone considers the improvement of human development. Sun-powered energy is accessible in the majority of the areas around world and supplies gigantic green energy that can undoubtedly cover world energy requests [1]. Cadmium sulfide (CdS) is the most normally utilized in window layer materials for high-productive cadmium telluride (CdTe) and chalcopyrite polycrystalline thin film of photovoltaic gadgets [2]. Cadmium sulfide (CdS) is a very important material in II-VI group compound semiconductors in optoelectronic devices, and extensive research and development efforts have been undertaken. The utilization of sustainable and non-contaminating energy has acquired for significance on the planet because of the weariness of petroleum products and the elevated degrees of contamination created by non-renewable energy source use. A promising type of perfect and sustainable power is hydrogen, created by the separation of water utilizing sunlight-based energy [3].

Quantum confinement effects in semiconductor nanoparticles are known to make their structural, electrical and optical properties significantly used with different from those of the bulk material [4]. Cadmium telluride has a direct band gap of 1.43 eV that is a good match to the solar spectrum for solar cell applications. The surface recombination velocity for CdTe is large so that a hetero junction structure is better suited for CdTe solar cells. Cadmium sulfide have band gap of 2.43 eV is a tunable window material for a CdS/CdTe heterojunction solar cell [5]. The cadmium (Cd) nuclei 48 and sulphur nuclei contains 16 protons with only single pair of the magic proton number  $Z = 50$  and 20 respectively, so they are providing nuclear properties like the sub shell effect and also provides outstanding test case for nuclear model calculations [6]. Thin films of CdS have used in many devices as electrochemical cells, metal Schottky barrier cells, light emitting diodes (LED), photo sensor detection, semiconductor lasers, thin films transistor, photo detectors, photoluminescence, photosensitization, photo catalytic properties solar cellular and gas sensor [6-9]. CdS used in the bulk as well as in the nano-scale form of thin film and quantum dot. Often CdS semiconductor has been worked for a long time and it has been very a fascinating material due to its band gap value, n-type conductivity and high transparency for optoelectronic device applications. The n-type CdS semiconductor can be utilized as a window layer along with retention layers of CdTe or CIGS to create high-effective sunlight-based cells [10]. Cadmium telluride (CdTe) and CdS based slender film sun-oriented cells have drawn in for overall exploration consideration throughout recent many years to foster minimal expense and high productivity sun powered chargers appropriate for photovoltaic sun-based energy change. It is a special interesting choice due to its appropriate band gap (2.42 eV) relatively high absorption coefficients, particular optical properties and pattern of fabrication. CdS exhibits n-type semi conduction properties due to sulfur deficiency. The dispersion parameters of the pure and F: CdS films were used to determine the nonlinear optical susceptibility [12-14]. The highest 1.25% efficiency was obtained from inexpensive materials in this used porous CdS as a photo electrode [15]. Many techniques as spin coating radio frequency, vacuum evaporation, sputtering, electro-deposition, molecular beam

<sup>†</sup> Cite as: J.L. Sharma, S.K. Jain, B. Tripathi, M.C. Mishra, East Eur. J. Phys. 3, 599 (2023), <https://doi.org/10.26565/2312-4334-2023-3-71>  
© J.L. Sharma, S.K. Jain, B. Tripathi, M.C. Mishra, 2023

epitaxial (MBE), metal organic chemical vapor deposition (MOCVD), pulsed laser evaporation, spray pyrolysis deposition (SPD), micelle method, chemical bath deposition (CBD), close-spaced sublimation (CSS) and successive ionic layer adsorption have been used to synthesis thin films for a good quality and long time. These techniques have also been used for the preparation of CdS films [16-17]. The synthesis of nanoparticles for the green approach is favored over traditional methodologies due to environmental concerns [21].

In the present work CdS thin films synthesized by spin coating method. Films dried in vacuum oven at 70°C and 24 hours to analyzed structural, optical and electrical properties of powder and thin films of CdS.

## 2. Experimental details

### 2.1. Solution preparation method

Cadmium sulphide (CdS) yellow colour and powder form purchased from Sigmachemie specialty Pvt. Ltd. (Amaranth West, Maharashtra) with  $144.47\text{g mol}^{-1}$  molecular weight and 99.9% and above purity. Dichloromethane ( $\text{CH}_2\text{Cl}_2$ ) Qualikemes, Propane -2-ol ( $(\text{CH}_3)_2\text{CHOH}$ ), and Triton X-100 were also purchased Fine chem. Pvt. Ltd. in liquid form. Cadmium sulphide (CdS), dichloromethane ( $\text{CH}_2\text{Cl}_2$ ), propane -2-ol ( $(\text{CH}_3)_2\text{CHOH}$ ) were used to prepared CdS solution. Dichloromethane ( $\text{CH}_2\text{Cl}_2$ ) and propane -2-ol ( $(\text{CH}_3)_2\text{CHOH}$ ) were taken with 10:1 volume ratio 0.5 wt% CdS powder was dissolved in the mixed co-solvents. The color of the CdS solution was yellow. After that the CdS solution was stirred on the hot plate of magnetic stirrer for 8 hours at room temperature. After stirring a small amount of triton X-100 was added in the solution to make uniform and high-quality surface of CdS thin films.

### 2.2. Deposition of CdS thin films

The CdS thin film was synthesized on glass and ITO surface by using spin coating method. The glass substrate was first cleaned with acetone and DI water. The CdS precursor solution was spin coated one time on glass and ITO  $1 \times 1\text{ cm}^2$  surface at speeds of 1500 rpm for 60 sec. The prepared CdS films were dried at 70°C in vacuum oven.

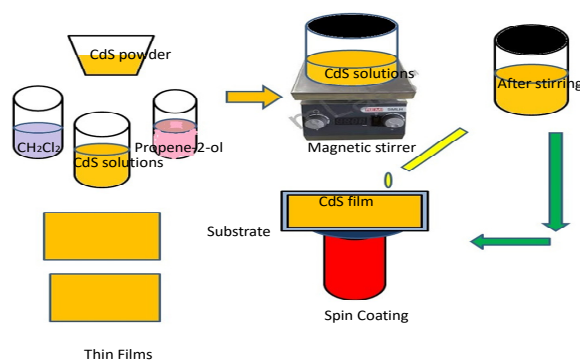


Figure 1. Schematic diagram of CdS thin film deposition process

## 3. CHARACTERIZATION

The X-ray Diffraction (XRD) spectra have been collected of powder and thin film of CdS sample by using copper (Cu)  $\text{K}\alpha$  Bruker AXS Single Crystal X-ray Diffractometer (modal Apex II) in the range  $(2\theta)$   $10^\circ$ - $80^\circ$  with step size  $1/100^\circ$ . UV-visible and FTIR spectra have collected shimadzu (UV-2600) wave length range 200-900nm, ALPHA Bruker FTIR spectroscopy (ECO-ATR) in the transmittance mode at room temperature in the wave number range  $4000$ - $200\text{ cm}^{-1}$ . Horiba FluoroMax-4 spectrometer have used for photoluminescence spectra (PL). Current-voltage curves were obtained by a Keithley M236 source measure unit.

## 4. Results and discussion

### 4.1. Structural studies (X-Ray diffraction)

The structural analysis of CdS powder and synthesized CdS thin film was studied using X-ray diffraction pattern. XRD pattern of the CdS illustrated in below Figure 1 which presents the indexed of cubic structure of CdS (JCPDS – file No. 10-0454) with prominent peaks observed corresponding to the reflections at (111), (220), (311) planes at angles  $2\theta$  equal to  $26.680$ ,  $43.570$ ,  $52.060$  respectively. The sharp peaks of thin film Figure a) indicating transparency of thin film. XRD pattern in Figure b) intensity decreases and FWHM width increases indicating that the difference of particle sizes between film and powder. The d-spacing for both samples can be evaluated from the position of the major peak at about  $26.06^\circ$ .

The average particle size of the CdS calculated using Scherer formula

$$D = k\lambda / \beta \cos\theta,$$

where, constant k is a shape factor usually  $= 0.94$ , D is the average crystalline size,  $\lambda$  is the wavelength of X-ray radiation,  $\beta$  is also a constant define by the full-width at half-maximum (FMWH) of the peak, and  $\theta$  is the diffraction angle.

The lattice constant of synthesized CdS is found to be equal to  $a = b = c = 5.86 \text{ \AA}$ , which is close to reported values of cubic CdS by literature of review [17].

The crystallites size and dislocation density can be found from

$$\delta = 1/D^2.$$

The lattice strain in the film can be found by,

$$\epsilon = \frac{\beta \cos\theta}{4}.$$

**Table 1.** Shows the results of thin film and powder of CdS

| S.N. | Sample name   | Average particle size (D) (nm) | Dislocation density ( $\delta$ ) | Strain ( $\epsilon$ ) | Energy Band gap (eV) | Resistivity ( $\rho \times 10^{-2}$ ) ( $\Omega\text{-cm}$ ) |
|------|---------------|--------------------------------|----------------------------------|-----------------------|----------------------|--|
| 1    | CdS Thin Film | 34.45                          | 0.08426                          | 0.3279                | 2.41                 | 3.351  |
| 2    | CdS Powder    | 26.06                          | 0.01472                          | 0.12639               | 2.40                 | 4.166  |

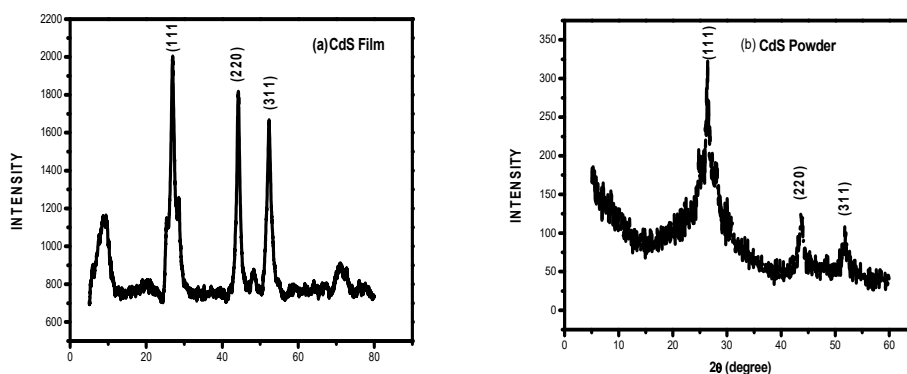


**Figure 2.** X-Ray diffraction pattern of a) CdS Thin film b) CdS powder

#### 4.2. Scanning electron microscope

SEM microscope produces images of material by scanning of the surface. The SEM measurements were performed of CdS thin films to study their surface morphology with different images. The particle size distribution and corresponding Gaussian curve fitting of sample is show in Figure 3. It has observed that the CdS thin film surface become uniform and particle distribute everywhere but random conformed amorphous shapes. SEM image clarify that the thin film surface was smooth, random distribution of particles and contains spherically formed grains. The surface was enclosed in grains with uniform size. The thin sheets display no cracks or pin prick in the materials [26].

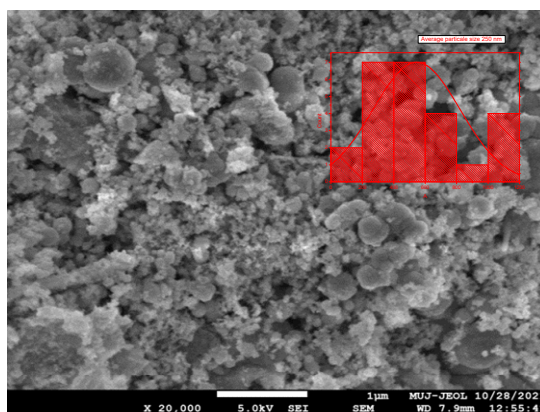


**Figure 3.** SEM image of CdS thin film

#### 4.3. Optical studies

UV-Visible absorption spectrum of the cadmium sulphide powder and films are show in Figure 4. The optical properties of CdS reflected on the UV-Visible spectral data in the region of 370-400 nm wavelengths with a red shift of absorption wavelength. The results of above analysis are similar to other researcher by literature. A strong absorption in the ultraviolet region was observed at wavelength about 397 nm, 400 nm for film and powder respectively. Which was fairly blue shifted from the absorption edge due to quantum confinement effects [16, 18].

The optical band gap of CdS powder and film calculated using Tauc's plot method. The Tauc's equation

$$\alpha h\nu = B (h\nu - E_g)^n \tag{1}$$

is used, where the absorption coefficient is  $\alpha$ , the energy of photon is  $h\nu$ , B is an also constant,  $E_g$  is the band gap and  $n = 1/2$  for direct allowed transition. The optical band gap is decided from the boundaries gotten of a straight contraction of the term  $(\alpha h\nu)^2$ , [27] whose convergence with the x-axis (in  $\alpha=0$ ) gives the optical band gap. This graphical interpretation starts by replacing the wavelength values to energy level using the equation (1), which comes from:  $E_g = ch/\lambda$ . To obtain absorption coefficient by measured absorbance assume that sample thickness is  $1\mu\text{m}$  which is measured by cross section of SEM micrograph of the Sample  $\alpha = 2.303A/t$ , 'A' measured by UV-Visible spectrometer and 't' sample thickness. According to Figure 4 band gap obtained CdS powder 2.40 eV and CdS film 2.41 eV approximately equal.

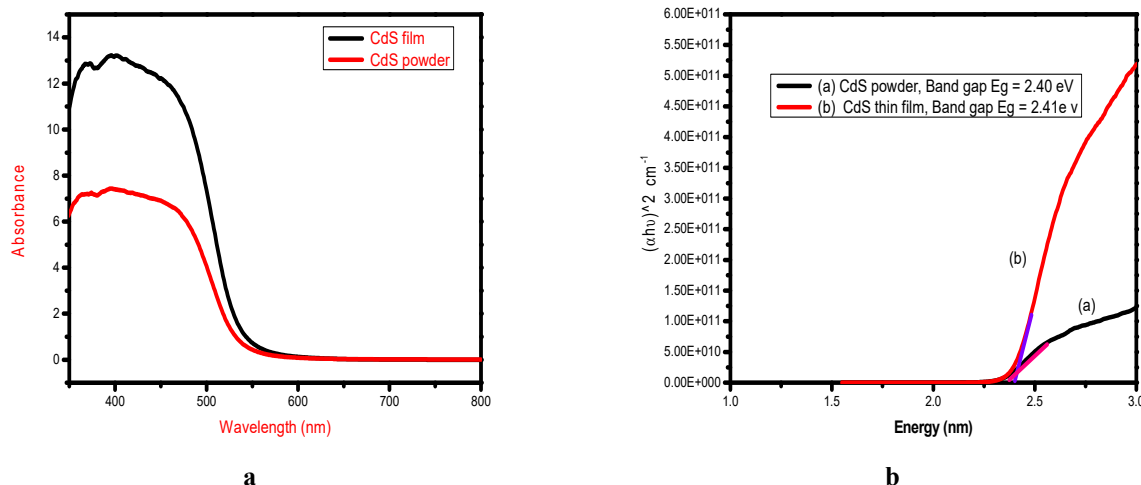


Figure 4. a) Absorption v/s wave length, 4b) Band gap by Tauc's plot method

#### 4.4. Fourier transforms infrared spectra (FTIR)

Figure 5 shows the Fourier transform infrared (FTIR) spectra of deposited powder and films are recorded on a FTIR spectrometer. The more vibration in powder form and less vibration in film represent good agreement with solvent. The FTIR spectra CdS conforming to the existence of constitutional elements functional group and chemical bonding between Cd and S. FTIR spectra were lies from  $400$  to  $4000\text{ cm}^{-1}$  at room temperature. The absorption bands of FTIR spectra on wave number  $1030\text{--}1070\text{ cm}^{-1}$  represents the S = O sulphide group. The sharp bending at the infrared active spectrum due to absorption band  $1365\text{--}1465\text{ cm}^{-1}$ , it is indicated by C–H and N–H bonding goes to  $1580\text{--}1650\text{ cm}^{-1}$ . The prominent  $2250\text{ cm}^{-1}$  caused by  $\text{C}\equiv\text{N}$ . The powder form of CdS shows water molecules stretching O–H between  $3000\text{--}3550\text{ cm}^{-1}$  due to solvent. The band at  $720\text{ cm}^{-1}$  relate to the Cd–S bond which substantiate the formation of CdS particles [22].

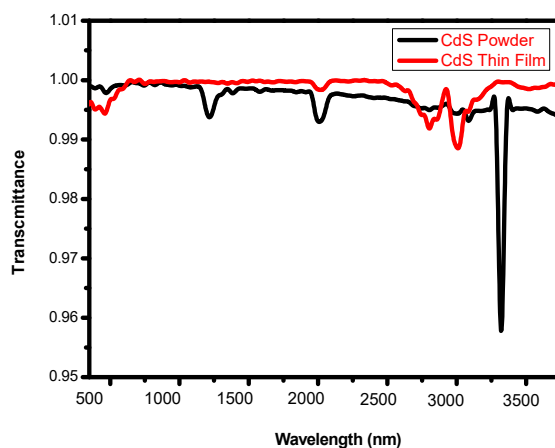


Figure 5. FTIR graphs of powder and film of CdS

#### 4.5. Photoluminescence spectra (PL)

Photoluminescence (PL) spectroscopy has been used to study of the photo luminescence spectra of CdS powder and films with an excitation wavelength of  $507\text{ nm}$ . The PL spectra of the deposited CdS powder and films have been recorded the wavelength range between  $600\text{ nm} - 650\text{ nm}$  (Fig. 6). PL spectra indicate of the CdS exhibited two distinct PL bands but the peak positions and PL intensities of the powder and film were remains same due to different physical condition of cadmium sources [19]. The PL emission peaks centered around  $630\text{ nm}$  for powder and film both. CdS shows band to band transition and direct band gap.

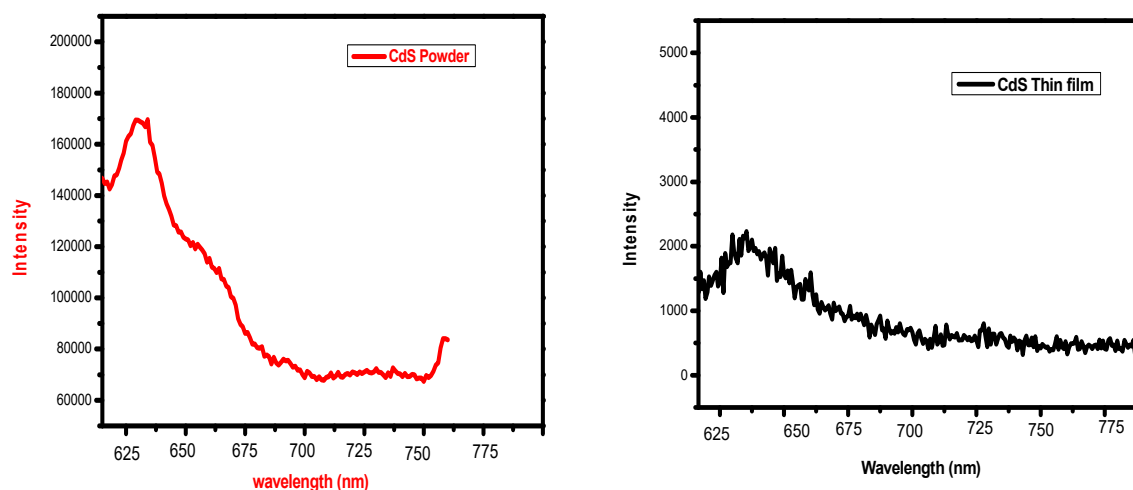


Figure 6. PL graph of powder and thin film CdS

#### 4.6. Electrical studies (V-I Characteristics)

Figure 7 Shows I-V characteristics of the CdS films, were traced out by the Keithley spectrometer. The non Ohmic I-V characteristics can be attributed to the schottky contacts between CdS and metal contacts by silver paste. The current difference  $\Delta I$  is defined as current  $I_{max}$  -  $I_{min}$  at a specific bias voltage.  $I_{max}$  is the maximum current and  $I_{min}$  is the minimum currents on the linear part of the curve. The electrical resistivity is calculated using  $\rho = VA/IL$ , where  $I$  is the current in mA,  $L$  the thickness of the sample ( $1\mu\text{m}$ ),  $V$  the applied voltage, and  $A$  is the cross-section area of the sample. The calculated resistivity of film and powder were  $3.351\ \Omega\cdot\text{cm}$ ,  $4.166\ \Omega\cdot\text{cm}$  respectively [25, 26].

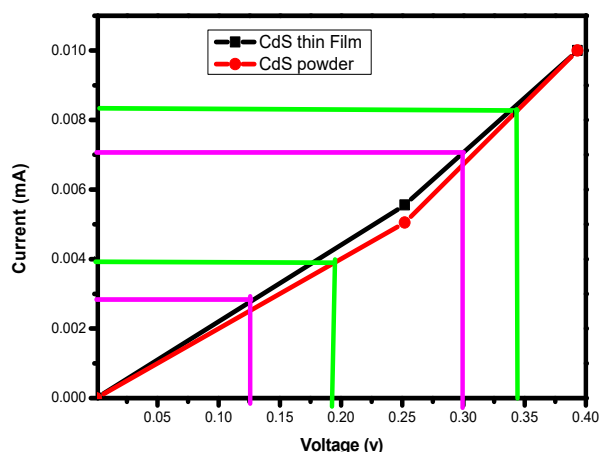


Figure 7. I-V Characteristics of powder and thin film CdS

### 5. CONCLUSION

In this paper spin coating method is used for CdS thin film. The prepared thin film has a bandgap of 2.41 eV. X-ray diffraction spectra show that film exists in the cubic phase. FTIR spectra confirmed sharp and strong bonding of composition. PL spectra indicate one strong visible emission band at about 630 nm for CdS. Intensity decreases of thin film comparatively to powder form due to bond formation. SEM image shows that particles are distributed randomly on the surface of thin films. The obtained resistivity of the CdS thin film was  $3.351\ \Omega\cdot\text{cm}$ .

#### Acknowledgement

We are appreciativeness RUSA component-8 R.R. College Alwar, Principal of S.S. Jain Subodh College, Jaipur and Vice Chancellor of Manipal University, Jaipur for provided material synthesis facilities and characterization facility.

#### ORCID

🌐 Jagmohan Lal Sharma, <https://orcid.org/0009-0004-9223-7634>; 🌐 Balram Tripathi, <https://orcid.org/0000-0002-8324-7863>  
 🌐 S.K. Jain, <https://orcid.org/0000-0001-6454-2392>; 🌐 M.C. Mishra, <https://orcid.org/0009-0006-5797-0085>

#### REFERENCES

- [1] A. Ashok, G. Regmi, A. Romero-Núñez, M. Solis-López, S. Velumani, and H. Castaneda, "Comparative studies of CdS thin films by chemical bath deposition techniques as a buffer layer for solar cell applications," *J. Mater. Sci: Mater Electron.* **31**, 7499-7518, (2020). <https://doi.org/10.1007/s10854-020-03024-3A>

- [2] O. Adnan, and A.N. Naje, "Manal enhancement of CdS nanoparticles photoconductive detector by adding TPD conductive polymer," *Materials for Renewable and Sustainable Energy*, **7**, 28, (2018). <https://doi.org/10.1007/s40243-018-0135-71>
- [3] J.R. González-Moya, Y. Garcia-Basabe, M.L.M. Rocco, M.B. Pereira, J.L. Princival, L.C. Almeida, C.M. Araújo, et al., "Effects of the large distribution of CdS quantum dot sizes on the charge transfer interactions into TiO<sub>2</sub> nanotubes for photo catalytic photo catalytic hydrogen generation," *Nanotechnology*, **27**, 285401 (2016). <https://doi.org/10.1088/0957-4484/27/28/285401>
- [4] P. Rodríguez, N. Muñoz-Aguirre, E.S.-M. Martínez, G. Gonzalez, O. Zelaya, and J. Mendoza, "Formation of CdS nanoparticles using starch as capping agent," *Applied Surface Science*, **255**, 740-742, (2008). <https://doi.org/10.1016/j.apsusc.2008.07.032>
- [5] M. Shaban, M. Mustafa, and H. Hamdy, "Morphological and optical study of sol-gel spin coated nanostructured CdS thin films," *IOSR Journal of Applied Physics (IOSR-JAP)*, **7**(6), 19-22 (2015). <https://doi.org/10.9790/4861-07611922>
- [6] J.Z. Han, C. Pan, K.Y. Zhang, X.F. Yang, S.Q. Zhang, J.C. Berengut, S. Goriely, et al., "Isotope shift factors for the Cd+ 5s 2S1/2 → 5p 2P3/2 transition and determination of Cd nuclear charge radii," *Physical review research*, **4**, 033049 (2022). <https://doi.org/10.1103/PhysRevResearch.4.033049>
- [7] X. Wang, A. Han, Y. Huang, X. Liu, and Z. Liu, "Structural, optical and impurity-absorption properties of CdS thin films deposited by chemical bath using four cadmium sources," *Semicond. Sci. Technol.* **32**, 075008 (2017). <https://doi.org/10.1088/1361-6641/aa7299>
- [8] N.J. Egwunyenga, I.S. Okunzuwa, I.L. Imosobomeh, "Synthesis of SnS/SnO nanostructure material for photovoltaic application *East European journal of physics*, **1**, 154-161 (2023). <https://doi.org/10.26565/2312-4334-2023-1-19>
- [9] A. Zyoud, I. Saa, S. Khudruj, Z.M. Hawash, D.H. Park, G. Campet, and H.S. Hilal, "CdS/FTO thin film electrodes deposited by chemical bath deposition and by electrochemical deposition: A comparative assessment of photo-electrochemical characteristics," *Solid State Sciences*, **18**, 83-90 (2013). <http://dx.doi.org/10.1016/j.solidstatesciences.2013.01.004>
- [10] A. Kar, S. Kundu, and A. Patra, "Photocatalytic properties of semiconductor SnO<sub>2</sub>/CdS heterostructure," *Nanocrystals, RSC Advances*, **2**, 10222-10230 (2012). <https://doi.org/10.1039/c2ra21065g>
- [11] M.I., Dharmadasa, "Review of the CdCl<sub>2</sub> treatment used in CdS/CdTe thin film solar cell development and new evidence towards improved understanding," *Coatings*, **4**, 282-307 (2014). <https://doi.org/10.3390/coatings4020282>
- [12] R. Zahid, Z. Azmi, S. Mohd, G. Mohd, J. Atefeh, and F.U.D.Z. Reza, "Effect of Annealing Temperature on the Optical Spectra of CdS Thin Films Deposited at Low Solution Concentrations by Chemical Bath Deposition (CBD) Techniques," *Int. J. Mol. Sci.* **12**, 1293-1305 (2011). <https://doi.org/10.3390/ijms12021293>
- [13] I.M.El. Radaf, T.A. Hamid, and I.S. Yahia, "Synthesis and characterization of F-doped CdS thin films by spray pyrolysis for photovoltaic applications," *Mater. Res. Express*, **5**, 066416 (2018). <https://doi.org/10.1088/2053-1591/aaca7b>
- [14] R. Udayakumar, V. Khanaa, and T. Saravanan, "Synthesis and structural characterization of thin films of SnO<sub>2</sub> prepared by spray pyrolysis technique," *Indian Journal of Science and Technology*, **6**(6S), 1-4 (2013). <https://doi.org/10.17485/ijst/2013/v6isp6.19>
- [15] A.A. Hussain, H. Abdulelah, A.H. Amteghy, R.A. Dheyab, and B.H. AlMulla, "Effect of multilayers CdS nanocrystalline thin films on the performance of dye-sensitized solar cells," *Hindawi Journal of Nanotechnology*, **2023**, 7998917 (2023). <https://doi.org/10.1155/2023/7998917>
- [16] R. Elilarssi, I.S. Maheshwari, and G. Chandrasekaran, "Structural and optical characterization of CdS nanoparticles synthesized using a simple chemical reaction route optoelectronics and advanced materials," *Rapid communication*, **4**(3), 309-312 (2010).
- [17] E.N. Josephine, O.S. Ikponmwosa, and I.L. Ikhioya, "Synthesis of SnS/SnO nanostructure material for photovoltaic application," *East European Journal of Physics*, **1**, 154-161, (2023). <https://doi.org/10.26565/2312-4334-2023-1-19>
- [18] M.M. Rose, R.S. Christy, T.A. Benitta, and J.T.T. Kumaran, "Structural, electrical and optical studies of NixCd1-xS (x = 0.8, 0.6, 0.4 and 0.2) nanoparticles system," *East European Journal of Physics*, **1**, 146-153, (2023), <https://doi.org/10.26565/2312-4334-2023-1-18>
- [19] V. Narasimman, V.S. Nagarethinam, K. Usharani, and A.R. Balu, "Structural, morphological, optical and electrical properties of spray deposited ternary CdAgS thin films towards optoelectronic applications," **22**(2), 79-84 (2018). <https://doi.org/10.1080/14328917.2016.1264857>
- [20] I. Kulandaishamy, K.D.A. Kumar, K. Ramesh, H.A. Ibrahim, and N.S. Awwad, "Ag-doped PbS thin films by nebulizer spray pyrolysis for solar cells," *Int. J. Energy Res.* **44**(6), 4505-4515 (2020). <https://doi.org/10.1002/er.5227>
- [21] H. Dabhane, S. Ghotekar, P. Tambade, S. Pansambal, H.C.A. Murthy, R. Oza, and V. Medhane, "A review on environmentally benevolent synthesis of CdS nanocoarticle and their applications," *Environmental chemistry and ecotoxicology*, **3**, 209-219 (2021). <http://dx.doi.org/10.1016/j.eneco.2021.06.002>
- [22] T. Iqbal, G. Ara, N.R. Khalid, and M. Ijaz, "Simple synthesis of Ag-doped CdS nanostructure material with excellent properties," *Applied Nanoscience*, **10**, 23-28 (2020). <https://doi.org/10.1007/s13204-019-01044-y>
- [23] S. Preeti, "Synthesis and characterization of CdS nanoparticles," *International journal of engineering & technology (IJERT)*, **6**(01), (2018).
- [24] Surbhi, D. Shalya, and S. Kumar, "Molecular geometry, homo-lumo analysis and mulliken charge distribution of 2,6- dichloro-4-fluoro phenol using DFT and HF method," *East European Journal of Physics*, **1**, 205-209 (2023). <https://doi.org/10.26565/2312-4334-2023-1-27>
- [25] H. Das, and P. Datta, "Optically sensitive I-V properties of CdS and CdS:Cu Quantum dots," *Materials Research Express*, **6**, 045023 (2018). <https://doi.org/10.1088/2053-1591/aafaaa>
- [26] T. Chandan, S.K. Dwivedi, M.B. Zaman, and P. Rajaram, "Structural, optical and photoelectric properties of sprayed CdS thin films," *American Institute of Physics*, **1953**, 100067 (2018). <https://doi.org/10.1063/1.5033003>
- [27] A.S. Najm, H.S. Naeem, D.A.R.M. Alwarid, A. Aljuhani, S.A. Hasbullah, H.A. Has, K. Sopian, et al., "Mechanism of chemical bath deposition of CdS thin films: influence of sulphur precursor concentration microstructural and optoelectronic characterizations," *Coatings*, **12**(10), 1400 (2022). <https://doi.org/10.3390/coatings12101400>

**ДОСЛІДЖЕННЯ СИНТЕЗУ ТОНКИХ ПЛІВОК СУЛЬФІДУ КАДМІЮ ОТРИМАНИХ МЕТОДОМ  
ПРОСТОГО ОБЕРТАННЯ ДЛЯ ЗАСТОСУВАННЯ В ЕНЕРГЕТИЦІ**

**Джагмохан Лал Шарма<sup>a</sup>, С.К. Джейн<sup>b</sup>, Бальрам Тріпаті<sup>c</sup>, М.С. Мішра<sup>d</sup>**

<sup>a</sup>Університет Радж Ріші Бхартарі Матсія, Алвар-301001, Індія

<sup>b</sup>Кафедра фізики Маніпальського університету Джайтур, Джайтур-302017, Індія

<sup>c</sup>Кафедра фізики, С.С. Джайн Субод коледж, Джайтур-302004, Індія

<sup>d</sup>Кафедра фізики, Р.Р. державний коледж, Алвар -304001, Індія

У статті досліджено властивості тонкої плівки CdS, яка використовується для виготовлення віконних матеріалів сонячних батарей та оптичних пристроїв. Тонка плівка сульфід кадмію (CdS), отримана золь-гель методом на склі та підкладці ІТО. Підготовлену тонку плівку сушать у вакуумній печі при 70 °С. Тонка плівка та порошок CdS характеризуються структурними, оптичними та електричними властивостями за допомогою рентгенівського дифрактометра (XRD), УФ-видимого спектрометра та спектрометра Кейтлі. Середні розміри кристалітів, мікродеформації та густину дислокацій зразків розраховують за формулою Дебая Шеррера. Ширина забороненої зони CdS, розрахована методом Таус-plot, становить 2,40 та 2,41 еВ для порошку та плівки. Довжина хвилі поглинання CdS раптово зменшується біля 280 нм і стає плоскою у вищій області довжин хвиль. Спектрометр FTIR використовується для ідентифікації матеріалів і утворення зв'язків. Утворення зв'язків, дефектів та домішок спостерігали на спектрометрі Кейтлі, який використовується для вимірювання ВАХ і обчислення питомого електричного опору за законом Ома.

**Ключові слова:** *ультразвукова обробка; CdS; XRD; видимий УФ; електричні властивості*

## THE EFFECT OF PLASMA ACTIVATION OF REACTIVE GAS IN REACTIVE MAGNETRON SPUTTERING<sup>†</sup>

Stanislav V. Dudin, Stanislav D. Yakovin, Aleksandr V. Zykov

V.N. Karazin Kharkiv National University

4 Svobody Sq., Kharkiv 61022, Ukraine

Corresponding Author e-mail: [dudin@karazin.ua](mailto:dudin@karazin.ua)

Received July, 11, 2023; revised August 5, 2023; accepted August 10

The effect of plasma activation of reactive gas on the process of reactive magnetron synthesis of oxide coatings was theoretically and experimentally investigated using a radio-frequency inductively coupled plasma source, which creates a flow of activated reactive gas directed towards the surface on which the oxide coating is deposited. The reactive gas passes through a dense inductively coupled plasma located inside the plasma source, while argon is supplied through a separate channel near the magnetron. A theoretical model has been built allowing the calculation of spatial distributions of fluxes of metal atoms and molecules of activated reaction gas, as well as the stoichiometry area of the synthesized coatings. Calculations were performed on the example of aluminum oxide. It was found that the plasma activation of the reactive gas allows to increase the sticking coefficient of oxygen to the surface of the growing coating from values less than 0.1 for non-activated molecular oxygen to 0.9 when 500 W of RF power is introduced into the inductive discharge. In order to verify the developed model, experiments were conducted on depositing an aluminum oxide film on glass substrates located at different distances from the magnetron target, followed by measuring the distribution of film transparency along the substrate length and comparing it with the calculated distribution. A comparison of the calculation results with the experimental data shows a good agreement in the entire studied range of parameters. Based on the generalization of the obtained results, an empirical rule was formulated that the power ratio of the magnetron discharge and the plasma activator should be approximately 8:1.

**Keywords:** *Reactive magnetron synthesis, Inductively coupled plasma, Plasma activation of reactive gas, Mathematical simulation*

**PACS:** 52.77.Dq

### INTRODUCTION

Reactive magnetron sputtering is one of the promising methods for the synthesis of high-quality coatings of metal oxides or nitrides on the surface of various products for mechanical engineering, microelectronics, optics, and also for medical applications. A significant disadvantage of the reactive magnetron sputtering is the interaction of the reactive gas not only with the growing film but also with the surface of the magnetron target. Because of this, the target is covered with oxide film causing a decrease in the sputtering rate and the appearance of process instability. The main challenge of reactive magnetron sputtering is the preferential delivery of reactive gas to the surface of the growing film keeping the magnetron target non-oxidized.

It is known that when alumina coatings are deposited by reactive magnetron synthesis, one of the main problems is the low sticking coefficient of molecular oxygen to the aluminum surface. In particular, in [1], the sticking coefficient of oxygen molecules to an atomically pure aluminum surface in ultrahigh vacuum was experimentally measured, while it was found that the probability of an oxygen molecule in the ground state sticking to the aluminum surface at room temperature is about 2%. In [2], similar results were obtained using mathematical modeling by the molecular dynamics method. The results of [3, 4] show that even in conditions typical for industrial technologies (not perfect vacuum, limited surface cleanliness), the sticking coefficient of molecular oxygen to the surface of a growing film in the process of reactive magnetron synthesis does not exceed several percent and the ratio of the flows of oxygen and aluminum required to obtain a stoichiometric film is at least 17.

Since in the reactive magnetron synthesis of  $\text{Al}_2\text{O}_3$  it is necessary to achieve a high sticking coefficient of oxygen to the almost completely oxidized surface of the growing film, the described results of fundamental studies of molecular oxygen sticking to the atomically clean surface of aluminum can be applied to the description of the synthesis of stoichiometric films of aluminum oxide only indirectly. Therefore, for the practical use of scientific data, it is necessary to build a mathematical model based on the results of systematic measurements of the stoichiometric composition of the synthesized coatings at different ratios of metal and reactive gas flows. As we showed earlier [5], an extremely important role is played not only by the value of the reactive gas flow, but also by the oxygen state (vibrational excitation and dissociation degree of the molecules), and plasma activation of the reactive gas flow can increase the oxygen sticking coefficient dramatically.

Attempts to use plasma activation of reactive gas are known, moreover, in almost any magnetron sputtering system (especially when using an unbalanced magnetron), gas activation occurs in the magnetron plasma, but the effect of such activation is usually small, and to this day there is no clear understanding of the mechanisms of plasma activation and precise "recipes" for the organization of technological processes.

Plasma is a powerful tool, but its effect on gas is quite complex: ionization, excitation, dissociation, and the relationship between these processes strongly depends on the type and pressure of the gas, the density and temperature of

<sup>†</sup> *Cite as:* S.V. Dudin, S.D. Yakovin, A.V. Zykov, East Eur. J. Phys. 3, 606 (2023), <https://doi.org/10.26565/2312-4334-2023-3-72>

© S.V. Dudin, S.D. Yakovin, A.V. Zykov, 2023

electrons, and the properties of the surfaces limiting the plasma. It is very difficult to separate these effects, so here we use the term "plasma activation", under which we understand the complex effect of plasma on a neutral gas, which increases its reactive properties. The effectiveness of plasma activation in reactive magnetron synthesis can be quantified through an increase in the sticking coefficient of the reactive gas.

It is well known that additional activation of the reactive gas significantly improves gas utilization, thus reducing the required gas flow rate that allows the target sputtering in metallic mode. To increase the degree of activation of reactive gas particles, magnetron sputtering technology with additional ionization was used. In particular, this is described in [6]. The process of film growth during reactive deposition consists of two stages. The first is the condensation of the material sputtered from the target. The second is the reaction of the film material with the reactive gas. It was shown that an increase in the plasma density near the substrate by means of an additional inductively coupled discharge makes it possible to increase the activity of the gas and the sticking coefficient of its molecules to the growing film. However, this approach puts RF power not only into the reactive gas but also into the sputtering gas (which takes most of the gas mixture) that greatly reduces the efficiency of the system. In addition, this power is deposited into a large volume of plasma, which also leads to its inefficient use.

In this paper, we explore a different approach. The reactive gas passes through a dense inductively coupled plasma localized inside a dedicated plasma source, while argon is fed through a separate channel near the magnetron. As a result of the concentration of high RF power in a small volume, a dense plasma is created there, which makes it possible to achieve a higher degree of activation of the reactive gas. As a result, a directed flow of activated reactive gas is formed, which, if the process is properly organized, can be delivered directly to the surface of the growing film. Taking into account the complexity of choosing the optimal geometry of the system a mathematical model has been developed and experimentally verified that is described below.

### EXPERIMENTAL RESULTS

The process of reactive magnetron sputtering was studied using the multifunctional Cluster Ion-Plasma System (CIPS) [7], which consists of compatible sources of fluxes of metal atoms, ions, and chemically active particles for a complex effect on the growing film. In the current research, the unbalanced magnetron was used in pair with the gas-activating plasma source. The layout of the system may be found in [7]. The RF inductively coupled plasma source is designed to create a flow of activated reactive gas particles, as well as a flow of slow ions and electrons. It can be also used to clean the surface of processed parts prior to coating deposition. The ICP source is located inside the vacuum chamber and can be moved, which allows choosing the optimal ratio between the distances from the sample to the magnetron and to the plasma source. The plasma in such a source is concentrated in a chamber made of a ceramic tube (Fig. 1).

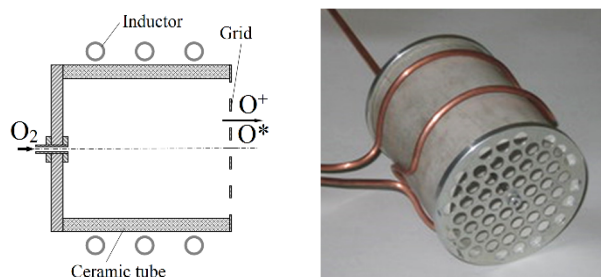


**Figure 1.** ICP source for reactive gas activation

At the outlet of the source, a metal grid is installed, which limits the plasma and ensures a pressure difference between the source and the technological chamber. An RF generator with a frequency of 13.56 MHz and a power of up to 1 kW is connected to the inductor coil through a matching circuit. Fig. 2 presents a photo of the simultaneous operation of the magnetron and the plasma source. Details of the gas activation in plasma are discussed in [8].

When studying the transparency of oxide films depending on stoichiometry, an interesting fact was found: a non-stoichiometric film is more transparent to long-wave light with the greatest transparency in the infrared range. This phenomenon is illustrated in Fig. 3.

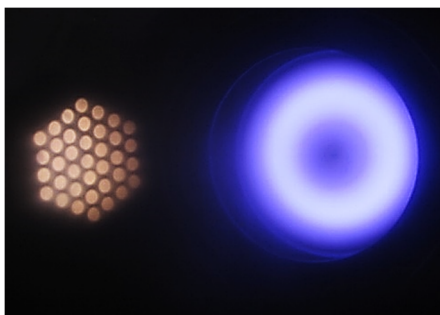


**Figure 2.** Photograph of the simultaneous operation of the magnetron and the plasma source.

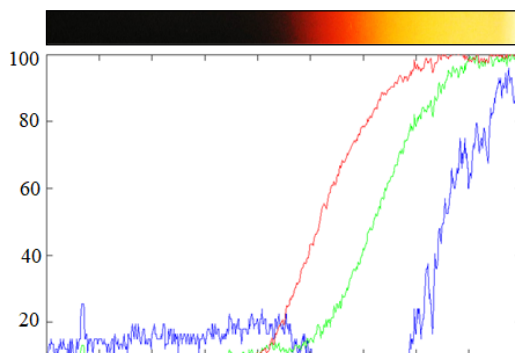


**Figure 3.** Distribution of the transparency of the alumina film along the sample for radiation with different wavelengths: 650 nm (red line), 450 nm (blue line), 550 nm (green line). On the right edge of the sample, the film is completely stoichiometric

**THEORETICAL MODEL**

To improve the understanding of the process of plasma activation of the reactive gas during reactive magnetron synthesis of oxide coatings, a mathematical model was built, which is described below.

The dependence of the current density of argon ions on the target surface from the radius is given by the following piecewise linear approximation:

$$J_{Ar}(r) := \left( \frac{R2 - R1}{2} - \left| r - \frac{R1 + R2}{2} \right| \right), \tag{1}$$

where  $R1 = 2$  cm and  $R2 = 7$  cm are the inner and outer radii of the erosion area of the magnetron target. The normalization constant for this dependence was determined by calculating the integral current of argon ions on the target, which is equal to the magnetron discharge current measured in the experiment:

$$I_{Ar\_norm} := \int_{R1}^{R2} J_{Ar}(r) \cdot 2 \cdot \pi \cdot r dr. \tag{2}$$

The flux density of sputtered aluminum atoms at a point with coordinates  $r, z$  through a surface located at an angle  $\alpha_s$  to the axis of the magnetron is determined by the following expression:

$$j_A(r, z) := S \cdot \frac{1}{I_{Ar\_norm}} \cdot \int_{R1}^{R2} \int_0^\pi \frac{4r'}{\pi} \cdot J_{Ar}(r') \cdot \frac{\cos(\alpha_s)}{2} \times \frac{z^2 + r^2 + r'^2 + 2rr' \cos(\varphi) + \left( \frac{z}{\cos(\alpha_s)} \right)^2 - r'^2 \cdot \sin^2(\varphi) - (-r - r' \cdot \cos(\varphi) - z \cdot \tan(\alpha_s))^2}{(z^2 + r^2 + r'^2 + 2rr' \cos(\varphi))^2} d\varphi dr \tag{3}$$

In this expression, the sputtering coefficient  $S$  is defined as a function of the discharge voltage  $U$ :

$$S := 0.4 \cdot \frac{U}{530} \tag{4}$$

Fig. 4 shows the calculated distributions of the aluminum film deposition rate at different distances from the magnetron. The diagram of the relative location of the magnetron target, the oxygen plasma activator, and the substrate is shown in Fig. 5. All calculations and experiments were performed with the magnetron current of 7.8 A, magnetron voltage of 520 V, and oxygen flow rate of 20 sccm.

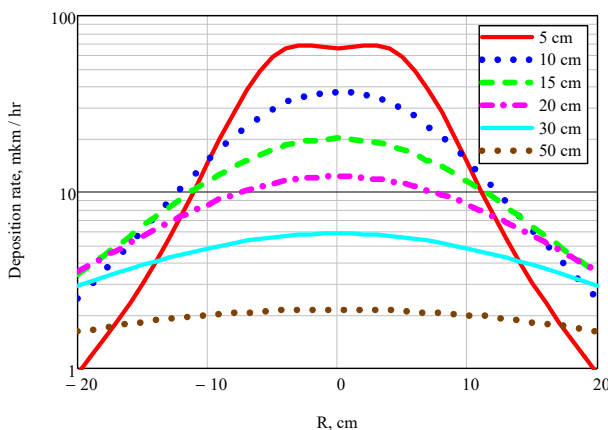


**Figure 4.** Calculated distributions of the aluminum film deposition rate in  $\mu\text{m/h}$  at different distances from the magnetron. The curves correspond to the following distances from the magnetron target (from top to bottom): 5, 10, 15, 20, 30, 50 cm

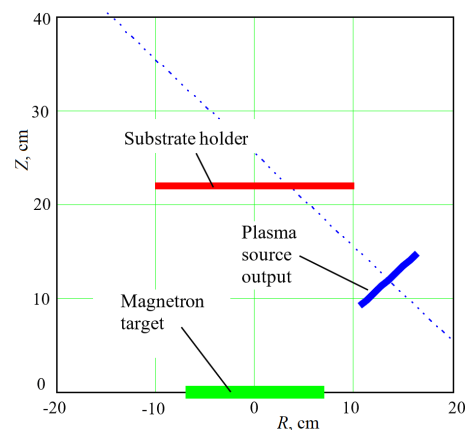


**Figure 5.** Schematic of the relative location of the magnetron target, the oxygen plasma activator, and the substrate. The dotted line shows the axis of the plasma activator. Coordinates are in cm

The molecular oxygen flux density at the point with coordinates  $r, z$  (the coordinate origin is in the center of the outlet of the plasma source) through the surface located at an angle  $\beta_s$  to the axis of the reactive gas activator is determined by an expression similar to (3):

$$j_{O_2}(r, z) := \int_0^{R_{O_2}} \int_0^\pi \frac{4r'}{\pi} \cdot J_{O_2} \cdot \frac{\cos(\beta_s)}{2} \times \frac{z^2 + r^2 + r'^2 + 2rr' \cos(\varphi) + \left(\frac{z}{\cos(\beta_s)}\right)^2 - r'^2 \cdot \sin(\varphi)^2 - (-r - r' \cdot \cos(\varphi) - z \cdot \tan(\beta_s))^2}{(z^2 + r^2 + r'^2 + 2rr' \cos(\varphi))^2} d\varphi dr \tag{5}$$

In this expression,  $R_{O_2} = 4$  cm is the radius of the plasma source,  $J_{O_2} := 1/\pi \cdot R_{O_2}^2$ .

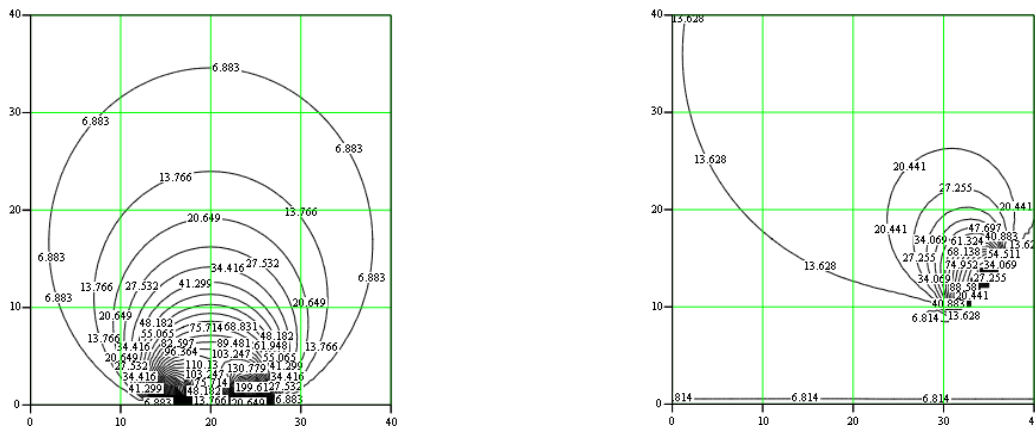
To convert the coordinates to the system with the origin in the center of the magnetron target, the following expression may be applied:

$$j'_{O_2}(r, z) := j_{O_2}[(r - x_{O_2}) \cdot \cos(\alpha_{O_2}) + (z - y_{O_2}) \cdot \sin(\alpha_{O_2}) - (r - x_{O_2}) \cdot \sin(\alpha_{O_2}) + (z - y_{O_2}) \cdot \cos(\alpha_{O_2})] \tag{6}$$

In addition, it is necessary to take into account the isotropic flow  $j_{O_{2ost}}$  of non-activated oxygen with the partial pressure  $p_{O_2}$  from the chamber to the substrate:

$$j_{O_{2ost}} := \frac{1}{4} \cdot e \cdot p_{O_2} \cdot 3.5 \cdot 10^{16} \cdot \sqrt{\frac{8 \cdot T}{\pi \cdot M}} \tag{7}$$

The calculated spatial distributions of aluminum and oxygen flux density on the substrate, which is perpendicular to the magnetron axis, are shown in Fig. 6.



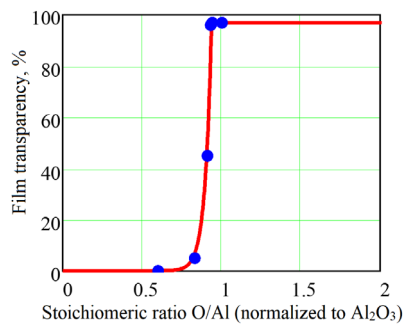


**Figure 7.** Experimental values of transparency (points) compared to analytical approximation (curve) depending on the stoichiometric ratio of oxygen and aluminum flows (taking into account the sticking coefficient)

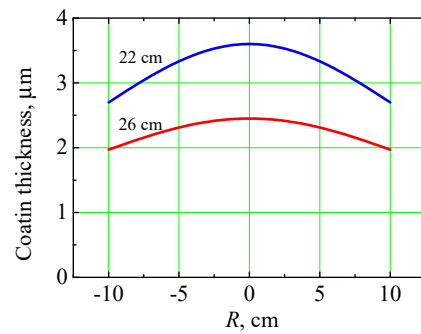


**Figure 8.** Calculated oxide coating thickness distribution along the 20 cm long substrate at different distances from the magnetron target

Thus, using the above expressions, we can calculate the stoichiometric ratio and transparency of the film at any point of the technological chamber at any size and relative location of the magnetron, the substrate, and the plasma activator of the reactive gas, and finally, at arbitrary process parameters. Fig. 9 shows the calculated spatial distributions of the stoichiometric ratio and transparency of the film in the process chamber. It can be seen that near the magnetron, where the flow of aluminum is high, it is impossible to obtain a stoichiometric film, at the same time there is a rather large region of stoichiometry, in which the samples should be placed during technological processes.

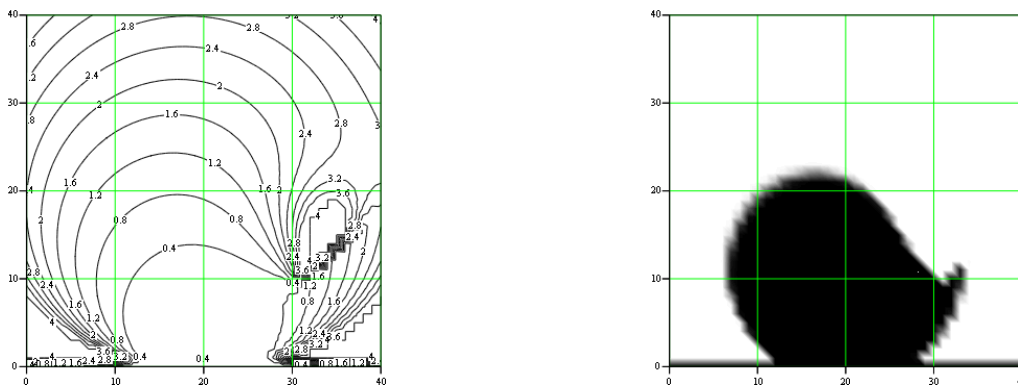


**Figure 9.** Spatial distributions of the stoichiometric ratio (left) and film transparency (right) in the technological chamber

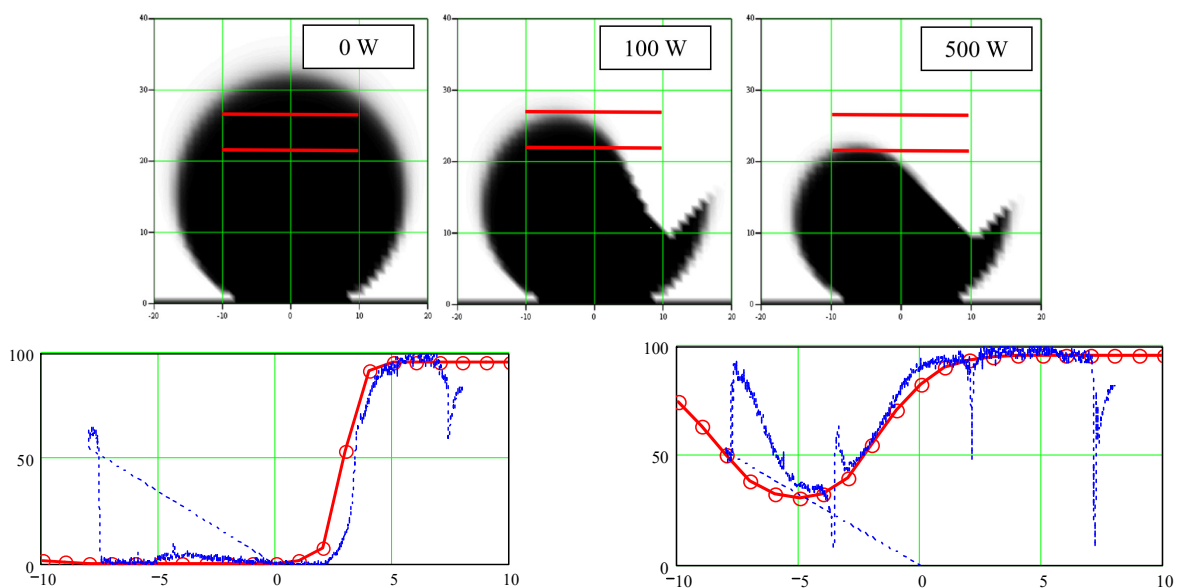


**Figure 10.** Comparison of experimental data on the spatial distribution of the coating transparency with the simulation results. In the upper figures, the calculated transparency is shown by grayscale. Two positions of the substrates are shown in red: 22 cm and 26 cm from the magnetron target. The lower pictures compare theoretical (red) and experimental (blue) transparency course along the sample for the distance of 22 cm (left) and 26 cm (right)

To verify the developed model, experiments were carried out on depositing an aluminum oxide film to glass substrates located at different distances from the magnetron target, followed by measuring the distribution of film transparency (at 600 nm wavelength) along the length of the substrate and comparing it with the calculated distribution. All the parameters were input into the model according to the experimental conditions, excluding the sticking coefficient for oxygen, which is predominantly unknown. Then, the sticking coefficient was iteratively fit to achieve the maximum possible accordance between the calculation result and the experimental data. The results of calculations, experiments, and their comparison are shown in Fig. 10.

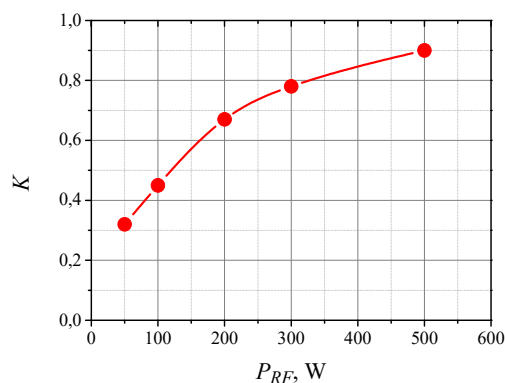


**Figure 11.** Dependence of the oxygen sticking coefficient on RF power supplied to the plasma activator

The obtained results allow us to find a very important principle of the process of plasma activation of reactive gas, namely the dependence of the oxygen sticking coefficient on the RF power supplied to the plasma activator. The found dependence is shown in Fig. 11. It is quite obvious that the sticking coefficient increases with increasing RF power input into the gas-activator plasma source and approaches almost unity at a power of 500 W or more. Thus, the further increase of RF power does not make sense, which is very important in view of the high price of powerful RF generators. To generalize the obtained results, it is possible to formulate the following empirical rule: the power ratio of the magnetron discharge and the plasma activator should be approximately 8:1.

### CONCLUSION

In this paper, we discussed the possibility of improvement of the technology of reactive magnetron sputtering by addition to the sputtering system of a dedicated plasma source activating the reactive gas being passed through the dense plasma inside the source. The source creates a flow of activated reactive gas directed towards the surface on which the oxide coating is deposited. It has been shown that when alumina coatings are deposited by reactive magnetron synthesis, the problem of the low sticking coefficient of molecular oxygen to the aluminum surface can be solved if sufficient RF power is input to the source. This possibility of plasma activation of reactive gas in the process of reactive magnetron synthesis of oxide coatings was theoretically and experimentally investigated. The theoretical model has been built that allows the calculation of spatial distributions of flows of metal and reaction gas, as well as the stoichiometry area of the synthesized coatings. Calculations were performed on the example of aluminum oxide. It was found that the plasma activation of the reactive gas allows to increase significantly the sticking coefficient of oxygen to the surface of the growing coating. In our experiments, the sticking coefficient changed from values less than 0.1 without additional gas activation to 0.9 when 500 W of RF power was introduced into the inductive discharge.

The developed model has been experimentally verified. In the experiments, an aluminum oxide film was deposited on glass substrates located at different distances from the magnetron target at different levels of RF power input. The resulting distribution of film transparency along the substrate was measured and compared with the simulation output. A comparison of the calculation results with the experimental data shows a good agreement in the entire studied range of parameters. Analyzing the obtained results, we formulated an empirical rule giving the way of estimation of the additional RF power required to reach the oxygen sticking coefficient close to unity. According to this rule, the optimal power ratio of the magnetron discharge and the plasma activator should be approximately 8:1.

### Acknowledgement

This work was supported by the National Research Foundation of Ukraine in the framework of the project 2021.01/0204.

### ORCID

✉Stanislav V. Dudin, <https://orcid.org/0000-0001-9161-4654>; ✉Stanislav D. Yakovin, <https://orcid.org/0000-0001-8588-8835>  
✉Aleksandr V. Zykov, <https://orcid.org/0000-0002-5409-2655>

### REFERENCES

- [1] L. Osterlund, I. Zoric, and B. Kasemo, Phys. Rev. B, **55**, 15, 452 (1997). <https://doi.org/10.1103/PhysRevB.55.15452>
- [2] J. Behler, B. Delley, S. Lorenz, K. Reuter, and M. Scheffler, Phys. Rev. Lett. **94**, 036104 (2005). <https://doi.org/10.1103/PhysRevLett.94.036104>

- [3] J.M. Schneider, and W.D. Sproul, in: *Handbook of Thin Film Process Technology*, edited by D.A. Glocker, and S.I. Shah, (Imprint CRC Press, Boca Raton, 1998), Ch. pA5.1, pp. 1-12.
- [4] M.K. Olsson, K. Macak, U. Helmersson, and B. Hjorvarsson, *J. Vac. Sci. Technol.* **16**, 639 (1998). <https://doi.org/10.1116/1.581081>
- [5] J. Walkowicz, A. Zykov, S. Dudin, S. Yakovin, and R. Brudnias, *Tribologia*, **6**, 163-174 (2006). [https://www.tribologia.org/ptt-old/trib/Tribol\\_6\\_2006\\_s\\_163\\_174.pdf](https://www.tribologia.org/ptt-old/trib/Tribol_6_2006_s_163_174.pdf)
- [6] R. Snyders, J.P. Dauchot, and M. Hecq, *Plasma Process. Polym.* **4**, 113–126 (2007). <https://doi.org/10.1002/ppap.200600103>
- [7] S. Yakovin, S. Dudin, A. Zykov, and V. Farenik, *Problems of Atomic Science and Technology*, **1**, 152-154 (2011). [https://vant.kipt.kharkov.ua/ARTICLE/VANT\\_2011\\_1/article\\_2011\\_1\\_152.pdf](https://vant.kipt.kharkov.ua/ARTICLE/VANT_2011_1/article_2011_1_152.pdf)
- [8] G. Primc, *Frontiers in Physics*, **10**, 895264 (2022). <https://doi.org/10.3389/fphy.2022.895264>
- [9] J.Y. Jung, Ph.D. thesis, *Optical modeling off-stoichiometric amorphous Al<sub>2</sub>O<sub>3</sub> thin films deposited by reactive sputtering*, University of Illinois, 2012. <https://core.ac.uk/download/pdf/4838787.pdf>

### ВПЛИВ ПЛАЗМОВОЇ АКТИВАЦІЇ РЕАКТИВНОГО ГАЗУ ПРИ РЕАКТИВНОМУ МАГНЕТРОННОМУ РОЗПИЛЕННІ

Станіслав В. Дудін, Станіслав Д. Яковін, Олександр В. Зиков

*Харківський національний університет імені В.Н. Каразіна  
майдан Свободи 4, Харків, 61022, Україна*

Теоретично та експериментально досліджено вплив плазмової активації реактивного газу на процес реактивного магнетронного синтезу оксидних покриттів з використанням ВЧ індукційного джерела плазми, яке створює потік активованого реактивного газу, спрямований у напрямку поверхні, на яку наноситься оксидне покриття. Реактивний газ проходить через щільну індуктивно зв'язану плазму, розташовану всередині джерела плазми, тоді як аргон подається через окремий канал поблизу магнетрона. Побудовано теоретичну модель, яка дозволяє розрахувати просторові розподіли потоків атомів металу та молекул активованого реакційного газу, а також розподіл стехіометрії синтезованих покриттів. Виконано розрахунки на прикладі оксиду алюмінію. Виявлено, що плазмова активація реактивного газу дозволяє збільшити коефіцієнт прилипання кисню до поверхні покриття, що зростає, від значень, менших за 0,1 для неактивованого молекулярного кисню, до 0,9 при введенні в індукційний розряд ВЧ потужності 500 Вт. Для перевірки розробленої моделі були проведені експерименти з нанесення плівки оксиду алюмінію на скляні підкладки, розташовані на різних відстанях від мішені магнетрона, з подальшим вимірюванням розподілу прозорості плівки по довжині підкладки та порівнянням його з розрахунковим розподілом. Порівняння результатів розрахунків з експериментальними даними демонструє добре узгодження в усьому дослідженому діапазоні параметрів. На підставі узагальнення отриманих результатів було сформульоване емпіричне правило, що співвідношення потужностей магнетронного розряду та плазмового активатора має бути приблизно 8:1.

**Ключові слова:** реактивний магнетронний синтез, індуктивно зв'язана плазма, плазмова активація реактивного газу, математичне моделювання

# INSTRUCTIONS FOR PREPARING MANUSCRIPT IN THE EAST EUROPEAN JOURNAL OF PHYSICS

Name A. Author<sup>a\*</sup>, Name B. Co-Author(s)<sup>b†</sup>

<sup>a</sup>Affiliation of first author

<sup>b</sup>Affiliation of second author (if different from the first Author)

\*Corresponding Author: [corresponding\\_authors@mail.com](mailto:corresponding_authors@mail.com)

†E-mail: [co\\_authors@mail.com](mailto:co_authors@mail.com)

Received June 25, 2023; revised August 25, 2023 accepted September 5, 2023

Each paper must begin with an abstract. The abstract should be typed in the same manner as the body text (see below). Please note that these Instructions are typed just like the manuscripts should be. The abstract must have at least **200-300 words**, supplying general information about the achievements, and objectives of the paper, experimental technique, methods applied, significant results and conclusions. Page layout: the text should be printed on the paper A4 format, at least **5 pages**, with margins of: **Top - 3, Bottom, Left and Right - 2 cm**. The abstract, keywords should be presented in **English** (only for foreign authors), and **Ukrainian**. The text should be prepared in “**doc**”, “**docx**” or **LaTeX** format (LaTeX Template is available at [periodicals.karazin.ua/eejp](http://periodicals.karazin.ua/eejp)).

**Keywords:** there, must, be, 5-10 keywords

**PACS:** specify PACS code(s) here

## INSTRUCTIONS

The text should be typed as follows:

- **title:** Times New Roman, 11 pt, ALL CAPS, bold, 1 spacing, centred;
- **authors:** name, initials and family names; Times New Roman, 11 pt, bold, 1 spacing, centred;
- **affiliation(s):** Times New Roman, 9 pt, italic, 1 spacing, centred;
- **abstract:** Times New Roman, 9 pt, 1 spacing, justified;
- **body text:** Times New Roman, 10 pt, 1 spacing, justified; paragraphs in sections should be indented right (tabulated) for 0.75 cm;
- **section titles:** Times New Roman, 10 pt, bold, 1 spacing, centred, without numbering, one line should be left, blank above section title;
- **subsection titles:** Times New Roman, 10 pt, bold, 1 spacing, centred, without numbering in accordance to the section (see below), one line should be left blank above subsection title;
- **figure captions:** width of the figure should be 85 or 170 mm, Figures should be numbered (**Figure 1.**) and titled below Figures using sentence format, Times New Roman, 9 pt, 1 spacing, centred (if one line) or justified (if more than one line); one line should be left blank below figure captions;
- **table captions:** width of the table should be 85 or 170 mm, Tables should be numbered (**Table 1.**) and titled above tables using sentence format, Times New Roman, 10 pt, 1 spacing, left, Tables should be formatted with a single-line box around the outside border and single ruling lines between rows and columns; one line should be left blank below tables;
- **equations:** place equations centred, numbered in Arabic: (1), flush right, equations should be specially prepared in **MathType** or “**Microsoft Equation**”, Times New Roman, 10 pt.

## Additional Instructions

Numerated figures and tables should be embedded in your text and placed after they are cited. Only sharp photographs and drawings are acceptable. Letters in the figures should be 3 mm high. The figures should be presented in one of the following graphic formats: jpg, gif, pcx, bmp, tif.

## REFERENCES

List of References must contain **at least 30% of articles published over the past 5 years** and **no more than 30% of links to their own work**. Cite References by number in AIP style (<https://aip.scitation.org/php/authors/manuscript>). Numbering in the order of referring in the text, e.g. [1], [2-5], etc. References should be listed in numerical order of citation in the text at the end of the paper (justified), Times New Roman, 9 pt, 1 spacing.

### Journal Articles

- [1] T. Mikolajick, C. Dehm, W. Hartner, I. Kasko, M.J. Kastner, N. Nagel, M. Moert, and C. Mazure, *Microelectron. Reliab.* **41**, 947 (2001), [https://doi.org/10.1016/S0026-2714\(01\)00049-X](https://doi.org/10.1016/S0026-2714(01)00049-X).
- [2] S. Bushkova, B.K. Ostafiychuk, and O.V. Copaiev, *Physics and Chemistry of Solid State.* **15**(1), 182 (2014), <http://page.if.ua/uploads/pcss/vol15/1501-27.pdf>. (in Ukrainian)
- [3] M. Yoshimura, E. Nakai, K. Tomioka, and T. Fukui, *Appl. Phys. Lett.* **103**, 243111 (2013), <http://dx.doi.org/10.7567/APEX.6.052301>

### E-print Resources with Collaboration Research or Preprint

- [4] M. Aaboud, et al. (ATLAS Collaboration), *Eur. Phys. J. C.* **77**, 531 (2017), <http://dx.doi.org/10.1140/epjc/s10052-017-5061-9>
- [5] Sjöstrand, et al., *Comput. Phys. Commun.* **191**, 159 (2015), <https://doi.org/10.1016/j.cpc.2015.01.024>
- [6] Boudreau, C. Escobar, J. Mueller, K. Sapp, and J. Su, (2013), <http://arxiv.org/abs/1304.5639>

### Books

- [7] S. Inoue, and K.R. Spring, *Video Microscopy: The fundamentals*, 2nd ed. (Plenum, New York, 1997), pp. 19-24.
- [8] I. Gonsky, T.P. Maksymchuk, and M.I. Kalinsky, *Біохімія Людини [Biochemistry of Man]*, (Ukrmedknyga, Ternopil, 2002), pp. 16. (in Ukrainian)

### Edited Books

- [9] Z.C. Feng, editor, *Handbook of Zinc Oxide and Related Materials: Devices and Nano Engineering, vol. 2*, (CRC Press/Taylor & Francis, Boca Raton, FL, 2012)

### Book Chapters

- [10] P. Blaha, K. Schwarz, G.K.H. Madsen, D. Kvasnicka, and J. Luitz, in: *WIEN2K. An Augmented Plane Wave Plus Local Orbitals Program for Calculating Crystal Properties*, edited by K. Schwarz (Techn. Universität Wien, Austria, 2001).
- [11] M. Gonzalez-Leal, P. Krecmer, J. Prokop, and S.R. Elliot, in: *Photo-Induced Metastability in Amorphous Semiconductors*, edited by A.V. Kolobov (Wiley-VCH, Weinheim, 2003), pp. 338-340.
- [12] A. Kochelap, and S.I. Pekar, in: *Теорія Спонтанної і Стимульованої Хемілюмінесценції Газов [Theory of Spontaneous and Stimulated Gas Chemiluminescence]* (Naukova dumka, Kyiv, 1986), pp. 16-29. (in Russian)

### Conference or Symposium Proceedings

- [13] C. Yaakov, and R. Huque, in: *Second International Telecommunications Energy Symposium Proceedings*, edited by E. Yow (IEEE, New York, 1996), pp. 17-27.
- [14] V. Nikolsky, A.K. Sandler, and M.S. Stetsenko, in: *Автоматика-2004: Матеріали 11 Міжнародної Конференції по Автоматичному Управлінню [Automation-2004: Materials of the 11th International Conference on Automated Management]* (NUHT, Kyiv, 2004), pp. 46-48. (in Ukrainian)

### Patent

- [15] I.M. Vikulin, V.I. Irha, and M.I. Panfilov, Patent Ukraine No. 26020 (27 August 2007). (in Ukrainian)

### Thesis / Dissertation

- [16] R.E. Teodorescu, Ph.D. dissertation, The George Washington University, 2009.

### Special Notes

1. Use International System of Units (SI system). 2. It is undesirable to use acronyms in the titles. Please define the acronym on its first use in the paper. 3. Refer to isotopes as <sup>14</sup>C, <sup>3</sup>H, <sup>60</sup>Co, etc.

Наукове видання

**СХІДНО-ЄВРОПЕЙСЬКИЙ ФІЗИЧНИЙ ЖУРНАЛ**

**Номер 3, 2023**

**EAST EUROPEAN JOURNAL OF PHYSICS**

**No 3, 2023**

Збірник наукових праць  
англійською та українською мовами

Коректор – Коваленко Т.О.  
Технічний редактор – Гірник С.А.  
Комп'ютерне верстання – Гірник С.А.

Підписано до друку 28.06.2023. Формат 60×84/8. Папір офсетний.

Друк цифровий.

Ум. друк. арк. 10,5. Обл.-вид. арк. 10,9

Тираж 50 пр. Зам. . Ціна договірна

Видавець і виготовлювач

Харківський національний університет імені В.Н. Каразіна

61022, Харків, майдан Свободи, 4

Свідоцтво суб'єкта видавничої справи ДК № 3367 від 13.01.09

Видавництво Харківський національний університет імені В.Н. Каразіна  
тел. +380-057-705-24-32